Author:
Gomez Rojas, Omar

Title:
The role of ionic liquids/deep eutectic solvents in sol-gel syntheses of complex metal oxides

The role of ionic liquids/deep eutectic solvents in sol-gel syntheses of complex metal oxides

By Omar Gómez Rojas

A dissertation submitted to the University of Bristol in accordance with the requirements of the degree of Doctor of Philosophy in the Faculty of Science, School of Chemistry, September 2018.

Project Supervisors

Dr. Simon R. Hall and Dr. Chris Bell.

Word count: 44625

Abstract

The wide range of interesting properties that metal oxides exhibit has always driven creative research in this area. Recently a new method for the synthesis of metal oxides has been reported, using ionic liquids as an effective metal cation solvent and chelating agent. Despite ionic liquids/deep eutectic solvents being extensively utilized in many different areas, these systems have not been widely used for their chelating properties as a route to synthesize high yields (> 98 %) metal oxides. This is mainly due to the high cost of the ionic liquid and the lack of ability to solubilize some water-insoluble metal salts, also, the lack of understanding of how these materials interact with the metal cation and which factors can be beneficial or detrimental for, the synthesis of single-phase metal oxides.

In this work we discuss the mechanism of action of this technique and demonstrate its efficacy as a means to synthesise single-phase strontium niobates of controlled stoichiometry. Also, the interaction between an ionic liquid, 1-ethyl-3-methylimidazolium acetate (emim)OAc, and biopolymers. It was demonstrated how they are intimately involved in the control of shape, size and crystallinity of a strontium niobate, and the direct involvement of the oxygen content of the resultant crystal composition in the synthesis of $YBa_2Cu_3O_{7-\delta}$ (YBCO) superconductor.

An extensive mechanistic study of the synthesis of the high temperature superconductor $YBa_2Cu_3O_{7-\delta}$ using different ionic liquids and deep eutectic solvents, as well as mono-molecular chelating agents is also presented. Key experimental factors required for the synthesis of a metal oxide were recognised, focussing on the identification of precursory phases and elements that will augment or disrupt the synthesis, thereby assuring finer control over the desired crystal composition.

Furthermore, it is presented for the first time the use of a deep eutectic solvent (DES), namely betaine:D-(+)-glucose which is capable of solubilize insoluble-in-water metal salts, like barium nitrate, and produce after calcination, high yields (>90 %) of $Bi_2Sr_2CaCu_2O_{8+x}$ (BSCCO or Bi-2212) superconductor. Moreover, the stability of the DES is studied along several days to comprehend how the evolution of the DES is directly involved in the synthesis of the metal oxide. Lastly, the synthesis of a new sodium strontium niobate crystal composition is reported, $Na_{0.1}Sr_{0.9}NbO_3$, via a choline chloride-based DES by forming, during the calcination process, high temperature-stable crystal compositions which, eventually will re-combine to form and entirely new crystal composition. Additionally, as a comparative analysis the synthesis is also studied via (emim)OAc.

Acknowledgments

I have always believed on what Mark Twain once said, “actions speak louder than words but not nearly as often”. Therefore, I just hope that by my future action I will demonstrate all the appreciation that I have for every human being and institutions involved in my personal growth as a scientist and person during my PhD. Thank you.

Author's declaration

I declare that the work in this dissertation was carried out in accordance with the Regulations of the University of Bristol. The work is original, except where indicated by special reference in the text and no part of the dissertation has been submitted for any other academic award.

Any views expressed in the dissertation are those of the author and in no way represent those of the University of Bristol.

The dissertation has not been presented to any other University for examination either in the United Kingdom or overseas.

Signed:

Omar Gómez Rojas

Date:05/12/2018

Table of Contents

CHAPTER 1

CHAPTER 2

CHAPTER 3

CHAPTER 4

CHAPTER 5

List of figures

List of tables

References of Figures & Table

A. Longo, E.; La Porta, F. D. A. *Recent Advances in Complex Functional Materials : From Design to Application*; Springer, 2017.

B. Ishizawa, N.; Marumo, F.; Kawamura, T.; Kimura, M. The Crystal Structure of $Sr_2Nb_2O_7$, a Compound with Perovskite-Type Slabs. *C. R. Acad. Sci. Paris, S~r. C C. R. Acad. Sci. Paris, S~r. C. Acta Cryst. Acta Cryst. B Tetrahedron Canad. J. Phys. Acta Cryst* **1973**, *644* (350), 260–261.

C. Levin, I.; Chan, J. Y.; Scott, J. H.; Farber, L.; Vanderah, T. A.; Maslar, J. E. Complex Polymorphic Behavior and Dielectric Properties of Perovskite-Related $Sr(Sr_{1/3}Nb_{2/3})O_3$. *J. Solid State Chem.* **2002**, *166* (1), 24–41.

D. Teneze, N.; Mercurio, D.; Trolliard, G.; Champarnaud-Mesjard, J. C. Reinvestigation of the Crystal Structure of Pentastrontium Tetraniobate, $Sr_5Nb_4O_{15}$. *Zeitschrift für Krist. - New Cryst. Struct.* **2000**, *215* (1), 11–12.

E. Ishizawa, N.; Marumo, F.; Kawamura, T.; Kimura, M. The Crystal Structure of $Sr_2Nb_2O_7$, a Compound with Perovskite-Type Slabs. *C. R. Acad. Sci. Paris, S~r. C C. R. Acad. Sci. Paris, S~r. C. Acta Cryst. Acta Cryst. B Tetrahedron Canad. J. Phys. Acta Cryst* **1973**, *644* (350), 260–261.

F. Marinder, B.-O.; Wang, P.-L.; Werner, P.-E.; Karvinen, S.; Niinistö, L.; Volden, H. V.; Weidlein, J.; Zingaro, R. A. Powder Diffraction Studies of $SrNb_2O_6$ and $SrNb_6O_{16}$. *Acta Chem. Scand.* **1986**, *40a*, 467–475.

G. Capponi, J. J.; Chaillout, C.; Hewat, A. W.; Lejay, P.; Marezio, M.; Nguyen, N.; Raveau, B.; Soubeyroux, J. L.; Tholence, J. L.; Tournier, R. Structure of the 100 K Superconductor $Ba_2YCu_3O_7$ between 5 to 300 K by Neutron Powder Diffraction. *Europhys. Lett.* **1987**, *3* (12), 1301–1307.

H. Sunshine, S. A.; Siegrist, T.; Schneemeyer, L. F.; Murphy, D. W.; Cava, R. J.; Batlogg, B.; van Dover, R. B.; Fleming, R. M.; Glarum, S. H.; Nakahara, S.; et al. Structure and Physical

Properties of Single Crystals of the 84-K Superconductor $Bi_{2.2}Sr_2Ca_{0.8}Cu_2O_{8+\delta}$. *Phys. Rev. B* **1988**, *38* (1), 893–896.

I. Hurley, F. H.; WIer, T. P. Electrodeposition of Metals from Fused Quaternary Ammonium Salts. J. Electrochem. Soc. **1951**, 98 (5), 203.

J. Wilkes, J. S. A Short History of Ionic Liquids—from Molten Salts to Neoteric Solvents. *Green Chem.* **2002**, *4* (2), 73–80.

K. Smith, E. L.; Abbott, A. P.; Ryder, K. S. Deep Eutectic Solvents (DESs) and Their Applications. *Chem. Rev.* **2014**, *114* (21), 11060–11082.

L. Yong Z., Antonietti, M. Synthesis of Very Small TiO_2 Nanocrystals in a Room-Temperature Ionic Liquid and Their Self-Assembly toward Mesoporous Spherical Aggregates. *J. Am. Chem. Soc.*, **2003**, 125 (49), pp 14960–14961**.**

M. Hideaki I.; Kensuke N., Chujo, Y. Synthesis of Gold Nanoparticles Modified with Ionic Liquid Based on the Imidazolium Cation. *J. Am. Chem. Soc.*, **2004**, 126 (10), 3026–3027.

N. Yong Z., Jan H. S., Antonietti, M. Room-Temperature Ionic Liquids as Template to Monolithic Mesoporous Silica with Wormlike Pores via a Sol−Gel Nanocasting Technique. *Nano Letters*, **2004**, 4 (3), 477–481.

O. Antonietti, M.; Kuang, D.; Smarsly, B.; Zhou, Y. Ionic Liquids for the Convenient Synthesis of Functional Nanoparticles and Other Inorganic Nanostructures. *Angew. Chemie Int. Ed.* **2004**, *43* (38), 4988–4992.

P. Zhou, Y.; Antonietti, M. A Novel Tailored Bimodal Porous Silica with Well-Defined Inverse Opal Microstructure and Super-Microporous Lamellar NanostructureElectronic. *Chem. Commun.* **2003**, 1 (20), 2564.

Q. Celorrio, V.; Calvillo, L.; van den Bosch, C. A. M.; Granozzi, G.; Aguadero, A.; Russell, A. E.; Fermín, D. J. Mean Intrinsic Activity of Single Mn Sites at $LaMnO_3$ Nanoparticles Towards the Oxygen Reduction Reaction. *ChemElectroChem* **2018**, 5 (20), 3044-3051.

R. Gobaille-Shaw, G. P. A.; Celorrio, V.; Calvillo, L.; Morris, L. J.; Granozzi, G.; Fermín, D. J.

Effect of Ba Content on the Activity of $La_{1-x}Ba_xMnO_3$ Towards the Oxygen Reduction Reaction. *ChemElectroChem* **2018**, *5* (14), 1922–1927.

S. Boston, R.; Foeller, P. Y.; Sinclair, D. C.; Reaney, I. M. Synthesis of Barium Titanate Using Deep Eutectic Solvents. *Inorg. Chem.* **2017**, *56* (1), 542–547.

T. Patil, H. R.; Murthy, Z. V. P. Ionic Liquid Assisted Vanadium Pentoxide Synthesis through Sol-Gel Method: Catalyst Support for Broad Molecular Weight Distribution Polyethylene Synthesis. *Arab. J. Chem.* **2016**,1.

U. Ji, X.; Tang, S.; Gu, L.; Liu, T.; Zhang, X. Synthesis of Rod-like Mesoporous γ-Al_2O_3 by an Ionic Liquid-Assisted Sol–gel Method. *Mater. Lett.* **2015**, *151*, 20–23.

V. Soll, S.; Antonietti, M.; Yuan, J. Poly(Ionic Liquid) Nanoparticles as Novel Colloidal Template for Silica Nanocasting. *Polymer (Guildf).* **2014**, *55* (16), 3415–3422.

W. Chen, A.; Li, Y.; Liu, L.; Yu, Y.; Xia, K.; Wang, Y.; Li, S. Controllable Synthesis of Nitrogen-Doped Hollow Mesoporous Carbon Spheres Using Ionic Liquids as Template for Supercapacitors. *Appl. Surf. Sci.* **2017**, *393*, 151–158.

X. Green, D. C.; Glatzel, S.; Collins, A. M.; Patil, A. J.; Hall, S. R. A New General Synthetic Strategy for Phase-Pure Complex Functional Materials. *Adv. Mater.* **2012**, *24* (42), 5767–5772.

Y. Levin, I.; Chan, J. Y.; Scott, J. H.; Farber, L.; Vanderah, T. A.; Maslar, J. E. Complex Polymorphic Behavior and Dielectric Properties of Perovskite-Related $Sr(Sr_{1/3}Nb_{2/3})O_3$. *J. Solid State Chem.* **2002**, *166* (1), 24–41.

Z. Boury, B.; Plumejeau, S. Metal Oxides and Polysaccharides: An Efficient Hybrid Association for Materials Chemistry. *Green Chemistry*, **2015**, 17, 72–88.

AA. Dai, S.; Ju, Y. H.; Barnes, C. E. Solvent Extraction of Strontium Nitrate by a Crown Ether Using Room-Temperature Ionic Liquids. *J. Chem. Soc. Dalt. Trans.* **1999**, *0* (8), 1201–1202.

Chapter 1
Introduction

Parts of this chapter are published in the references indicated below printed in CrystEngComm or Materials Chemistry and Physics. The papers used in the creation of this chapter was written and submitted by myself involving the preparation of all figures and text contained herein.

Gómez Rojas, O.; Song, G.; Hall, S. R. Fast and Scalable Synthesis of Strontium Niobates with Controlled Stoichiometry. *CrystEngComm* **2017**, *19* (36), 5351–5355.

Gómez Rojas, O.; Hall, S. R. On the Synergistic Interaction of an Ionic Liquid and Biopolymers in the Synthesis of Strontium Niobate. *Mater. Chem. Phys.* **2017**, *202*, 220–224.

Gómez Rojas, O.; Sudoh, I.; Nakayama, T.; Hall, S. R. The Role of Ionic Liquids in the Synthesis of the High-Temperature Superconductor $YBa_2Cu_3O_{7-\delta}$. *CrystEngComm* **2018,** 20, 5814-5821.

1.1 Complex functional materials.

Since the first time the human kind was capable to mould raw materials into valuable tools, functional materials have been playing a crucial role in our society's evolution (Figure 1.1).[1]

Figure 1.1. Example of the evolution of functional materials along the human history.

A functional material has to fulfil certain criteria. Firstly, it most has the means to accomplish its purpose, and secondly it has to be able to process and adapt to an external variable. Consequently, the physico-chemical properties are sensitive to changes in the surroundings such as temperature, pressure, electric field, magnetic field, optical wavelength, adsorbed gas molecules and pH.[2]

During the last century, materials scientists focused heavily on understanding and finding possible applications of structurally simpler materials consisting in one or two elements of the periodic table. However, developments such as the discovery of high-temperature superconductors has drawn wide attention into multicomponent compounds with more complicated assemblies.[1]

Functional materials cover a plethora of organic and inorganic materials however, in this thesis, focus will be given to metal oxides. At the end of the 1980s it was estimated that around 24 000 inorganic phases were discovered. Among them 16 000 are binary and about 8 000 belong to more complicated systems, namely ternary compounds.[1]

If 60 elements of the periodic table are chosen, the number of possible ternary systems turns out to be around 34 000. Subsequently, the number of possible quaternary and more complex functional materials will exponentially grow. Within each different system, diversity of arrangements of the same elements in different quantities naturally give rise to a myriad of different structures and properties.[1]

Every exploratory process of new compounds can be divided in three main steps.[1]

- Synthesis
    - Process utilized to generate novel compounds.
- Materials diagnostics
    - Check and confirm the formation of the intended material.
- Rapid characterization of their physico-chemical properties
    - Ranging from superconductivity, electrical and dielectric, magnetic, mechanical, and thermal.

To create new materials, it is highly preferable to have a variety of synthetic routes which can be used to create a broad range of new compositional samples.

Searching new routes to prepare novel materials as well as understanding the relationship between the structures and properties is of equal importance. To assure success and to achieve superior properties it is essential to have careful control over the structure and composition of the resulting material.

Among the wide variety of complex functional materials ceramics are perhaps the class of material with the broadest diversity of functions for different applications. In these materials slight variations of their intrinsic characteristics, such as the lack of centre of symmetry, crystalline anisotropy, spontaneous and reversible-oriented dipoles, degree of order-disorder, bandgap energy, and the presence of intrinsic or promoted defect by former or modifier lattice, will derive in a diversification of properties.[3]

Apart from the functionality belonging to certain crystal structure (symmetry and atom distribution) valences of the elements (how elements are bonding each other), play also a crucial role. Thermodynamically, the most stable phases will be formed and, such stability is strongly affected by the bonding within elements. Therefore, the enthalpy of the system is defined by the bonding of the atoms meanwhile the entropy by the atomic lattice arrangement of the crystal.[2]

It is understandable that the electronic structure of a single element will vary when in interaction with another element to form a more complex compound, due to transfer and/or sharing of valence electrons among atoms; how these electrons are allocated and interchange is described by molecular orbitals. Therefore, valences states and molecular orbits are responsible for the inherent properties of a material detailing the electronic structure and the spatial distribution of atoms. Theoretical approaches such as the ligand field theory is used to elucidate the special assembly of atoms, whilst the molecular orbital theory and band structure theory are used to disclose the relationship between the structure and the properties.[2]

40 elements are capable of forming mix valent compounds, transition d-block elements and lanthanides, e.g. Yb, Nb, Eu, Tb, Ce. Consequently, compounds with these elements can form multivalent products where, an element holds different valence states but each one only has a single valence.[2]

Crystal structure can be altered by changing the spatial distribution of atoms (bonding angles, bonding lengths and symmetry of atom arrangement), but also by modifying the overall chemical composition (stoichiometry).[2]

1.2 Metal Oxides

Oxides are composed of a metal cation, positively charge, interconnected in a lattice of oxygen anions, O^{-2}. The number of oxygens coordinating a metal cation is determined by the size of the ionic radius of the metal. The ionic model gives a good insight of the size of the ionic radii however, reality shows that the size depends strongly upon the crystal surroundings.[4]

Small atoms, if oxygen packed either face-centred cubic (fcc) or hexagonal close packed (hcp), with a spherical cation radius approximatly to 32 pm ($r_{tet}= ((3/2)^{1/2} – 1)r_o$), is resolved in a tetrahedral arrangement with 4-fold coordination anions. On the other hand, for atoms with bigger atomic radius approximately 58 pm ($r_{oct}= ((2)^{1/2} – 1)r_o$), an octahedral arrangement with 6-fold coordinating anions is preferred. Here r_o is taken to be 140 pm (Pauling's O^{-2} ion radius),[5] is important to bear in mind that the example given above considers the ions as hard spheres and does not take in account possible distortions.

In general, bigger atoms require bigger holes, consequently, the coordination number has to increase to produce geometrical arrangements with more internal capacity. Following this principle there are several coordination geometries, e.g. the aforementioned tetrahedral 4-fold coordinated, octahedral with 6-fold coordinated and distortions of the octahedral arrangement, square planar with 4-fold coordinated but all the anions in the same plane, and cubic 8-fold coordinated.[4]

The determinants of a crystal structure are the stoichiometry, relative number of different type of atoms and the coordination of ions. Moreover, for simplicity the crystal structures can be described based on well stablish equivalent crystal structures, for instance cuprite, antifluorite, rock salt, zincblende, wurtzite, PbO, spinel, corundum, fluorite, perovskite, and layer perovskite to mention some.[4]

1.3 Crystal structure of some strontium niobates, YBCO (123) and Bi (Bi-2212) superconductors

Strontium niobates have been widely studied for several reasons and find application in a wide range of areas. One of the most interesting yet to be exploited is the possibility of forming a new family of high temperature superconductors.[6] A strontium niobate was also the first metallic oxide-type material to be used as an effective photocatalyst[7,8]. Further properties that this materials exhibit range from large thermal expansion coefficients and low thermal conductivity[9], high frequency dielectric properties,[10] piezoelectric and electro-optic properties,[11,12] and photoluminescence.[13] Also, strontium niobates find use as the key component in diamagnetic insulators,[14] and ferroelectrics.[15,16] Such diversity is generated from the two possible arrangements of the NbO_6 octahedra, giving rise to perovskites, ABO_3, and pyrochlore, $A_2B_2O_7$, crystal structures.[17]

The perovskite (Figure 1.2 left) crystal structure can be expressed with the formula ABX_3 where A is normally occupied by an alkaline metal or rare earth, and B by transition metals. X when perovskites are in the form of oxides, refers to oxygen atoms. It is through them that a dense packing forming octahedral (BX_6) clusters bonded through the vertices are acquire. On the other hand, A is coordinated by 12 X anions which form cuboctahedral (AX_{12}) clusters. [3]

The pyrochlore (Figure 1.2 Right) is a superstructure derived of the simple fluorite structure (CaF_2) and can be identified by the formula $A_2B_2X_7$. In this crystal structure the B cation forms an octahedral array with 6 oxygen atoms. The A cation is coordinated by 12 oxygen atoms, forming a face cubic centre cation array. This type of crystal structure grows only in the (110) plane therefore those lattice parameters are double to that comprehended by CaF_2.[5,11]

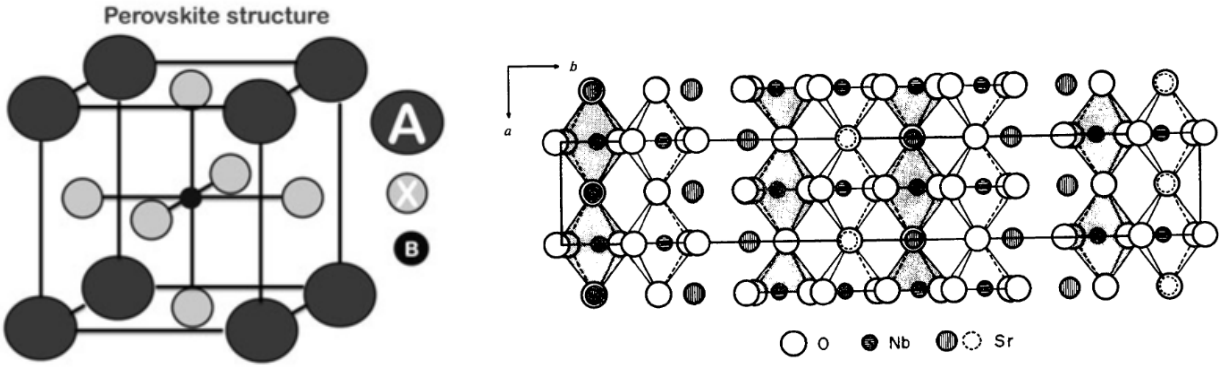

Figure 1.2. Left[3]: Representation of perovskite structure. Right[11]: Representation of a pyrochlore structure with Sr as A, Nb as B and O as X.

1.3.1 $Sr_4Nb_2O_9$

First off, this crystal composition arrays in two thermodynamically stable structures (polymorphs). Both structures were found to exist either above or below T = 1250 °C. The high temperature polymorph (HT) exhibits a cubic structure (Fm3m, a ≈ $2a_c$, where "c" refers to the cubic ~ 4 Å perovskite unit cell). The ordering belongs to NaCl-type with Sr^{2+} and Nb^{5+} on the B sites. The low temperature (LT) polymorphic structure is monoclinic ($P2_1/n$, $a \approx 6a_c\sqrt{3}$, $b \approx 2a_c\sqrt{2}$, $c \approx a_c\sqrt{6}$, $\beta \approx 90°$) with different but not identified B-cation arrangement. HT-$Sr_4Nb_2O_9$ crystals when annealed at 900 °C shown remarkably complex and structural behaviour. However, it was stablished via compositional analysis that at least 4 different crystal compositions were displayed (Figure 1.3). This crystal structures can not be considered as polymorphs but rather metastable crystal phases with slight differences in composition.[18]

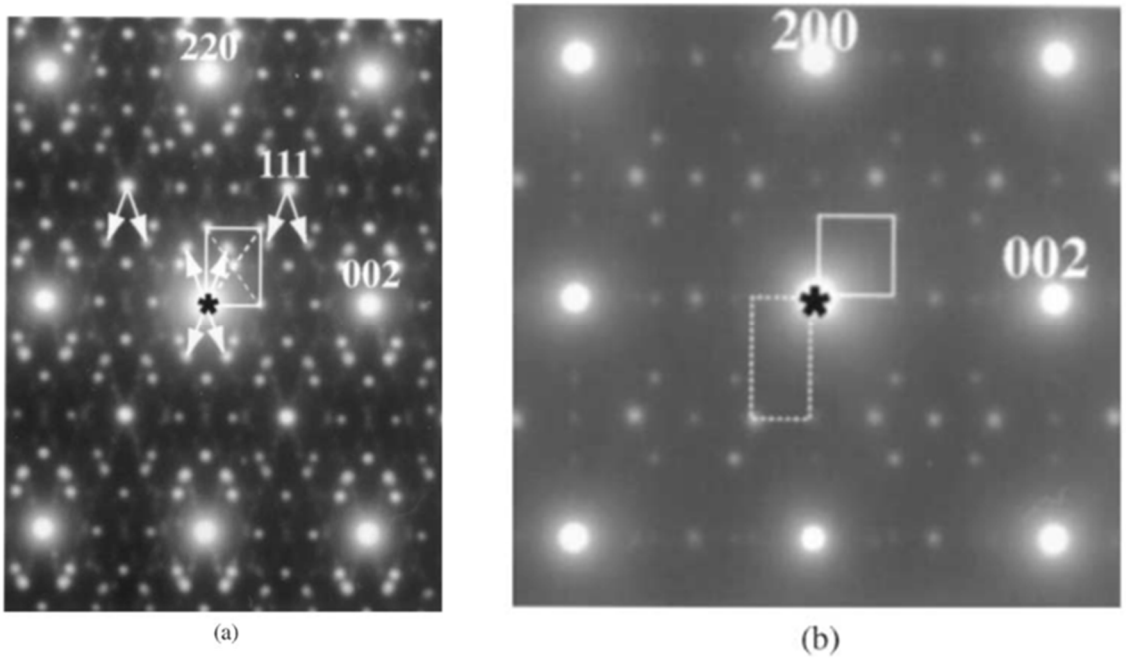

Figure 1.3. [18] SAED patterns in the [110] and [001] orientations proving the existence of slightly different crystals structures due to minimum changes in the stoichiometry of the analogue $Sr_4Nb_2O_9$ crystal composition. In the [001] orientation, the extra reflections of one of the four metastable phases is producing a centred rectangular pattern outlined in the figure.

1.3.2 $Sr_5Nb_4O_{15}$

This crystal structure (Figure 1.4) belongs to the homologous series of complex oxides with cation-deficient perovskite-related assembly with trigonal symmetry ($A_nB_{n-1}C_{3n}$). $P\bar{3}c1$as the symmetry group comes along due to the global rotation of the NbO_6 octahedra (~ 15°) around the *c* axis doubling its value. Rotations of the octahedra are needed to provide the correct stabilisation of Sr^{2+} cation with a [6 + 3] coordination without provoking a distortion of the octahedral arrangement. Moreover, due the ionic radius of Sr^{2+}, 9-fold coordination suits better than the [12] coordination.[19]

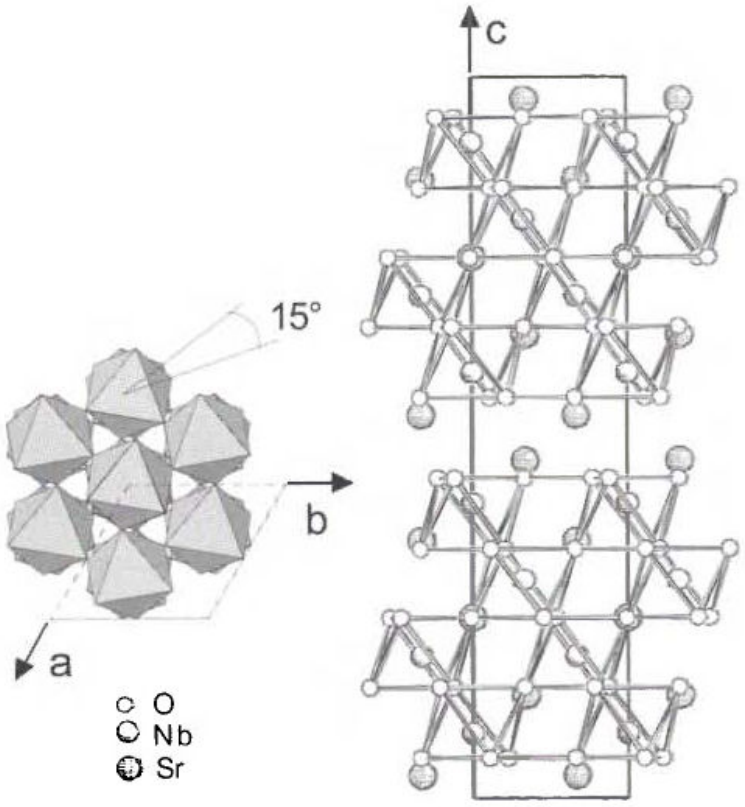

Figure 1.4.[19] Graphic representation of (left) the global rotation of the NbO_6 octahedra (~ 15°) and (right) the $Sr_5Nb_4O_{15}$ crystal structure.

1.3.3 $Sr_2Nb_2O_7$

The crystal structuration (Figure 1.5) of this composition forms slabs with a distorted perovskite-type structure separated by planes of O atoms. $Sr_2Nb_2O_7$ is orthorhombic with the symmetry group $Cmc2_1$ with *a*= 3.933 Å, *b*= 26.726 Å and *c*= 5.683 Å. The slab formation is composed by NbO_6 octahedral and Sr atoms. One Sr^{2+} atom is [12] coordinated by neighbouring oxygens, whereas the Sr^{2+} belonging to the boundaries is only [7] coordinated surrounded by 5 atoms of oxygen from the same slab and 2 from the neighbouring slab.[11]

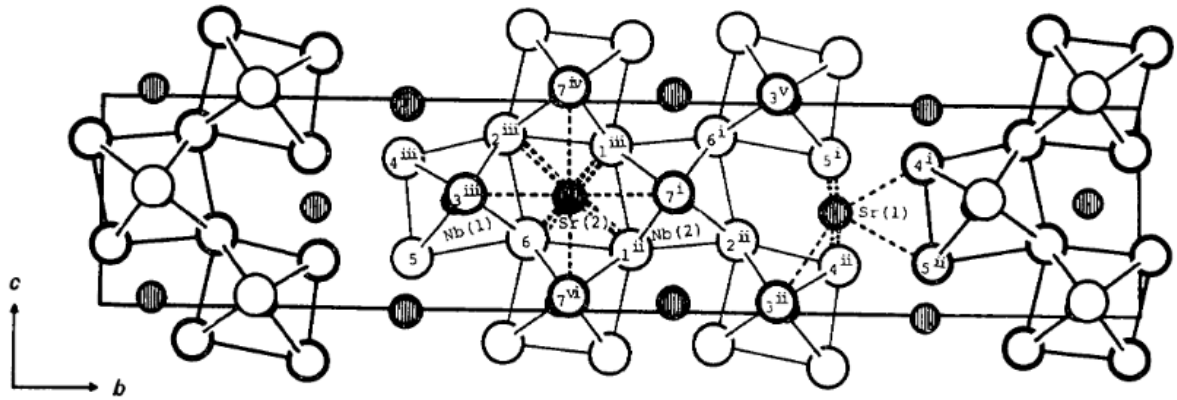

Figure 1.5.[11] Graphic representation of the crystal structure of $Sr_2Nb_2O_7$ viewed along *a* axis.

1.3.4 $SrNb_2O_6$

Better described by the formula $XSrO\text{-}YNb_2O_5$ where X/Y = 1/3. This crystal composition (Figure 1.6) possesses also polymorphic behaviour exhibiting two possible configurations. For the monoclinic, pseudo-orthorhombic, configuration with space group P21/c the cell dimensions are *a*= 7.72 Å, *b*= 5.59 Å and *c*= 10.98 Å.[20] To obtain the second polymorph temperature above 1450 °C for 96 hours is needed, and the symmetry belongs to a tetragonal system with cell parameters of *a*= 12.53 Å and *c*= 3.88 Å with a possible space group of P4/mmm, $P\bar{4}2m$ or $P\bar{4}m2$.[21]

Differently from a standard orthorhombic system the monoclinic version is built up by two different crystallographically independent NbO_6 octahedra, sharing edges and corners. The Sr atoms are [8] coordinated by oxygen atoms. Besides, the size of the ionic radii of Sr seems to be the cause of the monoclinic deviation due to lack of interstitial space in the tunnels for strontium ions to fit.[20]

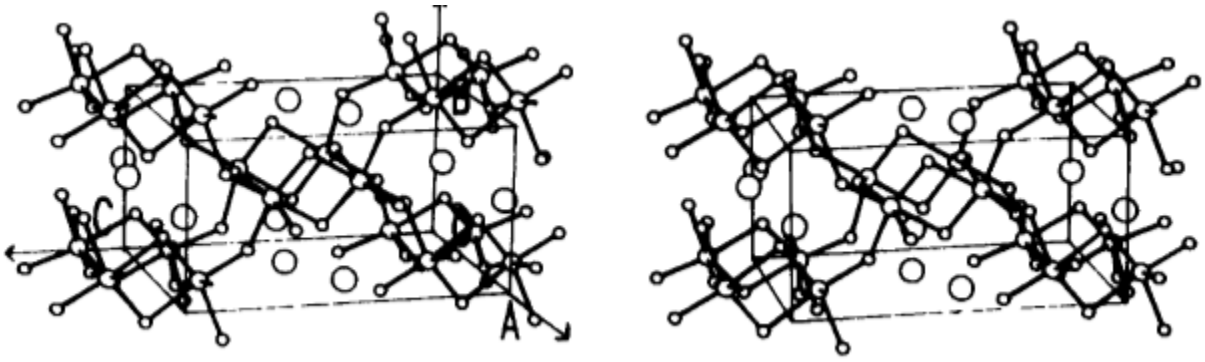

Figure 1.6.[20] Stereo view of monoclinic $SrNb_2O_6$. Large circles belong to Sr, medium circles to Nb and the smallest circles represent O.

1.3.5 $SrNb_6O_{16}$

The crystal lattice parameters were obtained from a mixed powder diffraction pattern, aside that it was possible to establish the unit cell dimensions, being *a*= 3.95 Å, *b*= 10.18 Å and *c*= 14.79 Å with Amm2 symmetry group.[20] The structural (Figure 1.7) determination was carried out using an analogue crystal phase, i.e. $NaNb_6O_{15}F$, consisting in one niobium atom, forming a pentagonal bipyramid, surrounded by 5 other niobium atoms with octahedra geometry bonded with oxygen and sharing edges with the centre atom.[20,22]

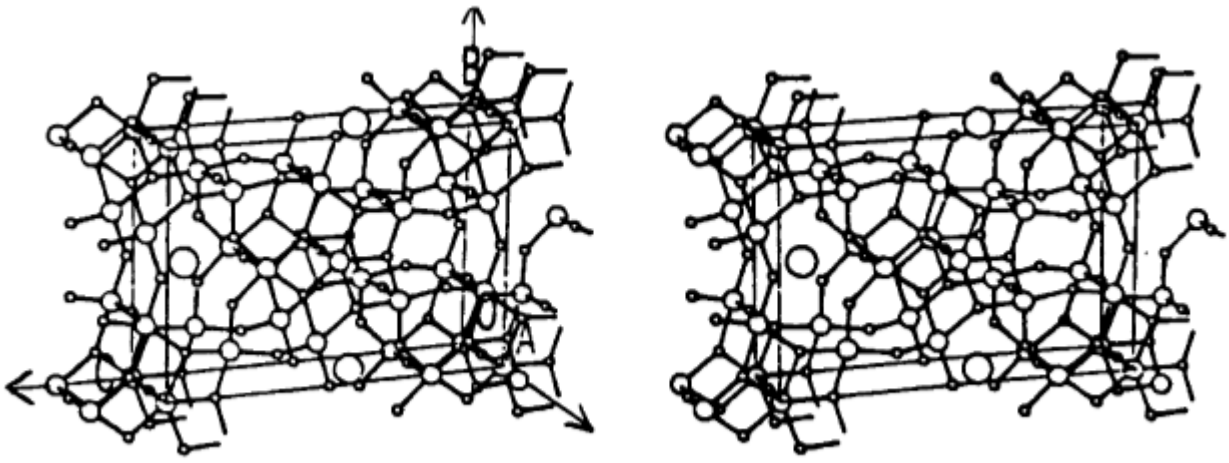

Figure 1.7[20] Stereo view of monoclinic $SrNb_6O_{16}$. Large circles belong to Sr, medium circles to Nb and the smallest circles represent O.

1.3.6 $YB_2C_3O_{7-x}$ (Y-123) and $Bi_2Sr_2CaCu_2O_{8+x}$ (BI-2212) superconductors

The synthesis of cuprate compounds is achievable due to two main properties of such complex materials[23]:

- The current ability of the perovskite structure AMO_3 to interact with rock salt type structures AO, cubic structure with each atom [6] coordinated, forming intergrowths $(AMO_3)_m(AO)_n$
- The inherent property of Cu to form coordination smaller than six, specifically square planar coordination and pyramidal, [4] and [5] respectively.

1.3.6.1 Y-123

$YBa_2Cu_30_{9-\delta}$ (δ=2.1+0.05) is categorized as a distorted, oxygen-deficient multi-layered perovskite with orthorhombic arrangement with Pmmm as the symmetry group. The unit cell (Figure 1.8) parameters can be accounted as a = 3.82 Å, b = 3.89 Å and c = 11.67 Å. $YBa_2Cu_3O_{7-x}$, better known as "123" has a triple perovskite structure with Ba and Y as A cations along the c-axis, tripling it, coordinated by ten and eight oxygen atoms correspondingly. On the other hand, copper is [5] and [4] coordinated forming pyramids and squares accordingly with the Cu atoms sitting at the centre of the rhombus-like squares.[24–26]

Slight changes in the crystal composition can also exhibit polymorphism triggered by changes in oxygen concentration, following the structural formula of $YBa_2Cu_3O_{7-x}$ then $0.3 < X > 0.5$. This polymorph has a tetragonal arrangement with P4/mmm symmetry group however, it does not exhibit superconductivity. This information will be cover with more detail further on.[26,27]

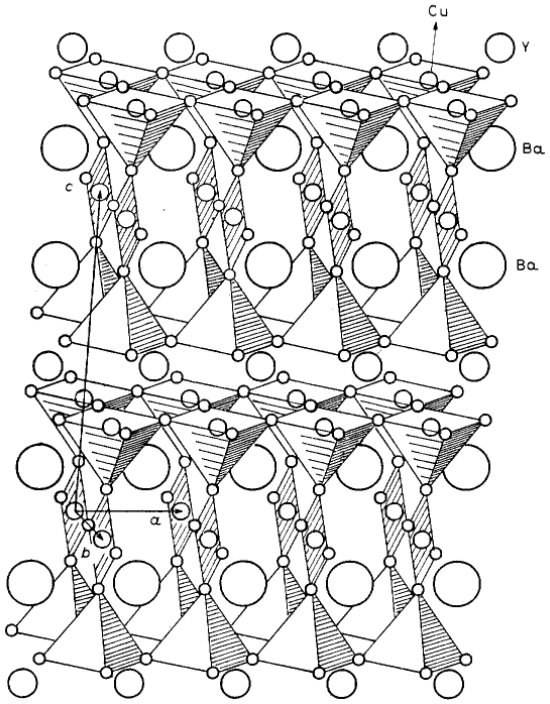

Figure 1.8.[25] Graphic representation of the structure of YBCO (Y-123) showing the CuO_5 pyramids and CuO_4 squares.

1.3.6.2 BI-2212

Crystal Bi-Sr-Ca-Cu-O can form three superconductive phases, namely Bi-2201, Bi-2212 and Bi-2223. Bi-2212 (Figure 1.9) has an orthorhombic unit cell with parameters equal to a & $b \approx 5.4$ Å and c= 30.89 Å with Fmmm space group. [28,29] Crystal formation in this system exhibits incommensurate super lattice owing the sheared stacking of the unit cells. Consequently, the unit cell has double Bi-O planes, octahedral coordination with 6 oxygen atoms in a rock salt type structure, which stack with a shift of (½ ½ z) with respect to the origin. Calcium atoms are in between the copper planes, [8] coordinated, which are equivalent to that observed with Y in the YBCO superconductor. Cooper also exhibits equivalent coordination with a pyramidal 5 oxygen coordination. Sr in [9] coordinated directly above and below the cooper sheets.[23,28–30]

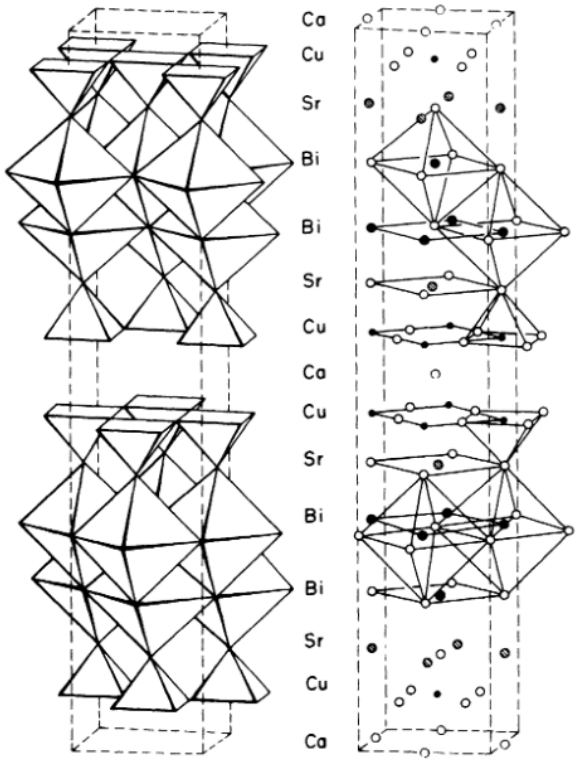

Figure 1.9.[28] Two graphical representations of the Bi-2212 sub-cell. CuO_5 pyramids are also observed.

1.4 Synthesis processes

Taking in to account the comprehensive parameters that define the functionality and efficiency, it is safe to state that the synthetic procedure is important.

The rapid progress of technological developments demands the discovery of new synthetic routes to create new materials with high efficiency. As a result of this, different synthetic approaches have been developed, among which solid-state reactions are without doubt the most commonly used, with well-established conditions and a fairly simple methodology. A feature of these reactions is that mass transport tends to be poor however and therefore formation of the desired target phase may require long synthesis times or simply may not occur. An alternative route is the hydrothermal method. Some key features of this process are the ability to synthesize ultrafine particles; morphology can be relatively controlled to some

extent through tuning pressure or temperature and control over stoichiometry is possible through reducing or oxidizing atmospheres, provided via adding extra components or gases.[31]

Recently, work has been done on the combination of sol–gel and hydrothermal methods. Combining features of both techniques, the sol–gel-hydrothermal method has achieved very interesting results in synthesis of metal oxides. [32,33]This technique has become an attractive tool as advantages range from a high degree of crystallinity, good control over the morphology, high purity and a more even particle size distribution, coupled with a reduction of time and temperature needed to obtain such materials. [34,35] Disadvantages come however from the complexity of the synthesis and a poor understanding of the mechanism of action as it is hard to monitor the reaction process in an enclosed environment.

Another interesting alternative method to synthesize complex functional materials is the molten salt synthesis (MSS). Compared to solid state reactions, MSS lowers significantly the reaction temperature as it allows faster mass transport in the liquid phase. Furthermore, MSS is good at solvating metals and oxides at high temperature owing to a destabilization of bonding by the strong polarizing forces provided by the salt melts. MSS has the additional advantage of low cost and low toxicity as well as abundant availability.[36]

Perhaps the most actively researched method in recent years is sol–gel chemistry. Broadly, is the preparation of inorganic phases from a transformation of liquid precursors to a sol and finally to a network structure called a gel. [37] Sol–gel chemistry has been widely used due to its ability to generate chemically homogeneous precursors allowing atomic level mixing of reagents. It is worth noting however that this does not ensure homogeneity throughout a reaction; having randomly well-distributed precursors does not necessarily guarantee an optimal reaction process.

Human evolution has been characterized by the constant capacity to improve the tools used to modify our environment. Synthetic protocols to create novel materials and or improve the already obtained, reducing the expenses and time invested, has not been the exception. Ionic liquids have taken that role.

1.5 History of ionic liquids

Ionic liquids have been known by different nomenclature throughout their history. Among them "molten salts" is the predominant term however, some differences between an ionic liquid and a molten salt can be highlighted. First off, molten salts are mainly liquid above certain temperature which tends to be higher than any organic compound can withstand (NaCl > 800 °C, KCl > 770 °C, LiCl > 600 °C, as some of the most commonly used).[38–42] Another feature exhibited by the ionic liquids that is not often seen in higher temperature molten salts is the strong ion-ion interaction.[43]

An ionic liquid can be defined as a non-conventional molten salt with melting point below the boiling point of water yet, this definition is rather arbitrary and has no true physical meaning. Such definition has become largely accepted mainly because it represents a condition at which these systems are easier to handle than salts that melt at higher temperatures. Moreover, the fact that are liquid at lower temperatures make them suitable for vast more applications. Based on this definition ionic liquids can be covered by synonyms such as "room temperature molten salt"[44] or "low temperature molten salt"[45]. Another label use to catalogue these systems is "neoteric solvent". Neoteric solvent refers as to a new type of solvents, or older, that are finding new applications. Based on the definition of an ionic liquid, stablish above, a brief historical literature review is presented.[43]

1.5.1.1 Ionic liquids.

The origin of the ionic liquids comes without doubt from traditional high temperature molten salts. Like every system, molten salts display serval properties that justify their use as reaction media. First and foremost, the great thermal, chemical, and electrochemical stability shown by salts. Secondly, due to such thermal stability and non-volatility, inorganic molten salts have a very wide liquidus range. Finally, inorganic salts tend to be rather cheap and are available in large amounts as are found in the form of natural minerals. However, there are also reasons not to use them. As stated above to produce a molten salt high temperature is required, for instance the popular "low-melting" alkali halide eutectic mixture LiCl-KCl has a melting point at 355 °C. The conditions therefore required imply that only a limited range of reactions can be done via these systems due to materials incompatibilities, i.e. thermal stability/decomposition. Moreover, considerable energy cost has to be taken in account as to maintain the high temperature. Owing to very specific conditions molten salt chemistry is generally unfamiliar and, in most cases, molten salts are not even considered as solvents by most chemists.[43]

To refer to the first ever documented ionic liquid it is necessary to date back to mid-19th century. The "red-oil" is an intermediate compound form during the Friedel-Crafts reaction (Figure 1.10) where an aromatic ring, benzene, reacts with an electrophile, chloromethane, to form toluene. During the synthesis a Lewis acid, such as $AlCl_3$, is use as a catalyser. When it was first discovered, this red coloured compound

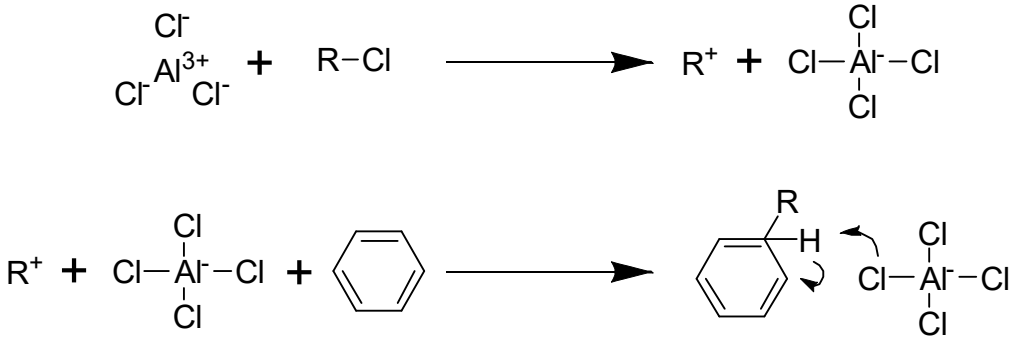

Figure 1.10. Schematic representation of a Friedel-Crafts alkylation.

was not identified due to the lack of tools. It was not until then when NMR became widely available that the structure of such red-oil was identified, for $AlCl_3$-catalyzed reactions the structure proposed was the heptachlorodialuminate salt form by a carbocation and the tetrachloroaluminate anion.[43,46]

The first ionic liquid properly synthesized was by Walden in 1914;[47] ethyl ammonium nitrate (EAN), by neutralizing ethyl-amine with concentrated HNO_3. This compound has a melting temperature of 12 °C.[47] This type of solvents received the name of protic ionic liquids (PILs). Newly synthesized this type of ionic liquids did not catch broad attention in the scientific media however, in the last decade they have been proving to be useful in several areas.[48]

It was in 1951 when the second generation of ionic liquids formed by mixing alkyl pyridinium chlorides with $AlCl_3$ were reported by Hurley and Wier (Figure 1.11).[49] These new compounds formed by heterocyclic cations, namely pyridinium and imidazolium halides, mixed with tetracholoroaluminate anion were further explored and found to be useful in applications such as electrolytes in batteries [50,51] and solvents for electroplating metals.[52–54]

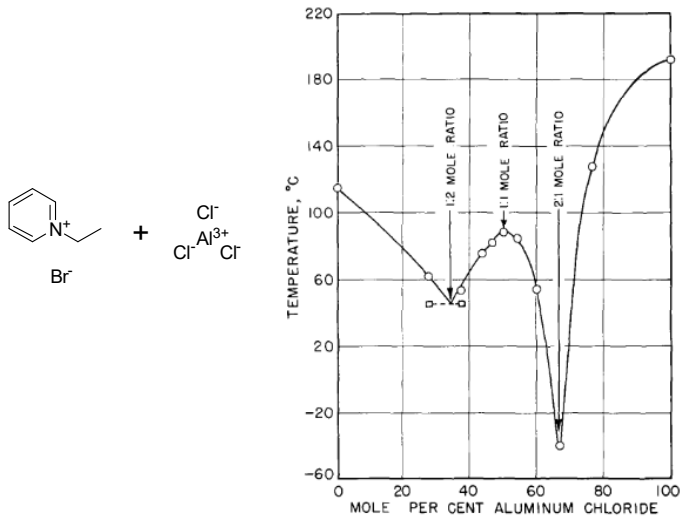

Figure 1.11. Right: schematic representation of aluminium chloride-ethyl pyridinium bromide. Left: [54] phase diagram of the system.

The chloroaluminate salts however, were of limited interest and applicability because both, the starting materials and the ionic liquid derived from the mixture are moisture-sensitive. For example $AlCl_3$ reacts in the presence of atmospheric moisture forming HCl.[55]

In 1992 the first moisture and air-stable ionic liquids were made. These solvents, reported by Wilkes and Zaworotko[56] (Figure 1.12) are based on imidazolium and tetrafluoroborate, and due to their novel properties, these systems started to receive broad attention in the scientific community. The main idea behind this proposal was to replace the moisture-sensitive precursors, i.e. $AlCl_3$, with more stable compounds such as tetrafluoroborate, hexafluorophosphate, nitrate, acetate, and sulfate salts.[43]

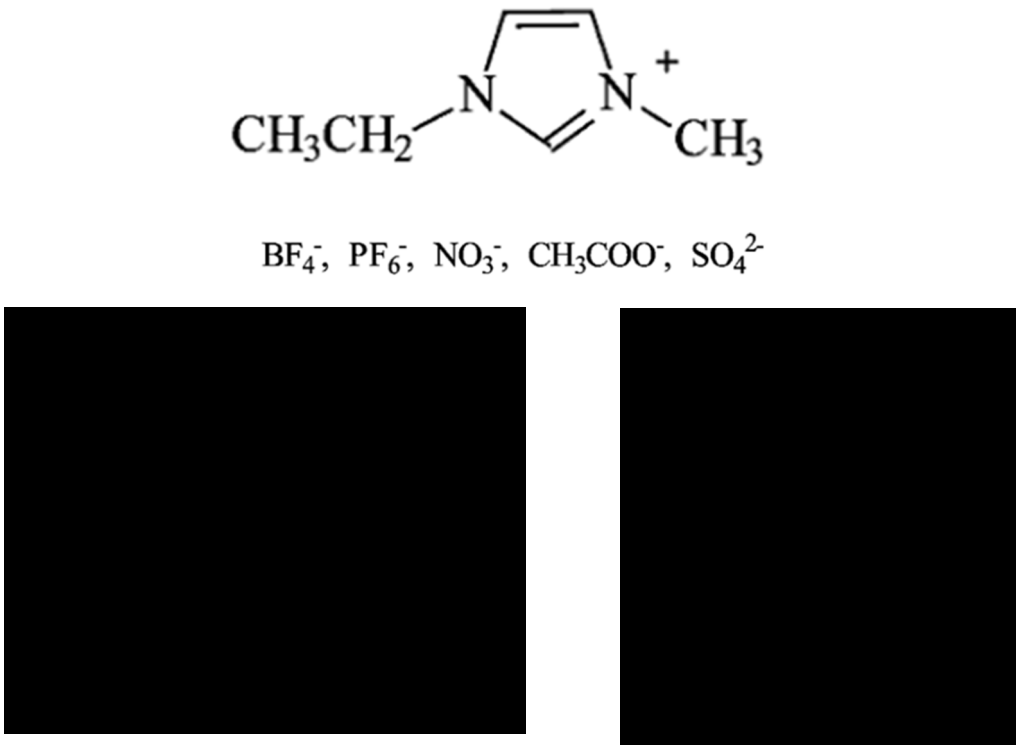

Figure 1.12.[43] Top: schematic representation of imidazolium based ILs. Bottom (Left): Professor Michael Zaworotko, bottom (right) Dr John S. Wilkes.

From this point onwards, a continuous desire to discover new ionic liquids has led to an incessant expansion of their properties such as hydrophobicity, hydrophilicity, conductivity, viscosity and electrochemical window. The number of potential candidates for new ionic liquids was found to be around one trillion (10^{12}) different ionic liquids.[57]

As an obvious result and the variety of physico-chemical properties shown by these compounds such as extremely low vapour pressure, high tuneability, nonflammability, wide solubility and high stability[58] have made them great candidates as gas absorbents,[59] lubricants,[60] catalysts,[61] extractants,[62] ionic liquid crystals[63] and chelators.[64,65]

Ionic liquids were initially classified as green however, such an attribution has been recently argued.[66] Several studies pointed out the hazardous toxicity and very low biodegradability of most of those ILs.[67,68] To obtain the desired functionality, ionic liquids must be of high purity otherwise their properties are compromised. In addition to this, the synthesis of ILs require large amount of salts and solvents to ensure complete ion exchange. Collectively the syntheses of some ILs are far away from being environmentally friendly and the synthetic complexity is also reflected in the high price of common ILs.[69] In 2001 a new generation of solvents emerged, namely deep eutectic solvents, firstly synthesized by Abbott et al.[70] Deep eutectic solvents overcome some drawbacks that the ionic liquids have due to a straightforward synthesis by only mixing together components capable of forming a eutectic mixture.

Deep eutectic solvents (DES) exhibit similar physico-chemical properties[71] as the ionic liquids and as a result these compounds are commonly considered as ionic liquids in the literature. However, deep eutectic solvents differ in the fact that they are not always formed only by ionic species and, actually, can be made from non-ionic species[69]. Many deep eutectic constituents have been explored[72,73] (Figure 1.13)

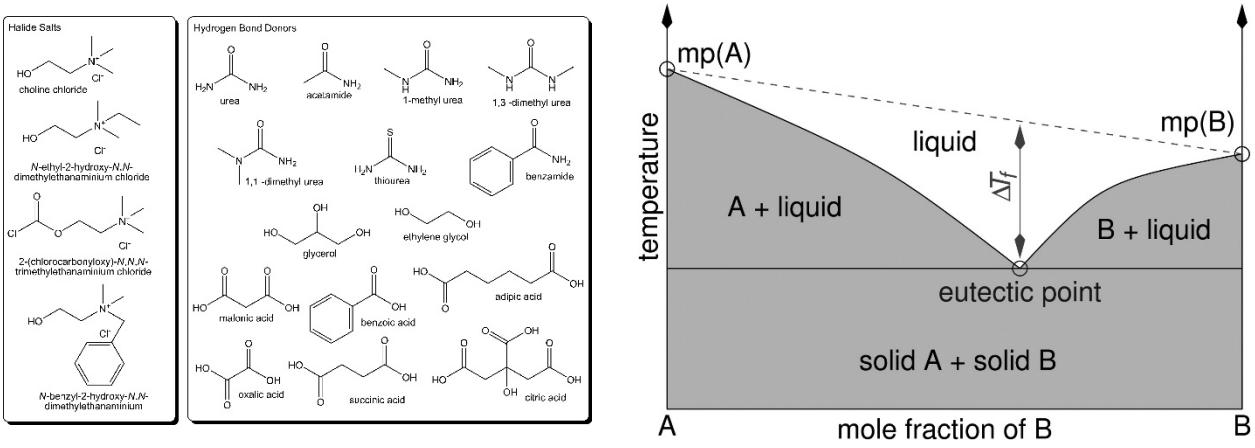

Figure1.13.[71] Right: Structures of some halide salts and hydrogen bond donors used in the formation of deep eutectic solvents. Left: Schematic representation of a eutectic point on a two-component phase diagram.

and include the use of natural products such as organic acids, amino acids and sugars.[72,74,75] Molecules used by nature are perfect candidates to produce new, green and exciting deep eutectic solvents, also their vast diversity provides different chemically biodegradable properties.

The first time an IL was used instead of a conventional solvent for the synthesis of an inorganic compound was in 2000 by Dai and co-workers. [76] The work made is based on the synthesis of porous silica gels termed as "ionogels", which are currently extensively studied. Afterwards, ionic liquids have been employed in the synthesis of a broad range of inorganic materials,[77–84] where properties and morphologies have been finely tuned.[79,85–87]

1.5.2 Improvement of classic synthetic protocols

In the last decade ionic liquids have made a profound influence to already established synthetic methods. A major change came by the replacement of water or organic solvents by ILs. Electrochemical approaches, due to the high ionic conductivity and the wide electrochemical potential window [88,89] certainly have been among the first to use ILs for the synthesis or inorganic particles or thin films.[90]

Solution chemistry has also seen an exponential increase in the use of these systems, for example via the transformation of metal organic precursors $(MOR)_4$ in the presence of an acid or base. Typically, this process has been used for the synthesis of metal oxides [86,91,92] and several types of nanoparticles, i.e. metal, alloy, metal oxide and metal sulfides. [82,93,94] Thioacetamide and metal acetates can also be used as oxygen sources leading to the production of the corresponding metal oxide or sulfide. [95,96] Synthetic procedures to accomplish the desired product range from thermal, microwave or chemical treatment.[97–102]

1.5.2.1 Ionothermal

A very active and novel technique is the ionothermal method. Ionothermal reactions are analogue of hydrothermal and solvothermal methodologies although differing from the aforementioned by the fact that reactions are carried out, due to the negligible vapor pressure exhibit in some ILs, in ambient pressures. Clear advantages such as avoiding the use of high pressures and the use of novel solvents rapidly lead to forming novel structures and new compounds.[102–106]

1.5.2.2 Ionogels

Sol-gel syntheses too have felt the influence of ionic liquids. The incorporation of an IL into a sol-gel matrix produced the so-called ionogels. Ionogels can be separated into physical and chemical gels, the difference being due to the strength of the bond formed where, in physical gels the internal structure is cross-linked through weak interactions, e.g. hydrogen bonds or hydrophobic interactions, whereas in chemical gels the structure is formed via covalent bonding. The main concept to form a physical gel is the use of a coagulant, e.g. polysaccharides, polymers, silicas, or even carbon nanotubes, to form jellies, slurries or pastes.[97]

1.5.2.2.1Sol–Gel Reactions in Water-Poor Ionic Liquids[94]

In order to explain the behaviour of an ionic liquid in dehydrated or poorly hydrated systems some examples will be needed. As stated before the first time an inorganic material was synthesized was in 2000, where an aerogel was produced without the need of a supercritical drying procedure.[107] This is possible due to the low interface tensions of the binary system joined by low capillary forces. Ionic liquids are capable

of forming crystal structures however, the mechanistic interaction is far more complicated. Zhou et al. were able to hydrolyse titanium tetrachloride in 1-butyl-3-methylimidazolium tetrafluoroborate to then dehydrate (Figure 1.14), becoming a water-poor system, at 80 °C. [108] The crystallites obtained were 2-3 nm in size which agglomerated to form sponge-like superstructures of pure phase anatase. The features of the synthesis, in addition to its simplicity, can be highlighted when close attention is paid to the product obtained. First, sol-gel reactions will provide amorphous titania, which will crystalize upon calcination above 350 °C. Secondly, the size of the particles show the high nucleation rate produced in the ionic liquid in comparison with the nucleation rate of titania in the bulk, usually achieving particles with diameter of ca. 20 nm. The ionic liquid not only facilitates and simplifies the synthesis of anatase but also, owing to its low interface energy and adaptability, increases the nucleation rate considerably (by more than a factor of 1000).[94]

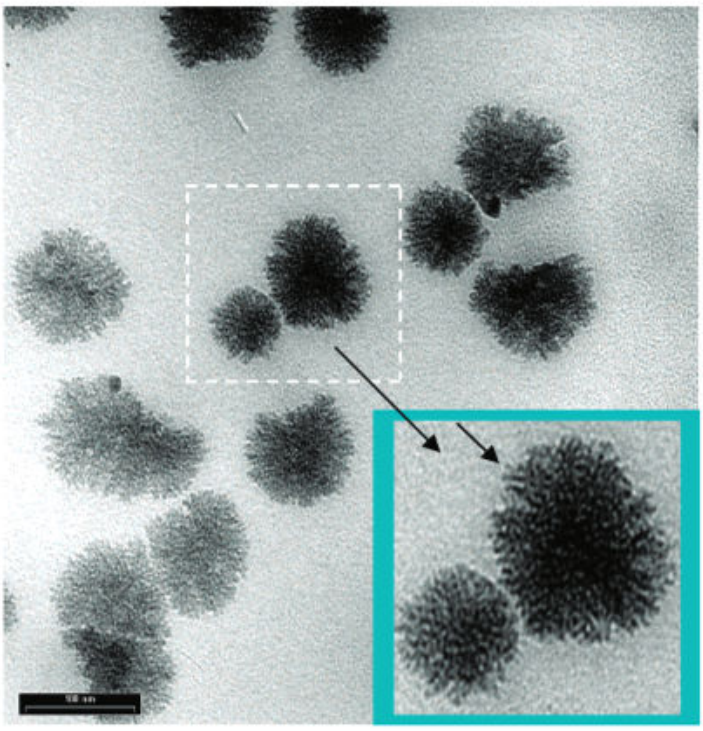

Figure 1.14.[108] TEM image of TiO2 nanoparticles synthesized in IL media. The image shows the self-assembly toward spherical, sponge-like superstructures. Scale bar = 500 nm.

Itoh et al. proved how owing to the strong surface binding of the ionic liquids properties of gold nanoparticles can be finely tuned between hydrophilicity and hydrophobicity (Figure 1.15) by exchange of anions in the IL moiety.[109]

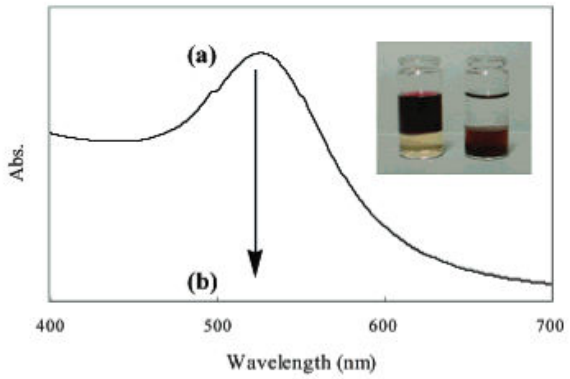

Figure 1.15[109] (a) uv-vis absorption spectrum before and (b) after addition of HPF_6. The inset shows the photograph of the solution (a) sample glass on the left and (b) sample glass on the right.

Another feature is the solvent self-organisation and supramolecular effects that are noticeable even with short-chain ILs such as 1-butyl-3-methylimidazolium tetrafluoroborate, IL used by Zhou et al. for the synthesis of porous silica via the production of nanostructured gels. Due to self-assembly by hydrogen bond-co-π-π stack mechanism between the tetrafluoroborate and the silane groups, as well as the π-π stack interaction of the neighbouring imidazolium rings (Figure 1.16 right), the resulting material presented a wormhole framework (Figure 1.16 left), mesopore of ca. 2.5 diameter and 2.5-3.1 nm in thickness. [94,110]

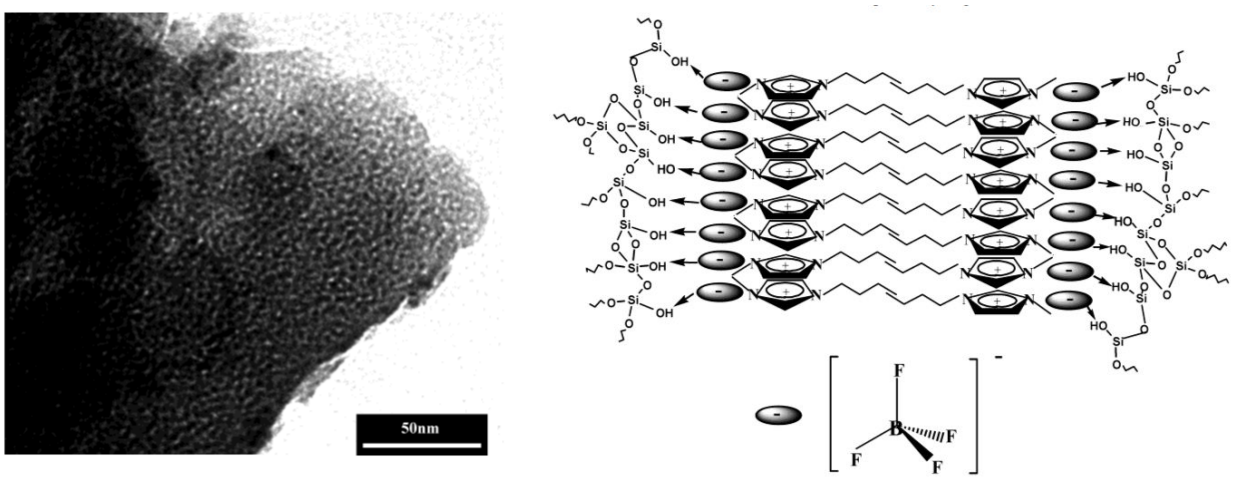

Figure 1.16.[110] Left: TEM image of the pore morphology and structure of the mesoporous silica. Scale bar= 50 nm. Right: Schematic representation of the proposed hydrogen bond-co-Π- Π stack mechanism.

1.5.2.2.2Water rich environments.

The effect of water will entirely depend on the supramolecular structure of the ionic liquid. It is safe to state that any reaction involving the mix of these two components will not proceed the same as when using the two components individually. Water molecules in contact with an ionic liquid will be tightly bound and be active in the H-bonding system of the IL.[111] On the other hand, as an active contributor of the H-bonding network, water cannot act in such circumstances as a solvating ligand. This conclusion was derived from the absence of solvent-free pores (water-born sol-gel silica contains solvent pores with a size below 1nm).[109] Water also alters the IL self-organization causing the structural outcome to be directly linked to the overall water content of the system. This behaviour becomes evident for example by comparing two sol-gel derived IL-silica hybrid materials (IL used, 1-hexadecyl-3-methylimidazolium chloride), synthesized with different amounts of water but maintaining the same ratio of IL-silica

Two samples were analysed in that work, sample 2 was obtained under water-poor conditions, while sample number 1 with ten times more water. The x-ray diffraction patterns (Figure 1.17 Left) clearly shown differences, pointing towards the fact that water, indeed, is affecting the self-organization behaviour. Sample one belongs to a 2D hexagonal mesophase, whereas sample 2 corresponds to a lamellar structure

with a long period of d= 5.6 nm (Figure 1.17 Right). Results indicated that the IL in water-rich media behaves merely as a classical surfactant but with high tendency towards self-organization.[112]

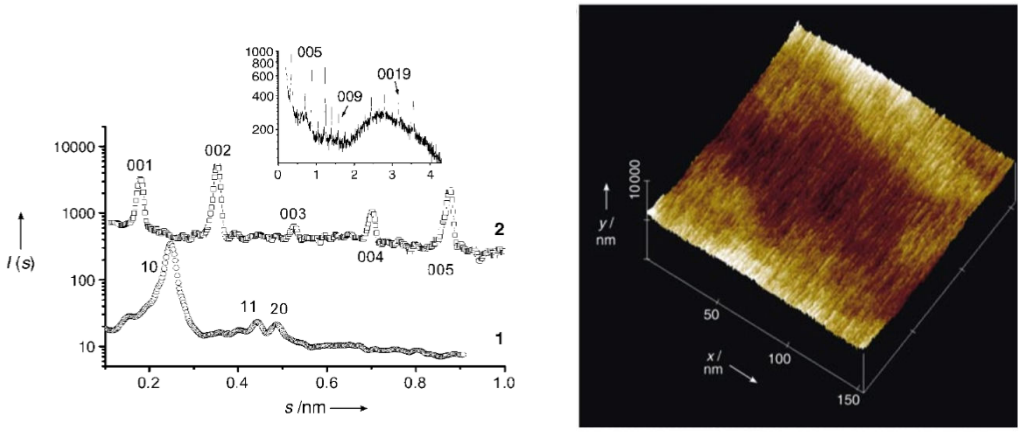

Figure 1.17.[94] Left: X-ray diffractograms of two mesostructured silica materials. The ratio of IL to silica is about 1:1. Sample 1: 2D mesostructure obtained with an excess of water. Sample 2: mesostructure obtained in water-poor conditions. Right: AFM picture of a surface of the porous silica prepared via sol-gel reaction in water-poor conditions.

Ionic liquids proved to be also efficient in water-rich environments when amphiphilic ILs were used as template, namely 1-hexadecyl-3-methylimidazolium-chloride reacted with porous silica. Results indeed displayed a bimodal structure were both typical textures, mesopores (2 nm< x < 50 nm in diameter) and micropores (> 2nm in diameter), coexisted (Figure 1.18).[113]

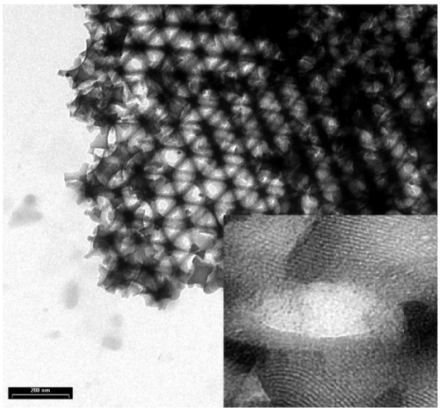

Figure 1.18[113] TEM image of the tailored bimodal porous silica. The inset is the ten times magnified image. Scale bar= 200 nm.

1.6 State of the art

Synthetic procedures recently involve less complicated, time consuming reaction medias, such as IL-assisted microwave synthesis, IL-assisted sonochemical reactions, ionothermal and IL-assisted sol-gel reactions. The broad use of the ILs in the synthesis of materials relies on their properties to form, interact, template and promote the formation of inorganic materials across temperature ranges from room temperature, most of the times, to just below the decomposition of the ILs.

However, something makes a study of the state of the art rather difficult, that is the study of how the inherent properties of an IL/DES affect in the synthesis of complex metal oxides upon calcination. As soon as high temperatures are involved in the synthesis of complex metal oxides, MSS (Molten salt synthesis) is primarily the reaction media. There are several reasons of why this could happen. First off, the price, e.g. an ionic liquid such as (emim)OAc (1-ethyl-3-methylimidazolium acetate) cost around £500 for 50 g (97 % pure, 689483-50G), from Sigma Aldrich UK. Density is ≈ 1 g/cm^3 hence is closely 50 ml of product. If 1 ml is used, every reaction will have a cost of 10 pounds plus the overall price of the other chemical reactants. Every time a reaction happens, due to the high temperatures that the reaction requires, the ionic liquid will be decomposed and eventually leave the synthesis in the form of gas, meaning that there is not possible way to recycle the IL. If the purity of the ionic liquid is compromised (95 %) then 100 g of product have a cost of ≈ £ 200 hence 2 pounds per reaction, which is more accessible.

Deep eutectic solvents could solve the elevated prices of the ionic liquids but that leads to the second point, the uncertainty of the outcome owing to the lack of knowledge around the area. The absence of appropriate experimentation, has impeded the understanding of how ILs and DESs behave in a high temperature synthesis, making the synthesis a rather random process between success and failure.

In an attempt to track the state of the art of the synthesis of complex metal oxides based on IL-assisted sol-gel methods, only work involving calcination is present from 2014 onwards.

Advances in the area can be categorized in three different branches.

- IL as a reliable synthetic media.[114–116]
- Influence of the IL towards crystal morphology.[117–120]
- IL as a mimicking templating agent.[121–125]

1.6.1 IL as a reliable synthetic media

Complex metal oxides have been synthesized by an ionic liquid media for different proposes. This area comprehends the use of ionic liquids/deep eutectic solvents for the synthesis of complex metal oxides simply because it works. The crystal growth is nicely tracked to understand the crystallization process of the latest desired product, indicating that the use of the ionic liquid is to maximize the production of single-phase material however, without taking in consideration the crystal morphology of the product. Another feature well exploited is the potential of precise tuning of the crystal composition.

The synthetic procedure can be described as: mix of the metal cations, predominantly nitrate/acetate salts dissolved previously in water or alkoxides, into the IL or DES to later dehydrate at temperatures around 70 °C. In most cases a polychelating agent such as cellulose is used to form a gel. This gel will be then calcined at different ramp rates, times and temperatures.

Celorrio et al. with the use of 1-ethyl-3-methylimidazolium acetate were able to synthesize $LaMnO_3$ (Figure 1.19) over a series of different temperatures to prove how the maximum temperature plays a crucial role into oxygen reduction reactions, as it determines the mean activity of surface of Mn sites. The particle size presented ranges from 16 to 38 nm but, the increase could not be linearly related to the increase of temperature.[114]

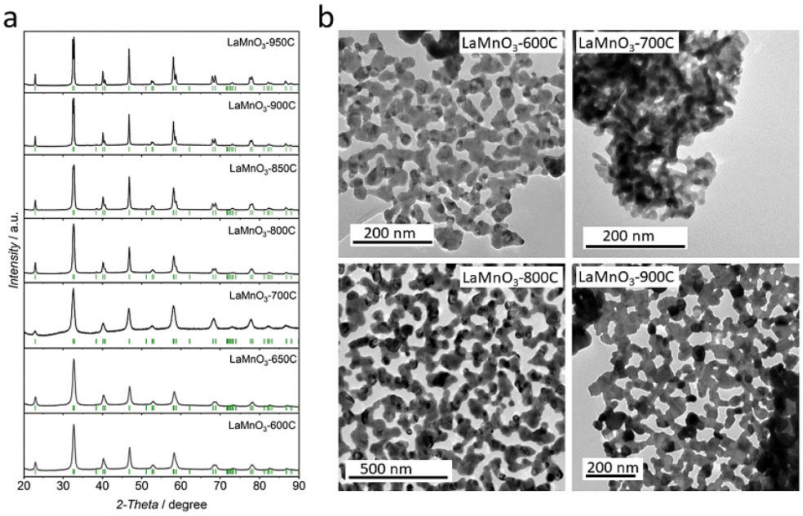

Figure 1.19.[114] Left: Temperature analysis of the synthesis of $LaMnO_3$ via powder X-ray diffraction patterns. Right: TEM images of the corresponding temperatures.

In another study Goblain et al. were able to produce $La_{1-x}Ba_xMnO_3$ with different levels of Ba concentration (Figure 1.20). The synthetic procedure carried out is fairly similar than the one reported previously however, in this case the use of an extra chelating agent such as EDTA is used to keep all the metal nitrates in solution and avoid early precipitation. Here is also reported how the increase in concentration of one element can produce an increase of the particle size. Here the Ba concentration increases from $Ba_{0.15}$ to $Ba_{0.30}$ and the particle size from 33.8 to 73.5 nm.[115]

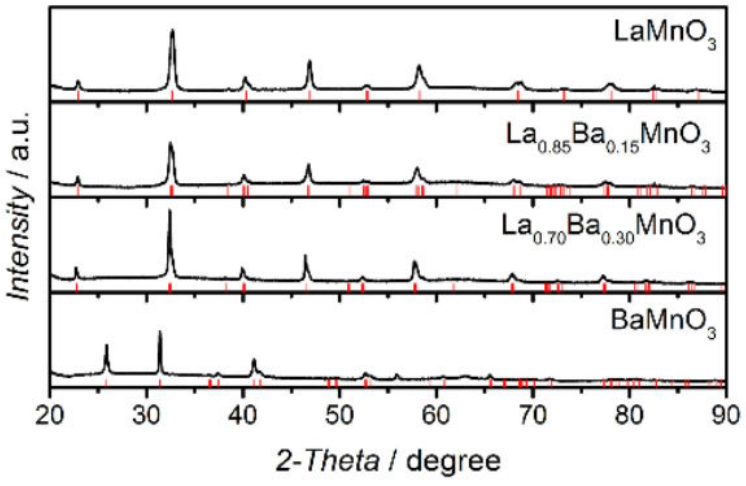

Figure 1.20[115] Powder diffraction patterns of the synthesis of $La_xBa_yMnO_3$ with different compositional ratios.

Another good example comes from Boston et al. were the synthesis of $BaTiO_3$ (Figure 1.21). The synthetic procedure begins with the synthesis of the DES, then barium acetate from solution was added, mix and dehydrated. Finally, titanium isopropoxide was added in the correct molar ratio. An intermediate calcination process will follow at 500 °C and finally a secondary calcination process to 950 °C takes place to obtain the main phase. The particle size ranges from 0.6 μm (roughly 25 % of the sample) to 3.2 μm (the remaining 75 %).[116]

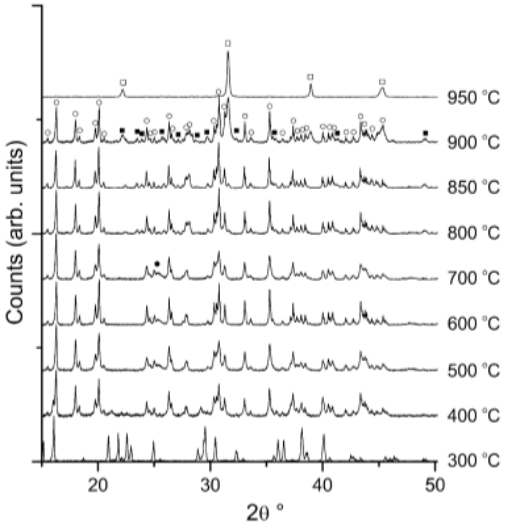

Figure 1.21.[116] Temperature analysis via powder diffraction patterns tracking the crystal growth of the product.

1.6.2 Influence of the IL towards crystal morphology

To allow the Ionic liquid/Deep eutectic solvent to be used as a template, there is a significant change in the synthetic protocol. Such a change can be described as follow: metal precursors are added to a solution, a process of hydrolysis then takes place to replace any functional group and forming hydroxide species which, co-condense forming a gel. Then time is given for the gel to age and at that time is washed to extract the templating agent. Finally, a calcination process occurs to form the oxidized specie.

Patil et al. synthesized vanadium pentoxide with chemical formula V_2O_5 via the formation of a sol-gel with different ionic liquids (Figure 1.22). The synthesis protocol can be described as: $VOCl_3$ was added

to isopropanol and heated at 70 °C to form vanadium oxytriisopropoxide. Ammonia is then added to bring the solution to basic range of pH 8-10 and kept under heating to allow complete gelation. To compare 1-butyl-3-methylimidazolium tetrafluoroborate (98%, [bmim][BF_4]) and 1-octyl-3-methylimidazolium tetrafluoroborate (98%, [omim][BF_4]) were added individually and stirred for 30 min before hydrolysis. After hydrolysis solids were washed to remove impurities as well as the IL.[119]

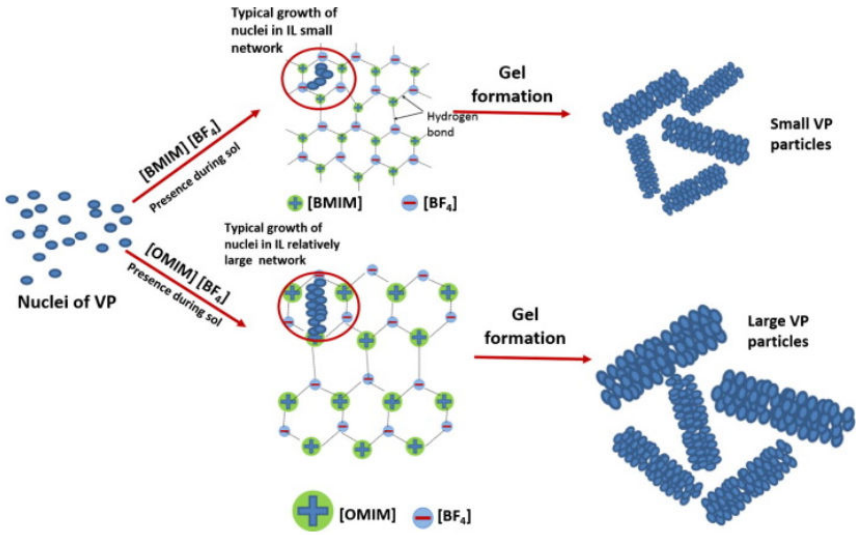

Figure 1.22.[119] Schematic representation of the synthesis of V_2O_5 nanoparticles via different ILs showing how the nucleation and growth rate assisted by the ionic liquid influences the crystal final shape and size.

Results proved that the ionic liquid plays a critical role into nanoparticles formation. Nucleation and growth rate assisted by the ionic liquid influences the crystal final shape and size. The synthesis carried out as control, without IL, gave large metal particles. The nucleation arises during hydrolysis, without a directing network, particles combine each other forming uncontrolled albeit thermodynamically stable large particles. On the other hand, two type of directing networks are present when different ionic liquids are present. On one side [bmim][BF_4], due to a smaller size of cation, form little compact/small 3-D networks, whereas on the other side [omim][BF_4], with a significant larger size of cation, forms bigger and less compact 3-D networks. As a consequence, smaller size nano to micro-particles are displayed when the synthesis was carried out via [bmim][BF_4] in comparison with the obtained via [omim][BF_4].

Ji et al. were able to synthesize mesoporous γ-Al_2O_3 with a variation in the morphology based on the molar ratio of IL/aluminium isopropoxide. The synthesis was carried out mixing 1-butyl-3-methylimidazolium hexafluorophosphate [bmim]PF_6 with aluminium isopropoxide in ethanol. After 5 hours of agitation a process of 24 h aging is proceeded. The precipitated is filtered and washed. The solid is dried and finally calcined at different temperatures.[120]

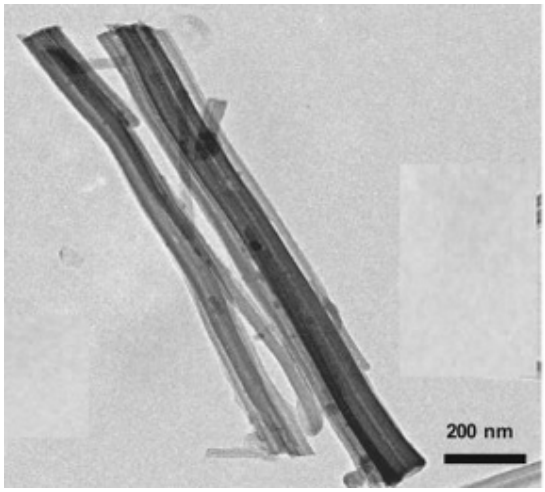

Figure 1.23.[120] [bmim]PF_6/aluminium hydroxide hybrid with the [bmim]PF_6/aluminium isopropoxide molar ratio of 0.18.

Studies via TEM (Figure 1.23) and SEM (Figure 1.24) images of the morphology of the crystals before and after calcination were done. Elongated roads were obtained with the addition of the IL however, the molar concentration shows to be a factor to consider. With the increase of the molar ration from 0 to 0.18 the alumina roads became highly uniform, particularly at 0.18. The average diameter obtained was of 260 nm and the length of 2.8-6 μm. However, interestingly high molar ratios of [bmim]PF_6/aluminium isopropoxide derived in a rupture of the growth of road like particles, indicating that if the concentration of the IL is to high may cover the entire surface of the aluminium hydroxide forming a denser 3-D structure, confining the crystal growth to small rods and nanoparticles. On the other hand, if the quantity of the IL is not enough to completely cover the side surface of the rods, weak control over the longitudinal rod growth and as consequence aggregates of crystallites is exhibited.

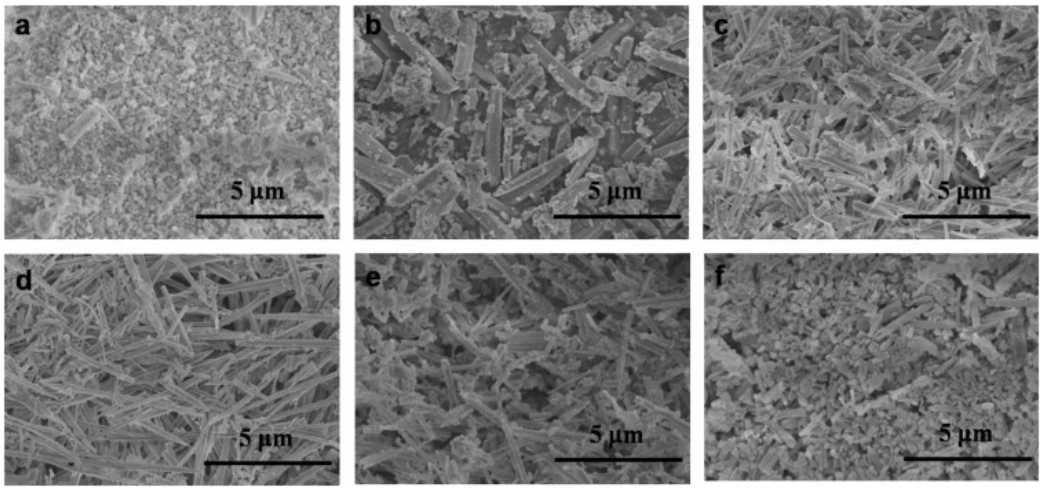

Figure 1.24[120] SEM images showing the differences in crystal growth depending the concentration of the IL involved in the reaction (a = 0, b = 0.03, c = 0.12, d = 0.18, e = 0.24, f = 0.3). Scale bars = 5 µm.

1.6.3 IL as a mimicking templating agent

There are truly two approaches in this area. A typical synthesis process can be described as follow: First, there is the need to build a template structure, normally silica, to then add the IL, which forms a coating around the templating structure. Finally, calcination under a neutral atmosphere (nitrogen or argon), to avoid combustion, is used to carbonize the product, therefore, the IL behaves here as carbon source and soft template. To remove the silica HF solution or NH_4HF_2 are commonly use, leaving just the carbonized material.

The second approach is in fact an inverse process. First a monomer of an IL is synthesized and self-assembled ensuing the templating structure. Silica is added to attach this time to the surface of the poly-ionic liquid nanostructures. Lastly calcination under oxygen atmosphere results in the removal of the poly-ionic liquid.

Sebastian et al. prepared 3-n-tetradecyl-l-vinylimidazolium dicyanamide and 1,4-butanediyl-3,3′-bis-l-vinylimidazoliurn dicyanamide as monomers. To induce polymerization 2,2'-azobis[2-methyl-**N**-(2-

hydroxyethyl)propionamide] as the crosslinking agent is mixed with each respective IL monomer in a flask with water and mix for 48 h. Metal cation, Pt, was added to the poly-ionic liquid (PIL) nanoparticles in a deposition process. As to prepared porous silica tetramethyl orthosilicate is integrated in the reaction media with PIL nanoparticles and also to the hybrid Pt-PIL nanoparticle dispersion. The PIL template was removed via calcination in air for 12 h at 750 °C. [124] A schematic representation of the synthesis can be seen in Figure 1.25.

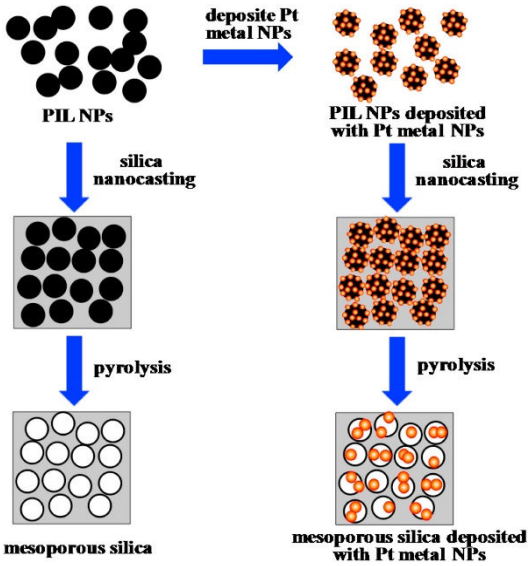

Figure 1.25.[124] Schematic representation of the synthesis of mesoporous silica via the prior synthesis of PIL NPs with and without metal.

Chen et al. synthesized nitrogen-doped hollow mesoporous carbon spheres (N-HMCSs) with 1-alkyl-3-methylimidazolium bromide, [$c_n$mim]Br, n = 4, 8, 12, and 16). Also in another line of the experiment, [c_{16}mim]Br was added varying the amount per reaction (0.2, 0.4, 0.6, 0.8, 1.0, and 1.2 g)

Via SEM they were able to characterize the influence of the content of the IL in the reaction (Figure 1.26). The tendency can be described as, low concentration (0.2 g) of IL derives in spherical domains but sizes are nonuniform, i.e. larger spheres with diameter of ~960 nm, medium spheres with ~600 nm of diameter and smaller spheres with ~200 nm diameters. When the concentration of IL is increased (0.4 g), larger and smaller spheres and a more uniform size of 600 nm in diameter spheres are observed. Moreover, short rods can also be spotted which is believed to be due to aggregation of the adjacent spheres. As the

concentration of the IL is constantly increased (0.6 g), relatively uniform spheres, ~470 nm in diameter, and some small spheres with diameter of ~280 nm are also displayed, noting that the rods are not seen anymore. The right amount of IL is generated when 0.8 g of IL is used, representing in the sample uniform spheres in large domains with the mean diameter of 380 nm. It is evident therefore that the increase in content of the IL is reflected via the reduction and uniformity of the diameter of the spheres.

Furthermore, the effect of the length of alkyl chain is also investigated. Shorter lengths, when n = 4 and 8 in [$c_n$mim]Br, produced larger spheres with nanoparticle agglomeration between the spheres. Increasing the length, n = 12, uniformity starts to take place with diameters around 530 nm. Lastly, when n = 16, uniform sizes are visible around the sample with spheres of ~380 nm in diameter.

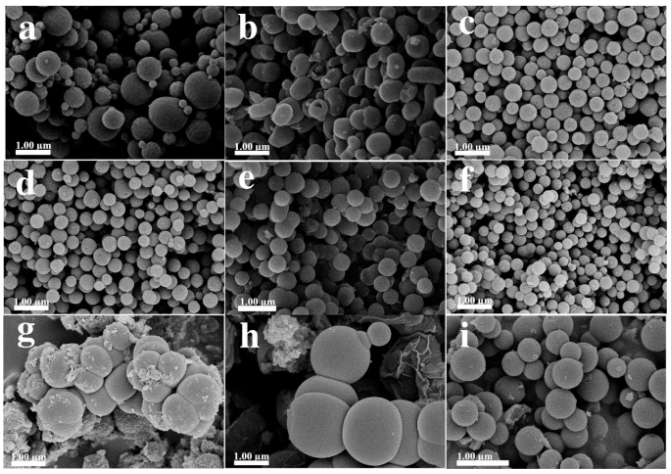

Figure 1.26.[125] SEM Images of the N-HMCSs with a = 0.2 g, b = 0.4 g, c = 0.6 g, d = 0.8 g, e = 1.0 g, and f = 1.2 g of IL. The effect of the length of alkyl chain is observed in g-i with n = 4, 8, and 12 respectively. Scale bars = 1 μm.

1.7 Aims

The first use of an ionic liquid in the synthesis of a complex metal oxide was done by a former member of the research group at Bristol. In that paper Green et al described results of the synthesis of a variety of complex metal oxides with diverse properties, i.e. superconductivity and piezo electricity, via ionic liquids.[77]

The synthetic protocol involved an IL as a reliable synthetic media. For most of the crystal compositions in that study, the ionic liquid used was 1-ethyl-3-methylimidazolium acetate however, interestingly 1-ethyl-3-methylimidazolium nitrate was specifically used for crystal phases that contain bismuth nitrate, an insoluble salt in water. Unfortunately, no crystal growth was shown making it difficult to know what differences using nitrate instead of acetate in the ionic liquid composition would make.

SEM studies showed also another noteworthy feature: despite using the same ionic liquid for most of the crystal compositions synthesized, different macro-morphologies were exhibited (Figure 1.27), hinting that metal cations interact differently with the ionic liquid, and play a role in the overall morphology.

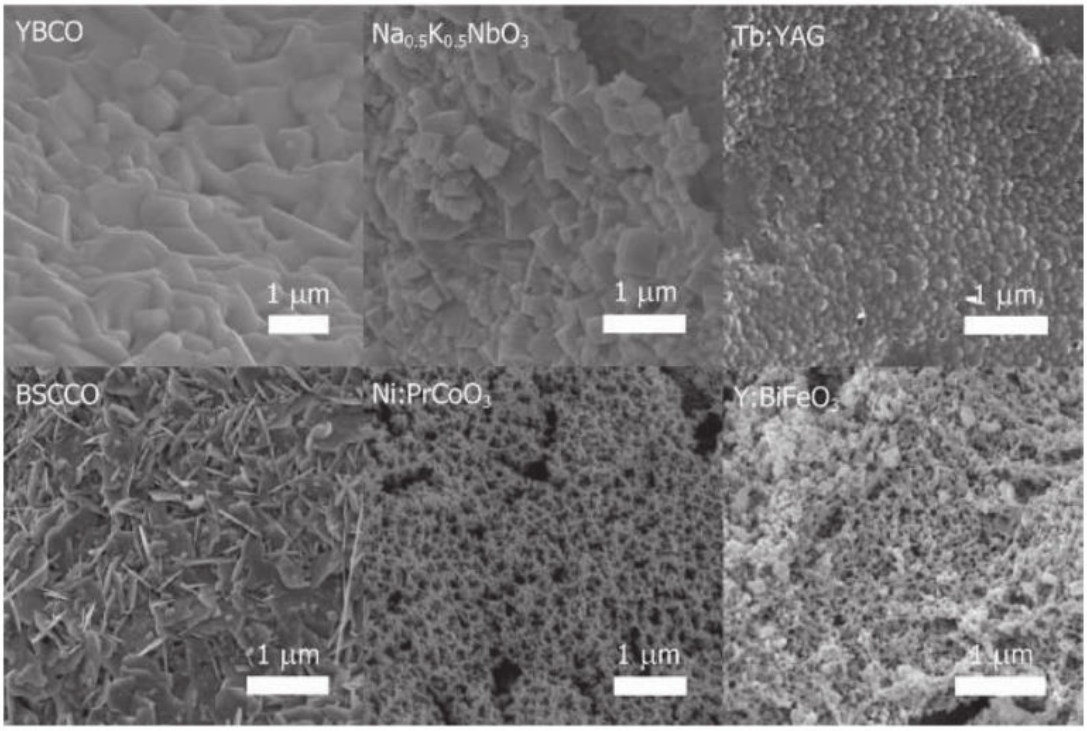

Figure 1.27[77] SEM image of every crystal synthesized via ionic liquid-assisted sol-gel synthesis. Scale bars = 1 μm.

The overall synthetic procedure can be divided in three main components: the metal cations, the polysaccharide and the ionic liquid.

Strontium niobates have exhibited several valuable properties including the potential of being a new family of superconductors (refer to pp. 5), therefore Chapter 3 explores the role played by every component in terms of chelating ability and the result of varying the stoichiometry of the metal cations in the overall outcome in the synthesis of strontium niobates. As a result, five single-phase strontium niobates were successfully synthesized, thereby proving the exquisite control obtained through this synthetic process. Furthermore, four crystal structures similar to $Sr_4Nb_2O_9$ stoichiometry composition were synthesized and characterized.

Chapter 4 covers the role played by the polysaccharide. What happens when different polysaccharides in various amounts, in combination with an IL, are employed in the synthesis of a strontium niobate. Also based on the synthesis of a YBCO superconductor with different organic sources and SQUID characterization it was possible to establish differences in the Tc onset, a physical parameter which is closely related to the level of oxygen in the crystal composition.

Lastly, Chapter 5 elucidates the role played by the ionic liquid in the synthesis of metal oxides, by exploring the synthesis with a range of ILs/DES, answering the question of what truly defines a good IL/DES for the synthesis of complex metal oxides. Based on this study it was possible to determine the key experimental factors required for the synthesis of a metal oxide, focussing on the identification of precursory phases and elements that will augment or disrupt the synthesis, thereby assuring finer control over the desired crystal phase. During the analysis a YBCO superconductor was synthesized at a temperature of 100 °C below the standard synthetic temperature (920 °C). Moreover, as a result of the knowledge generated, a cost-effective deep eutectic solvent was found to succeed in the synthesis of a more complicated BSCCO superconductor. Finally, with the use of a choline chloride-based DES the synthesis of a new sodium strontium niobate was synthesized.

1.8 References

(1) Xiang, X.-D.; Takeuchi, I. *Combinatorial Materials Synthesis*; Marcel Dekker, 2003.

(2) Wang, Z. L.; Kang, Z. C. *Functional and smart materials -Structural Evolution and Structure Analysis*. Plenum Publishing Corp, 1998, New York.

(3) Longo, E.; La Porta, F. D. A. *Recent Advances in Complex Functional Materials : From Design to Application*; Springer, 2017, Switzerland.

(4) V. E. Henrich and P.A. Cox. *The Surface Science of Metal Oxides*; Cambridge University Press, 1996, Cambridge.

(5) Ogale, S. B.; Venkatesan, T.; Blamire, M. G. *Functional Metal Oxides : New Science and Novel Applications*. Weinheim.

(6) Lichtenberg, F.; Herrnberger, A.; Wiedenmann, K. Synthesis, Structural, Magnetic and Transport Properties of Layered Perovskite-Related Titanates, Niobates and Tantalates of the Type $A_nB_nO_{3n+2}$, $A'A_{k-1}B_kO_{3k+1}$ and $A_mB_{m-1}O_{3m}$. *Prog. Solid State Chem.* **2008**, *36* (4), 253–387.

(7) Xu, X.; Randorn, C.; Efstathiou, P.; Irvine, J. T. S. A Red Metallic Oxide Photocatalyst. *Nat. Mater.* **2012**, *11* (7), 595–598.

(8) Wan, D. Y.; Zhao, Y. L.; Cai, Y.; Asmara, T. C.; Huang, Z.; Chen, J. Q.; Hong, J.; Yin, S. M.; Nelson, C. T.; Motapothula, M. R.; et al. Electron Transport and Visible Light Absorption in a Plasmonic Photocatalyst Based on Strontium Niobate. *Nat. Commun.* **2017**, *8*, 15070.

(9) Shida, M.; Akiyama, K.; Nagano, I.; Murakami, Y.; Ohta, S. Investigation of Strontium-Niobium Oxides for Application to Thermal Barrier Coatings. *Key Eng. Mater.* **2006**, *317–318*, 517–520.

(10) Kamba, S.; Petzelt, J.; Buixaderas, E.; Haubrich, D.; Vaněk, P.; Kužel, P.; Jawahar, I. N.; Sebastian, M. T.; Mohanan, P. High Frequency Dielectric Properties of $A_5B_4O_{15}$ Microwave Ceramics. *J. Appl. Phys.* **2001**, *89* (7), 3900–3906.

(11) Ishizawa, N.; Marumo, F.; Kawamura, T.; Kimura, M. The Crystal Structure of $Sr_2Nb_2O_7$, a Compound with Perovskite-Type Slabs. *C. R. Acad. Sci. Paris, S~r. C C. R. Acad. Sci. Paris, S~r.*

C. Acta Cryst. Acta Cryst. B Tetrahedron Canad. J. Phys. Acta Cryst **1973**, *644* (350), 260–261.

(12) Yamamoto, J. K.; Bhalla, A. S. Microwave Dielectric Properties of Layered Perovskite $A_2B_2O_7$ Single-Crystal Fibers. *Mater. Lett.* **1991**, *10* (11–12), 497–500.

(13) Zhou, Y.; Ma, Q.; Lü, M.; Qiu, Z.; Zhang, A.; Yang, Z. Preparation and Photoluminescence of $SrNb_2O_6$ Nanoparticles Prepared by Combustion Method. *Mater. Sci. Eng. B* **2008**, *150* (1), 66–69.

(14) Fujimori, Y.; Izumi, N.; Nakamura, T.; Kamisawa, A. Application of $Sr_2Nb_2O_7$ Family Ferroelectric Films for Ferroelectric Memory Field Effect Transistor. *Jpn. J. Appl. Phys.* **1998**, *37* (Part 1, No. 9B), 5207–5210.

(15) Bai, L.; Zhu, K.; Su, L.; Qiu, J.; Ji, H. Synthesis of (K, Na)NbO_3 Particles by High Temperature Mixing Method under Hydrothermal Conditions. *Mater. Lett.* **2010**, *64* (1), 77–79.

(16) D'yachenko, O. G.; Istomin, S. Y.; Abakumov, A. M.; Antipov, E. V. Synthesis, Structure, and Properties of Mixed Niobium(IV,V) Oxides. *Inorg. Mater.* **2000**, *36* (3), 247–259.

(17) Gu, H.; Zhu, K.; Pang, X.; Shao, B.; Qiu, J.; Ji, H. Synthesis of (K, Na) (Nb, Ta)O_3 Lead-Free Piezoelectric Ceramic Powders by High Temperature Mixing Method under Hydrothermal Conditions. *Ceram. Int.* **2012**, *38* (3), 1807–1813.

(18) Levin, I.; Chan, J. Y.; Scott, J. H.; Farber, L.; Vanderah, T. A.; Maslar, J. E. Complex Polymorphic Behavior and Dielectric Properties of Perovskite-Related $Sr(Sr_{1/3}Nb_{2/3})O_3$. *J. Solid State Chem.* **2002**, *166* (1), 24–41.

(19) Teneze, N.; Mercurio, D.; Trolliard, G.; Champarnaud-Mesjard, J. C. Reinvestigation of the Crystal Structure of Pentastrontium Tetraniobate, $Sr_5Nb_4O_{15}$. *Zeitschrift für Krist. - New Cryst. Struct.* **2000**, *215* (1), 11–12.

(20) Marinder, B.-O.; Wang, P.-L.; Werner, P.-E.; Karvinen, S.; Niinistö, L.; Volden, H. V.; Weidlein, J.; Zingaro, R. A. Powder Diffraction Studies of $SrNb_2O_6$ and $SrNb_6O_{16}$. *Acta Chem. Scand.* **1986**, *40a*, 467–475.

(21) Brusset, H.; Gillier-Pandraud, M.; Voliotis, S. D. Etude Du Polymorphisme Du Metaniobate de Strontium $SrNb_2O_6$. *Mater. Res. Bull.* **1971**, *6* (1), 5–14.

(22) Andersson, S.; Ottinger, R.; Cyvin, S. J.; Fedorcsák, I.; Hoffman, R. A.; Westerdahl, A. The Crystal Structure of $NaNb_6O_{15}$ and $NaNb_6O_{15}OH$. *Acta Chem. Scand.* **1965**, *19*, 2285–2290.

(23) Vanderah, T. A. *Chemistry of Superconductor Materials : Preparation, Chemistry, Characterization, and Theory*; Noyes Publications, 1992, Noyes Park Ridges.

(24) Cava, R. J.; Batlogg, B.; van Dover, R. B.; Murphy, D. W.; Sunshine, S.; Siegrist, T.; Remeika, J. P.; Rietman, E. A.; Zahurak, S.; Espinosa, G. P. Bulk Superconductivity at 91 K in Single-Phase Oxygen-Deficient Perovskite $Ba_2YCu_3O_{9-\delta}$. *Phys. Rev. Lett.* **1987**, *58* (16), 1676–1679.

(25) Capponi, J. J.; Chaillout, C.; Hewat, A. W.; Lejay, P.; Marezio, M.; Nguyen, N.; Raveau, B.; Soubeyroux, J. L.; Tholence, J. L.; Tournier, R. Structure of the 100 K Superconductor $Ba_2YCu_3O_7$ between (5 ÷ 300) K by Neutron Powder Diffraction. *Europhys. Lett.* **1987**, *3* (12), 1301–1307.

(26) Jorgensen, J. D.; Veal, B. W.; Paulikas, A. P.; Nowicki, L. J.; Crabtree, G. W.; Claus, H.; Kwok, W. K. Structural Properties of Oxygen-Deficient $YBa_2Cu_3O_{7-\delta}$. *Phys. Rev. B* **1990**, *41* (4), 1863–1877.

(27) De Graef, M.; McHenry, M. E. *Structure of Materials : An Introduction to Crystallography, Diffraction and Symmetry*; Cambridge University Press, 2007.

(28) Sunshine, S. A.; Siegrist, T.; Schneemeyer, L. F.; Murphy, D. W.; Cava, R. J.; Batlogg, B.; van Dover, R. B.; Fleming, R. M.; Glarum, S. H.; Nakahara, S.; et al. Structure and Physical Properties of Single Crystals of the 84-K Superconductor $Bi_{2.2}Sr_2Ca_{0.8}Cu_2O_{8+\delta}$. *Phys. Rev. B* **1988**, *38* (1), 893–896.

(29) Mourachkine, A. *Room-Temperature Superconductivity*; Cambridge International Science Pub, 2004, Cambridge.

(30) Khare, N. *Handbook of High-Temperature Superconductor Electronics*; Marcel Dekker, 2003, New Delhi.

(31) Adschiri, T.; Hakuta, Y.; Arai, K. Hydrothermal Synthesis of Metal Oxide Fine Particles at Supercritical Conditions. In *Industrial and Engineering Chemistry Research*; American Chemical

Society, **2000**; 39, 4901–4907.

(32) Sun, Q.; Gu, Q.; Zhu, K.; Jin, R.; Liu, J.; Wang, J.; Qiu, J. Crystalline Structure, Defect Chemistry and Room Temperature Colossal Permittivity of Nd-Doped Barium Titanate. *Sci. Rep.* **2017**, *7* (1), 42274.

(33) Gu, Q.; Zhu, K.; Zhang, N.; Sun, Q.; Liu, P.; Liu, J.; Wang, J.; Li, Z. Modified Solvothermal Strategy for Straightforward Synthesis of Cubic $NaNbO_3$ Nanowires with Enhanced Photocatalytic H_2 Evolution. *J. Phys. Chem. C* **2015**, *119* (46), 25956–25964.

(34) Li, Z.; Hou, B.; Xu, Y.; Wu, D.; Sun, Y.; Hu, W.; Deng, F. Comparative Study of Sol–gel-Hydrothermal and Sol–gel Synthesis of Titania–silica Composite Nanoparticles. *J. Solid State Chem.* **2005**, *178* (5), 1395–1405.

(35) Wang, H.; Wang, L.; Liu, J.; Wang, B.; Yan, H. Preparation of $Pb_{1-x}La_xTi_{1-x/4}O$ (X=0.28) Powders by a Sol–gel-Hydrothermal Method. *Mater. Sci. Eng. B* **2003**, *99* (1–3), 495–498.

(36) Liu, X.; Fechler, N.; Antonietti, M. Salt Melt Synthesis of Ceramics, Semiconductors and Carbon Nanostructures. *Chem. Soc. Rev.* **2013**, *42* (21), 8237.

(37) Brinker, C. J.; Scherer, G. W. *Sol-Gel Science : The Physics and Chemistry of Sol-Gel Processing*; Academic Press, 1990.

(38) Li, L.; Deng, J.; Chen, J.; Xing, X. Topochemical Molten Salt Synthesis for Functional Perovskite Compounds. *Chem. Sci.* **2016**, *7* (2), 855–865.

(39) Xu, C. Y.; Zhen, L.; Yang, R.; Zhong, L. W. Synthesis of Single-Crystalline Niobate Nanorods via Ion-Exchange Based on Molten-Salt Reaction. *J. Am. Chem. Soc.* **2007**, *129* (50), 15444–15445.

(40) Li, L.; Deng, J.; Chen, J.; Sun, X.; Yu, R.; Liu, G.; Xing, X. Wire Structure and Morphology Transformation of Niobium Oxide and Niobates by Molten Salt Synthesis. *Chem. Mater.* **2009**, *21* (7), 1207–1213.

(41) Santulli, A. C.; Zhou, H.; Berweger, S.; Raschke, M. B.; Sutter, E.; Wong, S. S. Synthesis of Single-Crystalline One-Dimensional $LiNbO_3$ Nanowires. *CrystEngComm* **2010**, *12* (10), 2675.

(42) Huang, K.-C.; Huang, T.-C.; Hsieh, W.-F. Morphology-Controlled Synthesis of Barium Titanate

Nanostructures. *Inorg. Chem.* **2009**, *48* (19), 9180–9184.

(43) Wilkes, J. S. A Short History of Ionic Liquids—from Molten Salts to Neoteric Solvents. *Green Chem.* **2002**, *4* (2), 73–80.

(44) Sun, J.; Forsyth, M.; MacFarlane, D. R. Room-Temperature Molten Salts Based on the Quaternary Ammonium Ion. *J. Phys. Chem. B* **1998**, *102* (44), 8858–8864.

(45) Bonhôte, P.; Dias, A.-P.; Papageorgiou, N.; Kalyanasundaram, K.; Grätzel, M. Hydrophobic, Highly Conductive Ambient-Temperature Molten Salts. *Inorg. Chem.* **1996**, *35* (5), 1168–1178.

(46) Calloway, N. O. The Friedel-Crafts Syntheses. *Chem. Rev.* **1935**, *17* (3), 327–392.

(47) P. Walden. Eber Die Molekulargro¨Sse Und Elektrische Leitfa¨Higkeit Einiger Geschmolzenen Salze. *Bull. Acad. Imp. Sci. St.- Petersbourg, Ser.* **1914**, *8* (6), 405 − 422.

(48) Greaves, T. L.; Drummond, C. J. Protic Ionic Liquids: Properties and Applications. *Chemical Reviews*. American Chemical Society **2008**, 108 (1), 206–237.

(49) Hurley, F. H.; WIer, T. P. The Electrodeposition of Aluminum from Nonaqueous Solutions at Room Temperature. *J. Electrochem. Soc.* **1951**, *98* (5), 207.

(50) Wilkes, J. S.; Levisky, J. A.; Wilson, R. A.; Hussey, C. L. Dialkylimidazolium Chloroaluminate Melts: A New Class of Room-Temperature Ionic Liquids for Electrochemistry, Spectroscopy and Synthesis. *Inorg. Chem.* **1982**, *21* (3), 1263–1264.

(51) Hussey, C. L.; Scheffler, T. B.; Wilkes, J. S.; Fannin, A. A. Chloroaluminate Equilibria in the Aluminum Chloride-1-Methyl-3-Ethylimidazolium Chloride Ionic Liquid. *J. Electrochem. Soc.* **1986**, *133* (7), 1389.

(52) George E. McManis, I.; Fletcher, A. N.; Bliss, D. E. Preparation of Ionic Liquids for Electrodeposition, June 5, 1985.

(53) Xu, X.-H.; Hussey, C. L. Electrodeposition of Silver on Metallic and Nonmetallic Electrodes from the Acidic Aluminum Chloride-1-Methyl-3-Ethylimidazolium Chloride Molten Salt. *J. Electrochem. Soc.* **1992**, *139* (5), 1295.

(54) Hurley, F. H.; WIer, T. P. Electrodeposition of Metals from Fused Quaternary Ammonium Salts.

J. Electrochem. Soc. **1951**, *98* (5), 203.

(55) Forsyth, S. A.; Pringle, J. M.; MacFarlane, D. R. Ionic Liquids—An Overview. *Aust. J. Chem.* **2004**, *57* (2), 113.

(56) Wilkes, J. S.; Zaworotko, M. J. Air and Water Stable 1-Ethyl-3-Methylimidazolium Based Ionic Liquids. *J. Chem. Soc. Chem. Commun.* **1992**, *0* (13), 965.

(57) Holbrey, J. D.; Seddon, K. R. Ionic Liquids. *Clean Technol. Environ. Policy* **1999**, *1* (4), 223–236.

(58) Ma, Z.; Yu, J.; Dai, S. Preparation of Inorganic Materials Using Ionic Liquids. *Adv. Mater.* **2010**, *22* (2), 261–285.

(59) García, G.; Aparicio, S.; Ullah, R.; Atilhan, M. Deep Eutectic Solvents: Physicochemical Properties and Gas Separation Applications. *Energy & Fuels* **2015**, *29* (4), 2616–2644.

(60) Abbott, A. P.; Ahmed, E. I.; Harris, R. C.; Ryder, K. S. Evaluating Water Miscible Deep Eutectic Solvents (DESs) and Ionic Liquids as Potential Lubricants. *Green Chem.* **2014**, *16* (9), 4156–4161.

(61) Liu, P.; Hao, J.-W.; Mo, L.-P.; Zhang, Z.-H. Recent Advances in the Application of Deep Eutectic Solvents as Sustainable Media as Well as Catalysts in Organic Reactions. *RSC Adv.* **2015**, *5* (60), 48675–48704.

(62) Dai, Y.; van Spronsen, J.; Witkamp, G.-J.; Verpoorte, R.; Choi, Y. H. Ionic Liquids and Deep Eutectic Solvents in Natural Products Research: Mixtures of Solids as Extraction Solvents. *J. Nat. Prod.* **2013**, *76* (11), 2162–2173.

(63) Abbott, A. P.; Capper, G.; Gray, S. Design of Improved Deep Eutectic Solvents Using Hole Theory. *ChemPhysChem* **2006**, *7* (4), 803–806.

(64) Gómez Rojas, O.; Song, G.; Hall, S. R. Fast and Scalable Synthesis of Strontium Niobates with Controlled Stoichiometry. *CrystEngComm* **2017**, *19* (36), 5351–5355.

(65) Green, D. C.; Glatzel, S.; Collins, A. M.; Patil, A. J.; Hall, S. R. A New General Synthetic Strategy for Phase-Pure Complex Functional Materials. *Adv. Mater.* **2012**, *24* (42), 5767–5772.

(66) Deetlefs, M.; Seddon, K. R. Assessing the Greenness of Some Typical Laboratory Ionic Liquid Preparations. *Green Chem.* **2010**, *12* (1), 17–30.

(67) Plechkova, N. V.; Seddon, K. R. Applications of Ionic Liquids in the Chemical Industry. *Chem. Soc. Rev.* **2008**, *37* (1), 123–150.

(68) Romero, A.; Santos, A.; Tojo, J.; Rodríguez, A. Toxicity and Biodegradability of Imidazolium Ionic Liquids. *J. Hazard. Mater.* **2008**, *151* (1), 268–273.

(69) Zhang, Q.; De Oliveira Vigier, K.; Royer, S.; Jérôme, F. Deep Eutectic Solvents: Syntheses, Properties and Applications. *Chem. Soc. Rev.* **2012**, *41* (21), 7108.

(70) Abbott, A. P.; Capper, G.; Davies, D. L.; Munro, H. L.; Rasheed, R. K.; Tambyrajah, V. Preparation of Novel, Moisture-Stable, Lewis-Acidic Ionic Liquids Containing Quaternary Ammonium Salts with Functional Side Chains. *Chem. Commun.* **2001**, *0* (19), 2010–2011.

(71) Smith, E. L.; Abbott, A. P.; Ryder, K. S. Deep Eutectic Solvents (DESs) and Their Applications. *Chem. Rev.* **2014**, *114* (21), 11060–11082.

(72) Dai, Y.; van Spronsen, J.; Witkamp, G.-J.; Verpoorte, R.; Choi, Y. H. Natural Deep Eutectic Solvents as New Potential Media for Green Technology. *Anal. Chim. Acta* **2013**, *766*, 61–68.

(73) Dai, Y.; Witkamp, G.-J.; Verpoorte, R.; Choi, Y. H. Tailoring Properties of Natural Deep Eutectic Solvents with Water to Facilitate Their Applications. *Food Chem.* **2015**, *187*, 14–19.

(74) Paiva, A.; Craveiro, R.; Aroso, I.; Martins, M.; Reis, R. L.; Duarte, A. R. C. Natural Deep Eutectic Solvents – Solvents for the 21st Century. *ACS Sustain. Chem. Eng.* **2014**, *2* (5), 1063–1071.

(75) Choi, Y. H.; van Spronsen, J.; Dai, Y.; Verberne, M.; Hollmann, F.; Arends, I. W. C. E.; Witkamp, G.-J.; Verpoorte, R. Are Natural Deep Eutectic Solvents the Missing Link in Understanding Cellular Metabolism and Physiology? *PLANT Physiol.* **2011**, *156* (4), 1701–1705.

(76) Dai, S.; Ju, Y. H.; Gao, H. J.; Lin, J. S.; Pennycook, S. J.; Barnes, C. E. Preparation of Silica Aerogel Using Ionic Liquids as Solvents. *Chem. Commun.* **2000**, *0* (3), 243–244.

(77) Green, D. C.; Glatzel, S.; Collins, A. M.; Patil, A. J.; Hall, S. R. A New General Synthetic Strategy for Phase-Pure Complex Functional Materials. *Adv. Mater.* **2012**, *24* (42), 5767–5772.

(78) Jiang, Y.; Zhu, Y.-J. Microwave-Assisted Synthesis of Sulfide M 2 S 3 (M = Bi, Sb) Nanorods Using an Ionic Liquid. *J. Phys. Chem. B* **2005**, *109* (10), 4361–4364.

(79) Nakashima, T.; Kimizuka, N. Interfacial Synthesis of Hollow TiO_2 Microspheres in Ionic Liquids. *J. Am. Chem. Soc.* **2003**, *125* (21), 6386–6387.

(80) Haoguo Z.; Jing-Fang H.; Zhengwei P.; Dai, S. Ionothermal Synthesis of Hierarchical ZnO Nanostructures from Ionic-Liquid Precursors. *Chem. Mater.*, **2006**, 18 (18), 4473–4477.

(81) Taubert, A. CuCl Nanoplatelets from an Ionic Liquid-Crystal Precursor. *Angew. Chemie* **2004**, *116* (40), 5494–5496.

(82) Dupont J., Fonseca G.; Umpierre A.,F. P. Fichtner P.; Teixeira, S. R. Transition-Metal Nanoparticles in Imidazolium Ionic Liquids: Recycable Catalysts for Biphasic Hydrogenation Reactions. *J. Am. Chem. Soc.*, **2002**, 124 (16), 4228–4229.

(83) Ma, Z.; Yu, J.; Dai, S. Preparation of Inorganic Materials Using Ionic Liquids. *Adv. Mater.* **2010**, *22* (2), 261–285.

(84) Armand, M.; Endres, F.; MacFarlane, D. R.; Ohno, H.; Scrosati, B. Ionic-Liquid Materials for the Electrochemical Challenges of the Future. *Nat. Mater.* **2009**, *8* (8), 621–629.

(85) Duan, X.; Ma, J.; Lian, J.; Zheng, W. The Art of Using Ionic Liquids in the Synthesis of Inorganic Nanomaterials. *CrystEngComm* **2014**, *16* (13), 2550.

(86) Yong Z., Antonietti, M. Synthesis of Very Small TiO_2 Nanocrystals in a Room-Temperature Ionic Liquid and Their Self-Assembly toward Mesoporous Spherical Aggregates. *J. Am. Chem. Soc.*, **2003**, 125 (49), 14960–14961.

(87) Dupont, J.; Fonseca, G. S.; Umpierre, A. P.; Fichtner, P. F. P.; Teixeira, S. R. Transition-Metal Nanoparticles in Imidazolium Ionic Liquids: Recycable Catalysts for Biphasic Hydrogenation Reactions. *J. Am. Chem. Soc.* **2002**, *124* (16), 4228–4229.

(88) Galiński, M.; Lewandowski, A.; Stępniak, I. Ionic Liquids as Electrolytes. *Electrochim. Acta* **2006**, *51* (26), 5567–5580.

(89) Hapiot, P.; Lagrost, C. Electrochemical Reactivity in Room-Temperature Ionic Liquids. *Chem. Rev.* **2008**, *108* (7), 2238–2264.

(90) Bhatt, A. I.; Bond, A. M.; MacFarlane, D. R.; Zhang, J.; Scott, J. L.; Strauss, C. R.; Iotov, P. I.;

Kalcheva, S. V. A Critical Assessment of Electrochemistry in a Distillable Room Temperature Ionic Liquid, DIMCARB. *Green Chem.* **2006**, *8* (2), 161–171.

(91) Li-Xia Y., Ying-Jie Z., Wei-Wei W., Hua T., Ruan, M.-L. Synthesis and Formation Mechanism of Nanoneedles and Nanorods of Manganese Oxide Octahedral Molecular Sieve Using an Ionic Liquid. *J. Phys. Chem. B*, **2006**, 110 (13), 6609–6614.

(92) Zhou, Y.; Antonietti, M. Preparation of Highly Ordered Monolithic Super-Microporous Lamellar Silica with a Room-Temperature Ionic Liquid as Template via the Nanocasting Technique. *Adv. Mater.* **2003**, *15* (17), 1452–1455.

(93) Gao, S.; Zhang, H.; Wang, X.; Mai, W.; Peng, C.; Ge, L. Palladium Nanowires Stabilized by Thiol-Functionalized Ionic Liquid: Seed-Mediated Synthesis and Heterogeneous Catalyst for Sonogashira Coupling Reaction. *Nanotechnology* **2005**, *16* (8), 1234–1237.

(94) Antonietti, M.; Kuang, D.; Smarsly, B.; Zhou, Y. Ionic Liquids for the Convenient Synthesis of Functional Nanoparticles and Other Inorganic Nanostructures. *Angew. Chemie Int. Ed.* **2004**, *43* (38), 4988–4992.

(95) Brezesinski, T.; Erpen, C.; Iimura, K. I.; Smarsly, B. Mesostructured Crystalline Ceria with a Bimodal Pore System Using Block Copolymers and Ionic Liquids as Rational Templates. *Chem. Mater.* **2005**, *17* (7), 1683–1690.

(96) Jiang, J.; Yu, S. H.; Yao, W. T.; Ge, H.; Zhang, G. Z. Morphogenesis and Crystallization of Bi_2S_3 nanostructures by an Ionic Liquid-Assisted Templating Route: Synthesis, Formation Mechanism, and Properties. *Chem. Mater.* **2005**, *17* (24), 6094–6100.

(97) Le Bideau, J.; Viau, L.; Vioux, A. Ionogels, Ionic Liquid Based Hybrid Materials. *Chem. Soc. Rev.* **2011**, *40* (2), 907–925.

(98) Ravishankar, T. N.; Nagaraju, G.; Dupont, J. Photocatalytic Activity of Li-Doped TiO_2 Nanoparticles: Synthesis via Ionic Liquid-Assisted Hydrothermal Route. *Mater. Res. Bull.* **2016**, *78*, 103–111.

(99) Tian, Y.; McPherson, M. J.; Wheatley, P. S.; Morris, R. E. Ionic Liquid Assisted Synthesis of

Zeolite-TON. *Zeitschrift für Anorg. und Allg. Chemie* **2014**, *640* (6), 1177–1181.

(100) Li, F.; Wang, X.; Zhao, Y.; Liu, J.; Hao, Y.; Liu, R.; Zhao, D. Ionic-Liquid-Assisted Synthesis of High-Visible-Light-Activated N–B–F-Tri-Doped Mesoporous TiO_2 via a Microwave Route. *Appl. Catal. B Environ.* **2014**, *144*, 442–453.

(101) Chen, Y.; Li, W.; Wang, J.; Gan, Y.; Liu, L.; Ju, M. Microwave-Assisted Ionic Liquid Synthesis of Ti^{3+} Self-Doped TiO_2 Hollow Nanocrystals with Enhanced Visible-Light Photoactivity. *Appl. Catal. B Environ.* **2016**, *191*, 94–105.

(102) Taubert, A.; Li, Z. Inorganic Materials from Ionic Liquids. *Dalt. Trans.* **2007**, *0* (7), 723–727.

(103) Guan, X.; Ma, Y.; Li, H.; Yusran, Y.; Xue, M.; Fang, Q.; Yan, Y.; Valtchev, V.; Qiu, S. Fast, Ambient Temperature and Pressure Ionothermal Synthesis of Three-Dimensional Covalent Organic Frameworks. *J. Am. Chem. Soc.* **2018**, *140* (13), 4494–4498.

(104) Lin, X.-X.; Tan, B.; Peng, L.; Wu, Z.-F.; Xie, Z.-L. Ionothermal Synthesis of Microporous and Mesoporous Carbon Aerogels from Fructose as Electrode Materials for Supercapacitors. *J. Mater. Chem. A* **2016**, *4* (12), 4497–4505.

(105) Chen, F.; Xie, S.; Huang, X.; Qiu, X. Ionothermal Synthesis of Fe_3O_4 Magnetic Nanoparticles as Efficient Heterogeneous Fenton-like Catalysts for Degradation of Organic Pollutants with H_2O_2. *J. Hazard. Mater.* **2017**, *322*, 152–162.

(106) Li, G.; Lian, Z.; Li, X.; Xu, Y.; Wang, W.; Zhang, D.; Tian, F.; Li, H. Ionothermal Synthesis of Black Ti^{3+} -Doped Single-Crystal TiO_2 as an Active Photocatalyst for Pollutant Degradation and H_2 Generation. *J. Mater. Chem. A* **2015**, *3* (7), 3748–3756.

(107) Dai, S.; Ju, Y. H.; Gao, H. J.; Lin, J. S.; Pennycook, S. J.; Barnes, C. E. Preparation of Silica Aerogel Using Ionic Liquids as Solvents. *Chem. Commun.* **2000**, *0* (3), 243–244.

(108) Yong Z., Antonietti, M. Synthesis of Very Small TiO_2 Nanocrystals in a Room-Temperature Ionic Liquid and Their Self-Assembly toward Mesoporous Spherical Aggregates. *J. Am. Chem. Soc.*, **2003**, 125 (49), 14960–14961

(109) Hideaki I.; Kensuke N., Chujo, Y. Synthesis of Gold Nanoparticles Modified with Ionic Liquid

Based on the Imidazolium Cation. *J. Am. Chem. Soc.*, **2004**, 126 (10), 3026–3027.

(110) Yong Z., Jan H. S., Antonietti, M. Room-Temperature Ionic Liquids as Template to Monolithic Mesoporous Silica with Wormlike Pores via a Sol−Gel Nanocasting Technique. *Nano Letters*, **2004**, 4 (3), 477–481.

(111) Mukhopadhyay, I.; Freyland, W. Electrodeposition of Ti Nanowires on Highly Oriented Pyrolytic Graphite from an Ionic Liquid at Room Temperature. *Langmuir* **2003**, *19* (6), 1951–1953.

(112) Yong Z., Antonietti, M. A Series of Highly Ordered, Super-Microporous, Lamellar Silicas Prepared by Nanocasting with Ionic Liquids. *Chem. Mater.*, **2004**, 16 (3), 544–550.

(113) Zhou, Y.; Antonietti, M. A Novel Tailored Bimodal Porous Silica with Well-Defined Inverse Opal Microstructure and Super-Microporous Lamellar NanostructureElectronic. *Chem. Commun.* **2003**, *0* (20), 2564.

(114) Celorrio, V.; Calvillo, L.; van den Bosch, C. A. M.; Granozzi, G.; Aguadero, A.; Russell, A. E.; Fermín, D. J. Mean Intrinsic Activity of Single Mn Sites at $LaMnO_3$ Nanoparticles Towards the Oxygen Reduction Reaction. *ChemElectroChem* **2018**.

(115) Gobaille-Shaw, G. P. A.; Celorrio, V.; Calvillo, L.; Morris, L. J.; Granozzi, G.; Fermín, D. J. Effect of Ba Content on the Activity of $La_{1-x}Ba_xMnO_3$ Towards the Oxygen Reduction Reaction. *ChemElectroChem* **2018**, *5* (14), 1922–1927.

(116) Boston, R.; Foeller, P. Y.; Sinclair, D. C.; Reaney, I. M. Synthesis of Barium Titanate Using Deep Eutectic Solvents. *Inorg. Chem.* **2017**, *56* (1), 542–547.

(117) Li, X.; Guo, W.; Liu, Y.; He, W.; Xiao, Z. Spinel $LiNi_{0.5}Mn_{1.5}O_4$ as Superior Electrode Materials for Lithium-Ion Batteries: Ionic Liquid Assisted Synthesis and the Effect of CuO Coating. *Electrochim. Acta* **2014**, *116*, 278–283.

(118) Preethi, T.; Padmapriya, M. P.; Abarna, B.; Rajarajeswari, G. R. Choline Chloride–zinc Chloride Ionic Liquid as a Green Template for the Sol–gel Synthesis of Mesoporous Titania. *RSC Adv.* **2017**, *7* (17), 10081–10091.

(119) Patil, H. R.; Murthy, Z. V. P. Ionic Liquid Assisted Vanadium Pentoxide Synthesis through Sol-

Gel Method: Catalyst Support for Broad Molecular Weight Distribution Polyethylene Synthesis. *Arab. J. Chem.* **2016**, 1.

(120) Ji, X.; Tang, S.; Gu, L.; Liu, T.; Zhang, X. Synthesis of Rod-like Mesoporous γ-Al_2O_3 by an Ionic Liquid-Assisted Sol–gel Method. *Mater. Lett.* **2015**, *151*, 20–23.

(121) Zhang, S.; Dokko, K.; Watanabe, M. Carbon Materialization of Ionic Liquids: From Solvents to Materials. *Mater. Horizons* **2015**, *2* (2), 168–197.

(122) Dutta, S.; Bhaumik, A.; Wu, K. C.-W. Hierarchically Porous Carbon Derived from Polymers and Biomass: Effect of Interconnected Pores on Energy Applications. *Energy Environ. Sci.* **2014**, *7* (11), 3574–3592.

(123) Han, C.; Wang, J.; Gong, Y.; Xu, X.; Li, H.; Wang, Y. Nitrogen-Doped Hollow Carbon Hemispheres as Efficient Metal-Free Electrocatalysts for Oxygen Reduction Reaction in Alkaline Medium. *J. Mater. Chem. A* **2014**, *2* (3), 605–609.

(124) Soll, S.; Antonietti, M.; Yuan, J. Poly(Ionic Liquid) Nanoparticles as Novel Colloidal Template for Silica Nanocasting. *Polymer (Guildf).* **2014**, *55* (16), 3415–3422.

(125) Chen, A.; Li, Y.; Liu, L.; Yu, Y.; Xia, K.; Wang, Y.; Li, S. Controllable Synthesis of Nitrogen-Doped Hollow Mesoporous Carbon Spheres Using Ionic Liquids as Template for Supercapacitors. *Appl. Surf. Sci.* **2017**, *393*, 151–158.

Web links for images

Figure 1.1

Https://www.fh- muenster.de/ciw/downloads/personal/juestel/juestel/Funktionsmaterialien_englisch_.pdf

Chapter 2
Experimental and characterisation

2.1 Reactants

Name	CAS number	Linear formula	Molecular weight	Form	Company	Id
Barium nitrate	10022-31-8	$Ba(NO_3)_2$	261.34	Crystals and lumps	Sigma-Aldrich	202754
Betaine	107-43-7	$(CH_3)_3N^+CH_2COO^-$	117.15	Powder	Sigma-Aldrich	61962
Bismuth(III) nitrate pentahydrate	10035-06-0	$Bi(NO_3)_3 \cdot 5H_2O$	485.07	Crystals and lumps	Sigma-Aldrich	467839
Calcium nitrate tetrahydrate	13477-34-4	$Ca(NO_3)_2 \cdot 4H_2O$	236.15	Crystals and lumps	Sigma-Aldrich	C1396
Cellulose	9004-34-6	$(C_6H_{10}O_5)_n$	Not specified	Microcrystalline powder (51 µm particle size)	Sigma-Aldrich	435236
Chitosan	9012-76-4	$(C_6H_{11}NO_4)_n$	190000-375000	Powder	Sigma-Aldrich	417963
Choline chloride	67-48-1	$(CH_3)_3N(Cl)CH_2CH_2OH$	139.62	Powder	Sigma-Aldrich	C7017
Copper(II) nitrate hemi(pentahydrate)	19004-19-4	$Cu(NO_3)_2 \cdot 2.5H_2O$	232.59	Crystals and lumps	Sigma-Aldrich	467855
Dextran from *Leuconostoc* spp.	9004-54-0	$(C_6H_{10}O_5)_n$	~70,000	Powder	Sigma-Aldrich	31390
D-(+)-Glucose	50-99-7	$C_6H_{12}O_6$	180.16	Powder	Sigma-Aldrich	G8270
Ethylene glycol	107-21-1	$HOCH_2CH_2OH$	62.07	Liquid	Sigma-Aldrich	324558
Imidazole	288-32-4	$C_3H_4N_2$	68.08	Solid	Sigma-Aldrich	I2399
Niobium(V) ethoxide	3236-82-6	$Nb(OCH_2CH_3)_5$	318.21	Liquid	Sigma-Aldrich	339202
Sodium hydroxide	1310-73-2	NaOH	39.98	Pellet	Sigma-Aldrich	221465
Starch	9005-84-9	$(C_6H_{10}O_5)_n$	Not specified	Powder	Sigma-Aldrich	179930
Strontium nitrate	10042-76-9	$Sr(NO_3)_2$	211.63	Crystals and lumps	Sigma-Aldrich	204498
Yttrium(III) nitrate hexahydrate	13494-98-9	$Y(NO_3)_3 \cdot 6H_2O$	383.01	Crystals and lumps	Sigma-Aldrich	237957
1-Ethyl-3-methylimidazolium acetate	143314-17-4	$C_8H_{14}N_2O_2$	170.21	Liquid	Sigma-Aldrich	51053

Table 2.1. List of reactants used accommodated by alphabetical order.

2.2 Fast and scalable synthesis of strontium niobates with controlled stoichiometry

2.2.1 Generation of aqueous precursors

Strontium nitrate 0.1 M solution was prepared by adding 0.212 g of strontium nitrate to 10 ml of deionized water.

2.2.2 Generation of ionic liquid-based precursors

1 ml of strontium nitrate solution was added to 1 mL (emim)OAc under stirring until evenly dispersed. The whole was then heated to 80 °C in an alumina crucible under stirring to remove water from the mixture for 1 to 2 h. Different amounts of niobium ethoxide was then added depending on the desired stoichiometry, ranging from 12.55 to 0.11 Sr/Nb molar ratio. The mixture remained under heating and constant stirring for one further hour, ensuring full dehydration of the system.

2.2.3 Polysaccharide dissolution

Dextran was added as a weakly coordinating, nonspecific chelating agent, (1 g) and mechanically mixed until a dense paste-like gel was formed.

2.2.4 Heating protocols

Dehydrated precursors were calcined immediately after preparation in air in crucibles for 2 h with a heating ramp rate of 5 °C min^{-1} at 1000 °C. For temperature analysis samples were calcine from 550 °C to 1000 °C with increases of 50 °C.

2.3 On the synergistic interaction of an ionic liquid and biopolymers in the synthesis of strontium niobate and high-temperature superconductor $YBa_2Cu_3O_{7-\delta}$

2.3.1 Generation of aqueous precursors

2.3.1.1 Synthesis of strontium niobate

Strontium nitrate 0.1 M solution was prepared by adding 0.212 g of strontium nitrate to 10 ml of deionized water.

2.3.1.2 Synthesis of $YBa_2Cu_3O_{7-\delta}$

Following the same conditions that were previously reported[1], yttrium nitrate hexahydrate (0.1915 g, 0.05 M), barium nitrate (0.2614 g, 0.1 M) and copper nitrate hemipentahydrate (0.3489 g, 0.15 M) were added to DI water (10 ml) under stirring until all salts dissolved, forming a light blue solution.

2.3.2 Generation of ionic liquid-based precursors

2.3.2.1 Synthesis of strontium niobate

1 ml of strontium nitrate was added to 1 ml (emim)OAc under stirring and heated at 70 °C in an alumina crucible for 2 h to ensure dehydration of the precursor. Niobium ethoxide in a 1:1 Sr/Nb molar ratio was then added and remain under stirring and heat for another 30 min.

2.3.2.2 Synthesis of $YBa_2Cu_3O_{7-\delta}$

1 ml of nitrates solution was added to 1 ml (emim)OAc under stirring and heated at 70 °C in an alumina crucible for 2 h to ensure dehydration of the precursor.

2.3.3 Polysaccharide dissolution

The organic source, namely dextran, chitosan, starch, and cellulose, 0.1 g and 1.0 g, was added for and mechanically mix to form a paste-like mixture. For the synthesis of YBCO superconductor only 0.1 g is used.

2.3.4 Heating protocols

2.3.4.1 Synthesis of strontium niobate

Dehydrated precursors were calcined immediately after preparation in air in crucibles for 2 h with a heating ramp rate of 5 °C min $^{-1}$ at 1000 °C.

2.3.4.2 Synthesis of $YBa_2Cu_3O_{7-\delta}$

Dehydrated precursors were calcined immediately after preparation in air in crucibles for 2 h with a heating ramp rate of 5 °C min $^{-1}$ at 920 °C.

2.4 The role of ionic liquids/deep eutectic solvents in the synthesis of the high-temperature superconductors $YBa_2Cu_3O_{7-\delta}$ and $Bi_2Sr_2CaCu_2O_{8+x}$

2.4.1 Generation of deep eutectic solvents

2.4.1.1 Imidazole 7:3 choline chloride DES

Synthesized by mixing both solids in the stated molar ratio. After that it was put in an oven at 70 °C to allow the mixture of such. The liquid will start forming after a few hours and can be mixed at two-hour intervals for 24 h in order to allow a complete interaction of both compounds.

2.4.1.2 Ethylene glycol 2:1 choline chloride DES

Synthesized by mixing choline chloride with the stated molar ratio of ethylene glycol. The mixture was placed in an oven at 70 °C for half an hour to ensure complete interaction of both components.

2.4.1.3 Betaine 5:2 D-(+)-glucose DES

Synthesized by mixing both solids in the stated molar ratio, 3 g with 1.8453 g respectively. After that, water (6.336 ml) was added to allow the mixture of such with a final volume of 10 ml. The complete mixture will start forming after a few minutes under strong agitation

2.4.2 Generation of aqueous precursors

2.4.2.1 Synthesis of $YBa_2Cu_3O_{7-\delta}$

As reported above, yttrium nitrate hexahydrate (0.1915 g, 0.05 M), barium nitrate (0.2614 g, 0.1 M) and copper nitrate hemipentahydrate (0.3489 g, 0.15 M) were added to DI water (10 mL) under stirring until all salts dissolved, forming a light blue solution.

2.4.2.2 Synthesis of $Bi_2Sr_2CaCu_2O_{8+x}$

Calcium nitrate tetrahydrate (0.05 M), 0.2116 g strontium nitrate (0.1 M), and 0.2326 g copper nitrate hemi(pentahydrate) (0.1 M) were mixed in a vial with 10 ml DI water under stirring until all salts dissolved, forming a light blue solution.

2.4.2.3 Synthesis of $Na_{0.1}Sr_{0.9}NbO_3$

Strontium nitrate 0.1 M solution was prepared by adding 0.212 g of strontium nitrate to 10 ml of deionized water. Sodium hydroxide 0.05 M solution was prepared by adding 0.0199 g of sodium hydroxide to 10 ml of deionized water. After stirring for a few minutes transparent solutions were prepared.

2.4.3 Generation of ionic liquid-based precursors

2.4.3.1 Synthesis of $YBa_2Cu_3O_{7-\delta}$

The aqueous solution was mixed in a 1:1 v/v ratio with the different solvents, namely (emim)OAc, imidazole 7:3 choline chloride DES and ethylene glycol 2:1 choline chloride DES, as well as with 7.12 M Imidazole and 8.29 M Ethylene glycol. The mixtures were heated to 70 °C for 2 hours to allow full dehydration

2.4.3.2 Synthesis of $Bi_2Sr_2CaCu_2O_{8+x}$

Solutions were prepared by mixing bismuth nitrate (0.242 g, 0.1 M) in 5 ml of DES. Then, 1 ml of betaine/bismuth solution was then added to 1 ml of the rest of metal nitrates solution plus an extra 1.05 ml of betaine: D-(+)-glucose DES solution. The final volume ratio was 0.75:1 v/v betaine: D-(+)-glucose DES/metal nitrate solution. The mixture was then heated at 70 °C for 2 hours to allow full dehydration.

2.4.3.3 Synthesis of $Na_{0.1}Sr_{0.9}NbO_3$

1 ml of strontium nitrate (0.1 M) solution was added to 1 ml of (emim)OAc or imidazole: choline chloride DES. After 2 h of dehydration under 70 °C niobium ethoxide was added (Sr/Nb 1:2 molar ratio) and dehydrated for further 30 minutes. Finally, 1 ml of sodium hydroxide (0.05 M) is added and the solution, with a final Na/Sr/Nb molar ratio of 1:2:3, is left for further 2 h under heating to dehydrate.

2.4.4 Polysaccharide dissolution

2.4.4.1 Synthesis of $YBa_2Cu_3O_{7-\delta}$

To form a gel, 100 mg of dextran was added to every solution previously dehydrated and mixed mechanically using a spatula.

2.4.4.2 Synthesis of $Bi_2Sr_2CaCu_2O_{8+x}$

After complete dehydration a gel will be obtained therefore there is no need to add extra poly-chelating agents.

2.4.4.3 Synthesis of $Na_{0.1}Sr_{0.9}NbO_3$

After complete dehydration 1.0 g of dextran is added and mechanically mixed until a paste-like product is formed.

2.4.5 Heating protocols

2.4.5.1 Synthesis of $YBa_2Cu_3O_{7-\delta}$

Dehydrated precursors were calcined immediately after preparation in air in crucibles for 2 h with a heating ramp rate of 5 °C min^{-1} at 920 °C. For temperature analysis samples were calcine from 320 °C to 920 °C with increases of 100 °C.

2.4.5.2 Synthesis of $Bi_2Sr_2CaCu_2O_{8+x}$

Dehydrated precursors were calcined immediately after preparation in air in crucibles for 2 h with a heating ramp rate of 5 °C min $^{-1}$ at 850 °C. For temperature analysis samples were calcine from 350 °C to 750 °C with increases of 100 °C, and from 775 °C to 850 °C with increases of 25 °C.

2.4.5.3 Synthesis of $Na_{0.1}Sr_{0.9}NbO_3$

The paste-like product is places in the furnace for calcination process with a dwelling time of 6 h, ramp rate of 1 °C min $^{-1}$ at 1100 °C. For temperature analysis samples were calcined from 400 °C to 1100 °C with increases of 100 °C.

2.5 Sample preparation and characterizations

2.5.1 Powder X-ray Diffraction

2.5.1.1 Sample preparation

All the samples where powder x-ray diffraction was carried out were in form of fine powder. If the sample was not, then materials were previously pulverised in a pestle and mortar to generate a uniform fine powder to later be mounted on silicon wafer holder.

2.5.1.2 Equipment

Powder X-ray diffraction (XRD) was carried out on Bruker D8 Advance diffractometer (CuKα 1 radiation at λ = 1.54056 Å) equipped with a Lynx-eye position sensitive detector.

Rietvield analysis was done via Profex 3.12.1 Software[2] using the next ICSD cards:

28009	**$Bi2O_{2.5}$**
15865	**Bi_2CuO_4**
202841	**$Bi_{0.8}Ca_{0.2}O_{1.19}$**
56774	**$Bi_6Sr_{6.27}Ca_{4.73}O_{22}$**
71910	**$Bi_{1.916}Sr_{1.84}CuO_{5.482}$**
203210	**$Bi_{2.09}Sr_{1.9}CaCu_2O_{8.22}$**
63257	**$Ba(CO_3)$**
15196	**$Ba(CO_3)$**
261703	**$Ba(C_2O_4)$**
65801	**$BaCuO_2$**
262674	**$BaCl_2$**
35495	**$Ba(NO_3)_2$**
18164	**$CaCO_3$**
54129	**$(CuO_2)_4$**
54126	**CuO_2**
69757	**CuO**
16025	**CuO**
188351	**Cu_6O_8YCl**
100633	**NaCl**
51872	**$Na_{0.3}Sr_{0.7}NbO_3$**
201461 & 190073	**$Sr_{0.85}C_{a0.15}CO_3$ & $SrCa(CO_3)_2$**
27293	**$SrCO_3$**
79217	**$Sr_4Nb_2O_9$**
59581 to 59584	**$Sr_4Nb_2O_9$**
79218	**$Sr_5Nb_4O_{15}$**
187 & 40803	**$Sr_2Nb_2O_7$**
60782	**$SrNb_2O_6$**
60783	**$SrNb_6O_{16}$**
52276	**SrO**
27772	**Y_2O_3**
202877	**$Y_2Cu_2O_5$**
39456	**$Y_{0.98}Ba_{1.98}Cu_{2.91}O_{6.47}$**
67860	**$YBa_2Cu_{2.78}O_7$**
62463	**$YBa_2\ Cu_3O_{6.8}$**
68449	**$YBa_2Cu_{2.86}O_{6.6}$**
39359	**$YBa_2Cu_3O_{6.9}$**
67860	**$YBa_2Cu_{2.78}O_7$**
62915	**$YBa_2Cu_{2.87}O_{6.76}$**
32707	**Y_2BaCuO_5**
65550	**$Y_{0.5}Ba_3Cu_{1.5}O_{5.5}$**
65549	**$Y_{0.25}BaCu_{0.75}O_{2.25}$**

Table 2.2. ICSD numbers (left) with the corresponding crystal phases (right)

2.5.2 Electron Microscopy

2.5.2.1 Sample preparation

2.5.2.1.1Scanning electron microscopy (SEM)

Samples in the form of fine powder were place on the top of a sticky conductive carbon tab attached to the top of an aluminium sample stub. To analyse the morphology samples were place very carefully on top of the carbon sticky layer. It is important to ensure the stabilization of the sample on the sticky carbon layer to avoid damaging the equipment. When energy dispersive X-ray analysis was carried out, to avoid noise signal a pellet, pressing force of 2000 kg effective mass, was then used instead of the powder form.

2.5.2.1.2Transmission electron microscopy (TEM)

Samples if needed were pulverized in a pestle and mortar to obtain a uniform fine powder. If the powder was already in such conditions then, it was transferred to 5 ml volume vial. 1 ml of ethanol was then added and sonicated in a bath sonicator to brake any agglomerate previously formed. The exact volume of powder material was not measured however, the aim is to form a highly dispersed solution. With a 20 µl pipette 5 µl where extracted from the suspension solution and dropped onto a TEM carbon-coated copper grid and left to dry for 24 h.

2.5.2.2 Equipment

TEM analysis was carried out on JEOL JEM 1400EX microscope equipped with an Oxford energy dispersive X-Ray detector and JEOL 2100 Hi-Res TEM, also adapted with an Oxford energy dispersive X-Ray detector.

SEM samples were analysed on JEOL JSM 5600LV with Oxford energy dispersive X-ray detector.

2.5.3 Superconducting quantum interreference device magnetometry (SQUID)

2.5.3.1 Sample preparation

The superconductive properties were investigated using DC magnetic susceptibility measurements of the two superconductors synthesized along this project. For that, samples were mounted in the short portion of a plastic capsule. Cotton was then inserted on the top of the sample to create extra pressure. Finally, the capsule was closed when the large portion of the capsule is inserted into the small portion. This was to ensure high density of the material to enhance the quality of the signal provided. The amount of sample ranged depending on the availability however, an optimal value was in between 30 to 50 mg.

2.5.3.2 Equipment

Analyses were done with a superconducting quantum interference device magnetometer (Quantum Design MPMS-XL) equipped with a 5 T superconducting magnet. Samples were run under in zero-field cooling (ZFC) and 10 Oe field-cooling (FC) conditions with temperature ranges of 20 - 120 K.

2.5.4 Attenuated total reflection Fourier transform infra-red (ATR-FTIR) spectroscopy

2.5.4.1 Sample preparation

To ensure evenly conditions, when FTIR spectrums were taken from the mix of ionic liquids/deep eutectic solvents and metal cations, and to avoid solidification at room temperature, dehydrated samples (heated at 70 °C - 80 °C) were analysed immediately. Hydrated samples, on the other hand, due to the interaction of water with such solvents remained in liquid state, despite that, samples once water was added remained under strong agitation for five minutes and then immediately taken to be examined. With a 20 µl pipette 5 µl were taken out of the liquid solution and placed on the quartz window of the FTIR. Solid samples required no previous preparation and when placed on the quartz window pressure was added via

the UATR accessory for solids. Transmission (T%) vs. wavenumber (cm^{-1}) spectra were obtained in a range from 4000 to 400 cm^{-1}. Every spectrum is a combined result of four scans with a speed of 100 cm^{-1}/s.

2.5.4.2 Equipment

Attenuated total reflection Fourier transform infrared (ATR-FTIR) spectroscopy was conducted on a Perkin Elmer Spectrum two ATR-FTIR spectrometer mounted with UATR accessory for solids.

2.5.5 Ultra violet and visible light (UV-Vis) spectroscopy

2.5.5.1 Sample preparation

Liquid samples were deposited in quartz cuvettes of 500 µl volume. When the absorbance was measured, spectra were typically obtained between the range of 350-800 nm in intervals of 1 nm and accumulation time of 0.1 s, slit width 5 nm. For solid state samples in fine powder condition were mounted in a Shimadzu special cylindrical sample holder with round glass integrated. Transmittance was then measure under the same conditions stated above for liquid samples and transformed to absorbance via Kubelka-Munk transformation following the equation:

(1). $\frac{K}{S} = \frac{(1-R_\infty)^2}{2R_\infty}$ Where K is the absorption and R_∞ is the diffuse reflectance.

2.5.5.2 Equipment

Uv-Vis spectra were obtained using a Uv- 2600 uv-vis spectrophotometer from Shimadzu.

2.5.6 Differential scanning calorimetry & Thermogravimetric analysis (DSC-TGA)

2.5.6.1 Sample preparation

Small amount of the coagulated sample (IL + metal cations + polysaccharide) was placed in a ceramic alumina pan and weighted. The sample was then run in a small furnace at 10 °C /min under oxygen from 0 to 1100 °C. Heath flow (μV) and weight loss (mg) were measure during the run.

2.5.6.2 Equipment

Mettler Toledo TGA/DSC1 Star System.

2.5.7 Inductively coupled plasma atomic emission spectroscopy (ICP-OES)

2.5.7.1 Sample preparation

Samples must be in solution form, ideally 1 % nitric acid and free from suspended solids. Due to difficulties digesting samples instead of nitric acid aqua regia was used. The ideal final concentration range of the elements should be between 1 and 25 ppm (mg/L).

2.5.7.2 Equipment

The ICP-OES was run in an Agilent 710 simultaneous spectrometer.

2.5.8 Computational analysis/refinements

Rietvield analysis was done via Profex 3.12.1 Software[2] and all the size distributions were measured using ImageJ2 software.[3]

2.6 Bibliography

(1) Green, D. C.; Glatzel, S.; Collins, A. M.; Patil, A. J.; Hall, S. R. A New General Synthetic Strategy for Phase-Pure Complex Functional Materials. *Adv. Mater.* **2012**, *24* (42), 5767–5772.

(2) Doebelin, N.; Kleeberg, R. *Profex* : A Graphical User Interface for the Rietveld Refinement Program *BGMN*. *J. Appl. Crystallogr.* **2015**, *48* (5), 1573–1580.

(3) Rueden, C. T.; Schindelin, J.; Hiner, M. C.; DeZonia, B. E.; Walter, A. E.; Arena, E. T.; Eliceiri, K. W. ImageJ2: ImageJ for the next Generation of Scientific Image Data. *BMC Bioinformatics* **2017**, *18* (1), 529.

Chapter 3
Fast and scalable synthesis of strontium niobates with controlled stoichiometry

Parts of this chapter are published in the reference indicated below printed in CrystEngComm. The paper used in the creation of this chapter was written and submitted by myself involving the preparation of all figures and text contained herein. I was involved in analysis of all data collected both directly by myself and on behalf of the publication by co-authors. Any data used in this thesis, collected and analysed with only minimal input from myself has been referenced accordingly. Specifically, all data was collected by myself other than HRTEM images taken by Jean-Charles Eloi the Electron Microscopy Technician.

Gómez Rojas, O.; Song, G.; Hall, S. R. Fast and Scalable Synthesis of Strontium Niobates with Controlled Stoichiometry. *CrystEngComm* **2017**, *19* (36), 5351–5355

3.1 Introduction

Complex functional materials can be synthesized by a wide range of techniques, for example solid state, hydrothermal method, sol-gel/hydrothermal method, and molten salt synthesis. Advantages and disadvantages of those techniques were briefly discussed in the introduction section (pp. 13-14) however, greater disadvantages are, when methodologies tend to be highly time and energy consuming, the lack of understanding of the synthetic process, and high complexity. In addition, having control over the homogeneity of the sample can be a hard task to attain. The rapid progress of technological developments in ferroelectric,[1] ferromagnetic,[2] superconducting,[3] and piezoelectric[4] materials demand the discovery of new synthetic routes to create materials with high efficiency. One way to improve upon a solution-based synthetic approach is the use of ionic liquids. One of the properties of these systems that has been widely exploited is the fact that can dissolve a broad range of different compounds and keep them in solution.[5,6]

In 1998 Rogers and co-workers[7] suggested for the first time that ionic liquids may be suitable as the basis of novel liquid-liquid extraction systems. Since then numerous reports followed, describing the application of ionic liquids as solvents in the extraction of simple organic compounds, [8,9] biomolecules, [10,11] and metal ions. [12–17]

Soon after the first proposal, Dai et al. extracted strontium nitrate from water solution into a series of dialkylimidazolium-based, ionic liquids containing a crown ether, dicyclohexano-18-crown-6 (DCH18C6). For this purpose, hydrophobic ionic liquids were utilized. Dai made mention that thermodynamically the solvation of ionic species, such as NO_3^-, and SO_4^{2-}, in the ionic liquid, should be much more favourable than those in conventional solvents. Results show (Table 3.1) how the ether-crown capability to link to metals is augmented when mix with the ionic liquids. Moreover, despite not as high as when another complexing agent is used, the ionic liquid is capable to chelate the metal cation.[17]

Extract phase	D^a (with crown ether in melts)	D(without crown ether in melts)
$BuMe_2ImPF_6$	4.2	0.67
$BuMeImPF_6$	2.4×10^1	0.89
$EtMe_2ImTf_2N$	4.5×10^3	0.81
$EtMeImTf_2N$	1.1×10^4	0.64
$PrMe_2ImTf_2N$	1.8×10^3	0.47
$PrMeImTf_2N$	5.4×10^3	0.35
$C_6H_5CH_3$	7.6×10^{-1}	nm[b]
$CHCl_3$	7.7×10^{-1}	nm

Table 3.1[17] Comparison of the extraction results obtained using ionic liquids and conventional solvents. (The D value is defined as D = [Molten salt concentration of Sr^{2+}]/[aqueous solution concentration of Sr^{2+}]. When nm = not measurable.

ILs have shown proficiency performing metal extraction from mineral matrices, [18] or spent nuclear fuel, [19] as well as for electrodeposition and electrowinning of metals.[19] Metal extraction is without a doubt one of the biggest areas where ionic liquids have been applied, for that purpose ILs bearing Lewis base anions (principally chloride and bromide), as coordination anions with added halides to increase metal cation solubility, have been used. [20] As aforementioned, the solubility of metals in the IL can be increased by the additament of ligands such as crown ethers, [21] calizarenes,[12] ditizone, [22] or, more recently thione.[23] Metal solubility can also be increase by the incorporation of specific functional groups, for example thioether or thiourea, which favour Hg^{2+} and Cd^{2+} ion solubility,[24] or nitrile and disulfide functional groups which have been employed to extract Ag^+ and Pd $^{2+}$ or Hg^{2+} and Cu^{2+} respectively.[25]

Green et al.[26] saw the potential of these systems with a slight twist. Using functional groups, namely NO_3^- and carboxyl group in the form of acetate CH_3COO^-, to chelate the metal cation (Figure 3.1), they were able to form a multi cationic solution. A main difference of the process is the use of miscible ionic liquids, to avoid precipitates, and all salts used were nitrates that when, if possible, were previously dissolved in water. A dehydration process is followed removing water molecules from the system, leaving a rich stable multicationic solution. For the metal salt insoluble in water, i.e. bismuth nitrate, ethylenediaminetetraacetic

acid (EDTA) is also employed, to maintain it in solution, analogue to what was previously reported by Dai et al. with the ether crowns.

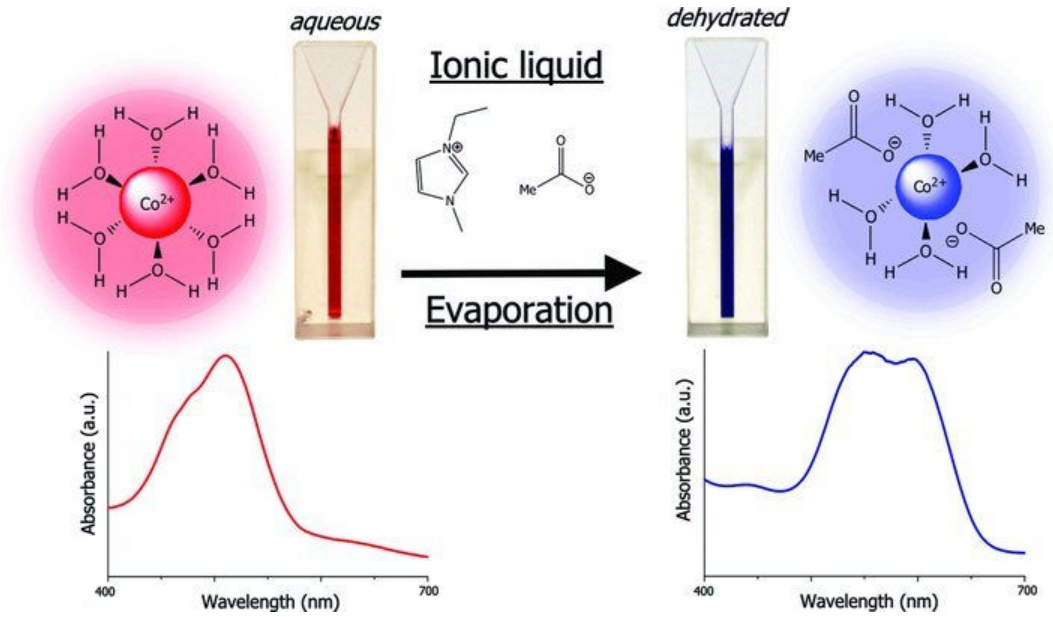

Figure 3.1.[26] Schematic representation of the dehydration process where, acetate actively participates in the chelation of the metal cation occasioning a shift towards higher wavelengths.

With this principle idea executed ILs proved to be capable to synthesize multi-element complex functional oxides, accomplishing single-phase crystals of different complex materials such as: superconductors, piezoresponsive, multiferroic, ferromagnetic and phosphor.[26] Another advantage to using ILs is that it is possible to solubilise other non-specific chelating agents such as dextran, chitosan, cellulose, and starch within them, thereby increasing the chelating ability of the system. Furthermore, this interaction between the organic molecule and the ionic liquid will be analysed in further detail later.

In the next section we seek to explore the full potential of the ionic liquids to form multicationic solutions. The aim is to demonstrate the capability of this synthetic procedure to allow maximum control over the stoichiometry of the final crystal composition.

3.2 Synthesis of high yields (> 98 %) of single-phase strontium niobates

3.2.1 Results and discussion

The sample preparation was carried out using 1-ethyl-3-methylimidazolium acetate (emim)OAc as a complexing agent. However, to avoid metal specific or preferential chelation and to keep homogeneity in the system, dextran was then added as a weakly coordinating, nonspecific chelating agent. Previously all metal ions were dissolved and dehydrated in the IL to then form a paste-like "gel" with the carbon source dissolution. Adding a carbon source into the reaction also serves a second purpose, as carbonization occurs over the calcination process, thereby providing a cocooning environment which prevents the sintering of crystallites restricting them to the nanoscale. Moreover, it provides a reducing atmosphere, generating CO_2 as the carbon is oxidised over the course of the synthesis, enabling a fine degree of control over the stoichiometry of the resultant inorganic product. All dehydrated precursors were calcined immediately after preparation in air in crucibles for 2 h with a heating ramp rate of 5 °C/min at 1000 °C.

3.2.1.1 TGA/DSC

To start unveiling the mechanistic crystal growth of the system TGA/DSC analysis was first performed. The initial wt. % of every component of the reaction are 51.1 % corresponding to dextran, 46 % to (emim)OAc, and 2.9 % to the metal nitrates. TGA (Figure 3.2 Left) does not exhibited a mass loss from 30 °C to 200 °C however, immediately after, a constant drop in mass percentage is observed displaying a mass loss of 12.1 % at 250 °C, being a water free system, this mass loss is assumed to be the early stages of (emim)OAc decomposition. Shortly after, at 300 °C the system has lost 64.4% of its total mass indicating the decomposition of the ionic liquid and the organic source. This carbonaceous material provided by the organic capping agent and the decomposition of the ionic liquid will be lost steadily having being completely consumed at 546 °C. At this point 11. 3 % of total mass is present in the system corresponding to materials containing strontium, niobium, carbon and oxygen. Notably surpassing this temperature, a constant mass gain is observed (Figure 3.2 Left inset). This can only be related to oxygen gain, suggesting

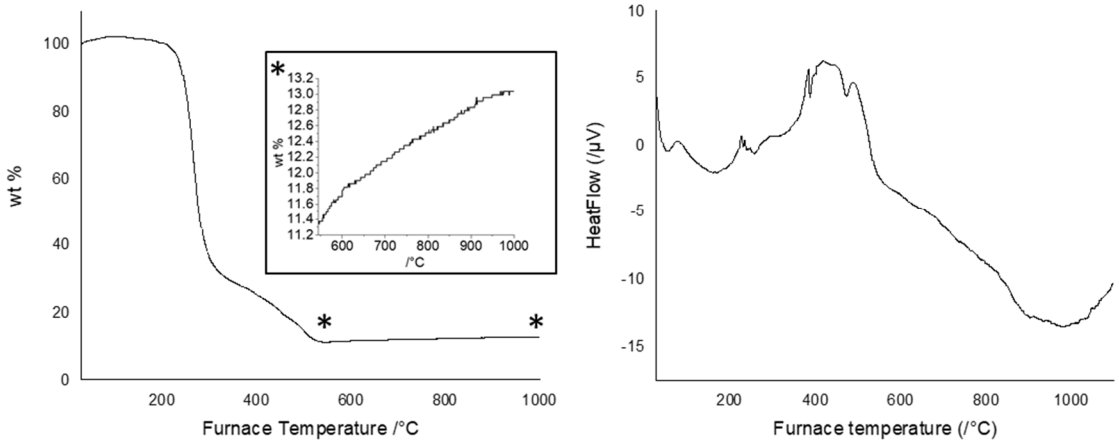

Figure 3.2. TGA (Left) and DSC (Right) analysis of the synthesis of $Sr_5Nb_4O_{15}$. Inset represents a zoom area from 545 °C to 1000 °C, showing the gain of mass assumed to be due to niobium oxidation.

that the crystal compositions formed are oxygen deficient. DSC shows that an exothermic process is being carried out from 160 °C to 489 °C which, coincide with the decomposition of both the ionic liquid and the organic capping agent, also represented by a big mass loss in the TGA. After this point an endothermic process is observed indicated by a steady tendency towards negative values in heath flow, linked to the formation of more stable compounds such as crystals. The lowest value was found to be from 950 °C to 1000 °C

3.2.1.2 Analysis via pXRD

To comprehend the crystal growth temperature analysis via powder X-ray diffraction patterns (Figure 3.3) and Rietvield refinement (Figure 3.4) were performed from 450 °C to 900 °C with a step size of 50 °C. The targeted phase was $Sr_5Nb_4O_{15}$. The crystal growth of the reaction is fairly simple and can be described as follows: at the beginning of the reaction, from 450 °C to 550 °C, only diffractions belonging strontium carbonate are indexable. Also present are broad peaks belonging to amorphous mass. From 550 °C to 700 °C peaks belonging to the phase $SrNbO_{3-x}$ are exhibited. This encounter creates some discordance. The powder diffraction peaks match, in essence, quite well with the diffraction peaks present from the crystal phase $SrNbO_{3-x}$. Moreover, TGA analysis does imply there is a gain in oxygen in the range of ~550 °C to 1000 °C, giving the possibility that a reduced niobium phase could form in the way of Nb (IV).

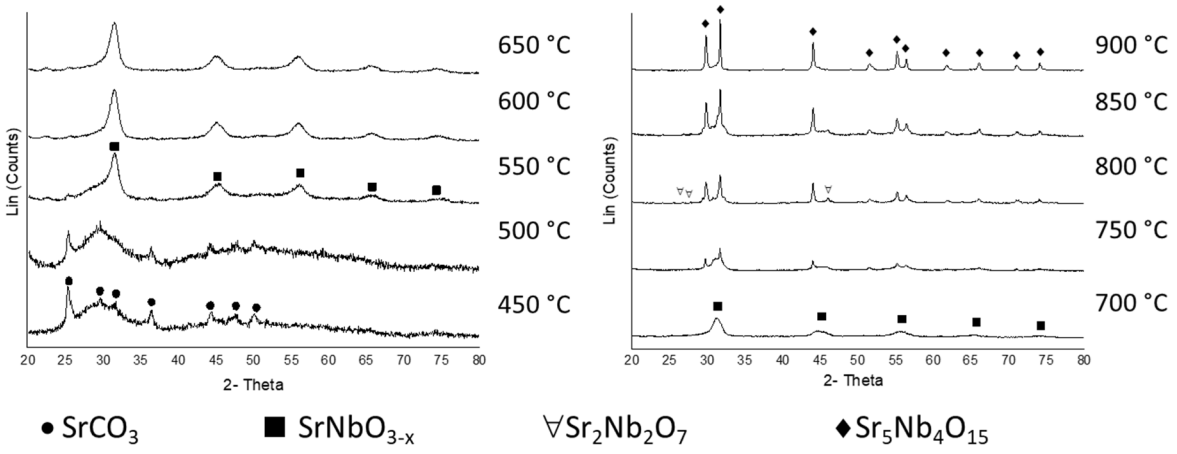

Figure 3.3. Temperature Analysis via powder X-ray diffraction patterns of the synthesis of $Sr_5Nb_4O_{15}$ using (emim)OAc and dextran as chelator agents.

However, crystal phases with, or with close composition to, $SrNbO_3$ have been investigated due to its intense red colour,[27] which is absent in the powder collected at those temperatures (Figure 3.4 Inset). Above 750 °C those peaks gradually vanishes giving arise to mainly the phase $Sr_5Nb_4O_{15}$ at 800 °C. At 900 °C the reaction is completed with high yields (> 98 %) of single-phase formation of the targeted phase.

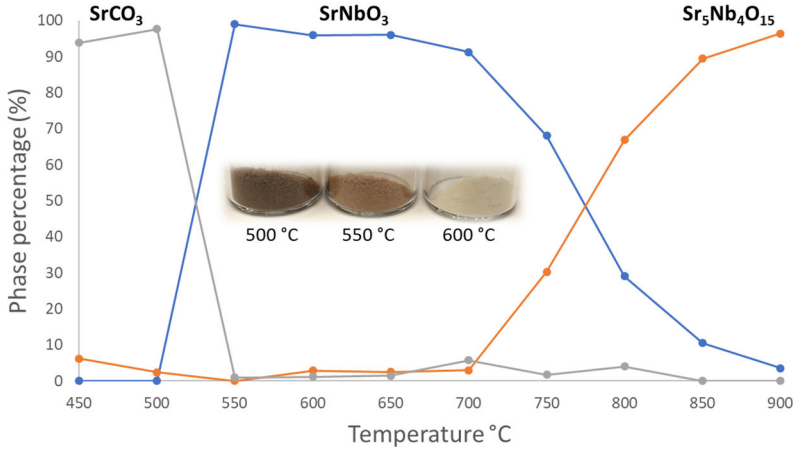

Figure 3.4. Graphical representation via qualitative analysis of pXRD patterns from the temperature analysis of the synthesis of $Sr_5Nb_4O_{15}$. Inset is a photography of the collected sample at 500 °C, 550 °C, and 600 °C.

To establish the function of each individual component, the crystal phase and purity of each synthesis, powder X-ray diffraction patterns were taken (Figure 3.5). The reactions were carried out using

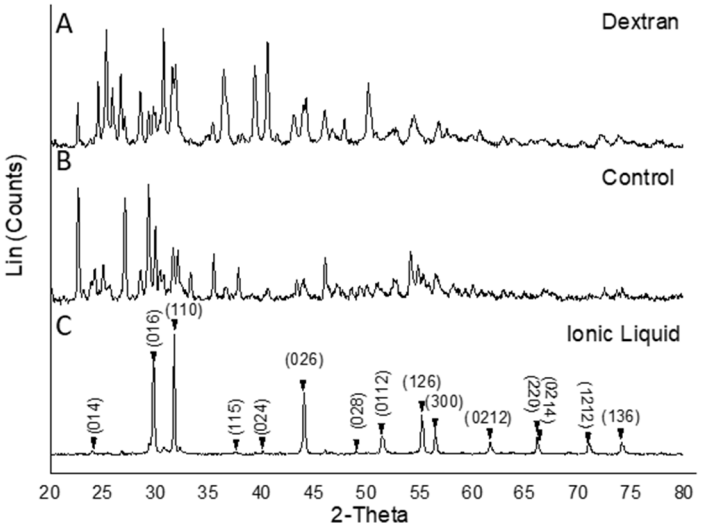

Figure 3.5. Powder X-ray diffraction pattern of the synthesis of $Sr_5Nb_4O_{15}$ with A) dextran and C) (emim)OAc as chelating agents. B) represents a control synthesis using no chelating agents.

1:1Sr/Nb stoichiometry targeting the phase $Sr_5Nb_4O_{15}$. All the reactions were made following the same heating ramp rate and dwell time previously described. For the control synthesis (Figure 3.5 "Raw materials") strontium nitrate and niobium ethoxide were mixed in an alumina crucible and calcined. As can be seen, the outcome is a multiphase system with no predominant phase, as did the second control synthesis (Figure3.5 "Dextran") using dextran as chelating agent. Interestingly, a different result crystallographically is seen when dextran is used. Finally, the reaction was carried out using the IL, for this reaction the raw materials were mixed with the IL and dehydrated before calcination. In this case, the target phase is obtained in a practically pure phase (> 98 %). However, it is important to mention that this reaction was repeated several times and in some of them the outcome was a mixture of $Sr_5Nb_4O_{15}$ and $Sr_2Nb_2O_7$. In addition, when the stoichiometry ratio was higher than X/Y <1, "X" being strontium and "Y" niobium, more specifically with the phases $SrNb_2O_6$ and $SrNb_6O_{16}$, single-phases were not obtained without the use of an additional chelating agent such as dextran. Therefore, it was decided that the best combination to obtain high yields (> 98 %) of single-phase with controllable stoichiometry was to use the IL with addition of another carbon source as chelating agent.

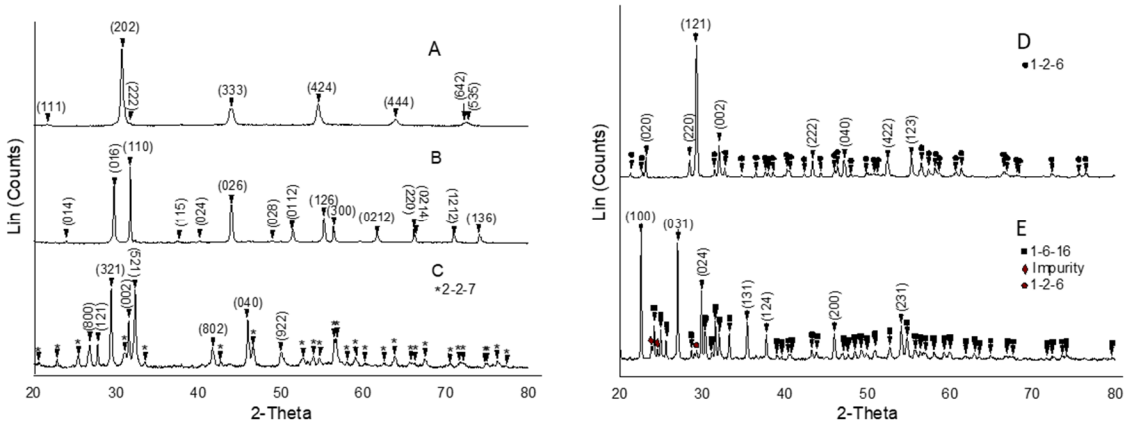

Figure 3.6. Powder X-ray diffraction patterns of: $Sr_4Nb_2O_9$ (A), $Sr_5Nb_4O_{15}$ (B), $Sr_2Nb_2O_7$ (C), $SrNb_2O_6$ (D) and $SrNb_6O_{16}$ (E). All samples were synthesized using (emim)OAc and dextran as chelating agents.

The key feature of the combination of IL and dextran shown here is the exploitation of the super dissociating nature of ILs, allowing the formation of perfect homogenous solutions via the interaction of hard anions of the IL with the metal cations, and the extra chelation provided by a non-specific chelating agent such as dextran. It was found that varying the amount of niobium in the reaction enabled us to control the stoichiometry finely and consistently, to produce four distinct stoichiometries of strontium niobate.

The specific Sr/Nb molar ratios are: 2 : 1 for $Sr_4Nb_2O_9$, 1.1 : 1 to 0.9 : 1 for $Sr_5Nb_4O_{15}$, 0.8 : 1 to 0.7 : 1 for $Sr_2Nb_2O_7$, 0.5 : 1 to 0.3 : 1 for $SrNb_2O_6$ and 0.11 : 1 for $SrNb_6O_{16}$. The addition of dextran followed by calcination at 1000 °C for 2 h in a 5 °C min^{-1} ramp ratio enabled two phases with a stoichiometry X/Y > 1 to be obtained, i.e. $Sr_4Nb_2O_9$ and $Sr_5Nb_4O_{15}$ (Figure 3.6). The phase $Sr_4Nb_2O_9$ (Figure 3.6 A) can exhibit different crystalline structures according to the temperature of synthesis. In this work, syntheses were carried out at 1000 °C, therefore, the phase is monoclinic with a symmetry group P21/n. In the case of $Sr_5Nb_4O_{15}$ (Figure 3.6 B), this possessed a trigonal crystal structure with the symmetry group $P\bar{3}c1$. The remaining phases in this work have the stoichiometry X/Y ≤ 1, viz. $Sr_2Nb_2O_7$ (Figure 3.6 C), $SrNb_2O_6$ (Figure 3.6 D) and $SrNb_6O_{16}$ (Figure 3.6 E). The phase (2-2-7) is orthorhombic with the symmetry group Cmc21 and it is determined that (1-2-6) exists as a monoclinic phase with space group P21/c. (1-6-16) has an orthorhombic array with Pmm2 symmetry group. All diffraction peaks in the patterns can be indexed to a single-phase with exception of (1-6-16). In this case, Rietveld refinement shows that

the desired phase is present as 95.7% of the sample, whereas 4.3% corresponds to (1-2-6) and niobium oxide (Figure 3.6). This last crystalline phase was synthesized under a 1 : 9 Sr/Nb molar ratio, which explains the appearance of the niobium-rich phase (1-2-6) and the impurity on the powder X-ray diffraction pattern, yet this molar ratio almost fully supresses the growth of any other crystal phase.

A diagram (Figure 3.7) was developed to track the change of crystal composition based on changes on the Sr/Nb mole fraction per reaction. All the reactions performed were using 1 mil of (emim)OAc with Sr/Nb mole fractions ranging from 12.55 to 0.11. The dwelling time is 2 h at 1000 °C being the max temperature.

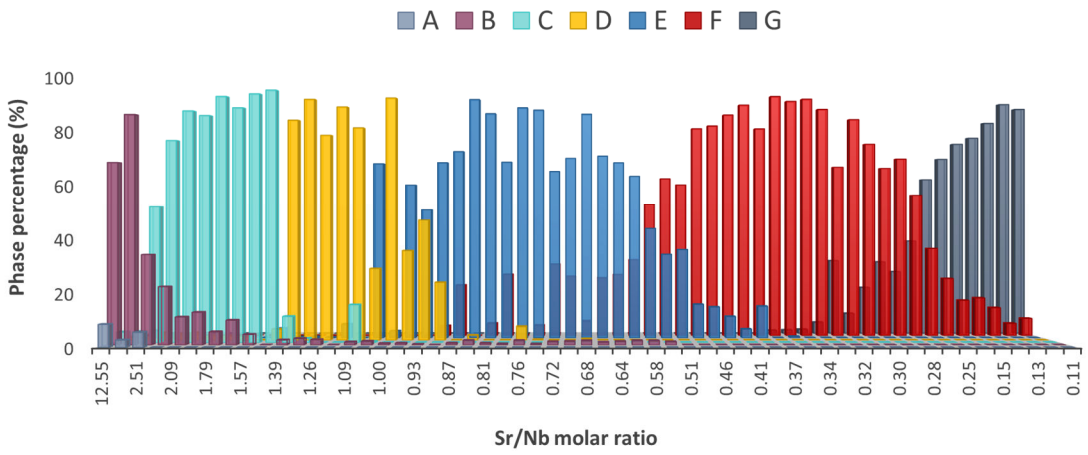

Figure 3.7. Diagram of the formation of different strontium niobate crystal compositions based on the Sr/Nb mole fractions in the reaction. A = Sr_2O, B = Sr (CO_3), C = $Sr_4Nb_2O_9$, D = $Sr_5Nb_4O_{15}$, E = $Sr_2Nb_2O_7$, F = $SrNb_2O_6$, G = $SrNb_6O_{16}$. All samples synthesized using (emim)OAc and dextran as chelating agents.

It was noticed that when the Sr/Nb mole fraction is in the range of $X/Y > 3$, strontium carbonate and small amount of strontium oxide is formed instead of a ternary crystal phase. Also, the fact that when Sr/Nb mole fraction fulfils the quantity for a ternary crystal composition, then strontium carbonate will share phase percentage with it, viz. $Sr_4Nb_2O_9$. Once the amount of niobium cations is increased, strontium carbonate will completely disappear, leaving just ternary phases. In fact, a very similar phenomenon is

observed when the niobium concentration reaches half way from one crystal composition to another, where in such cases both crystal compositions are exposed.

3.2.1.3 $Sr_4Nb_2O_9$ metastable phases

During the diagram construction some samples, in the Sr/Nb molar ratio of $1.52 < X/Y < 2.18$, were exhibiting different colours, namely tan, light red, and white. In 2002 Levin et al. reported a very complicated structural behaviour of the phase $Sr_4Nb_2O_9$ where four different crystal compositions were indexed. These crystal compositions were nominated as IC, T, M and R. (Figure 3.8)

Phase	Unit cell	Lattice parameters/ modulation vector	Sr/Nb ratio
IC	Incommensurate	$\mathbf{q} = (\frac{1}{4}\text{-}z)\langle 221\rangle_c^a$ $z = 0.009$	> 2
T[a]	Pseudotetragonal	$\mathbf{q} = \frac{1}{4}\langle 221\rangle_c^a$, $a = 2a_c\sqrt{2}$, $b = 2a_c\sqrt{2}$, $c = 8a_c$	> 2
M	Monoclinic	$a \approx \sqrt{6}a_c$, $b \approx \sqrt{2}a_c$, $c \approx 3\sqrt{2}a_c$, $\beta \approx 125^\circ$	≥ 2
R	Pseudocubic	$a = 6a_c$	< 2

Figure 3.8.[28] Structural and compositional parameters of the metastable phases. (Note. The lattice parameters and the symmetries were inferred using limited number of low-index diffraction patterns characteristic for each phase and should be considered as tentative only.

In comparison to the method of synthesis employed in this work (dwell time 2 h at 1000 °C), samples were first synthesized at 1550 °C for 2-4 days and annealed at 900 °C for 72 h to 500 h. Specimens colours were described as from white to tan without much more detail. The samples displayed are not in a single-phase fashion but rather a conglomerate of all the different crystal compositions and, the overall composition is defined to be IC, as dominant crystal composition, with >50 vol %, while both M and R domains had relatively similar volume fractions however, it does not state what that fraction is, and finally the T phase was present only in minor quantities.[28] The compositional analysis of these structures was conducted in TEM using a stationary electron probe and results can be seen in Figure 3.8. Along the compositional analysis it was possible to stablish the Sr/Nb ratios in the domains of both M (1.96 ± 0.006) and IC/T (1.99 ± 0.07). The Sr/Nb ratio for the R phase (1.76 ± 0.06) was found to be Sr-deficient and

based on this detail it was then concluded that the other three crystal compositions must have Sr/Nb ratios above 2. [28]

3.2.1.3.1Uv-Vis

In the case of the synthesis performed assisted by the ionic liquid five different crystal compositions were synthesized. Firstly, samples were studied via uv-vis analysis to differentiate all the different crystal compositions by the colour displayed (Figure 3.9). The synthesis was performed with different Sr/Nb (*X/Y)* molar ratios where, samples were identified to be similar in the ranges of *X/Y* = 2.18-2.09 (Figure 3.9 A), 2.00-1.93 (Figure 3.9 B), 1.85-1.79 (Figure 3.9 C), 1.73-.1.67 (Figure 3.9 D), and 1.61-1.56 (Figure 3.9 E). In terms of v/v ratios is 1 ml of a 0.1 M solution of strontium nitrate with 11.5-12.0 µl for A, 12.5-13.0 µl for B, 13.5-14.0 µl for C, 14.5-15.0 µl for D, and 15.5-16.0 µl for E, of niobium ethoxide in 1ml of ionic liquid. Via the Tauc plot method the optical band gap was determined providing values of 1.8 eV for *X/Y* = 2.18-2.09, 2.1 eV for 2.00-1.93, 2.15 eV for 1.85-1.79, 2 eV for 1.73-.1.67, and 2.8 eV for 1.61-1.56. Based on these results there are two conclusions that can be derived. First, all the materials are semiconductors, and second, the variations of the band gap are a representation of changes in the crystal lattice, which can occur by substitution or vacancies. This is an indicative of the formation of different but very similar crystal compositions. Uv-vis spectra and Tauc plots can be found in the appendix section (A1 – 5).

	Sr/Nb molar ratio	λ_{max}	E_g (eV)
A	2.18-2.09	552	1.9
B	2.00-1.93	450	2.2
C	1.85-1.79	460	2.2
D	1.73-.1.67	475	2.1
E	1.61-1.56	Near UV	2.8

Figure 3.9. Uv-vis analysis of the different crystal compositions based on the molar ratios of Sr/Nb (*X/Y*): A: 2.18 - 2.09, B: 2.00 - 1.93, C: 1.85 - 1.79, D: 1.73 - 1.67, and E: 1.61 – 1.56. The inset is a photograph of samples collected under the different Sr/Nb molar ratios.

3.2.1.3.2Analysis via pXRD

Powder X-ray diffraction patterns (Figure 3.10) of the five different samples were carried out. As expected the diffractions are all very similar however, diffraction peaks that were not common to all of the samples were found. These are highlighted in figure 3.10 and are at 2-theta 25.35 °, 32.49 °, 46.60 °, and 57.91 ° values. The first diffraction peak identified in Figure 3.10, highlighted in blue, belongs to remnants of strontium carbonate, after Rietvield refinement analysis it was found that it represents for A = 20.21 %, B = 10.9 %, C = 12.67 %, D = 5.03 %, and E = 6.47 %. For all the other diffractions it was not possible to index them as part of either Sr nor Nb related crystal phases. Another feature found via powder X-ray diffraction is the fact that while niobium concentration is increased, diffractions shift towards higher 2-theta angles (Figure 3.11), implying a decrease in the *d* spacing therefore, reducing the overall size of the unit cell. The shift is lower at lower angles whereas shift at higher angles is, consequently, larger towards higher angles indicating that it is due to an expansion/contraction of the unit cell rather than instrument specific displacement. To confirm that this observance was not coming from an equipment specific displacement, sample in the range of Sr/Nb (*X/Y*) molar ratio of 1.61-1.56 was re-synthesized. As can be noted in Figure 3.12 displacements are still witnessed confirming that such displacement belongs to a contraction of the unit cell when niobium concentration is increased.

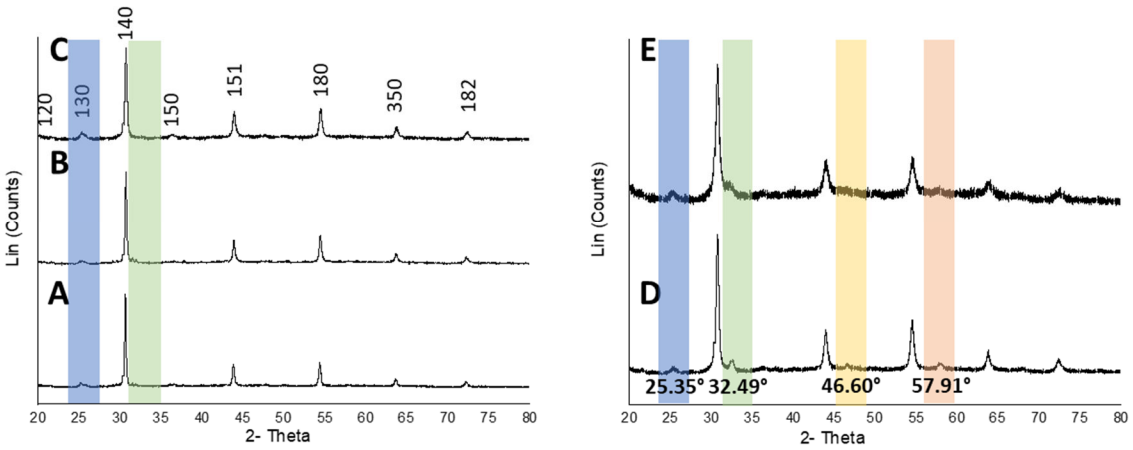

Figure 3.10. Powder X-ray diffraction patterns of the five different crystal compositions with Sr/Nb (*X/Y*) molar ratios: A :2.18-2.09, B: 2.00- 1.93, C: 1.85-1.79, D: 1.73-1.67, E: 1.61-1.56.

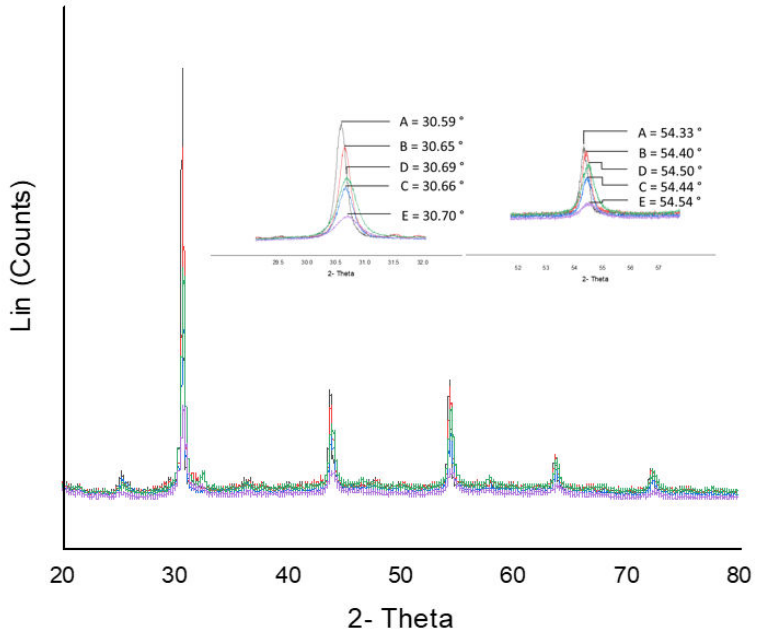

Figure 3.11. Powder X-ray diffractions confirming displacement towards bigger angles due to the increase in Nb concentration of Sr/Nb (*X/Y*): A :2.18-2.09, B: 2.00- 1.93, C: 1.85-1.79, D: 1.73-1.67, E: 1.61-1.56.

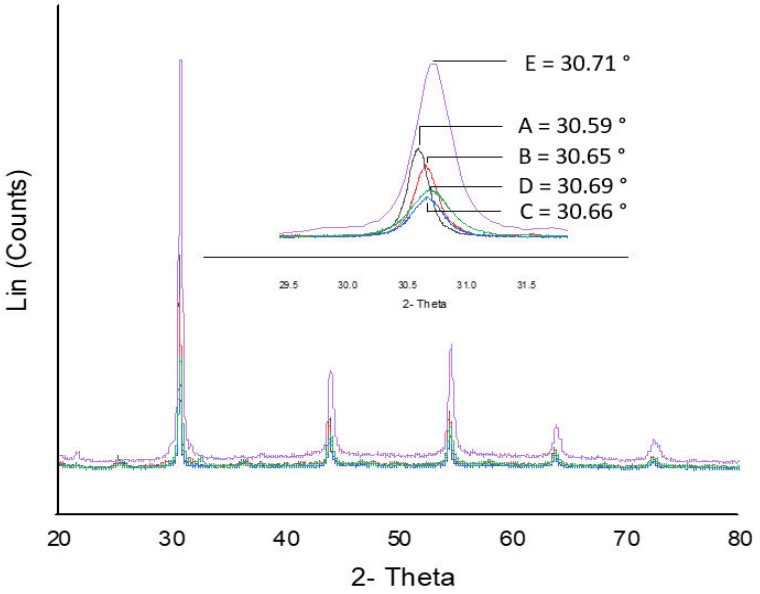

Figure 3.12. Powder X-ray diffractions demonstrating displacement towards bigger angles due to the increase in Nb concentration of Sr/Nb (*X/Y*): A :2.18-2.09, B: 2.00- 1.93, C: 1.85-1.79, D: 1.73-1.67, E: 1.61-1.56.

Displacements can be explained due to Sr^{2+} (1.32 Å)[29] having a much bigger atomic radii than Nb^{5+} (0.64 Å)[30] , therefore, in order to fit a larger Sr ion, the unit cell needs to expand. On the contrary, when niobium is increased in the reaction, the unit cell is more Nb rich, thereby reducing the size of the unit cell. Neutron diffraction or single crystal are very much needed to define the atomic arrangement and give further information of the crystal structure.

3.2.1.3.3ICP-OES

To confirm the exact metal composition of the samples ICP-OES was carried out twice with freshly prepared powders. In both cases results between the two measurements are very consistent and can be seen in table 3.2.

Sr/Nb (*X/Y*)	*Sample 1 (*X/Y)	Sample 2 (*X/Y)*
2.18-2.09	4.21	4.21
2.00- 1.93	3.23	3.23
1.85-1.79	3.09	3.09
1.73-1.67	2.66	2.66
1.61-1.56	2.22	2.22

Table 3.2. ICP-OES values obtained of the five different collected samples.

Sadly, it was not possible to stablish the exact composition of the crystal phases due to the presence of strontium carbonate however, knowing the composition of such via Rietvield refinement it was possible to re-adjust parameters and calculate a more accurate crystal composition (Table 3.3).

Sample 1					
Sr/Nb (*X/Y*)	**Sr (M)**	**Nb (M)**	**$Sr(CO_3)$ (M)**	**Sr-$Sr(CO_3)$**	**(*X/Y*) Molar ratio**
2.18-2.09	0.00015	3.74E-05	3.15E-05	0.00012	**3.36**
2.00- 1.93	0.00020	6.39E-05	2.25E-05	0.00018	**2.88**
1.85-1.79	0.00014	4.74E-05	1.86E-05	0.00012	**2.70**
1.73-1.67	0.00023	8.75E-05	1.16E-05	0.00022	**2.53**
1.61-1.56	0.00023	0.00010	1.52E-05	0.00022	**2.08**

Sample 2					
Sr/Nb (*X/Y*)	**Sr (M)**	**Nb (M)**	**$Sr(CO_3)$ (M)**	**Sr-$Sr(CO_3)$**	**(*X/Y*) Molar ratio**
2.18-2.09	0.00015	3.74E-05	3.15E-05	0.00012	**3.37**
2.00- 1.93	0.00020	6.39E-05	2.25E-05	0.00018	**2.88**
1.85-1.79	0.00014	4.74E-05	1.86E-05	0.00012	**2.70**
1.73-1.67	0.00023	8.75E-05	1.16E-05	0.00022	**2.53**
1.61-1.56	0.00023	0.00010	1.52E-05	0.00022	**2.08**

Table 3.3. Re-adjustment of the Sr/Nb (*X/Y*) molar ratios bases on data obtained via ICP-OES and Rietvield refinement.

As can be seen data seems to be much more consistent with what was expected. It is very interesting to note the fact that all of the products are phases rich in strontium which is in agreement with what was previously reported (Table 3.1[28]).

3.2.1.3.4HRTEM

HRTEM images (Figure 3.13) were taken and the interplanar distance measured. All the results are consistent with the interplanar distances per diffraction seen via powder diffraction patterns. Distances are related to the specific diffractions: 4.1 Å (120), 3.5 Å (130), 2.9 Å (140), and 2.5 Å (150).

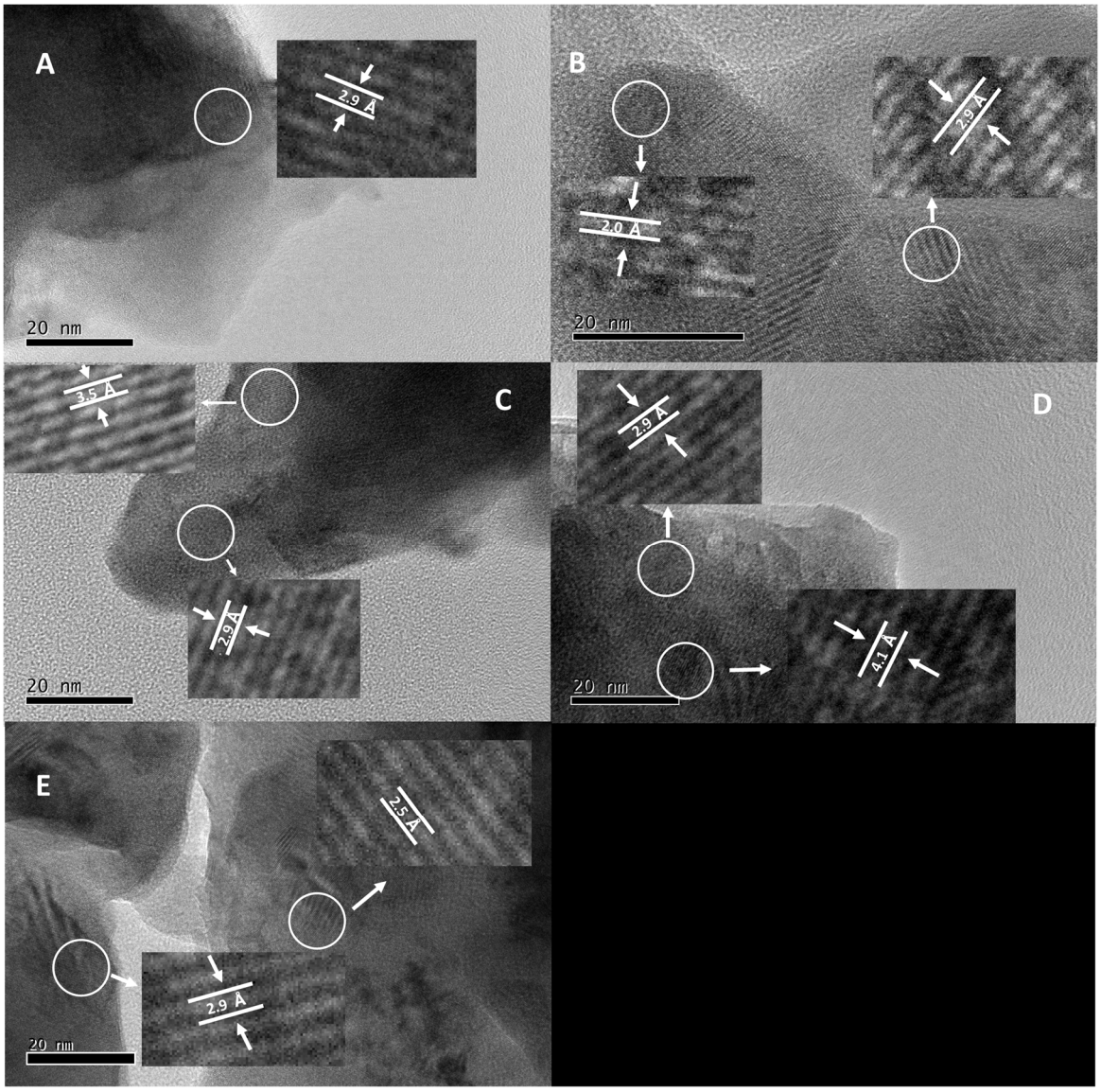

Figure 3.13. HRTEM images of the five different crystal compositions with Sr/Nb (*X/Y*): A :2.18-2.09, B: 2.00- 1.93, C: 1.85-1.79, D: 1.73-1.67, E: 1.61-1.56. Insets are zooming zones to measure the interplanar distance. White circles showing the exact area where the interplanar distance was measured. Scale bars = 20 nm.

SAED diffraction patterns (Figure 3.14) were also taken to confirm that every sample belongs to an analogue of the $Sr_4Nb_2O_9$ crystal structure. As expected in the form of ring patterns it is possible to index the same crystal planes observed via all the other characterization tools, displaying the planes (120), (130), (140), and (150) respectively.

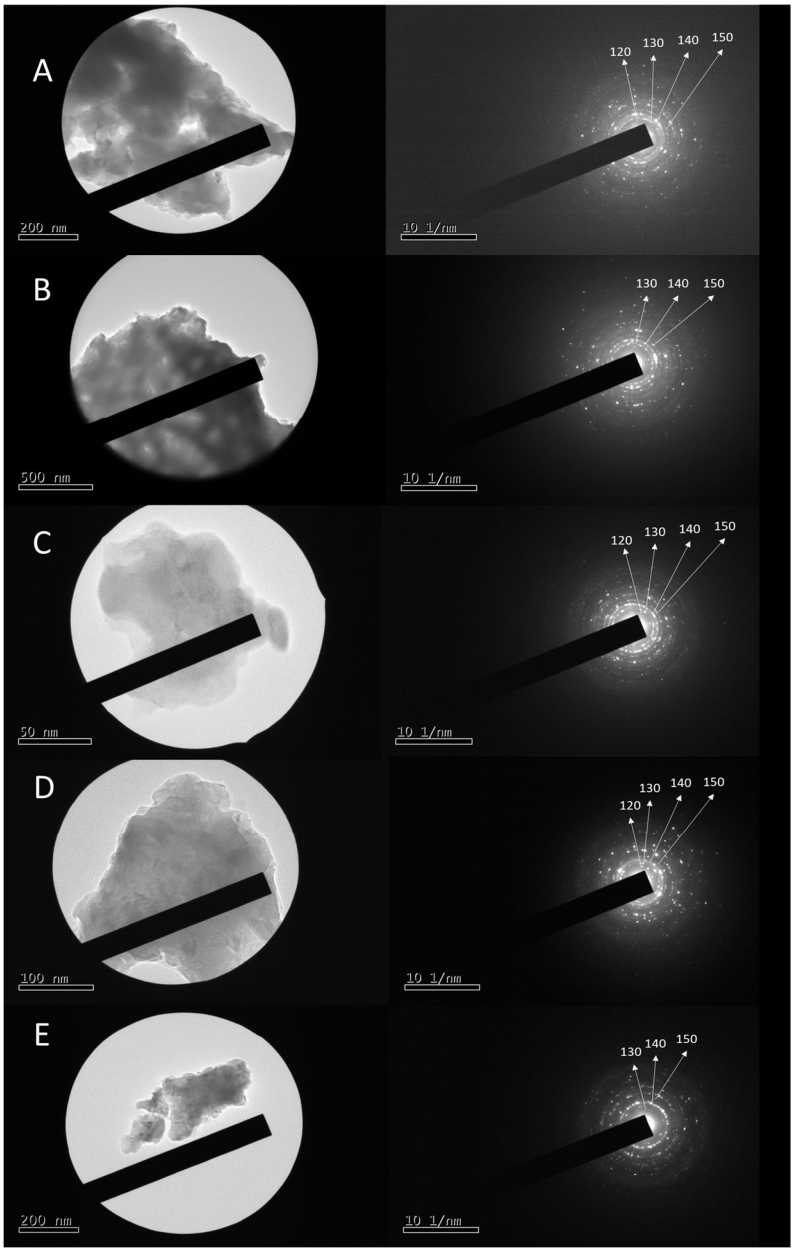

Figure 3.14. Left: HRTEM images of the five different crystal compositions, showing where the SAED pattern was taken, with Sr/Nb (*X/Y*): A :2.18-2.09, B: 2.00- 1.93, C: 1.85-1.79, D: 1.73-1.67, E: 1.61-1.56. Scale bar (A, B and E) = 200 nm, (D) = 100 nm and (C) = 50 nm. On the right side all their respective SAED diffraction patterns (Scale bars (A-E) = 10 1/nm).

3.2.1.4 Structural Characterization

3.2.1.4.1SEM and TEM

SEM and TEM studies followed in order to analyse the macro and nano-morphology displayed by this synthetic procedure. SEM studies show that this type of synthesis results in a polycrystalline aggregate exhibiting the same macromorphology in every single crystal phase. (Figure 3.15)

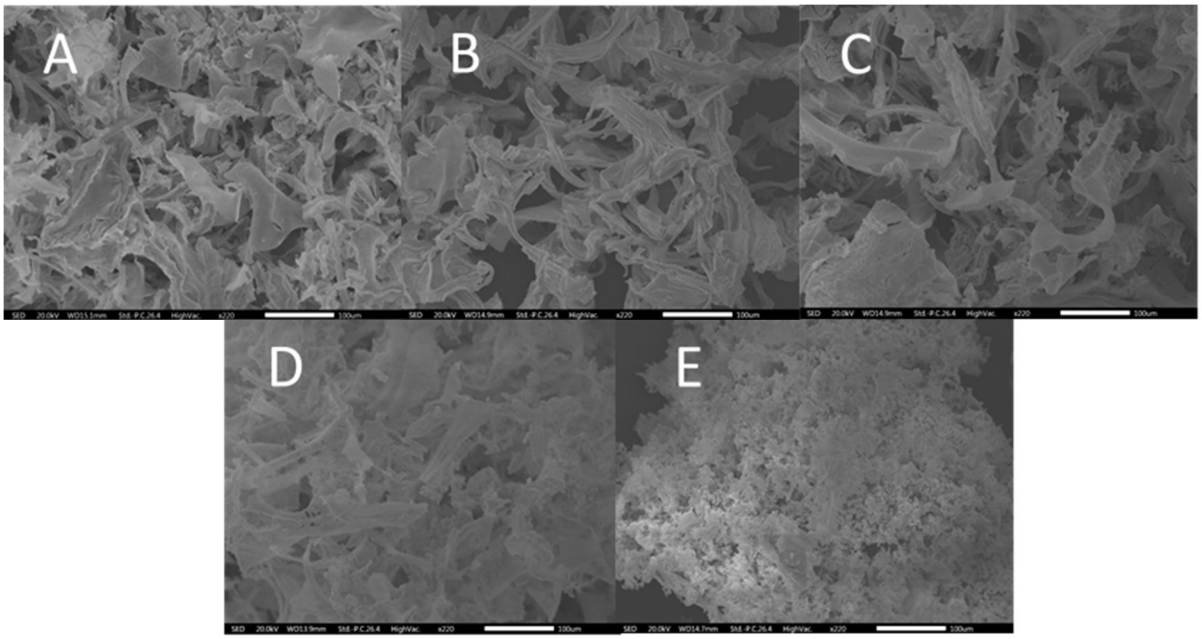

Figure 3.15. Scanning Electron microscopy images of polycrystalline aggregates of: A) $Sr_4Nb_2O_9$, B) $Sr_5Nb_4O_{15}$, C) $Sr_2Nb_2O_7$, D) $SrNb_2O_6$, E) $SrNb_6O_{16}$. Scale bars = 100 μm.

EDX shows that in each case, strontium and niobium are homogeneously distributed throughout the material (Figure 3.16). The homogeneity afforded by the IL/dextran mixture clearly results in a single-phase material through the facile mass transport of species during the synthesis.

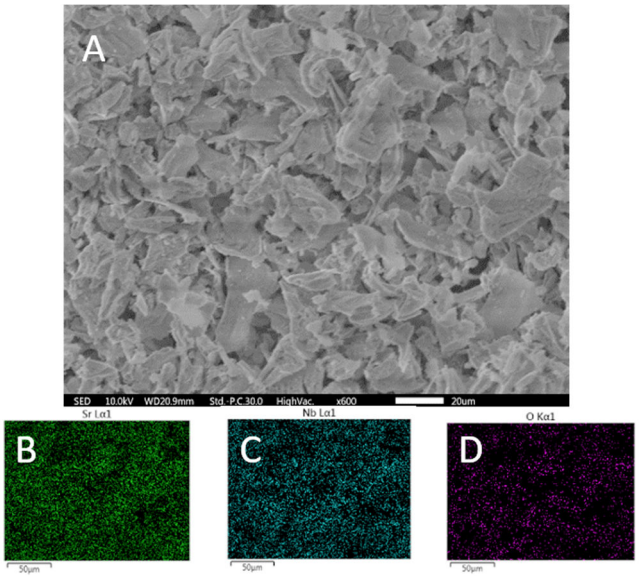

Figure 3.16. (A) Scanning electron microscopy image of $SrNbO_x$ and (B-D) Elemental mapping of the area of B = Sr, C = Nb, and C = O, shown in (A), exhibiting a homogenous distribution of all the elements involved. Scale bar of A = 200 μm, B-D = 50 μm.

In contrast with SEM studies of the macromorphology, TEM images (Figure 3.17) show some differences in the crystallite morphology, in particular for the phase $Sr_4Nb_2O_9$ (Figure 3.17 A) where a net of nanoparticles-like are commonly seen.

From the samples over the ratio 1 : 2 Sr/Nb most of the final product can be identified as plate-like and rod morphologies, however, star and needle-like morphologies are observed in all syntheses (Figure 3.18 F).

Selected area diffraction patterns (Figure 3.18 a-e) were also taken to ratify the obtained stated crystal compositions.

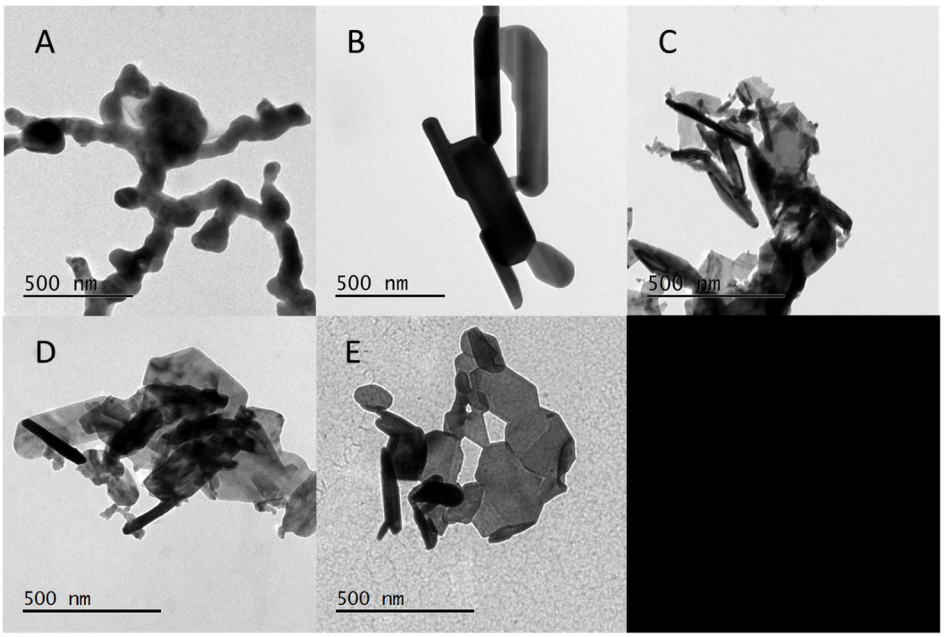

Figure 3.17. TEM image were different morphologies can be seen. Images correspond to: A: $Sr_4Nb_2O_9$, B: $Sr_5Nb_4O_{15}$, C: $Sr_2Nb_2O_7$, D: $SrNb_2O_6$, E: $SrNb_6O_{16}$. Scale bars = 500 nm.

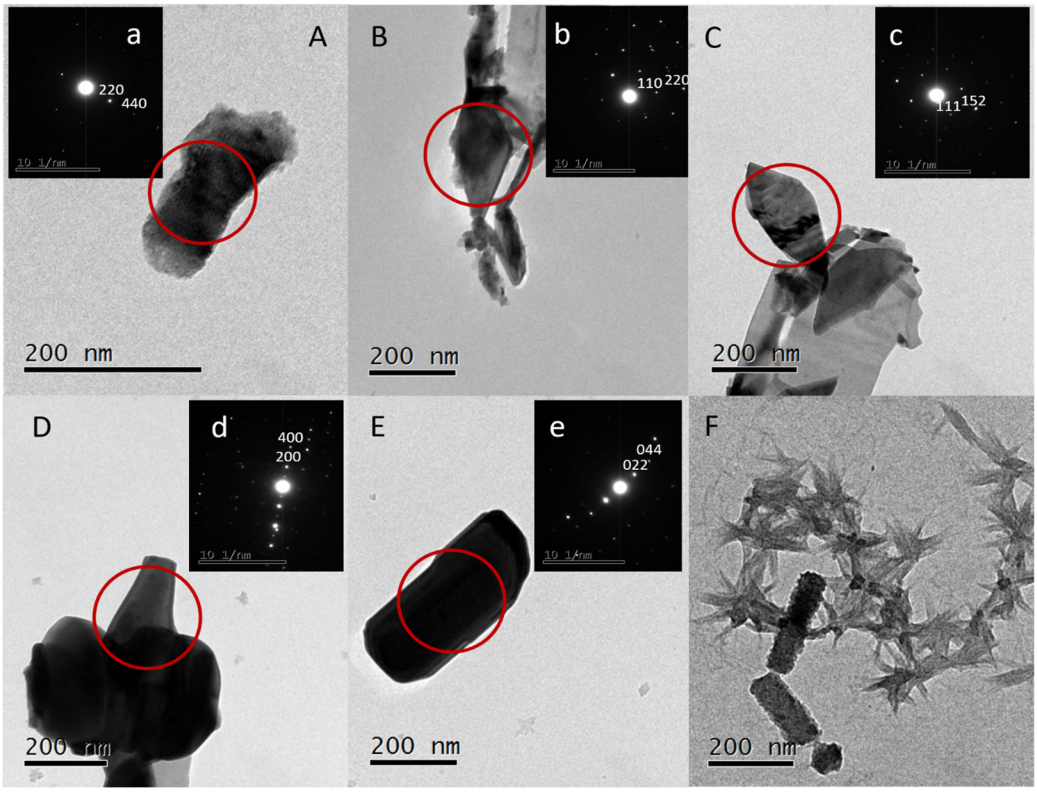

Figure 3.18. Transmission electron microscopy images and their respective SAED patterns of: A/a: $Sr_4Nb_2O_9$, B/b: $Sr_5Nb_4O_{15}$, C/c: $Sr_2Nb_2O_7$, D/d: $SrNb_2O_6$, E/e: $SrNb_6O_{16}$ and F: rod and star shape crystals. Scale bars = 200 nm, a-e = 10 1/nm.

3.3 Conclusions

In conclusion, the use of an IL/Dextran synthetic method has shown to be a very good technique in the synthesis of high yields of single-phase metal oxides of desired stoichiometries, namely $Sr_4Nb_2O_9$, $Sr_5Nb_4O_{15}$, $Sr_2Nb_2O_7$, $SrNb_2O_6$, $SrNb_6O_{16}$. The non-specific chelation and subsequent carbonization of the organic species in the calcination step are crucial in achieving this as it restricts inorganic oxide growth to the nanoscale, prevents sintering and provides a reducing atmosphere to enable the fine control of stoichiometry through simply varying the strontium : niobium ratio at the start of the synthesis.

Moreover, exploiting the control allowed by this synthetic procedure, it was possible to synthesize four, previously poorly characterized, phases. Via Rietvield refinement and ICP-OES analysis it was feasible to establish the Sr/Nb molar ratios between those four, being 3.37, 2.88, 2.70, and 2.53.

3.4 Bibliography

(1) Cohen, R. E. Origin of Ferroelectricity in Perovskite Oxides. *Nature* **1992**, *358* (6382), 136–138.

(2) Thakare, V. P.; Game, O. S.; Ogale, S. B. Ferromagnetism in Metal Oxide Systems: Interfaces, Dopants, and Defects. *J. Mater. Chem. C* **2013**, *1* (8), 1545.

(3) Lichtenberg, F.; Herrnberger, A.; Wiedenmann, K. Synthesis, Structural, Magnetic and Transport Properties of Layered Perovskite-Related Titanates, Niobates and Tantalates of the Type $A_nB_nO_{3n+2}$, $A'A_{k-1}B_kO_{3k+1}$ and $A_mB_{m-1}O_{3m}$. *Prog. Solid State Chem.* **2008**, *36* (4), 253–387.

(4) Wang, Z. L. Progress in Piezotronics and Piezo-Phototronics. *Adv. Mater.* **2012**, *24* (34), 4632–4646.

(5) Armand, M.; Endres, F.; MacFarlane, D. R.; Ohno, H.; Scrosati, B. Ionic-Liquid Materials for the Electrochemical Challenges of the Future. *Nat. Mater.* **2009**, *8* (8), 621–629.

(6) Dietz, M. L. Ionic Liquids as Extraction Solvents: Where Do We Stand? *Sep. Sci. Technol.* **2006**, *41* (10), 2047–2063.

(7) Huddleston, J. G.; Willauer, H. D.; Swatloski, R. P.; Visser, A. E.; Rogers, R. D. Room Temperature Ionic Liquids as Novel Media for 'Clean' Liquid–liquid Extraction. *Chem. Commun.* **1998**, *0* (16), 1765–1766.

(8) Liu, J. F.; Chi, Y. G.; Peng, J. F.; Jiang, G. Bin; Jönsson, J. Å. Ionic Liquids/Water Distribution Ratios of Some Polycyclic Aromatic Hydrocarbons. *J. Chem. Eng. Data* **2004**, *49* (5), 1422–1424.

(9) Abraham, M. H.; Zissimos, A. M.; Huddleston, J. G.; Willauer, H. D.; Rogers, R. D.; Acree, W. E. Some Novel Liquid Partitioning Systems: Water-Ionic Liquids and Aqueous Biphasic Systems. *Ind. Eng. Chem. Res.* **2003**, *42* (3), 413–418.

(10) Smirnova, S. V.; Torocheshnikova, I. I.; Formanovsky, A. A.; Pletnev, I. V. Solvent Extraction of Amino Acids into a Room Temperature Ionic Liquid with Dicyclohexano-18-Crown-6. *Anal. Bioanal. Chem.* **2004**, *378* (5), 1369–1375.

(11) Wang, J.; Pei, Y.; Zhao, Y.; Hu, Z. Recovery of Amino Acids by Imidazolium Based Ionic

Liquids from Aqueous Media. *Green Chem.* **2005**, *7* (4), 196.

(12) Luo, H.; Dai, S.; Bonnesen, P. V.; Buchanan, A. C.; Holbrey, J. D.; Bridges, N. J.; Rogers, R. D. Extraction of Cesium Ions from Aqueous Solutions Using Calix[4]Arene-Bis(Tert.Octylbenzo-Crown-6) in Ionic Liquids. *Anal. Chem.* **2004**, *76* (11), 3078–3083.

(13) Luo, H.; Dai, S.; Bonnesen, P. V. Solvent Extraction of Sr^{2+} and Cs^{+} Based on Room-Temperature Ionic Liquids Containing Monoaza-Substituted Crown Ethers. *Anal. Chem.* **2004**, *76* (10), 2773–2779.

(14) Visser, A. E.; Jensen, M. P.; Laszak, I.; Nash, K. L.; Choppin, G. R.; Rogers, R. D. Uranyl Coordination Environment in Hydrophobic Ionic Liquids: An in Situ Investigation. *Inorg. Chem.* **2003**, *42* (7), 2197–2199.

(15) Nakashima, K.; Kubota, F.; Maruyama, T.; Goto, M. Ionic Liquids as a Novel Solvent for Lanthanide Extraction. *Anal. Sci.* **2003**, *19* (8), 1097–1098.

(16) Visser, A. E.; Swatloski, R. P.; Reichert, W. M.; Griffin, S. T.; Rogers, R. D. Traditional Extractants in Nontraditional Solvents: Groups 1 and 2 Extraction by Crown Ethers in Room-Temperature Ionic Liquids. *Ind. Eng. Chem. Res.* **2000**, *39* (10), 3596–3604.

(17) Dai, S.; Ju, Y. H.; Barnes, C. E. Solvent Extraction of Strontium Nitrate by a Crown Ether Using Room-Temperature Ionic Liquids. *J. Chem. Soc. Dalt. Trans.* **1999**, *0* (8), 1201–1202.

(18) Whitehead, J. A.; Lawrance, G. A.; McCluskey, A. 'Green' Leaching: Recyclable and Selective Leaching of Gold-Bearing Ore in an Ionic Liquid. *Green Chem.* **2004**, *6* (7), 313–315.

(19) Cevasco, G.; Chiappe, C. Are Ionic Liquids a Proper Solution to Current Environmental Challenges? *Green Chem.* **2014**, *16* (5), 2375.

(20) Rodopoulos, T.; Smith, L.; Horne, M. D.; Rüther, T. Speciation of Aluminium in Mixtures of the Ionic Liquids [C3Mpip][NTf2] and [C4 Mpyr][NTf 2] with $AlCl_3$: An Electrochemical and NMR Spectroscopy Study. *Chem. - A Eur. J.* **2010**, *16* (12), 3815–3826.

(21) Chun S.; Dzyuba S., Bartsch, R. A. Influence of Structural Variation in Room-Temperature Ionic Liquids on the Selectivity and Efficiency of Competitive Alkali Metal Salt Extraction by a Crown

Ether. **2001**.

(22) Wei, G.-T.; Yang, Z.; Chen, C.-J. Room Temperature Ionic Liquid as a Novel Medium for Liquid/Liquid Extraction of Metal Ions. *Anal. Chim. Acta* **2003**, *488* (2), 183–192.

(23) Lu, W.; Barber, P. S.; Kelley, S. P.; Rogers, R. D. Coordination and Extraction of Mercury(II) with an Ionic Liquid-Based Thione Extractant. *Dalt. Trans.* **2013**, *42* (36), 12908–12916.

(24) Visser, A. E.; Swatloski, R. P.; Reichert, W. M.; Mayton, R.; Sheff, S.; Wierzbicki, A.; Davis, J. H.; Rogers, R. D. Task-Specific Ionic Liquids Incorporating Novel Cations for the Coordination and Extraction of Hg^{2+} and Cd^{2+}: Synthesis, Characterization, and Extraction Studies. *Environ. Sci. Technol.* **2002**, *36* (11), 2523–2529.

(25) Papaiconomou, N.; Lee, J.-M.; Salminen, J.; von Stosch, M.; Prausnitz, J. M. Selective Extraction of Copper, Mercury, Silver, and Palladium Ions from Water Using Hydrophobic Ionic Liquids. *Ind. Eng. Chem. Res.* **2008**, *47* (15), 5080–5086.

(26) Green, D. C.; Glatzel, S.; Collins, A. M.; Patil, A. J.; Hall, S. R. A New General Synthetic Strategy for Phase-Pure Complex Functional Materials. *Adv. Mater.* **2012**, *24* (42), 5767–5772.

(27) Xu, X.; Randorn, C.; Efstathiou, P.; Irvine, J. T. S. A Red Metallic Oxide Photocatalyst. *Nat. Mater.* **2012**, *11* (7), 595–598.

(28) Levin, I.; Chan, J. Y.; Scott, J. H.; Farber, L.; Vanderah, T. A.; Maslar, J. E. Complex Polymorphic Behavior and Dielectric Properties of Perovskite-Related $Sr(Sr_{1/3}Nb_{2/3})O_3$. *J. Solid State Chem.* **2002**, *166* (1), 24–41.

(29) Wiberg, E.; Wiberg, N.; Holleman, A. F. *Inorganic Chemistry*; Academic Press, 2001, New York.

(30) Müller, U. *Inorganic Structural Chemistry*; Wiley, 2007, San Francisco.

Chapter 4
On the synergistic interaction of an ionic liquid and biopolymers in the synthesis of strontium niobate and $YBa_2Cu_3O_{7-\delta}$ superconductor.

Parts of this chapter are published in the reference indicated below printed in Materials Chemistry and Physics. The paper used in the creation of this chapter was written and submitted by myself involving the preparation of all figures and text contained herein. I was involved in analysis of all data collected both directly by myself and on behalf of the publication by co-authors. Any data used in this thesis, collected and analysed with only minimal input from myself has been referenced accordingly. Specifically, all data was collected by myself.

Rojas, O. G.; Hall, S. R. On the Synergistic Interaction of an Ionic Liquid and Biopolymers in the Synthesis of Strontium Niobate. *Mater. Chem. Phys.* **2017**, *202*, 220–224.

4.1 Introduction

Inorganic oxides feature prominently in biomineralization; the organic-inorganic interaction has developed over millions of years to produce optimum structures for structural support, buoyancy control and defence mechanisms in shells, corals sponges and fishes.[1,2] From those bioinorganic materials, to complex metal oxides, research has been extensive due to the wide range of possible applications that these materials possess. One reason for such diversity is due to the high tunability of the properties, which can be modified by altering factors such as the porosity, crystallinity, morphology, doping or particle size. [3–6]

In nature, as in the laboratory, these physical properties can be controlled by the organic phase. Proteins and polysaccharides possess a plethora of structures and functionality, which can be used to influence the growth of the inorganic phase. An additional influence above and beyond the merely structural, is the influence of the functional side-group of the biopolymer, i.e. hydroxyls (agar, starch, cellulose), carboxyls (pectin, alginate), amide/amines (chitin/chitosan) and sulfate (carrageenan).[7] The interaction, both structural and chemical, with the inorganic phase invariably produces structure at the nano- and micro-scale. By judicious selection of the organic phase, laboratory-grown inorganic materials with structures such as nanocrystals, nanorods, nanoplatelets nanofibers or aerogels can be produced. [8–12]

A great deal of work has gone into understanding and establishing the optimal conditions for the synthesis of metal oxides using polysaccharides,[13] however, recent works using ionic liquids to chelate metal cations with the support of these organic compounds have opened up new synthetic pathways. An ionic liquid (IL) is a mixture of long-chain cations and coordinating anions.[10] These solvents are described as green, being environmentally friendly and able to solvate inorganic salts.[14] Some properties that make them worth of consideration are; good thermal stability, tuneable solubility, low vapour pressure,[15] as well as enabling fast mass transport. ILs have been used to synthesize diverse metal oxides with a wide range of physical properties.[16] ILs can even be considered to play a role in sol-gel chemistry, as they can dissolve

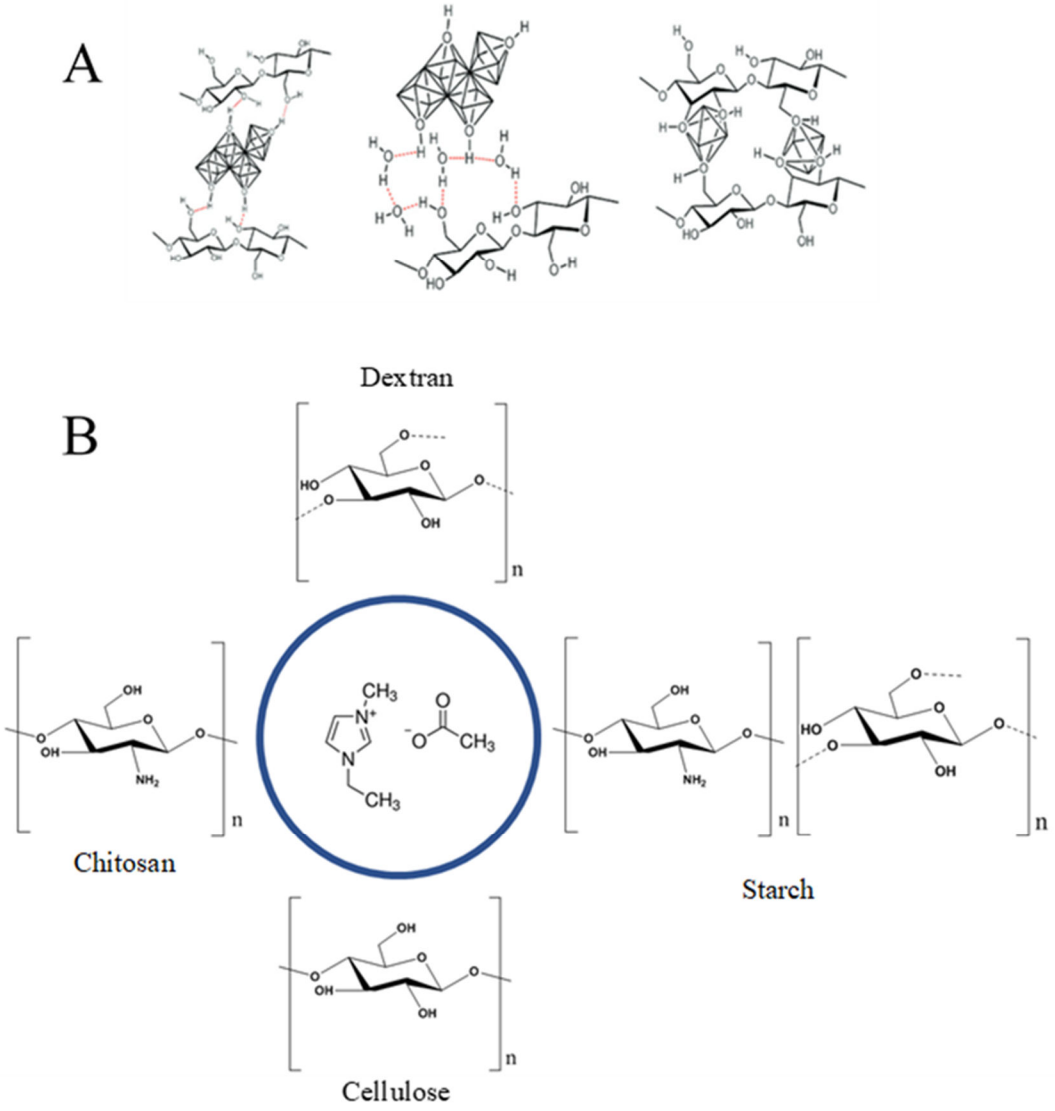

Figure 4.1. A)[13] Schematic representation of the possible interaction between functions of polysaccharide units and metal-containing species. B) Schematic representation of the polysaccharides, cellulose, starch, chitosan, and dextran, and the ionic liquid, (emim)OAc.

polymers to form a gel structure, particularly in the case of biopolymers such as dextran, chitosan, cellulose, and starch.

Both ILs and biopolymers have been used previously in the synthesis of inorganic phases and the chelating properties (Figure 4.1) as individuals has been gauged, yet the interaction between the ionic liquid and those polysaccharides have not yet been studied. Here we assess the contribution of the biopolymer in

an inorganic synthetic process involving an IL and how aspects of crystal structure such as size, morphology and composition differ. The polysaccharides have been limited to what we consider some of the most commonly used for metal oxide synthesis, namely the biopolymers dextran, chitosan, cellulose, and starch.

4.2 Results and discussion

4.2.1 Strontium niobate $Sr_5Nb_4O_{15}$

4.2.1.1 Ionic liquid

The synthesis without any complexing agent other than the ionic liquid (emim)OAc resulted in crystallites with a wide range of morphologies, both in macrostructure and at the nanoscale (Figure. 4.2 A&B). In addition to the target phase $Sr_5Nb_4O_{15}$, we additionally observed the closely-related $Sr_2Nb_2O_7$ phase (Figure 4.2 C). Thus, for the ionic liquid alone, neither phase-purity nor morphological control is achieved.

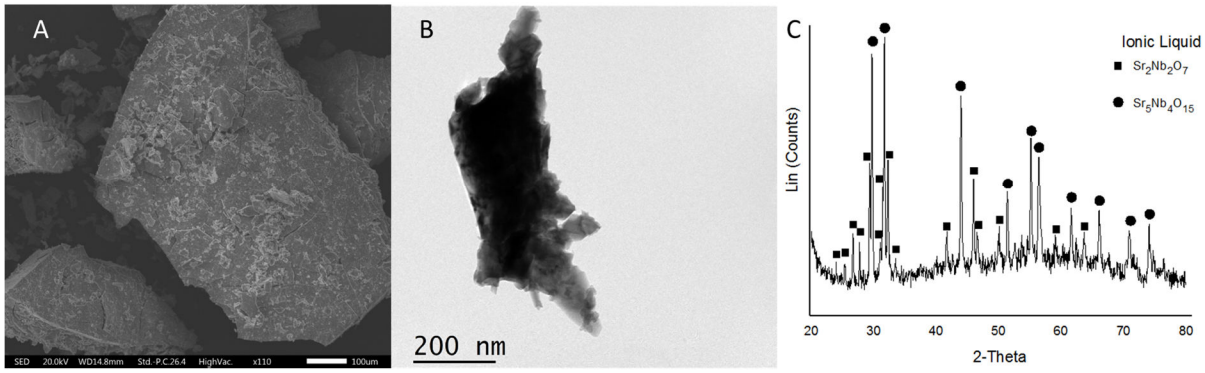

Figure 4.2. A) SEM and B) TEM images with (C) the corresponding powder X-ray diffraction pattern from the synthesis of $Sr_5Nb_4O_{15}$ using the ionic liquid (emim)OAc as chelating agent. Scale bars A = 100 μm, B = 200 nm.

4.2.1.2 Ionic liquid with cellulose

Cellulose is a polymeric chain composed of β(1 → 4) linked d-glucose units.[13] Cellulose has been used previously as a morphological agent, with fibres [17] cubic-like particles [18] or rods [19] being observed

when it is incorporated into syntheses. In the case of the synthesis of $Sr_5Nb_4O_{15}$, using cellulose as an extra chelating agent provided contrasting results. When 0.1 g was used, the outcome was agglomerated crystallites that ranged in size from 100 µm to 300 µm (Figure 4.3 C), whereas TEM image shown agglomerates of road-like particles (Figure 4.3 D). However, differences were seen when 1.0 g of cellulose was used. In this case, TEM images showed well-defined morphologies such as plate- and rod-like particles (Figure 4.3 A&B). The X-ray analysis showed that with 0.1 g, a single phase was the result, however, when 1.0 g was used, solidification of the cellulose resulted in a heterogeneous material prior to calcination. This resulted in the formation of a secondary phase, namely $Sr_2Nb_2O_7$ (Figure 4.3 E Top).

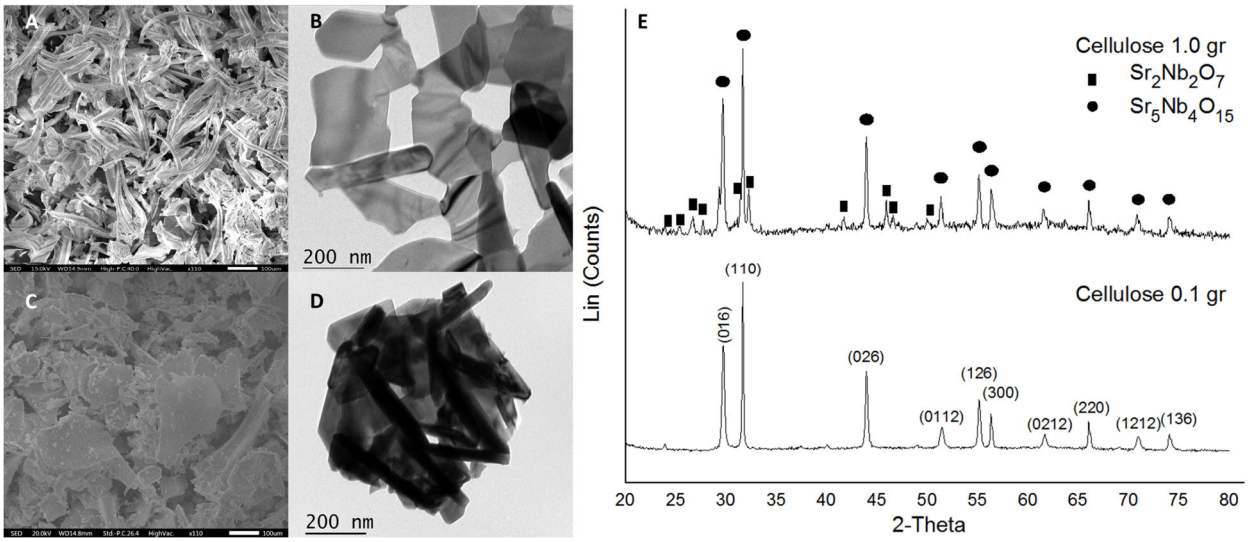

Figure 4.3. A) SEM and B) TEM images with the corresponding powder X-ray diffraction pattern (E, top pattern) from the synthesis of $Sr_5Nb_4O_{15}$ using ionic liquid and 1 g of cellulose. C) and D) show SEM and TEM images respectively, with the corresponding powder X-ray diffraction pattern (E, lower pattern) from the synthesis of $Sr_5Nb_4O_{15}$ using the ionic liquid and 0.1 g of cellulose. Indexed planes correspond to the phase $Sr_5Nb_4O_{15}$. Scale bars A & C = 100 µm, B & D = 200 nm.

4.2.1.3 Ionic liquid with chitosan

Chitosan is a high molecular weight linear polymer of 2-acetamido-2-deoxy-*d*-glucopyranose units linked together by 1,4-glycosidic bonds, obtained by the deacetylation of chitin. Chitin originates in fungi and exoskeletons of insects and crustaceans.[13] The most relevant feature of chitosan is the possession of

NH_2 groups which might vary the reactivity and chemistry significantly when compared to other polysaccharides.

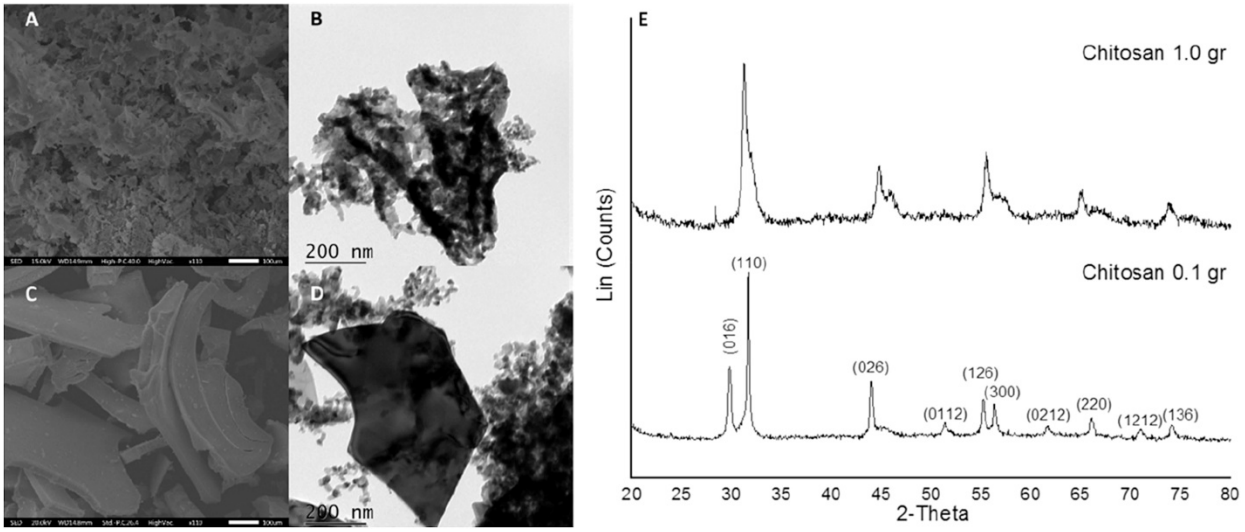

Figure 4.4. A) SEM and B) TEM images with the corresponding powder X-ray diffraction pattern (E, top pattern) from the synthesis of $Sr_5Nb_4O_{15}$ using ionic liquid and 1 g of chitosan. C) and D) show SEM and TEM images respectively, with the corresponding powder X-ray diffraction pattern (E, lower pattern) from the synthesis of $Sr_5Nb_4O_{15}$ using the ionic liquid and 0.1 g of chitosan. Indexed planes correspond to the phase $Sr_5Nb_4O_{15}$. Scale bars A & C = 100 μm, B & D = 200 nm.

In terms of micromorphology (Figure 4.4 A&C), syntheses performed with 0.1 g of chitosan as chelating agent resulted in a plate-like morphology. When 1.0 g was used however, a blocky morphology was evident. Under TEM (Figure 4.4 C&D), using 0.1 g, the sample displayed dazzling plates shadowed by spherical crystallites of smaller-scale with an average size of 20–30 nm (Figure 4.4 B and 4.5 A&B). However, when the amount was increased to 1.0 g, the plate-like crystals commute almost exclusively to clusters of spheres. Chitosan at low doses formed plates also with small spherical crystallites, however the uniform gel structure is heavily disrupted at high concentrations and only sphere-like crystals where synthesized. This could be attributed to the fact that an excess of this organic compound physically forms crumbs (Figure 4.5 C) instead of an evenly and uniform gel, generating multiple sites for the reaction to occur. Powder X-ray diffraction shows that at low concentrations, the addition of chitosan also provides a single crystal phase. At high concentrations however, the pattern does change significantly.

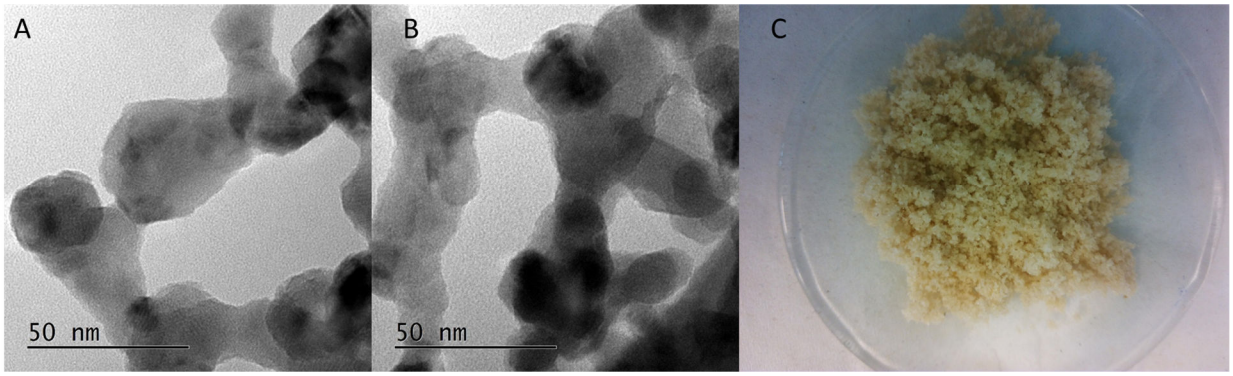

Figure 4.5. A&B) TEM Image of the synthesis of $Sr_5Nb_4O_{15}$ using 0.1 g of chitosan as the organic source, showing sphere-like nanocrystallites. C) Crumb formation instead of an even gel produced from the synthesis of $Sr_5Nb_4O_{15}$ using chitosan as the organic source. Scale bars A & B = 50 nm.

EDX analysis offers valuable information that could explain such change. Apart from the physical limitation by forming crumbs, in both cases, either low or high concentration of this compound, the elemental analysis indicated the presence of impurities (Figure 4.6) such as Na, Ca and Al. The alumina crucible and the SEM holder are likely the sources of aluminium, with sodium and calcium coming from the chitosan. Interestingly, there are no nitrogen-containing impurities in the sample, as has been previously observed in other studies using chitosan in the production of metal oxides. [20]

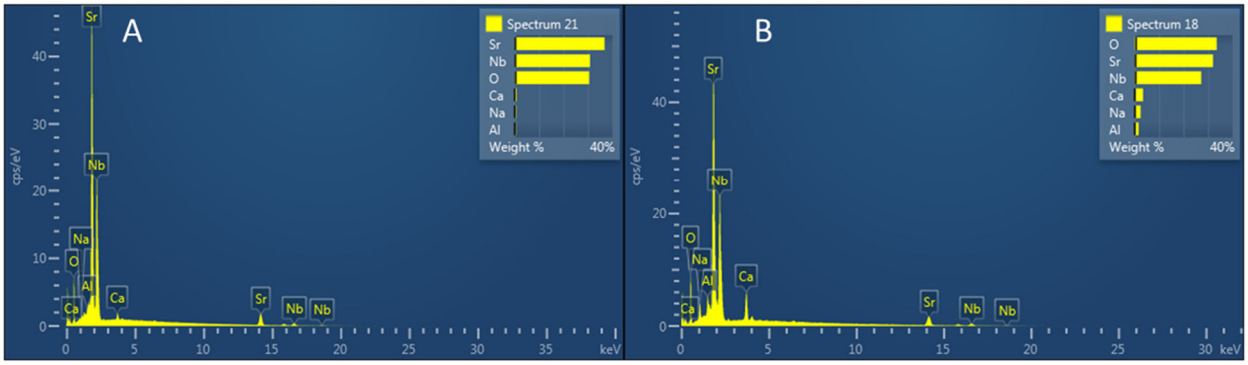

Figure 4.6. Scanning Electron microscopy energy dispersive X-ray analysis of the synthesis of $Sr_5Nb_4O_{15}$ with: A) 0.1 g and B) 1.0 g of chitosan. Insets show the quantitative analysis of elemental composition.

4.2.1.4 Ionic liquid with starch

Starch comes from green plants and is formed by two different polymers assembled of d-glucose sequences, namely amylose and amylopectin.[13]

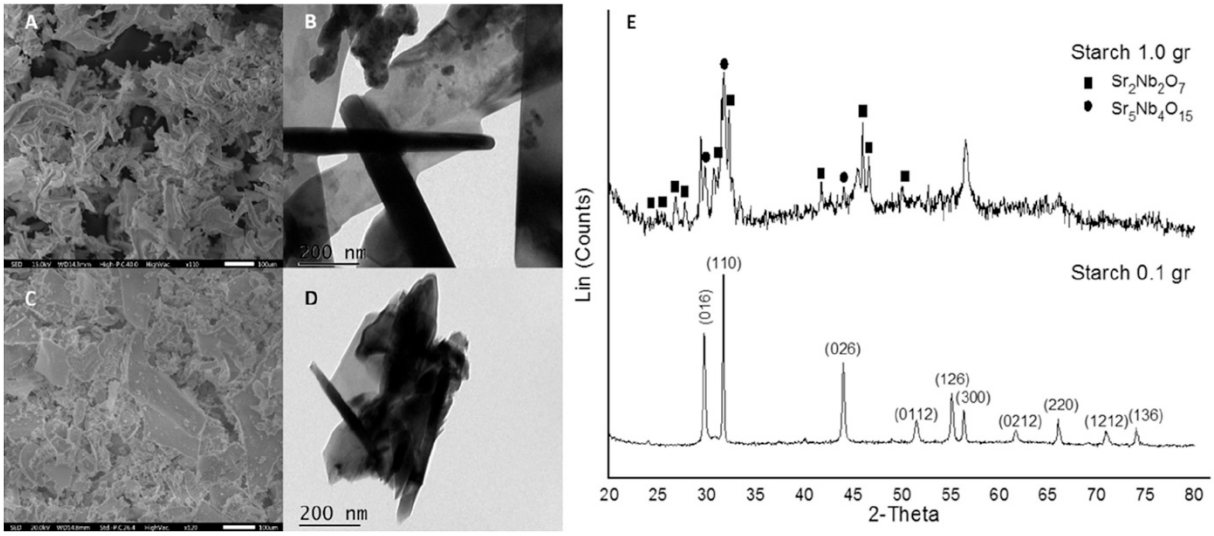

Figure 4.7. A) SEM and B) TEM images with the corresponding powder X-ray diffraction pattern (E, top pattern) from the synthesis of $Sr_5Nb_4O_{15}$ using ionic liquid and 1 g of starch. C) and D) show SEM and TEM images respectively, with the corresponding powder X-ray diffraction pattern (E, lower pattern) from the synthesis of $Sr_5Nb_4O_{15}$ using the ionic liquid and 0.1 g of starch. Indexed planes correspond to the phase $Sr_5Nb_4O_{15}$. Scale bars A & C = 100 μm, B & D = 200 nm.

When 0.1 g was used in the synthesis of strontium niobate, it shared a very similar crystal structure from that obtained via cellulose and the ionic liquid on its own (Figure 4.7 C). When the amount of the organic source is increased to 1.0 g, it showed an aggregated particle formation (Figure 4.7 A). In regards of the nanostructure, for both 0.1 g and 1.0 g, starch exhibited plate-like and rod-shaped crystals (Figure 4.7 B & D). In stark contrast to other biopolymers investigated here, starch seems to disrupt the chelating properties of the IL creating a mix of phases observable on the powder X-ray diffraction pattern at 1.0 g (Figure 4.7 E). Starch has been identified as an important component in the formation of homogenous and well dispersed nanoparticles while having a relevant impact on the crystal phase.[21] Moreover, the presence of rod shape crystals has been previously reported as a main crystal structure observed when using this polysaccharide.[19] Another reason a polyphasic product is observed via X-ray diffraction is the presence of K and Ca impurities present in the starch (Figure 4.8).

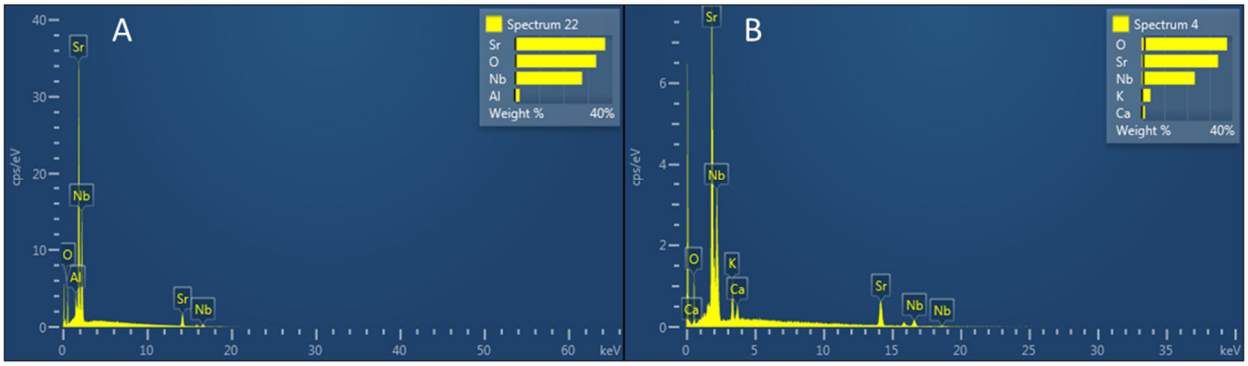

Figure 4.8. Scanning Electron microscopy energy dispersive X-ray analysis of the synthesis of $Sr_5Nb_4O_{15}$ with: A) 0.1 g and B) 1.0 g of starch. Insets show the quantitative analysis of elemental composition.

4.2.1.5 Ionic liquid with dextran

Dextran is a hyper-branched polymer of dextrose of very high molecular weight obtained from the lactic-acid bacteria, with the most frequently used acquired from Leuconostoc mesenteroides and Streptococcus mutans.[13]

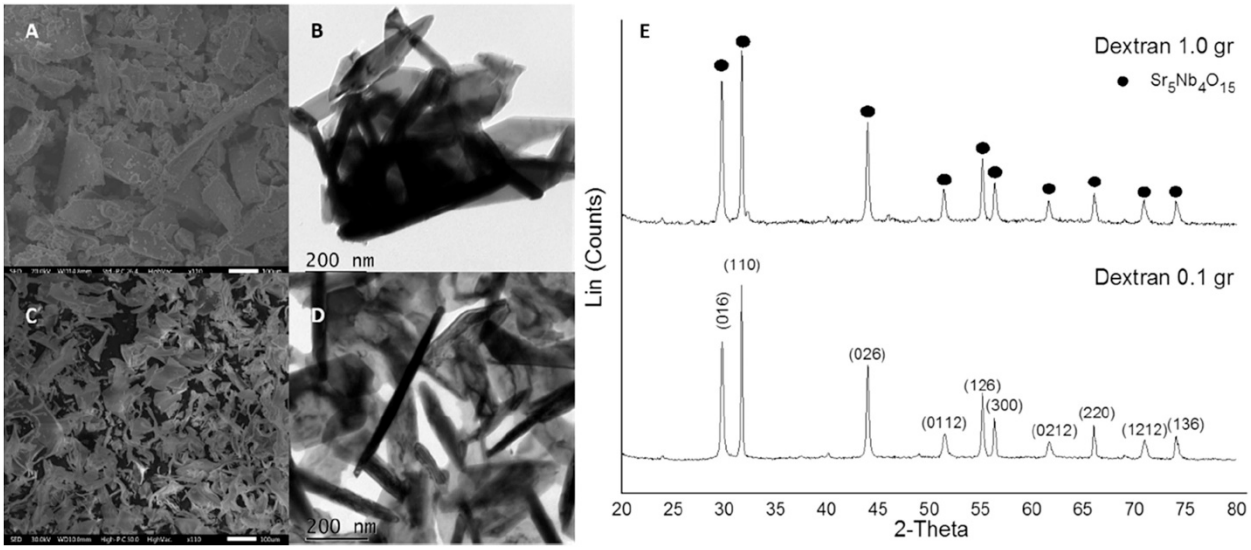

Figure 4.9. A) SEM and B) TEM images with the corresponding powder X-ray diffraction pattern (E, top pattern) from the synthesis of $Sr_5Nb_4O_{15}$ using ionic liquid and 1 g of dextran. C) and D) show SEM and TEM images respectively, with the corresponding powder X-ray diffraction pattern (E, lower pattern) from the synthesis of $Sr_5Nb_4O_{15}$ using the ionic liquid and 0.1 g of dextran. Indexed planes correspond to the phase $Sr_5Nb_4O_{15}$. Scale bars A & C = 100 μm, B & D = 200 nm.

Incorporation of dextran in the strontium niobate synthesis produced analogous morphological results to that obtained with starch (Figure 4.9 A-D). Interestingly, dextran is the only polysaccharide that exhibited single-phase at higher amounts (Figure E). It has been observed previously that the very high molecular weight of dextran acts as a more effective sparging agent on calcination, encouraging better mixing in the early stages of the synthesis and a totally homogeneous mixture of the precursor elements.[22]

EDX analysis of both cellulose (Figure 4.10 C & D) and dextran showed complete purity displaying only Sr, Nb and O in the sample (Figure 4.10 A & B).

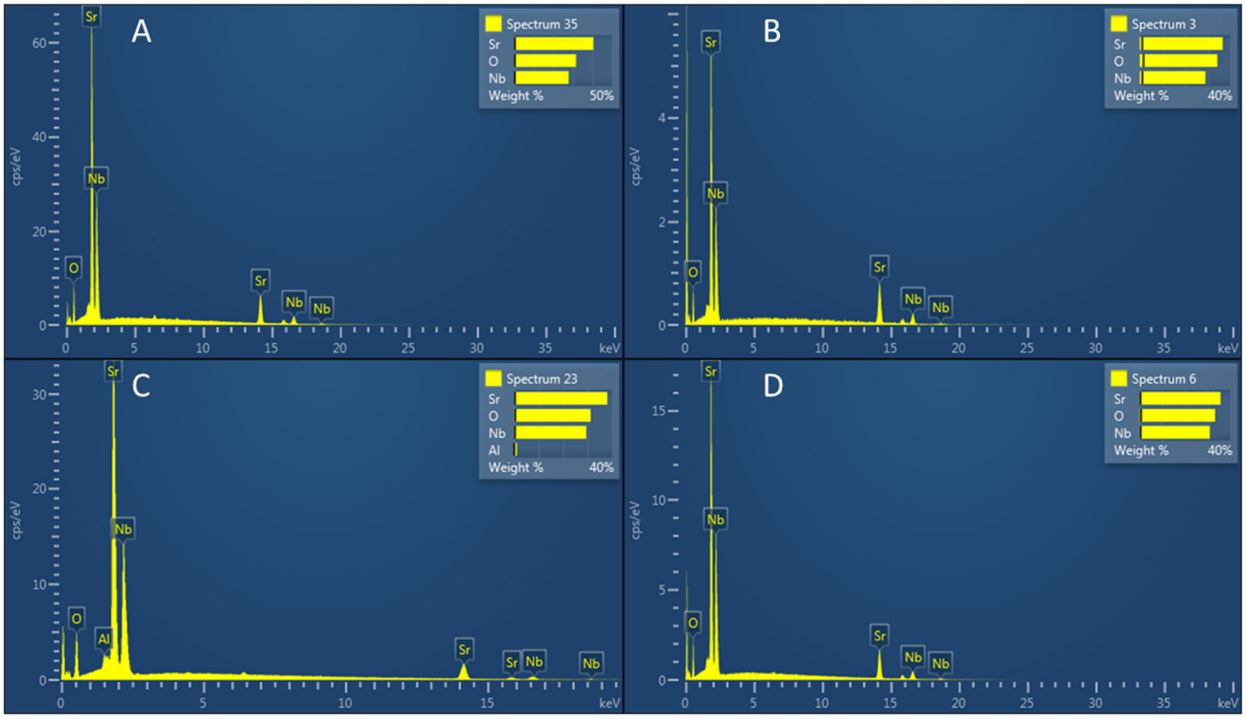

Figure 4.10. Scanning Electron microscopy energy dispersive X-ray analysis of the synthesis of $Sr_5Nb_4O_{15}$ with: A) 0.1 g and B) 1.0 g of dextran, and C) 0.1 gr and B) 1.0 gr of cellulose. Insets show the quantitative analysis of elemental composition.

4.2.2 $YBa_2Cu_3O_{7-\delta}$ (YBCO) superconductor

After defining that to obtain crystal purity low quantities (0.1 g) of the organic source was preferential, further experiments followed however, this time to obtain a deeper understanding on the effect of the physical properties. It is well established that the critical temperature at which the material exhibits superconductivity relies heavily on the oxygen content.[22–27] In fact, for $YBa_2Cu_3O_{7-}\delta$ when $0 < \delta < 0.2$ the critical temperature is slightly above 90 K however, with δ increasing to $0.2 < \delta < 0.3$ decreases sharply and remains nearly constant at approximately 60 K for $0.3 < \delta < 0.5$; above values of 0.5 a sharp decrease of critical temperature is observed from 60 K to 0 K.[27] Moreover, the transport properties are critically dependent on the partial oxidation of Cu^+. In YBCO superconductor oxidation is controlled almost exclusively by oxygen deficiency. [23] Controlling the oxygen content is crucial to obtain the highest possible critical temperature, therefore, characterization of YBCO superconductor synthesized via different polysaccharides was carried out in order to understand the role played by the organic compound.

4.2.2.1 Ionic liquid

Unfortunately, it was not possible to obtain SQUID magnetometry for this sample. However, via SEM analysis it was possible to demonstrate that the ionic liquid influences the morphology of the material. Two reactions were made, one where only the metal nitrates were employed and a second with the metal nitrates and the ionic liquid. (Figure 4.11 A&B). When the reaction was carried out only with the raw materials the product resembles to small crystallites aggregated forming huge masses with areas around 2 x 10^5 μm^2 (Figure 4.11 A). The second reaction, with the ionic liquid, shows a high contrast difference where particles look like dry leaves (Figure 4.11 B).

Also, when comparing results obtained by the same ionic liquid in the synthesis of $Sr_5Nb_4O_{15}$, blocks of agglomerated crystallites are obtained, whereas for the synthesis of the superconductor, results are no near close in similarity, suggesting that the interaction of the ionic liquid with different metal cations will vary the resulting morphology. With regards of the nanostructure (Figure 4.11 C), no particular

morphology is discernible. Most of the sample is represented by nanocrystallites with various sizes. Powder diffraction pattern shown minor impurities belonging to CuO and another marked (?) that could not be indexed.

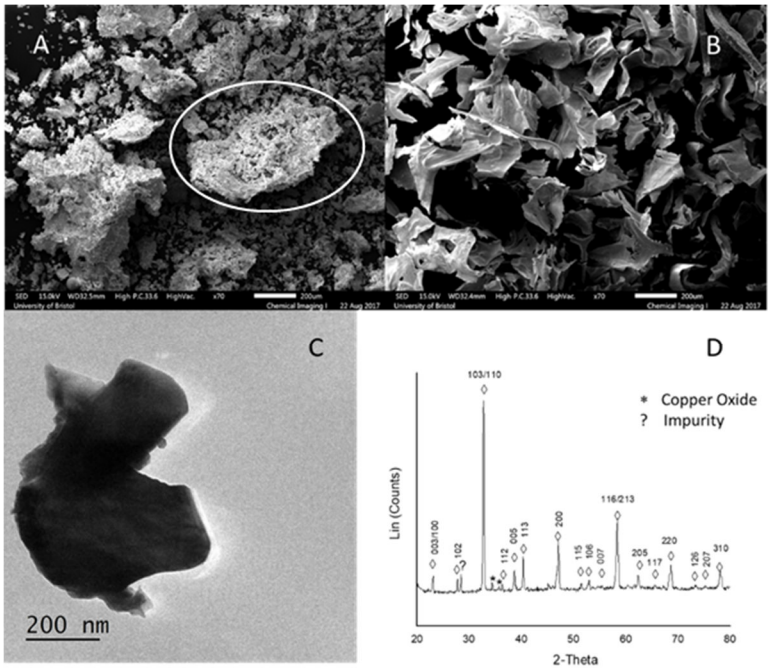

Figure 4.11. SEM image of the synthesis of YBCO superconductor A) using only metal nitrates, and B) using ionic liquid. C) TEM image and D) powder diffraction pattern of the synthesis of YBCO superconductor using (emim)OAc as chelating agent. White circle shows the crystallite measure via Image J software. Indexed planes correspond to the phase $YBa_2Cu_3O_{7-\delta}$. Scale bars A & B = 100 μm, C = 200 nm.

4.2.2.2 Ionic liquid with cellulose

SEM images (Figure 4.12 A) show a very similar result observed by the ionic liquid with dry leaves-like particles. On the other hand, TEM images (Figure 4.12 B) exhibit a difference where instead of bulky nanocrystals an agglomerate of thin wires-like nanocrystals is seen. This result is different from what was observed in the synthesis of $Sr_5Nb_4O_{15}$ producing plate-like and road-like morphologies. SQUID magnetometry (Figure 4.12 D) of the crystal phase obtained gave $T_{c\ onset}$ = 91 K indicating that the oxygen content of the superconductive phase is in between $0 < \delta < 0.2$. Powder diffraction pattern (Figure 4.12 C) confirms high purity around the sample with diffraction from the superconducting crystal phase alone.

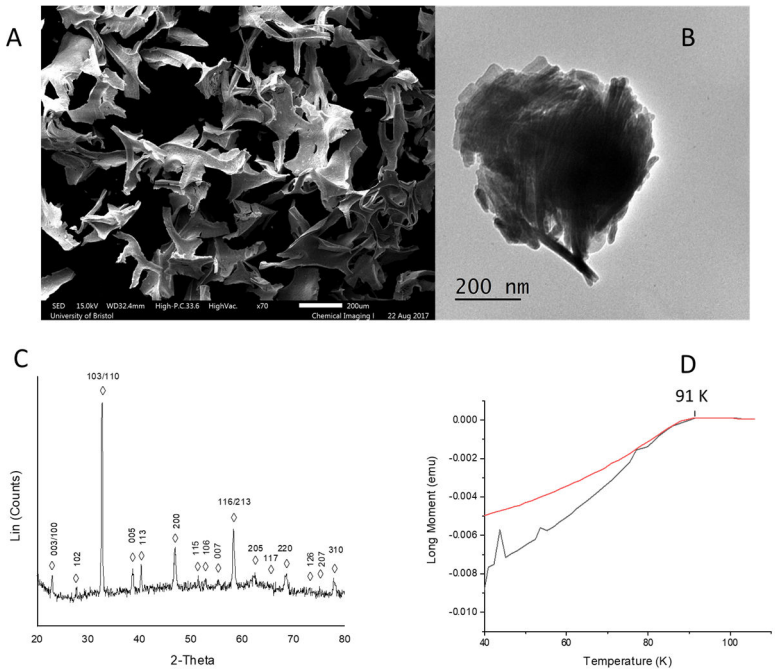

Figure 4.12. A) SEM and B) TEM images of the synthesis of YBCO superconductor via (emim)OAc and cellulose as chelating agents. C) Powder diffraction pattern of the superconductive phase. D) SQUID characterization, red line zero-field cooling, and black line field cooling, showing the $T_{c\ onset}$. Indexed planes correspond to the phase $YBa_2Cu_3O_{7-\delta}$. Scale bars A = 100 μm, B = 200 nm.

4.2.2.3 Ionic liquid with chitosan

The synthesis with chitosan does exhibit some similarities compared with what was previously observed in the synthesis of $Sr_5Nb_4O_{15}$. SEM image (Figure 4.13 A) clearly shows extended plate-like macro morphology. Moreover, TEM image (Figure 4.13 B) also shown an agglomerate of particles very similar to those spotted in the synthesis of the strontium niobate however, with size variations where instead of ~30 nm, are around ~185 nm. Lastly, SQUID magnetometry was difficult to obtain, but it is clear that the $T_{c\ onset}$ happens to be near 63 K (Zero Field Cooling, ZFC) and 66 K (Field Cooling, FC). The critical temperature is found to belong to the so called second "plateau"[27] meaning that the oxygen content must have $0.2 < \delta < 0.5$ values. More precisely a continues drop happens for $0.2 < \delta < 0.3$ values and the fact that the critical temperature is slightly above 60 K indicates that values have to be in that range of δ values.

Via powder diffraction pattern (Figure 4.13 C) it is possible to encounter with not only the superconductive phase but also with copper oxide (CuO) and barium copper oxide ($BaCuO_2$).

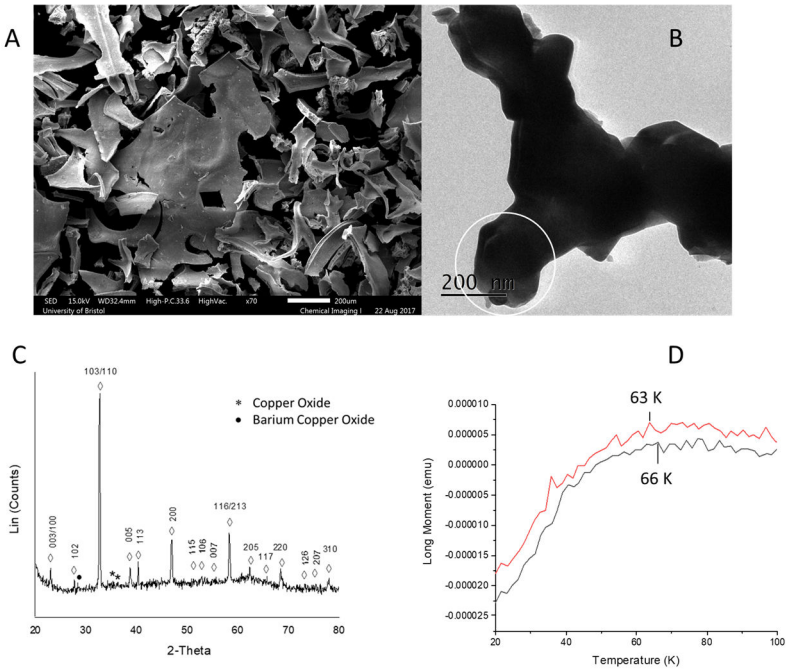

Figure 4.13. A) SEM and B) TEM images of the synthesis of YBCO superconductor via (emim)OAc and chitosan as chelating agents. C) Powder diffraction pattern of the superconductive phase. D) SQUID characterization, red line zero-field cooling, and black line field cooling, showing the $T_{c\ onset}$. White circle shows the crystallite measure via Image J software. Indexed planes correspond to the phase $YBa_2Cu_3O_{7-\delta}$. Scale bars A = 100 μm, B = 200 nm.

4.2.2.4 Ionic liquid with starch

SEM image (Figure 4.14 A) shown also plate-like particles very much like that observed with chitosan but, clearly different from results obtained in the synthesis of the strontium niobate, where the outcome was agglomerated crystallites. Moreover, in comparison with the predominant rod-like morphology observed in the synthesis of the strontium niobate, TEM image (Figure 4.14 B) did not exhibit any particular morphology. SQUID magnetometry analysis (Figure 4.14 D) shown $T_{c\ onset}$ = 60 K. Once again, we found this crystal phase to be oxygen deficient with $0.3 < \delta < 0.5$ values. Similarly to the reaction carried out with chitosan, extra crystal phases can be seen via powder diffraction pattern (Figure 4.14 C), namely copper oxide (CuO), barium copper oxide ($BaCuO_2$), and yttrium copper oxide ($Y_2Cu_2O_5$).

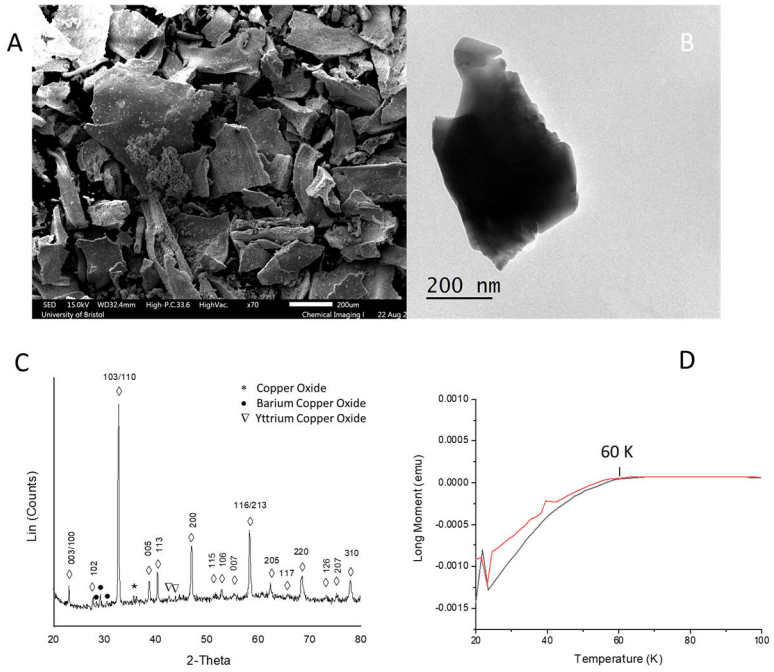

Figure 4.14. A) SEM and B) TEM images of the synthesis of YBCO superconductor via (emim)OAc and starch as chelating agents. C) Powder diffraction pattern of the superconductive phase. D) SQUID characterization, red line zero-field cooling, and black line field cooling, showing the $T_{c\ onset}$. Indexed planes correspond to the phase $YBa_2Cu_3O_{7-\delta}$. Scale bars A = 100 μm, B = 200 nm.

4.2.2.5 Ionic liquid with dextran

When comparing with previous experiment dextran surprisingly gave similar results in the synthesis of the strontium niobate and the YBCO superconductor. SEM image (Figure 4.15 A) in both cases displayed agglomerated crystallites with varying sizes. However, TEM images shown differences, in comparison with the rod-like and plate-like particles obtained for the strontium niobate, YBCO superconductor exhibited no definable morphology (Figure 4.15 B). SQUID magnetometry results (Figure 4.15 D) shown a $T_{c\ onset}$ = 94 K (FC) and 91 K (ZFC). Both critical temperatures indicate $0.0 < \delta < 0.2$ values, implying that the best quality of superconducting phase with the desired oxygen content was formed.

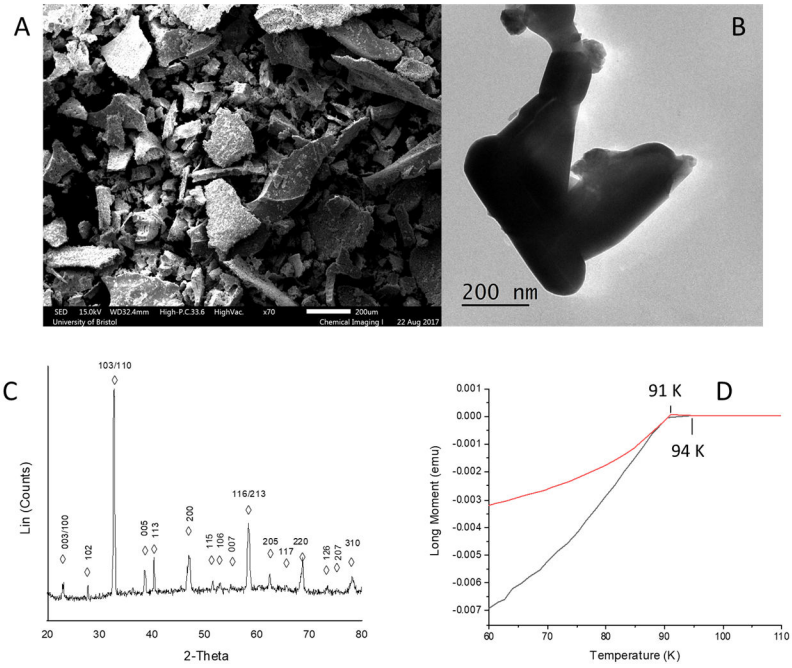

Figure 4.15. A) SEM and B) TEM images of the synthesis of YBCO superconductor via (emim)OAc and dextran as chelating agents. C) Powder diffraction pattern of the superconductive phase. D) SQUID characterization, red line zero-field cooling, and black line field cooling, showing the $T_{c\ onset}$. Indexed planes correspond to the phase $YBa_2Cu_3O_{7-\delta}$. Scale bars A = 100 μm, B = 200 nm.

4.3 Conclusions

The homogeneity afforded by the IL/biopolymer mixture at low concentrations clearly results in a single-phase material through the facile mass transport of species during the synthesis. However, it was also shown that despite the powder x-ray diffraction patterns exhibited mostly single-phase of YBCO superconductor, via SQUID characterization it was possible to establish that the oxygen content varied depending the organic source in use. The highest critical temperature exhibited belong to dextran with $T_{c\ onset}$ = 94 K and cellulose with $T_{c\ onset}$ = 91 K.

Furthermore, for the synthesis of the strontium niobate when the use of organic source is increased, only dextran is capable of delivering a single-phase material. This is presumably due to a disruption of mass transport through the gels. Moreover, elements present in the organic source, such as calcium, sodium and potassium, are more evident and in enough quantities to disrupt the production of a single-phase.

Additionally, it was proven in the synthesis of the strontium niobate that the organic source does help to lead the reaction into a specific crystal phase providing control over the stoichiometry of the reaction and the possibility to generate targeted single-phases where, on the contrary, without the organic source, a mixed phase was most commonly exhibited. Finally, the morphology of the crystals is still a task that requires further investigation, however, at low concentrations of the organic compound, in most of the cases, excepting chitosan which delivered plate-like macro and nano structures in the synthesis of $Sr_5Nb_4O_{15}$, the macromorphology and nanostructure is dictated by the ionic liquid. It is important to highlight the fact that the morphology exhibited by the interaction of the ionic liquid with the metal cations will vary depending the metal cations in use. This can be observed by comparing results between the ionic liquid with Sr and Nb for the synthesis of the strontium niobate, against Y, Ba, and Cu for the synthesis of the superconductor. Lastly, morphological changes, when synthesizing $Sr_5Nb_4O_{15}$, were observed when the amount of the organic source was increased, such as cellulose delivering elongated particles in both macro and nano scale, but this came at a cost to the overall phase purity of the product.

4.4 Bibliography

(1) Addadi, L.; Joester, D.; Nudelman, F.; Weiner, S. Mollusk Shell Formation: A Source of New Concepts for Understanding Biomineralization Processes. *Chem. - A Eur. J.* **2006**, *12* (4), 980–987.

(2) Killian, C. E.; Wilt, F. H. Molecular Aspects of Biomineralization of the Echinoderm Endoskeleton. *Chem. Rev.* **2008**, *108* (11), 4463–4474.

(3) Chen, X.; Mao, S. S. Titanium Dioxide Nanomaterials: Synthesis, Properties, Modifications and Applications. *Chemical Reviews*. American Chemical Society, **2007**, 2891–2959.

(4) Kubacka, A.; Fernández-García, M.; Colón, G. Advanced Nanoarchitectures for Solar Photocatalytic Applications. *Chem. Rev.* **2012**, *112* (3), 1555–1614.

(5) Sun, Y. F.; Liu, S. B.; Meng, F. L.; Liu, J. Y.; Jin, Z.; Kong, L. T.; Liu, J. H. Metal Oxide Nanostructures and Their Gas Sensing Properties: A Review. *Sensors*. Molecular Diversity Preservation International February 27, **2012**, 2610–2631.

(6) Zhao, X.; Sánchez, B. M.; Dobson, P. J.; Grant, P. S. The Role of Nanomaterials in Redox-Based Supercapacitors for next Generation Energy Storage Devices. *Nanoscale* **2011**, *3* (3), 839.

(7) Danks, A. E.; Hall, S. R.; Schnepp, Z. The Evolution of 'Sol–gel' Chemistry as a Technique for Materials Synthesis. *Mater. Horizons* **2016**, *3* (2), 91–112.

(8) Sarkar, S.; Guibal, E.; Quignard, F.; SenGupta, A. K. Polymer-Supported Metals and Metal Oxide Nanoparticles: Synthesis, Characterization, and Applications. *J. Nanoparticle Res.* **2012**, *14* (2), 715.

(9) Elazzouzi-Hafraoui, S.; Nishiyama, Y.; Putaux, J.-L.; Heux, L.; Dubreuil, F.; Rochas, C. The Shape and Size Distribution of Crystalline Nanoparticles Prepared by Acid Hydrolysis of Native Cellulose. *Biomacromolecules* **2008**, *9* (1), 57–65.

(10) Klemm, D.; Kramer, F.; Moritz, S.; Lindström, T.; Ankerfors, M.; Gray, D.; Dorris, A. Nanocelluloses: A New Family of Nature-Based Materials. *Angewandte Chemie - International*, **2011**, 50(24), 5438–5466.

(11) Lin, N.; Huang, J.; Dufresne, A. Preparation, Properties and Applications of Polysaccharide Nanocrystals in Advanced Functional Nanomaterials: A Review. *Nanoscale* **2012**, *4* (11), 3274-3294.

(12) Tingaut, P.; Zimmermann, T.; Sèbe, G. Cellulose Nanocrystals and Microfibrillated Cellulose as Building Blocks for the Design of Hierarchical Functional Materials. *J. Mater. Chem.* **2012**, *22* (38), 20105-20111.

(13) Boury, B.; Plumejeau, S. Metal Oxides and Polysaccharides: An Efficient Hybrid Association for Materials Chemistry. *Green Chemistry*. Royal Society of Chemistry, **2015**, 17, 72–88.

(14) Armand, M.; Endres, F.; MacFarlane, D. R.; Ohno, H.; Scrosati, B. Ionic-Liquid Materials for the Electrochemical Challenges of the Future. *Nature Materials*, **2009**, 8, 621–629.

(15) Ma, Z.; Yu, J.; Dai, S. Preparation of Inorganic Materials Using Ionic Liquids. *Adv. Mater.* **2010**, *22* (2), 261–285.

(16) Green, D. C.; Glatzel, S.; Collins, A. M.; Patil, A. J.; Hall, S. R. A New General Synthetic Strategy for Phase-Pure Complex Functional Materials. *Adv. Mater.* **2012**, *24* (42), 5767–5772.

(17) Zhang, W.; Chen, S.; Hu, W.; Zhou, B.; Yang, Z.; Yin, N.; Wang, H. Facile Fabrication of Flexible Magnetic Nanohybrid Membrane with Amphiphobic Surface Based on Bacterial Cellulose. *Carbohydr. Polym.* **2011**, *86* (4), 1760–1767.

(18) Barata, M. A. B.; Neves, M. C.; Pascoal Neto, C.; Trindade, T. Growth of $BiVO_4$ Particles in Cellulosic Fibres by in Situ Reaction. *Dye. Pigment.* **2005**, *65* (2), 125–127.

(19) Ibupoto, Z.; Khun, K.; Eriksson, M.; AlSalhi, M.; Atif, M.; Ansari, A.; Willander, M.; Ibupoto, Z. H.; Khun, K.; Eriksson, M.; et al. Hydrothermal Growth of Vertically Aligned ZnO Nanorods Using a Biocomposite Seed Layer of ZnO Nanoparticles. *Materials (Basel).* **2013**, *6* (8), 3584–3597.

(20) Matos, J.; Atienzar, P.; García, H.; Hernández-Garrido, J. C. Nanocrystalline Carbon-TiO_2 hybrid Hollow Spheres as Possible Electrodes for Solar Cells. *Carbon N. Y.* **2013**, *53*, 169–181.

(21) Bao, S. J.; Lei, C.; Xu, M. W.; Cai, C. J.; Cheng, C. J.; Li, C. M. Environmentally-Friendly

Biomimicking Synthesis of TiO_2 nanomaterials Using Saccharides to Tailor Morphology, Crystal Phase and Photocatalytic Activity. *CrystEngComm* **2013**, *15* (23), 4694–4699.

(22) Walsh, D.; Wimbush, S. C.; Hall, S. R. Reticulated Superconducting YBCO Materials of Designed Macromorphologies with Enhanced Structural Stability through Incorporation of Lithium. *Supercond. Sci. Technol.* **2009**, *22* (1), 015026.

(23) Cava, R. J.; Batlogg, B.; Van Dover, R. B.; Murphy, D. W.; Sunshine, S.; Siegrist, T.; Remeika, J. P.; Rietman, E. A.; Zahurak, S.; Espinosa, G. P. Bulk Superconductivity at 91 K in Single-Phase Oxygen-Deficient Perovskite $Ba_2YCu_3O_{9-x}$. *Phys. Rev. Lett.* **1987**, *58* (16), 1676–1679.

(24) Hanic, F.; Horváth, I.; Gáliková, L. Thermogravimetric Study of the Transition Copper Valency in the Superconductive System Y-Ba-Cu-O. *Thermochim. Acta* **1989**, *143*, 123–130.

(25) Appelman, E. H.; Morss, L. R.; Kini, A. M.; Geiser, U.; Umezawa, A.; Crabtree, G. W.; Carlson, K. D. Oxygen Content of Superconducting Perovskites, Lanthanum Strontium Copper Oxide $La_{2-x}Sr_xCuO_y$ and Yttrium Barium Copper Oxide $YBa_2Cu_3O_y$. *Inorg. Chem.* **1987**, *26* (20), 3237–3239.

(26) Hikami, S.; Matsuda, Y. High T c Superconductors of the Perovskite Structure Oxides. *Jpn. J. Appl. Phys.* **1987**, *26* (S3-2), 1027.

(27) Jorgensen, J. D.; Veal, B. W.; Paulikas, A. P.; Nowicki, L. J.; Crabtree, G. W.; Claus, H.; Kwok, W. K. Structural Properties of Oxygen-Deficient $YBa_2Cu_3O_{7-x}$. *Phys. Rev. B* **1990**, *41* (4), 1863–1877.

Chapter 5
The role of ionic liquid/deep eutectic solvents in the synthesis of metal oxides.

Parts of this chapter are published in the reference indicated below printed in CrystEngComm. The paper used in the creation of this chapter was written and submitted by myself involving the preparation of all figures and text contained herein. I was involved in analysis of all data collected both directly by myself and on behalf of the publication by co-authors. Any data used in this thesis, collected and analysed with only minimal input from myself has been referenced accordingly. Specifically, all data was collected by myself other than HRTEM images taken by Jean-Charles Eloi the Electron Microscopy Technician and the help provided by Iori Sudoh to obtain SQUID magnetometry data.

Gómez Rojas, O.; Sudoh, I.; Nakayama, T.; Hall, S. R. The Role of Ionic Liquids in the Synthesis of the High-Temperature Superconductor $YBa_2Cu_3O_{7-\delta}$. *CrystEngComm* **2018.**

5.1 General introduction

Since the discovery of the high temperature superconductors in 1986,[1] different synthetic routes have been used in order to achieve greater crystallographic control, with the objective of producing a product of high quality, faster and cheaper. The sol-gel synthesis route[2] has been constantly evolving to fulfil these criteria and has produced many variants. Ionic liquids have been shown to be a system which has the capability to synthesize various different inorganic compounds.[3–5] Mechanistically, this method relies on the ability of ionic liquids to solvate metal cations and act as chelating agents, subsequently producing a gel with the additional use of an organic source such as a polysaccharide, in order to create single-phase complex functional materials.[6,7]

In general terms an ionic liquid (IL) is a non-conventional molten salt usually composed of large organic cations and smaller organic or inorganic anions.[8] The popularity of these systems has been growing due to the fact that they are 'green', super dissociating solvents, with low melting points, negligible vapor pressures, and with high thermal stabilities, and ionic conductivities.[8–11] Due to the huge diversity of anions and cations that can be used to synthesize an IL, their properties can be fine-tuned to fulfil a desired purpose. Specifically, for the synthesis of inorganic materials, ionic liquids have additional advantages such as having low interfacial tension which allows for a high nucleation rate.[3] ILs can also form extensive hydrogen bonding systems thereby producing a complex structure that will further influence the structures of the final products.[12–14] Lastly ILs can provide a non-aqueous alternative for different types of synthesis procedures.[15–17]

ILs have yet big disadvantages, the price tends to be high due to their complicated process of synthesis. Moreover, ionic liquids were initially classified as green however, such an attribution has been recently argued.[18] Several studies pointed out the hazardous toxicity and very low biodegradability of most of those ILs.[19,20] To obtain the desired functionality, ionic liquids must be of high purity otherwise their

properties are compromised. In addition to this, the synthesis of ILs require large amount of salts and solvents to ensure complete ion exchange. Collectively the syntheses of some ILs are far away from being environmentally friendly and the synthetic complexity is also reflected in the high price of common ILs.[21]

In 2001 a new generation of solvents emerged, namely deep eutectic solvents.[22] Deep eutectic solvents overcome some of the drawbacks that the ionic liquids have due to a straightforward synthesis by only mixing together components capable of forming a eutectic mixture. Two of the most common compounds used are choline chloride combined with a hydrogen bond donor, both of which are green, cheap, renewable and biodegradable.

Several advantages can be highlighted such as their low price, easier storage and preparation. Deep eutectic solvents exhibit similar physico-chemical properties as the ionic liquids and as a result these compounds are commonly considered as ionic liquids in the literature. However, deep eutectic solvents differ in the fact that they are not always formed only by ionic species and, in fact, can be made from non-ionic species.[21] Many deep eutectic constituents have been explored[23,24] and include the use of natural products such as organic acids, amino acids and sugars.[23,25,26] Molecules used by nature are suitable candidates to produce new, green and exciting deep eutectic solvents, also their vast diversity provides different chemically biodegradable properties.

Despite the fact that the ionic liquids have been used in the synthesis of inorganic materials[27–30] and great efforts have been made to control the crystal phase and morphology, a lack of fundamental understanding of the role of the ionic liquid during the synthetic process has still not been achieved. The work presented in this chapter focus on unveiling the role played by the ionic liquid/deep eutectic solvent targeting the superconductive $YBa_2Cu_3O_{7-\delta}$ (YBCO) crystal composition. Furthermore, as a proof of concept, it was possible to synthesise $Bi_2Sr_2CaCu_2O_{8+x}$ (BSCCO or Bi-2212) using a natural deep eutectic

solvent (NADES). Finally, getting advantage of the knowledge obtained it was possible to synthesise a new sodium strontium niobate crystal composition via a choline chloride based deep eutectic solvent.

5.2 The role of ionic liquids in the synthesis of the high-temperature superconductor $YBa_2Cu_3O_{7-\delta}$

5.2.1 Results and discussion

5.2.1.1 Infrared spectroscopy

In order to understand the very first interaction of the ionic liquid/deep eutectic solvents with the metal cations, FTIR was carried out firstly of just the ionic liquid/deep eutectic solvents (Figure 5.1-5.3 Red lines), and second of the ionic liquid/deep eutectic solvents in interaction with the metal cations (Figure 5.1-5.3 Blue lines). All FTIR measurements were done after dehydration process to avoid, as much as possible, water in the system.

5.2.1.1.1 (emim)OAc

Important differences can be noted, especially in two indicative range of wavelengths. The first and most important is from 1130 to 1420 cm^{-1}, specifically 1130-1210 cm^{-1}, and 1340-1420 cm^{-1}, which correspond to the C-O stretching and the O-H in plane bend from the carbonyl group respectively. Solvated metal cations by (emim)OAc prompt a shift to lower wavelengths of the C-O stretching, namely from 1177 to 1171 cm^{-1}, whereas a shift towards higher wavelengths is present for the O-H in plane bend from 1376 to 1382 cm^{-1} (Figure 5.1 circled area). [31] This is a clear indicator of how the chemical environment of the carboxylic group has changed due to the insertion of metal cations. The second range of wavelengths is from 2650 to 3200 cm^{-1} which represents vibrations from the aromatic C=C (Above 3000 cm^{-1}) and alkanes present in both constituents (bellow 3000 cm^{-1}).[31] A clear shift to higher wavelength values can be seen in the (emim)OAc/chelated metal cation spectra (Figure 5.1 blue line) compared against only the ionic liquid

spectra (Figure 5.1 red line); this shift corresponds to a change in the electronegativity of the neighbouring atoms. It is important to note that despite the aim to fully dehydrate all samples, the FTIR spectra shows O-H stretching bands in the range of 3500-3200 cm^{-1} (Figure 5.1 blue line). It is also the case that water molecules will impact heavily in lower wavelengths as can be seen with the broadening of bands, from 800-400 cm^{-1} (Figure 5.1 blue line), due to a significant increase in the number of hydrogen bonds.[32]

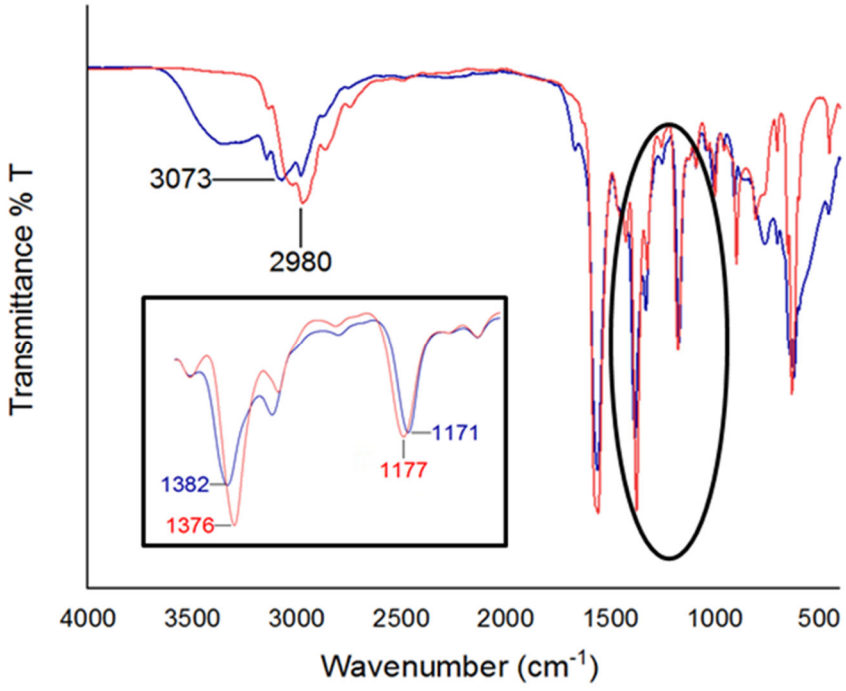

Figure 5.1. Fourier transformation infrared spectra of blue: (emim)OAc with Cu, Y, and Ba nitrates, red: only (emim)OAc. Inset represents a magnified frame of the circled area of the FTIR spectra.

5.2.1.1.2 Ethylene glycol: choline chloride DES

There are two main sections to highlight to elucidate the interaction between the DES and the metal cation. The first region can be found in the range of 800-400 cm^{-1} which corresponds to the presence of Cl^- in the DES by C-X stretching (Figure 5.2 Red line).[33] The clear change in shape of the band indicates that the chemical environment surrounding the Cl^- has changed due to the insertion of metal cations (Figure 5.2 Blue line). Also, at 955 cm^{-1} (Indicated in Figure 5.2 *) the band which corresponds to choline is intact which signposts the fact that the molecule is not involved in the chelation of the metal cation. The second

important feature is the appearance of a band in the wavelength 1650 cm^{-1} (Figure 5.2 Blue line). This band corresponds to the interaction of ethylene glycol as a ligand with the metal cations.[34, 35] Therefore, these spectra provide information about how the interaction happens in two separate ways; one will be between the chloride and the metal cations and the second, between the molecule of ethylene glycol and the metals cations. The formation of such complexes will change the chemical environment of the system; thus, changes can be observed in a shift to higher values of the bands in the wavelength range of 3000-2800 cm^{-1} (Figure 5.2 blue line), corresponding to C-H stretching of the alkanes, and 3700-3000 cm^{-1}, belonging to the O-H stretching of the ethylene glycol and of the overall hydrogen bonding network of the DES.[35]

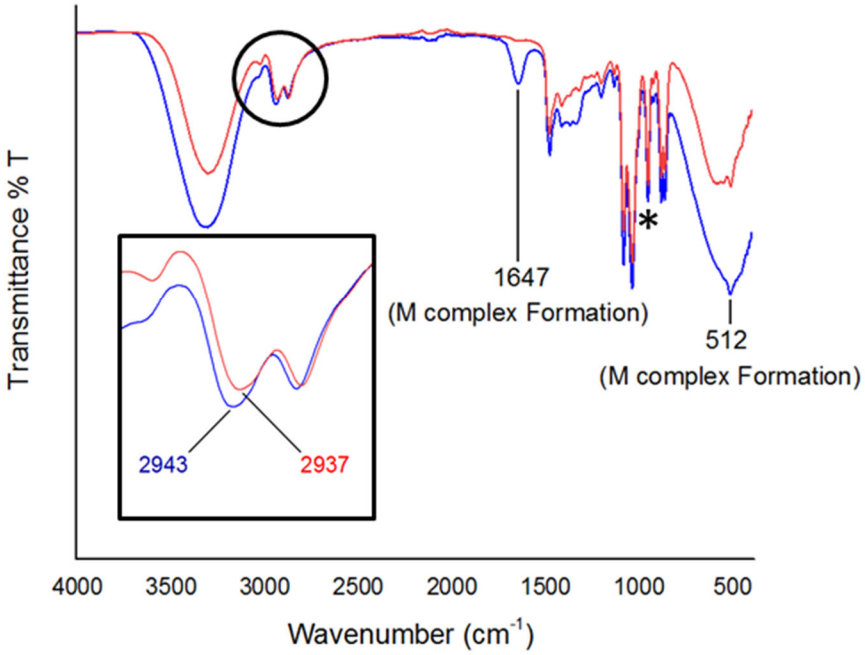

Figure 5.2. Fourier transformation infrared spectra of blue: ethylene glycol: choline chloride DES with Cu, Y, and Ba nitrates, red: only ethylene glycol: choline chloride DES. Inset represents a magnified frame of the circled area of the FTIR spectra.

5.2.1.1.3 Imidazole: choline chloride DES

The most important band to highlight comes at 3225 cm^{-1} (Figure 5.3 circled), which belongs to N-H stretching of secondary amines in interaction with the choline chloride, this band is not present in the

FTIR spectra of imidazole[31] nor of choline chloride,[33] therefore it is safe to assume that it belongs to the interaction of both components of the DES. Once the DES is exposed to the metal cations, the band vanishes (Figure 5.3 blue line), indicating the formation of a complex between the imidazole and the metal cations, substituting the direct interaction of imidazole with chlorine forming complexes where secondary amines are not present.[36–38]

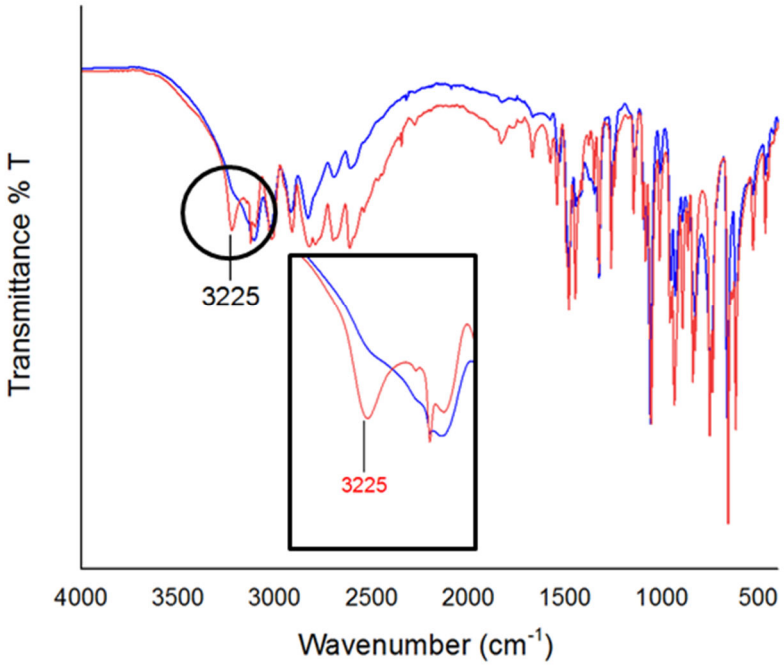

Figure 5.3. Fourier transformation infrared spectra of blue: imidazole: choline chloride with Cu, Y, and Ba nitrates, red: imidazole: only choline chloride DES. Inset represents a magnified frame of the circled area of the FTIR spectra.

5.2.1.2 Uv-Vis

5.2.1.2.1 (emim)OAc

The absorbance band of (emim)OAc with the hydrated metal cations is shown to be in the blue region of the spectrum with a maximum absorbance value at 470 nm (Figure 5.4A blue line). However, when the solution is dehydrated the absorbance band undergoes an expected reduction in intensity and a second band appears in the green region of the visible spectrum with a maximum absorbance at 560 nm

(Figure 5.4A red line). It is noteworthy that despite the dehydration process in both, Uv-vis absorbance and FTIR spectrum, bands related to remains of water content can still be seen. The colour exhibited by the solutions in both hydrated and dehydrated conditions correlates with the representative colour of copper acetate, hydrated and dehydrated respectively. [39]

5.2.1.2.2 Ethylene glycol: choline chloride DES

The hydrated solution of EG: ChCl DES with metal cations shows a maximum absorbance at 522 nm (Figure 5.4B blue line), which belongs to the green region of the visible spectrum. Once the solution is dehydrated the band shifts from 522 nm to 594 nm (Figure 5.4B red line), displaying a yellow-orange colour. These colours correlate with the expected colour of $CuCl_2$ in its hydrated and dehydrated forms respectively.[39]

5.2.1.2.3 Imidazole: choline chloride DES

Uv-vis spectra before and after dehydration indicate no change with a maximum absorbance band in the blue region of the spectrum at 445 nm (Figure 5.4C blue line & Figure 2C red line). The representative deep blue colour exhibited has been observed in coordinated complexes of copper with imidazole ligands.[39,40]

In good agreement with what was seen via FTIR, all the respective complexes expected to be formed are being observed via uv-vis absorption. Also, even by eye copper complexes in solution were able to be identified (Figure 5.4 1-9). To solve the question of how these complexes are involved with the outcome of the final crystal composition, a systematic temperature analysis was carried out.

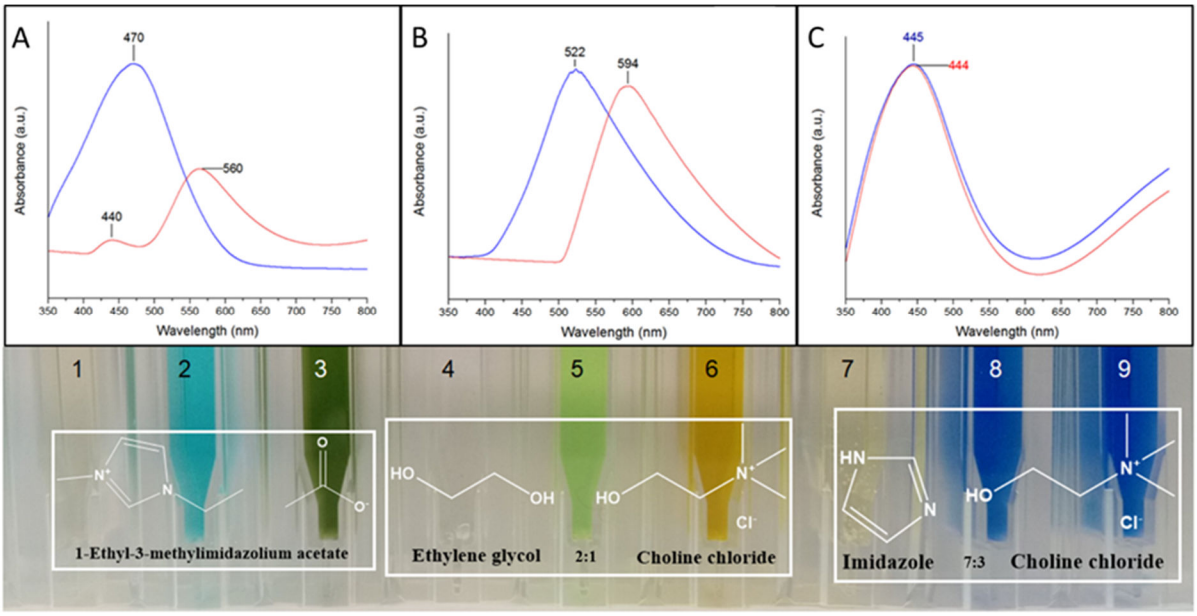

Figure 5.4. Top: Uv-Vis spectra of A) blue line: (emim)OAc /Y, Ba, Cu nitrates before, and red line: after dehydration. B) blue line: EG:ChCl DES/ Y, Ba, Cu nitrates before, and red line: after dehydration. C) blue line: imidazole:ChCl DES / Y, Ba, Cu nitrates before, and red line: after dehydration. Bottom: 1: (emim)OAc, 2: (emim)OAc / Y, Ba, Cu nitrates before, and 3: after dehydration, 4: EG/ChCl DES, 5: EG/ChCl DES/ Y, Ba, Cu nitrates before, and 6: after dehydration, 7: imidazole:ChCl DES, 8: imidazole:ChCl DES / Y, Ba, Cu nitrates before, and 9: after dehydration. dehydration.

A general aspect observed is that with the mix of metal nitrates, namely yttrium nitrate, barium nitrate and copper nitrate, and the ionic liquid/deep eutectic solvent systems, apart from a shift of λ_{max} to different wavelengths, there is a reduction of the transmitted beam. This indicates that the solution is not transparent (Figure 5.5 A) and therefore must be a colloidal solution of metal nanoparticles with a stabilizing anion layer around it and the cation acting as a surfactant (Figure 5.5 B). Therefore, the ionic liquid/deep eutectic solvent does not form a homogenous multicationic solution but rather a heterogenous nanoparticulate solution.

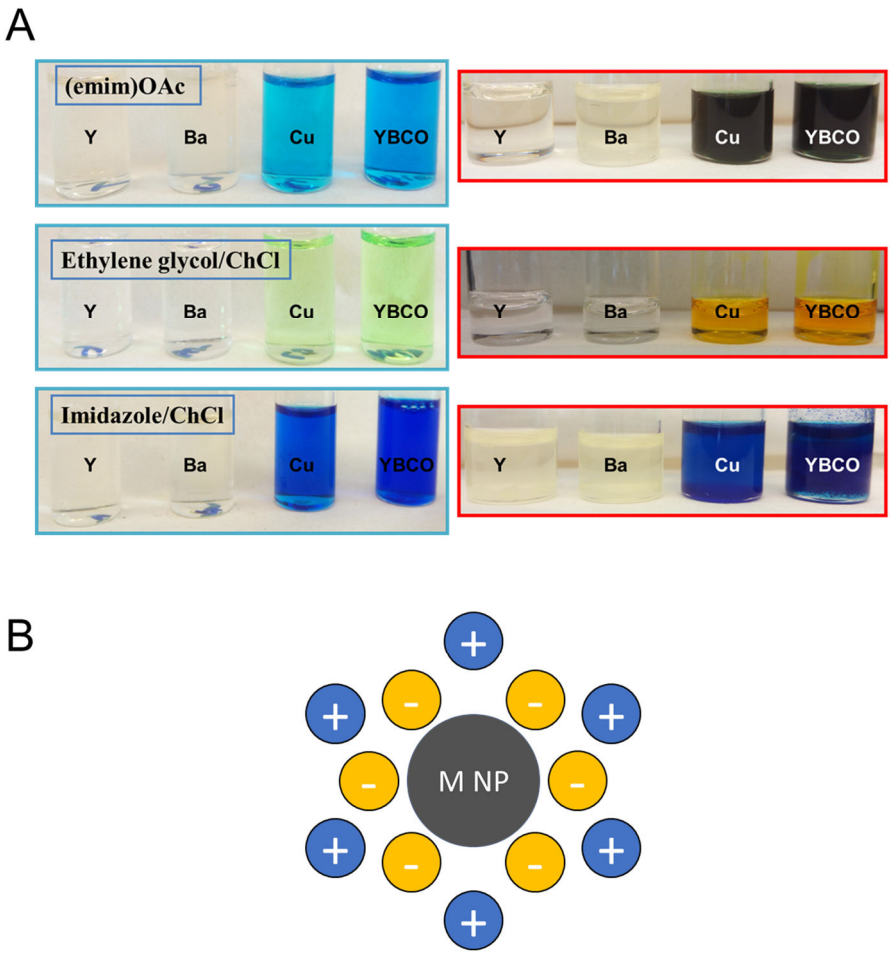

Figure 5.5. A) Photograph of the metal nitrates in the different solvents before (blue) and after (red) dehydration, showing cloudy solutions and in some cases a precipitate. B) Schematic representation of a metal nanoparticle being stabilized by the IL/DES.

5.2.1.3 Temperature Analysis via pXRD

To clarify the crystal growth of the different reaction medias used, namely IL/DES and the mono-molecular chelating agents, temperature analysis was carried out from 320 °C to 920 °C in increments of 100 °C. Also, a graphical representation obtained via Rietvield analysis is present with a schematic representation of the path followed by each corresponding chelating compound is used.

5.2.1.3.1 (emim)OAc

The overall crystallization process (Figure 5.6 A-C) can be described in three different periods. At early stages (Figure 5.6 B I) of the calcination process, from 320 °C to 520 °C, most of the diffraction patterns have extremely broad peaks and a low signal to noise ratio (Figure 5.6 A), implying that most of the material is amorphous. Rietvield analysis shows from those diffractions that can be identified belong to barium carbonate ($Ba(CO_3)$) representing 44.8% at 320 °C, 56.3 % at 420°C and 46.5 % at 520 °C, and copper oxides, being copper dioxide (CuO_2) with 44.4 %, 4.5 % and 5 % at 320 °C, 420 °C and 520 °C, and copper oxide (CuO) covering 5.5 %, 37.7 % and 42.2 % at 320 °C, 420 °C and 520 °C respectively.

The second period, from 520 °C to 720 °C, barium carbonate and cooper oxide will remain as the most predominant phases (Figure 5.6 B II) however, both crystal compositions will suffer from this point onwards a constant drop in percentage with copper oxide representing. 34 %, 22.2 %, 16.2 %, 5.8 % and 3.1% at 620 °C, 720 °C, 800 °C, 820 °C and 920 °C, and barium carbonate demonstrating a similar behaviour but with a more pronounced drop from 51.1% at 720 °C to 26.4 % at 800 °C, to end up undetectable at 820 °C. Furthermore, at the beginning of the second period, yttrium will be present in the form of yttrium oxide (Y_2O_3) with 6.3 % at 620 °C and it will decay immediately to less than 2% at 720 °C, reacting to give way to the formation of yttrium copper oxide $Y_2Cu_2O_5$ at the end of this period, going from 3.4 % to 16.4 % at 620 °C, and 720 °C respectively.

From this point onward the last and third period takes place (Figure 5.6 B III). At this point all the precursory phases are present, namely yttrium copper oxide, barium carbonate, and copper oxide. This period is significantly important as YBCO superconductor is firstly seen at 720 °C and it will see a constant growth, namely 18.1 % at 720 °C, 44.4 % at 800 °C and surprisingly at 820 °C already 94 %, at the expense of the depletion of the precursory phases. At the end of the calcination process 96.8 % will be YBCO and just a small percentage, 3.1 %, of copper oxide.

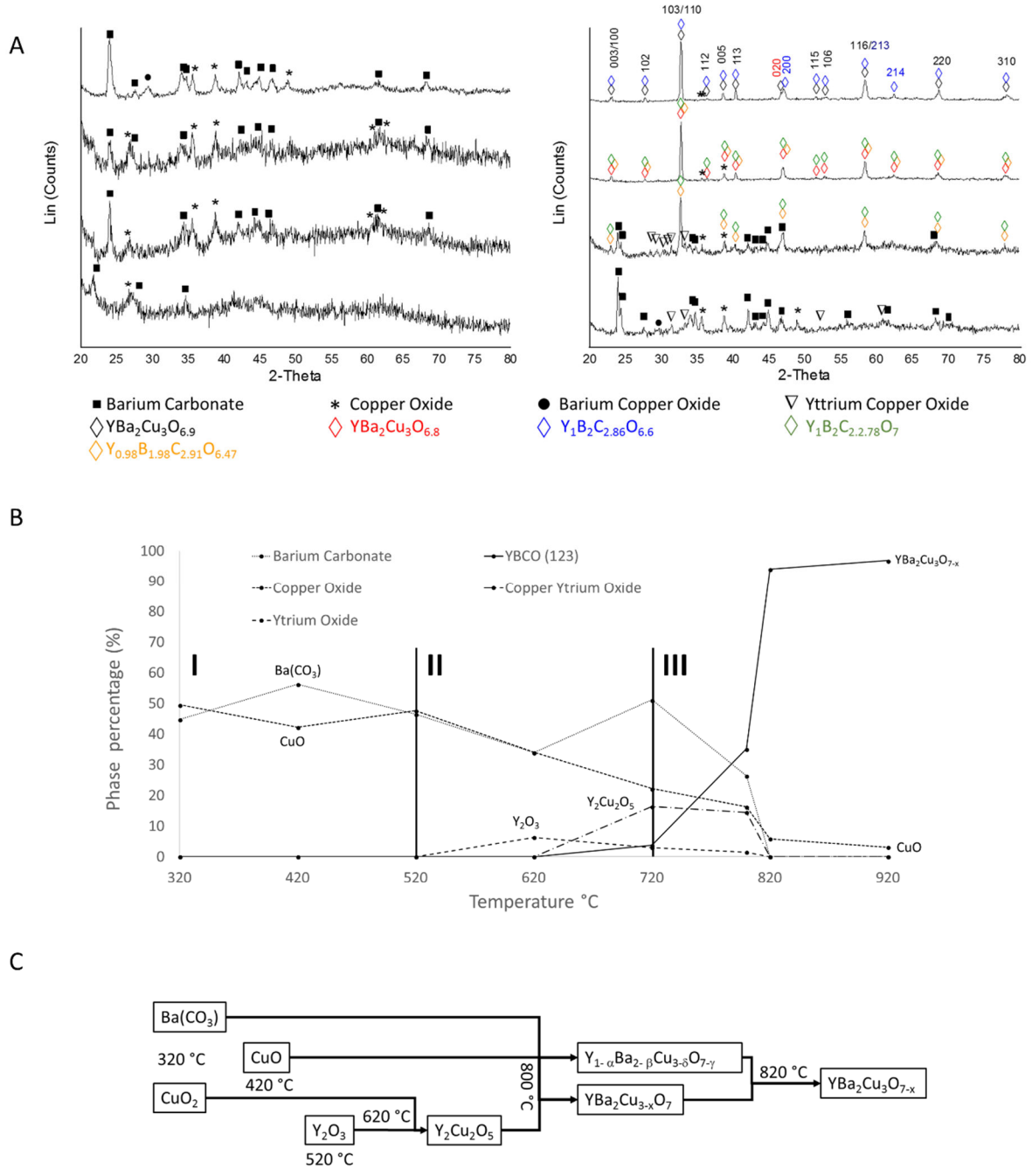

Figure 5.6. A) Temperature analysis via powder X-ray diffraction patterns, B) graphical representation via qualitative analysis of pXRD patterns, and C) diagram of crystal growth. of the synthesis of YBCO using (emim)OAc/dextran as chelating agents.

5.2.1.3.2 Ethylene glycol: choline chloride DES & imidazole: choline chloride DES

In both DESs the first and clear difference that can be observed is due to the insertion of chlorine to the reaction (Figure 5.7 A & B I), resulting in the presence of barium chloride ($BaCl_2$) at 320 °C,

which represents over 55 % of the total percentage. The involvement of chlorine in the reaction will also produce the clathrate-type copper oxide (Cu_6O_8YCl) at 420 °C covering 16.5 %, 23.5 %, and 12.9 % from 420 °C to 620 °C (Figure 5.7 A & B I). At 720 °C in the case of EG/ChCl DES, and 22.1 % of the sample at 420 °C for imidazole/ChCl DES, but this time it will decay to almost zero over the following 100 °C.

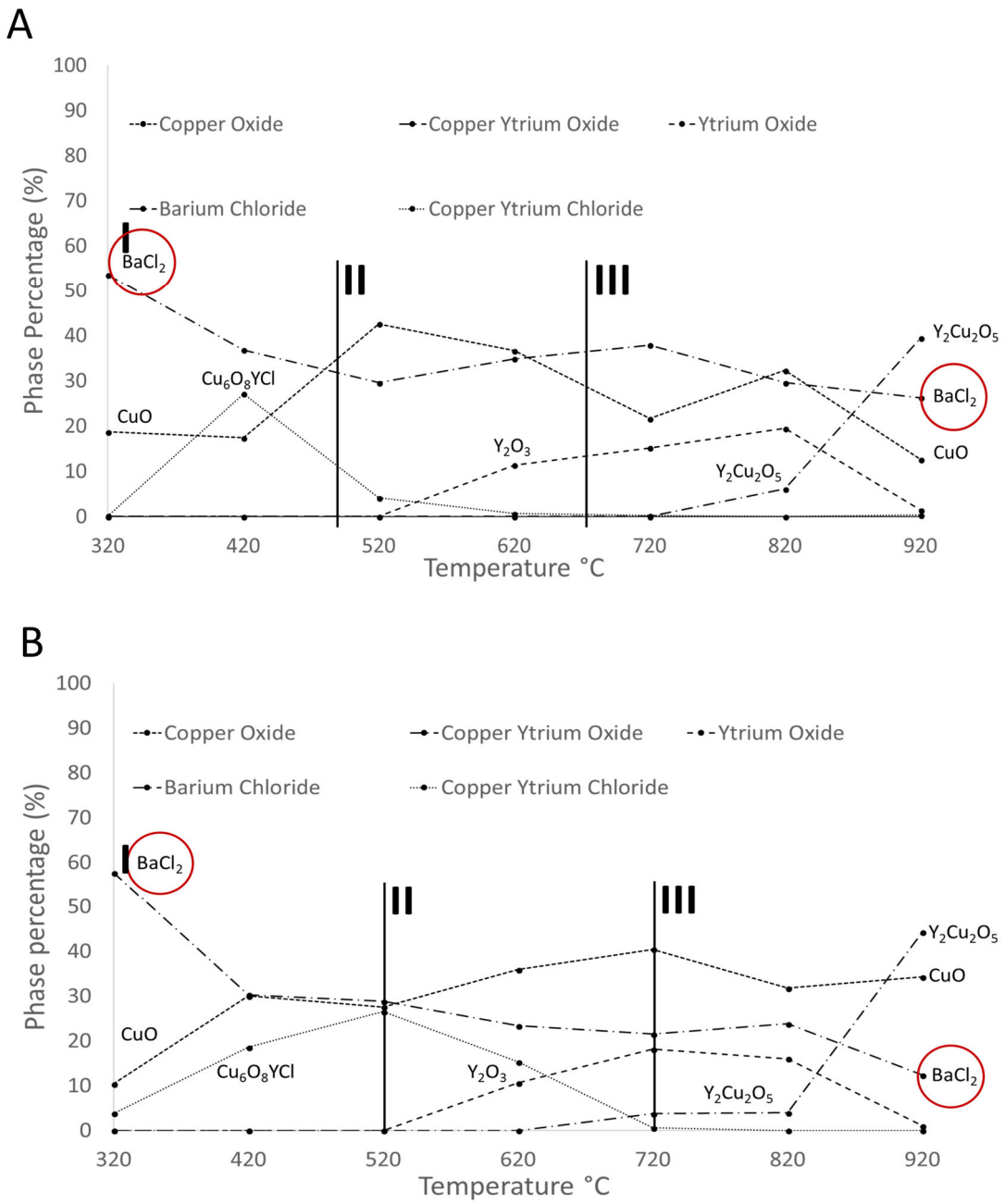

Figure 5.7. A) Graphical representation via qualitative analysis of pXRD patterns from the temperature analysis of the synthesis of YBCO using EG:ChCl DES/dextran as chelating agents. B) Graphical representation via qualitative analysis of pXRD patterns from the temperature analysis of the synthesis of YBCO using imidazole: ChCl DES/dextran as chelating agents.

In both scenarios the consumption of the clathrate-type copper oxide will give arise to the formation of yttrium oxide which will see a constant growth in percentage from 1.2 % at 320 °C to 18.1 % at 720 °C and 16 % at 820 °C, still, a massive drop is observed at 920 °C leaving it with only 1 % of the whole for EG/ChCl DES. Analogue results are faced with imidazole/ChCl DES where yttrium oxide represents 11.3 %, 15.1 %, 19.4 %, and 1.4 % from 620-920 °C (Figure 5.7 A & B II-III).

This drop coincides with the growth of copper yttrium oxide which will go from 3.9 % at 820 °C to 44.2 % at 920 °C for EG/ChCl DES, and 6 % at 820 °C to 39.4 % at 920 °C for imidazole/ChCl DES (Figure 5.7 A & B III). At the end of the reaction process two of the precursory phases are present however, the fact that barium chloride will not decompose compromises the formation of the superconductor in both DES. The schematic representation of the crystal growth can be seen in Figure 5.8. The crystal growth analysed via powder diffraction patterns can be seen in the appendix section (A6 & A7).

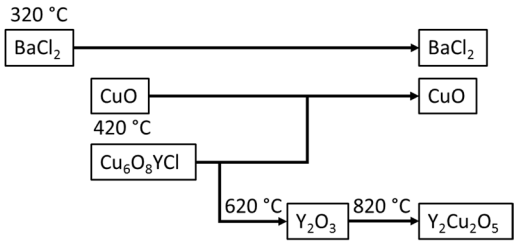

Figure 5.8. Diagram of crystal growth of the synthesis of YBCO using ethylene glycol: choline chloride DES/dextran and imidazole: choline chloride DES/dextran as chelating agents.

5.2.1.3.3 Imidazole/dextran & ethylene glycol/dextran

To clarify the chelating properties that each component provides to the reaction and the outcome of the synthetic process, subsequent experiments using imidazole and ethylene glycol with dextran, in the absence of choline chloride, were carried out. To ensure the same experimental conditions, volumes generated by each DES were measured and the molar concentration per ml of each molecule calculated, resulting in 7.12 M for imidazole and 8.29 M for ethylene glycol. The main difference observed in the temperature analysis, when compared with what was observed with (emim)OAc, comes at the beginning of the calcination process (Figure 5.9 A & B I) where, barium nitrate ($Ba(NO_3)_2$), with more than 50 % of

the overall, can be observed. This phase will steadily react with carbonized material forming barium carbonate, this is seen from the drop of percentage of 23.6 % to 9.7 % from 420-520 °C for imidazole, and 17.3 % to 6.7 % from the same range of temperature for ethylene glycol, finally reacting completely at 620 °C. The fact that barium is contained in another crystal specie will inhibit the early formation of barium carbonate at 320 °C, where only 3.5 % belongs to it when imidazole is used, and 4.7 % with ethylene glycol, causing an overall delay in the reaction process.

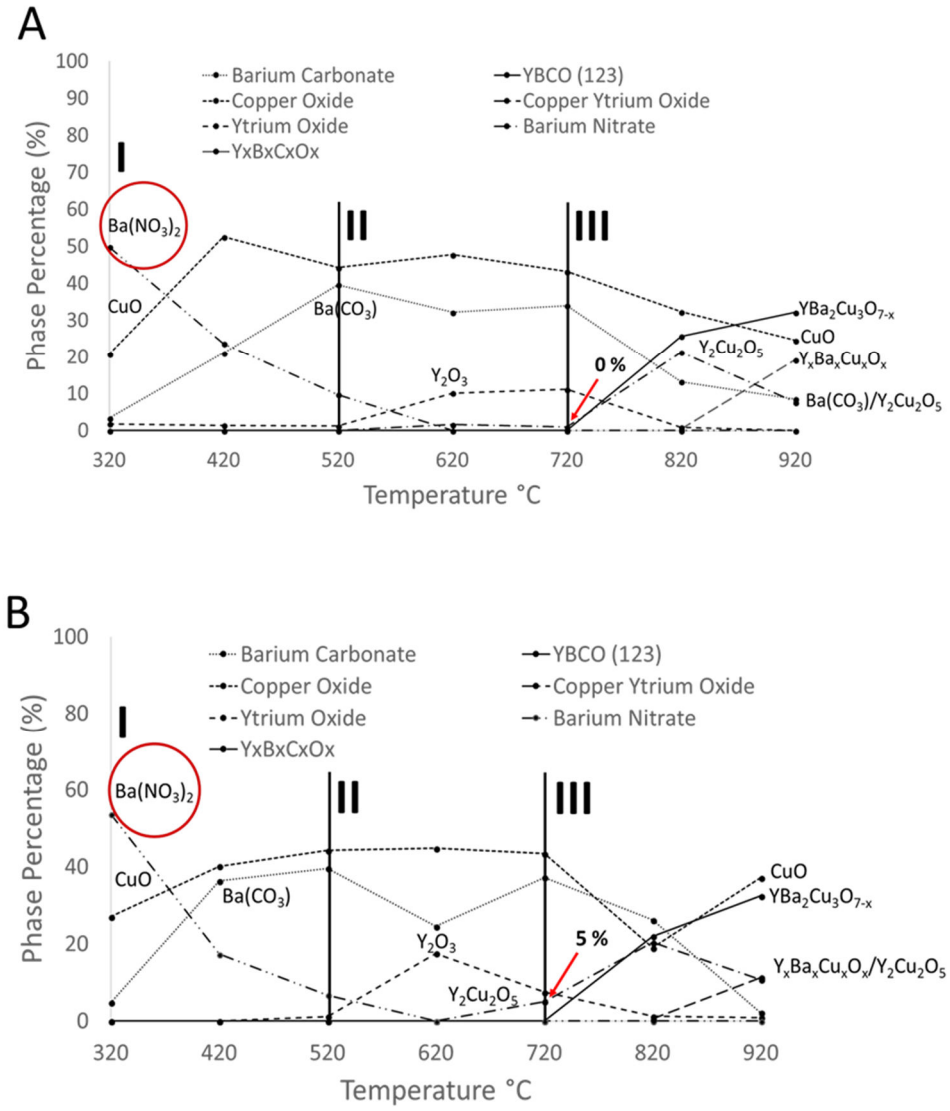

Figure 5.9. A) Graphical representation via qualitative analysis of pXRD patterns from the temperature analysis of the synthesis of YBCO using ethylene glycol /dextran as chelating agents. B) Graphical representation via qualitative analysis of pXRD patterns from the temperature analysis of the synthesis of YBCO using imidazole/dextran as chelating agents.

This delay heavily impacts in the formation of yttrium oxide and yttrium copper oxide. Yttrium oxide will be seen in the second period of the calcination process (Figure 5.9 A & B II), and it will react, decaying in percentage from 17.5 % to 7.4 % from 620-720 °C for ethylene, but it will stay steady in the case of imidazole with 10.1 % and 11.1 %. This differs significantly when (emim)OAc is used where yttrium oxide possesses 6.3 %, and barely 2.9 %, at 620 °C, and 720 °C respectively. Not only the percentage is lower but also the crystal phase appears 100 °C lower with respect of imidazole and ethylene glycol reactions. Consequently, yttrium copper oxide (Figure 5.9 A & C III) will cover only 5 % and 0 % with ethylene glycol and imidazole respectively. In comparison, when (emim)OAc was used, it is observed that yttrium cooper oxide will start to grow from 3.4 % to 16.4 % at 620 °C, and 720 °C respectively. This delay in growth/reaction times compromises the success of the outcome. Consequently, in addition to YBCO superconductor, varied versions of such crystal composition will be found. Crystals were identified as $BaY_{0.25}C_{u0.75}O_{2.25}$, $Ba_3Y_{0.5}Cu_{1.5}O_{5.5}$ and Y_2BaCuO_5, when imidazole/dextran was used and Y_2BaCuO_5 when the reaction was carried out using ethylene glycol/dextran as chelating agents. The schematic representation of the crystal growth can be found in Figure 5.10. The crystal growth analysed via powder diffraction patterns can be seen in the appendix section (A8 & A9).

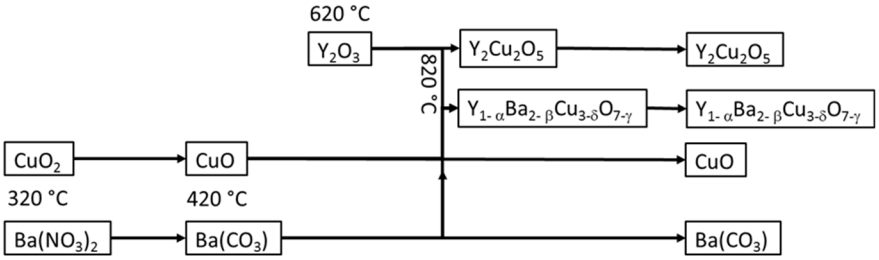

Figure 5.10. Diagram of crystal growth of the synthesis of YBCO using ethylene glycol/dextran and imidazole/dextran as chelating agents.

5.2.1.4 Structural Characterization

5.2.1.4.1 SEM and TEM

The sample prepared with (emim)OAc exhibited a plate-like morphology formed by agglomerated crystallites that fluctuated in sizes. (Figure 5.11 A). The smallest crystallite had an area calculated to be 1,655 μm^2 and the largest, 58,006 μm^2. Particles measured, and distribution size table can be seen in Figure 5.11 C. In terms of nanostructure, (emim)OAc shows some plate-like particles with dimensions of 250 nm in length and an average area of 141,333 nm^2 (Figure 5.11 B). This result is consistent with what has been observed before when this ionic liquid and dextran in low concentrations were used.[40]

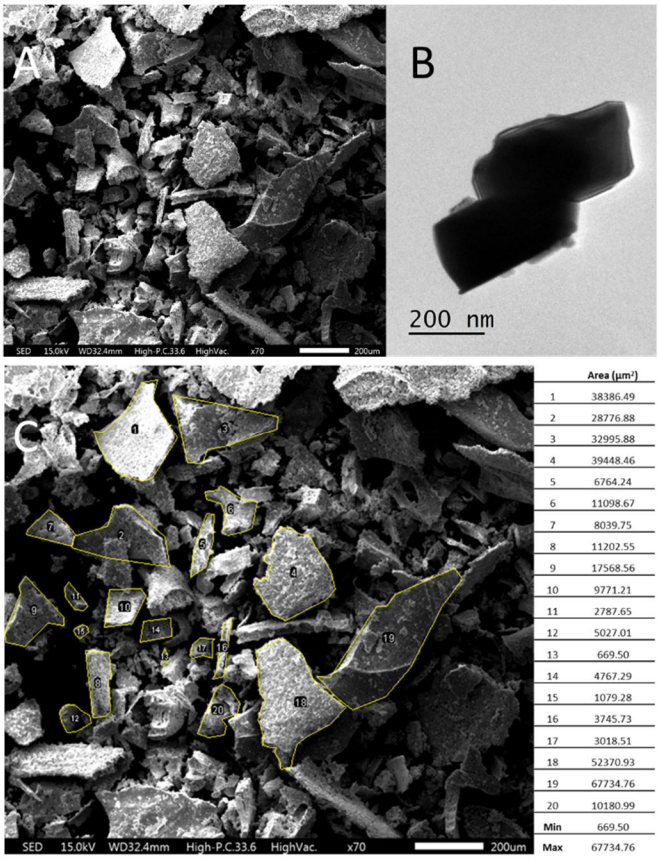

Figure 5.11. A) Scanning electron microscopy. B) Scanning Electron Microscopy image of the superconductive YBCO sample. Highlighted the crystals chosen to be measured (Left). Table of their relative surfaces areas (Right). Transmission electron microscopy All the data shown in this figure was produced using (emim)OAc /dextran as chelating agents.

5.2.1.4.2 Squid magnetometry

A superconducting quantum interference device was used as means to characterize the superconductive sample obtained during the series of experiments described above. Measuring the magnetic susceptibility against temperature one can determine the critical temperature at which the sample starts to exhibit a superconducting state. The sample prepared via (emim)OAc ionic liquid supported with dextran displayed T_c onset = 93.9 K (Figure 5.12) which is consistent to what has been previously reported.[41]

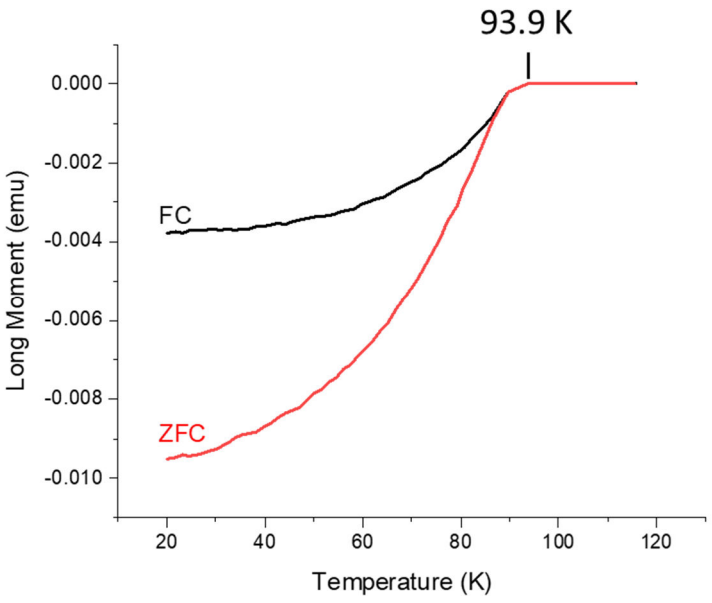

Figure 5.12. SQUID characterization of YBCO superconductive crystal phase produced using (emim)OAc /dextran as chelating agents.

5.2.1.4.3 pXRD

The pXRD pattern of YBCO (97 %) can be seen in Figure 5.13. All peaks could be indexed to YBCO. Diffraction patterns were analysed using the Inorganic Crystal Structure Database (ICSD) reference numbers for phase identification (Chapter 2 table 2.2).

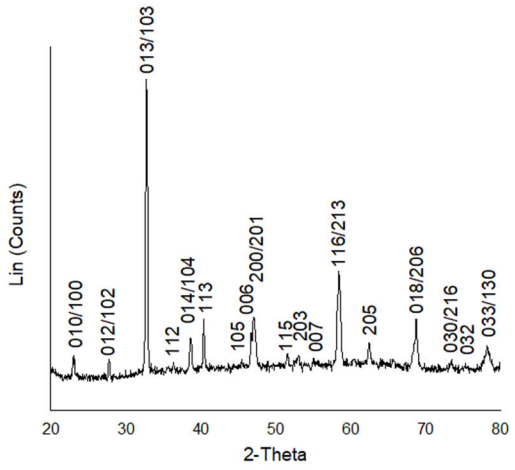

Figure 5.13. Powder X-ray diffraction pattern of YBCO superconductive crystal phase produced using (emim)OAc /dextran as chelating agents.

5.2.2 First conclusions

In order to elucidate the mechanism of reactions of the ionic liquids and to be able to explain why some produce greater product purity in the synthesis of metal oxides, different scenarios were studied. Under such conditions there were a few points that need to be taken in account that shown to be key factors on the pursuance of producing single-phase metal oxides.

First, it was proven that the IL/DES produces, in interaction with the metal cations, metal nanoparticles which, are stabilized by the anion layer around it and the cation acting as a surfactant. This is relevant as it constrains the system to the nanoscale, increasing the active surface area therefore, the reactivity of the system.

Second, extra components such as chlorine will take part in the reaction and produce metal chloride associate phases. These phases when stable along the whole temperature setup, such as the case of $BaCl_2$, will not decompose disabling the formation of YBCO superconductor. It has been proved however that

chlorinated phases could be also use for the synthesis of metal oxides provided the temperature of calcination is high enough to allow for recombination.[42]

Third, it is very important to identify, for every system, the precursory phases needed to form the target crystal phase. In this case copper oxide, yttrium copper oxide and barium carbonate were clearly identified as the precursor phases, consequently, allowing the formation of such phases at earlier stages will speed up the synthesis of the target phase. In this work we shown that YBCO phase appeared at a temperature 100 °C lower than the usual synthetic temperature of YBCO (920 °C),[7] even as low as 800 °C when (emim)OAc was used as a chelating agent.

Lastly, to promote environmental homogeneity and to strive for similar conditions in each synthesis, dextran was used as a non-specific, polychelating agent. It can be noted that even this addition did not produce the early formation of barium carbonate, the main crystal phase that differs between (emim)OAc and the rest, where barium carbonate is observed the formation at the early stages (320 °C) of calcination, whereas barium chloride is present in synthesis with ethylene glycol:ChCl DES/dextran and imidazole:ChCl DES/dextran, and barium nitrate when imidazole/dextran and ethylene glycol/dextran were employed. The carbonyl group of the acetate therefore is responsible of enabling the synthesis of barium carbonate at 320 °C, this will also restrict and prevent the synthesis of unwanted associate phases that will compromise the formation of the target crystal phase. Similar behaviour has been already observed before in an analogous system.[43]

5.3 Synthesis of the superconductor BSCCO (Bi-2212), using a deep eutectic solvent.

As the information suggested, the carbonyl group in interaction with the metal cations at the beginning of the whole synthetic process was leading, during the calcination process, towards the formation of carbonate phases. The fact that carbonate phases can decompose releasing $CO_{2(g)}$ allows a faster re-integration of metal ions to the synthetic process facilitating recombination and thus forming the desired crystal composition, whereas crystal phases without $(CO_3)^{2-}$ will undergo to solid state reactions until the final composition is acquire. Following this principle and to lower the overall expenses of the synthetic process, namely substituting (emim)OAc, research was done to encounter with a molecule with similar characteristics, i.e. containing a carbonyl group. A candidate proposed was a DES made by mixing betaine (chemical formula $(CH_3)_3N^+CH_2COO^-$) and D-(+)-glucose in 5:2 molar ratio.

The proposed DES was employed for the synthesis of $Bi_2Sr_2CaCu_2O_{8+x}$ (BSCCO or Bi-2212), another high-temperature superconductor. Previous work done to synthesise this crystal composition required prior preparation to integrate barium nitrate, an insoluble salt, into a solution. To achieve that ethylenediaminetetraacetic acid (EDTA) and ammonium hydroxide were used. Furthermore, instead of 1-ethyl-3-methylimidazolium acetate, 1-ethyl-3-methylimidazolium nitrate was utilized,[7] which is extremely expensive, 1 g cost £32.90 (Sigma Aldrich product 04363-1G). In contrast, via the use of betaine it was possible to solubilized bismuth nitrate in water, therefore avoiding previous steps. Further ahead the overall synthetic procedure was investigated in detail.

5.3.1 Results and discussion

5.3.1.1 Infrared spectroscopy

By FTIR it is possible to track first interactions between the chelating agent and the metal cation. The FTIR study was done by comparing the interaction of the DES itself and with all the metal cations (M-DES) before and after dehydration (Figure 5.14). Betaine is composed by carbonyl group on one side and tri-substitute amine on the second part. Tertiary amines exhibit no bands in the FTIR therefore the focus relies on the range of wavelengths from 3300-2500 cm^{-1} belonging to the O-H stretching, 1630 cm^{-1} to the C=O stretching, 1325 cm^{-1} and 885 cm^{-1} to the O-H in plane bend (Figure 5.14 *)[31]. Most of the bands remain in the same wavelength with the only one exception by the band found in the rage from 2958 cm^{-1} to 2970 cm^{-1}. When the hydrated metal nitrates are introduced in the DES the band is barely seen in the wavelength 2982 cm^{-1}, however, in comparison it is not visible for the DES itself. Furthermore, when the M-DES is dehydrated the band is clearly visible at wavelengths 2981cm^{-1} and 2971cm^{-1} The fact that all the other remaining bands corresponding to the carboxyl group are not shifted towards any directions implies that the band seen in the range of 2958 cm^{-1} to 2970 cm^{-1} belongs to the nitrate group of the metal cations [44,45] rather than the carboxyl group of the betaine. Overall, in contrast with what was observed previously when (emim)OAc was used, there is complex formation between the molecule betaine and the metal cations via electrostatic interactions forming a weak coordination sphere rather than the production of nanoparticles with stronger binding bonds which, would explain the lack of a shift in any band of the carboxyl group of the betaine molecule or the appearance of a new band due to the complex formation. Moreover, these purely electrostatic interactions can be observed by changes in the width of the infrared bands due to the number of chemical environments (Figure 5.14 A).

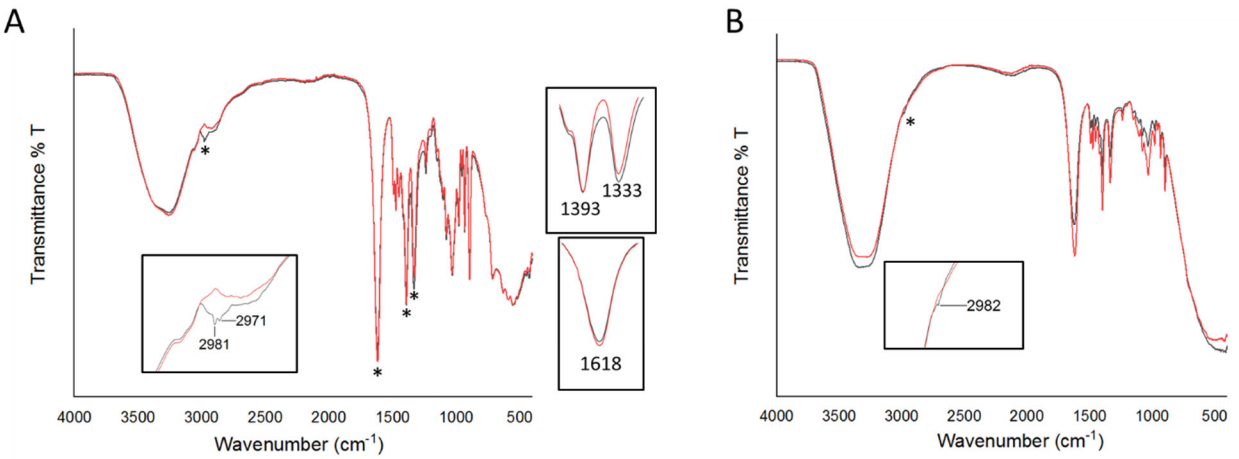

Figure 5.14. Fourier transformation infrared spectra of A) black: DES with Bi, Sr, Ca, and Cu nitrates, and red: just DES, both, black & red, dehydrated. B) Fourier transformation infrared spectra of black: DES with Bi, Sr, Ca, and Cu nitrates, and red: just DES, both, black & red, hydrated. Inset represent zoom areas of the respective bands marked with *.

5.3.1.2 Temperature analysis

Preliminary studies as control reactions were made to understand the role played by every component that forms part of the synthesis, namely glucose, betaine, and finally the DES. With the use of pXRD (Figure 5.15) it was established that just the mixture of betaine and glucose (Figure 5.15 C), will provide high yields of BSCCO superconductor. Nonetheless, using only betaine (Figure 5.15 B) as a mono-molecular chelating agent could produce, based on Rietveld refinement, 82.9 % of the superconductive phase, whereas the reaction carried out with D-(+)-glucose (Figure 5.15 A) gave only 22.5 %.

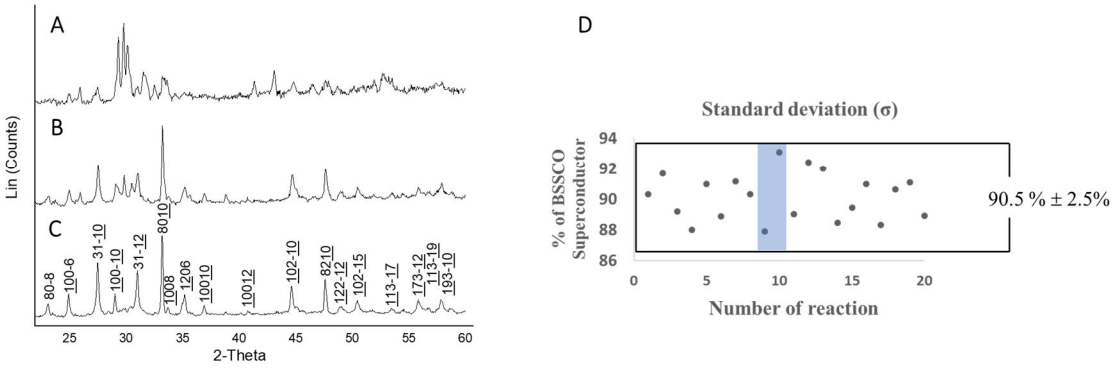

Figure 5.15. Powder X-ray diffraction pattern of the synthesis of Bi-2212 using A) glucose, B) betaine, C) betaine: D-(+)-glucose (5:2) DES as chelating agents, and D) Standard deviation of the synthesis of BSCCO superconductor via DES.

DESs stability has been subject of study,[46] therefore the analysis of the reaction over a period of time, for 21 days every 3 days (Figure 5.16), was performed. The reaction performed immediately after producing the DES gave 93 % of the desired crystal phase (Figure 5.15 C), this being the optimum result obtained. 20 reactions followed to truly prove the reproducibility of this synthesis, giving an average value of 90.5% ± 5 % of the superconductive phase (Figure 5.15 D). After the third day there was a drop in the percentage of the target Bi-2212 phase to 87.3 % and a further decrease to 81.7 % by the sixth day and all days after that (Figure 5.16). DES are highly interactive systems capable of forming complex structures via hydrogen-bonding networks, [21,47–49] however, continuous interaction between components can also occur, producing a chemical structure change of a component therefore, changing the chelating properties of the DES. In the case of betaine: glucose based on the powder x-ray diffraction patterns, is notorious after 6 days of aging.

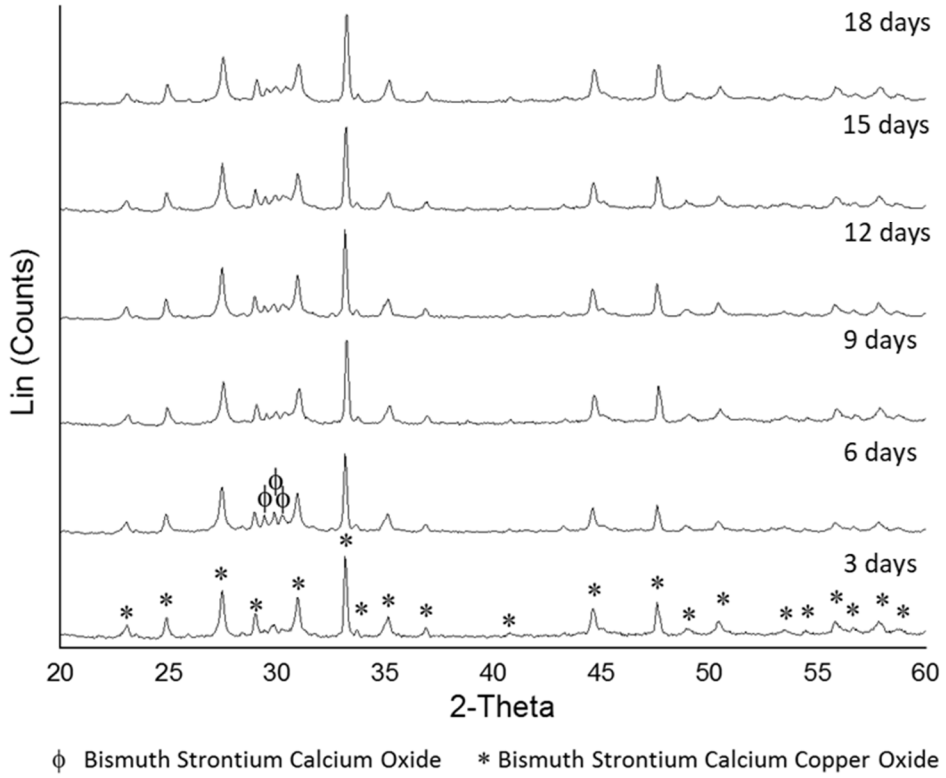

Figure 5.16. Powder X-ray diffraction patterns tracking the formation of undesired crystal phases while attempting the synthesis of Bi-2212 superconductor with betaine: glucose DES.

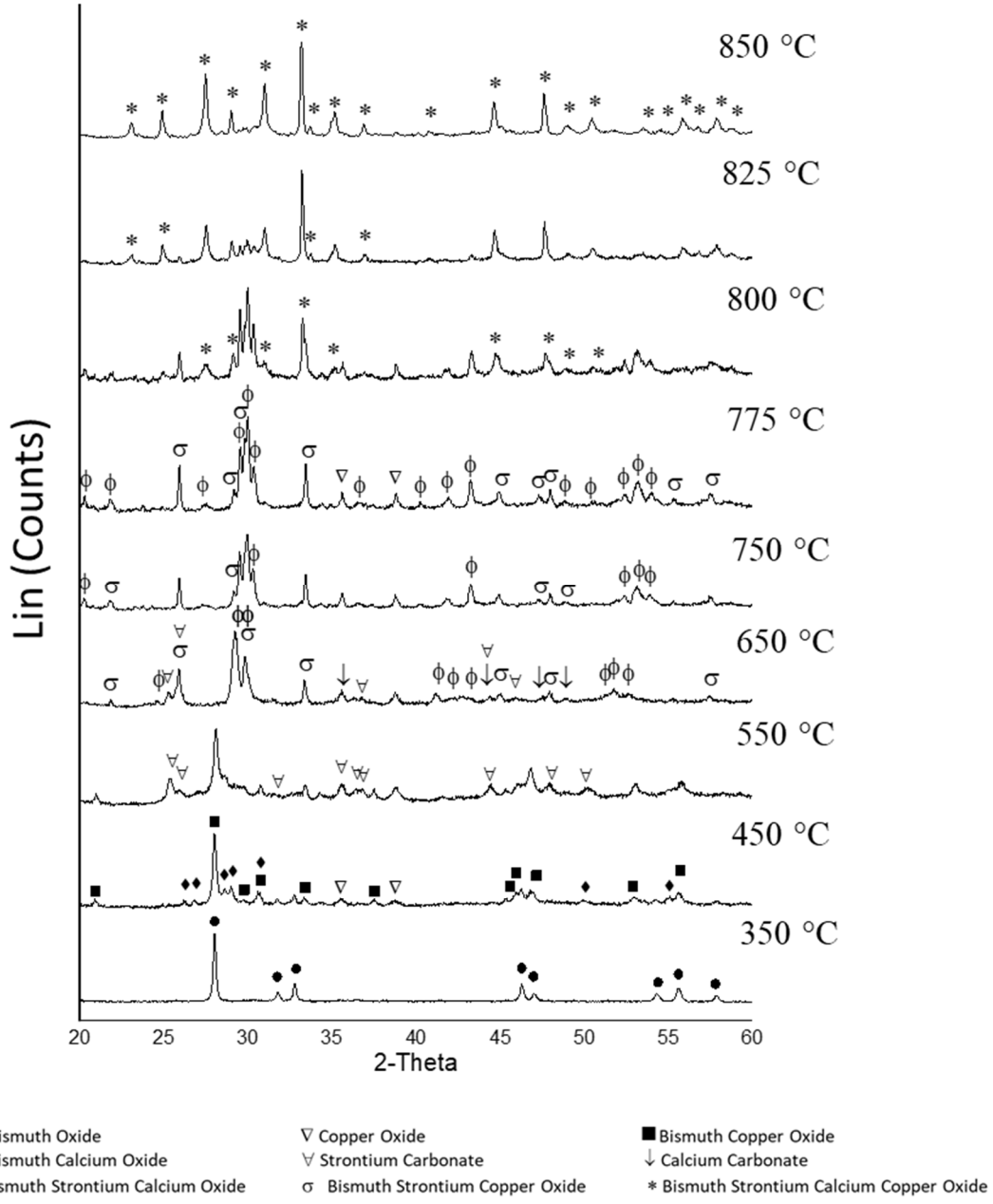

Figure 5.17. Temperature analysis of the crystal growth via powder X-ray diffraction patterns of the synthesis of Bi-2212 using freshly made betaine: glucose DES.

To elucidate what was happening during the synthetic process, temperature analyses via pXRD (Figure 5.17 & Appendix figure X) were executed. The crystal growth can be described in five different stages. The first part of the reaction (Figure 5.18 gray) shown singular metal oxides, mainly bismuth oxide (Bi_2O_3) and barely appreciated diffractions belonging to copper oxide (CuO). The second period (Figure

5.18 blue) is represented by the appearance of ternary metal oxides, bismuth copper oxide (Bi_2CuO_4) and bismuth calcium oxide ($Bi_{0.80}Ca_{0.20}O_{1.19}$). At this point there is not yet a crystalline phase containing strontium. The third period (Figure 5.18 red) covers the inception of carbonate phases such as strontium carbonate ($Sr(CO_3)$), calcium carbonate ($Ca(CO_3)$) and strontium calcium carbonate ($Sr_{0.50}Ca_{0.50}(CO_3)$). The fourth and last period (Figure 5.18 green) is significantly important as it represents the growth and evolution of the more complex quaternary phases, such as bismuth strontium calcium oxide ($Bi_6Sr_{6.27}Ca_{4.73}O_{22}$) and bismuth strontium copper oxide ($Bi_{1.91}Sr_{1.84}CuO_{5.48}$); the emergence of those crystal phases can be deduced

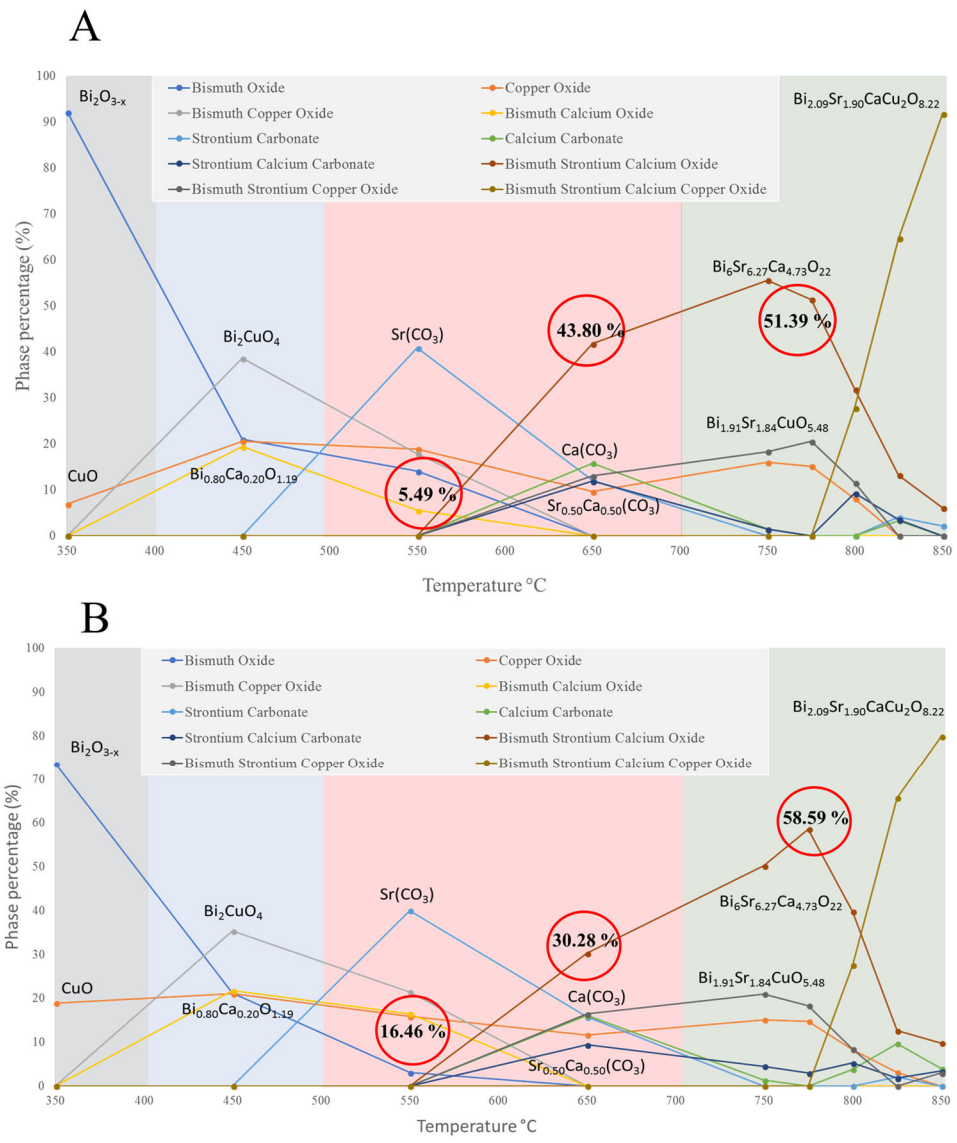

Figure 5.18. A) Graphical representation via qualitative analysis of pXRD patterns from the temperature analysis of the synthesis of Bi-2212 using A) Immediately prepared betaine: glucose DES, and B) betaine: glucose DES aged for 21 days.

as being due to the continuous decomposition of the carbonates and the constant reaction of the ternary crystal phases. In this period is also where the desire superconducting phase is firstly seen, at 775 °C, and ending at 850 °C with the final crystal composition of Bi2212. From this period is clearly defined that the precursory phases needed for the generation of the superconductive phase are bismuth strontium copper oxide, bismuth strontium calcium oxide, and copper oxide.

The crystal growth in both conditions, when the DES was freshly made and after 21 days of aging, appeared similar from pXRD results (Figure 5.18 & appendix Figure A10), however after doing a concise analysis with Rietveld refinement, a main difference can be observed. Highlighted in Figure 5.18, it is noticeable that the when the DES is freshly prepared, bismuth calcium oxide reacts faster than after the solution is left for days, change observable in values changes from 19.3 % at 450 °C to 5.4 % at 550 °C, whereas after the solution is aged, the percentage drops from 21.7 % at 450 °C to 16.4 % at 550°C. This will have a significant impact in the synthesis of Bi-2212 because the precursory quaternary phases are produced from the elements released from the decay of the carbonates and the recombination of ternary crystal phases. This implication is graphically seen for bismuth strontium calcium oxide, where when the DES is freshly prepared, it is present as 43.8 % at 650 °C of the total percentage, and only 30.2 % at the same temperature when the solvent was aged for 21 days; consequently, the crystal phase will start to re-combine 25 °C earlier in the first case. This will eventually result in >90 % of the superconductive phase against 81 % ± 5 % from an aged solution. A diagram representing the crystal growth can be found in Figure 5.19.

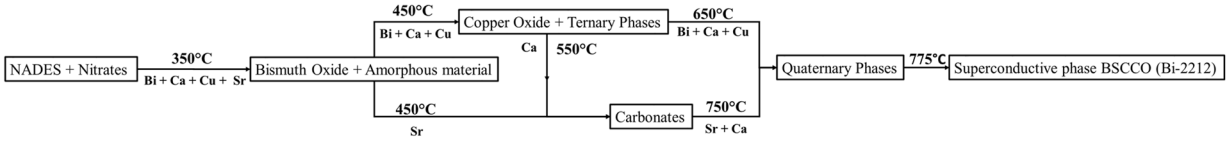

Figure 5.19. Diagram of the crystal growth of the synthesis of Bi-2212 using betaine: glucose DES.

5.3.1.3 Structural characterization

5.3.1.3.1 SEM and TEM

Characterization via TEM and SEM showed that in both cases neither the nano- or macromorphology was controlled in any significant way. The usual Bi-2212 structures that are found in typical control syntheses are present, namely that the material is mainly composed by planar crystallites at the microscale (Figure 5.20 A), albeit the macrostructure resembles a sponge-like morphology made of polycrystalline aggregates. (Figure 5.20 B).

EDX analysis showed a homogenous distribution, throughout all the material, of all the metal cations involved in the reaction (Figure 5.20 B).

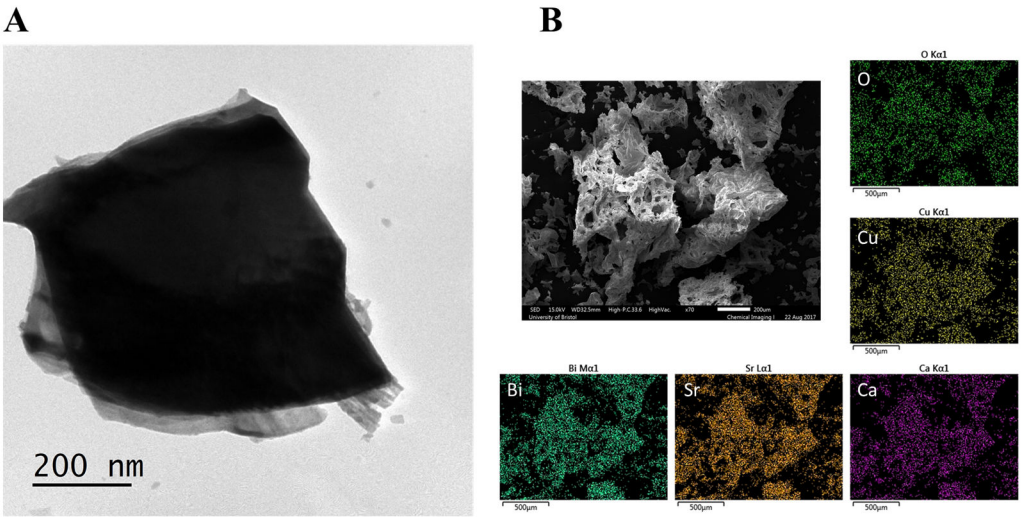

Figure 5.20. A) Transmission electron microscopy of Bi-2212 nanocrystals, and B) scanning electron microscopy of Bi-2212 with the elemental mapping of each respective element of the synthesis of Bi-2212 using freshly prepared betaine: glucose DES. Scale bars A = 200 nm, B = 200 µm, Bi-Sr-Ca-Cu-O = 500 µm.

5.3.1.3.2 Squid magnetometry

SQUID magnetometry (Figure 5.21), measuring the magnetic susceptibility as a function of temperature, showed that the critical temperature at which the sample starts to exhibit a superconducting

state, T_c onset, was 82 K. This compares favourably with the usually reported T_c onset for Bi-2212 as being between 82 K and 90 K.[50,51]

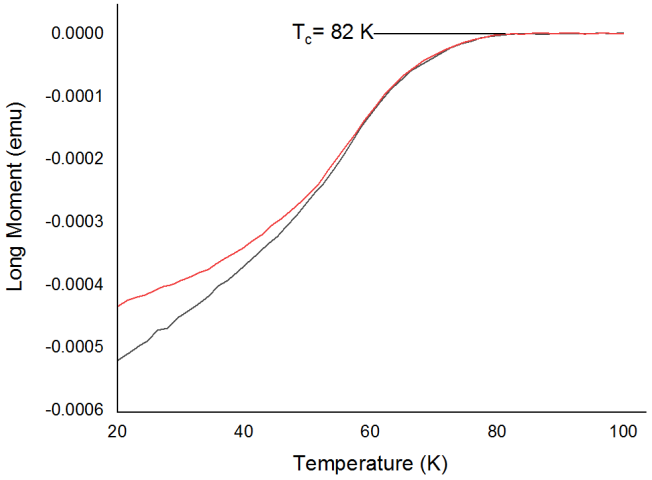

Figure 5.21. SQUID characterization of Bi-2212 synthesized using freshly prepared betaine: glucose DES.

5.3.2 Second conclusions

The use of betaine as a chelating molecule in a deep eutectic solvent allows the dissolution of bismuth nitrate (Figure 5.22), leading to the formation of a uniform multicationic solution in the DES. The evenly distribution allowed after calcination the creation of the superconductor Bi-2212 by a DES for the first time. Via this synthetic protocol it was possible to obtain > 90 % of the superconductive crystal composition. However, it was noted that after 6 days a considerable growth of precursory phases instead of the superconductive crystal.

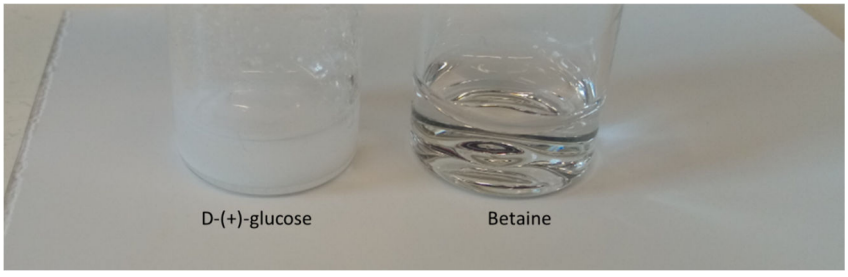

Figure 5.22. Photography showing the dissolution of bismuth nitrate in D-(+)-glucose (left) and betaine (right).

The mixture of the polysaccharide and betaine seems to continuously interact. This phenomenon can be visually observed by pictures taken at different times, namely freshly prepared being a transparent solution, after 2 months with a yellow coloration, and after 6 months turning into a dark yellow (Figure 5.23). Such changes can be related to the oxidation of the polysaccharide over time therefore, changing the chelating properties of the molecule.

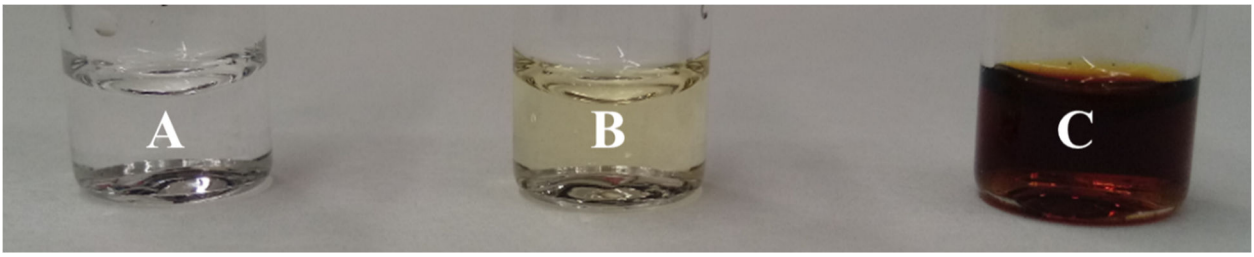

Figure 5.23. Photography of the DES freshly prepared (A), 2 months aged (B), and 6 months aged (C).

Certainly, further investigation is needed to provide more evidence of such process and how is that directly related to the change in the chelating properties of the DES. However, based on this observation should provide valuable guidance to those wishing to use deep eutectic solvents in the synthesis of complex functional materials, in that syntheses should be attempted within the first 48 hours of preparation of the DES to avoid any structural changes of the solvent.

5.4 Synthesis of a new sodium strontium niobate via imidazole: choline chloride DES.

Are carboxyl groups the only reliable synthetic media for the synthesis of metal oxides? The straight answer to that is no. Rebeca et al. were capable to synthesized barium titanate via malonic acid choline chloride DES.[42] As stated above, if the temperature is high enough to provide enough energy for a re-combination of a higher temperature-stable crystals, then chlorinated crystal compositions are not an issue.

To test this, it was decided to compare the crystal growth of sodium strontium niobates via (emim)OAc, and imidazole: choline chloride DES. Knowing that chlorine was going to take part of the reaction, in the case of imidazole: choline chloride DES, the formation of sodium chloride is expected, whereas on the other hand the formation of carbonates should be seen.

5.4.1 Results and discussion

5.4.1.1 Via (emim)OAC

5.4.1.1.1 Temperature Analysis via pXRD

The first attempt was done with the use of the ionic liquid, (emim)OAc, and analysed via powder x-ray diffraction pattern. The synthesis was done mixing 1 ml of the ionic liquid with sodium hydroxide, strontium nitrate, and niobium ethoxide in a final molar ratio of 1:2:3. After dehydration 1 g of dextran was added to form a gel and immediately placed in the furnace with a ramp rate of 1 °C/min, and dwelling time of 6 h at different temperatures.

The crystal growth was studied from 400 °C to 1100 °C (Figure 5.24). At the beginning of the crystal growth there is no appreciable crystal phases. Once 500 °C is reached, as expected, the formation of strontium carbonate is seen. Also, $Na_{0.3}Sr_{0.7}NbO_3$ is present in the powder diffraction pattern with two

more diffraction that could not been identified (highlighted in Figure 5.26 blue), 28.6 ° and 40.9 ° 2-theta. However, when the temperature increases those two diffractions almost disappear at 700 °C and are completely gone by 800 °C, where the powder diffraction pattern is covered by $Na_{0.3}Sr_{0.7}NbO_3$ and $Sr_5Nb_4O_{15}$, indicating that those two diffractions could belong to an unknown crystal composition made of an uncertain mixture of some or all of the participating elements. The strontium niobate will eventually react and by 900 °C and 1000 °C only the sodium strontium niobate is observable. At 1100 °C the strontium niobate appears again in the diffraction pattern, hinting a possible loss of sodium during the calcination process.

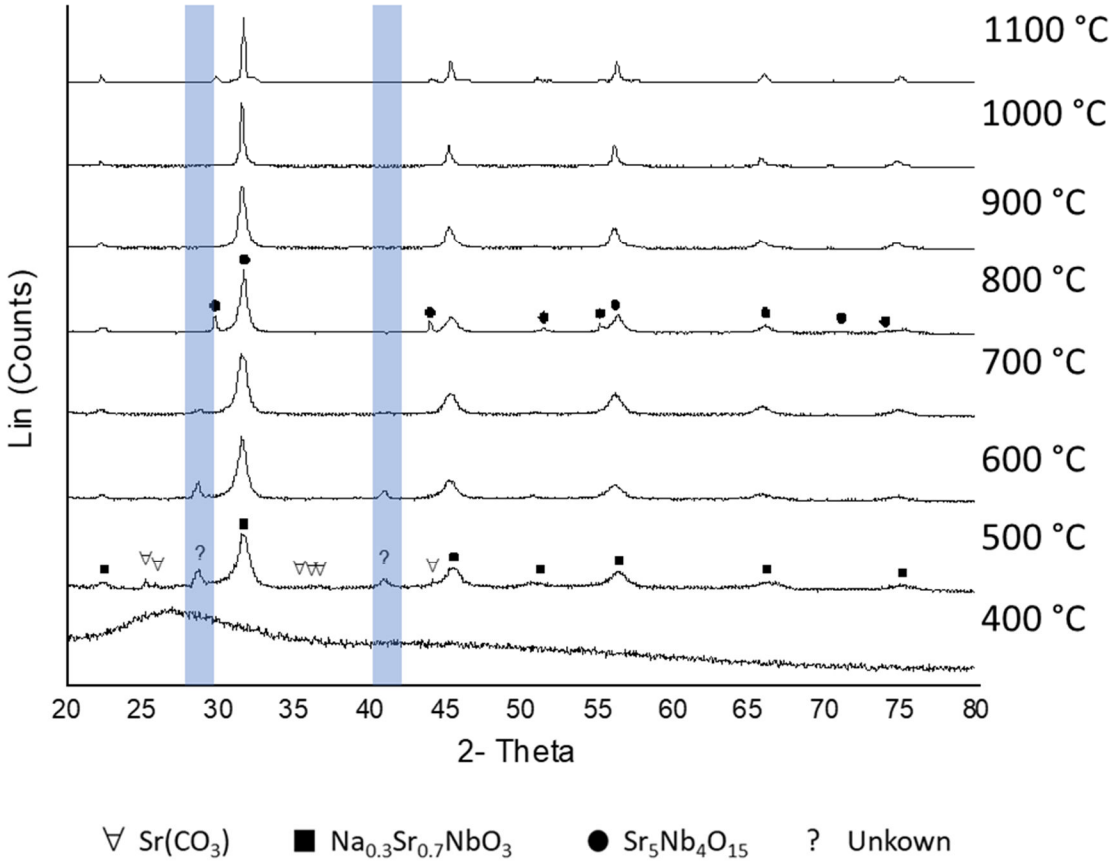

Figure 5.24. Temperature analysis of the crystal growth via powder X-ray diffraction patterns of the synthesis of a sodium strontium niobate using (emim)OAc and dextran as chelating agents.

This phenomenon can be studied by reviewing with more detail the diffraction patterns (Figure 5.25), where at 700 °C the most intense diffraction is located at 31.6 ° 2-theta however, at 800 °C this shifts to 31.6 °, where $Sr_5Nb_4O_{15}$ is also found in the powder diffraction pattern. From the next 200 °C a constant shift to lower angles is noticed, namely 31.5 ° at 900 °C, and 31.5 ° at 1000 °C. The exact position of the diffraction of the $Na_{0.3}Sr_{0.7}NbO_3$, analysed via profex software (ICSD number 51872), is at 31.6 ° and knowing that increasing the sodium concentration a shift to bigger angles is seen, 31.7 ° for $Na_{0.4}Sr_{0.6}NbO_3$ (ICSD number 51871) and 31.8 ° for $Na_{0.5}Sr_{0.5}NbO_3$ (ICSD number 51873), indicates that indeed there is a small loss of sodium during the calcination process. Moreover, at 1100 °C, when $Sr_5Nb_4O_{15}$ is again present, the position of the diffraction peak is found to be at 31.6 ° 2-theta. Therefore, during the calcination process the $Na_{0.3}Sr_{0.7}NbO_3$ is formed but it will steadily loss low amounts of sodium, from 700 °C to 1000 °C, where some portions of the sample will loss entirely sodium concentration re-forming $Sr_5Nb_4O_{15}$ and some other will compensate the sodium loss of the remaining sodium strontium niobate occasioning a shift back to the diffraction corresponding to $Na_{0.3}Sr_{0.7}NbO_3$.

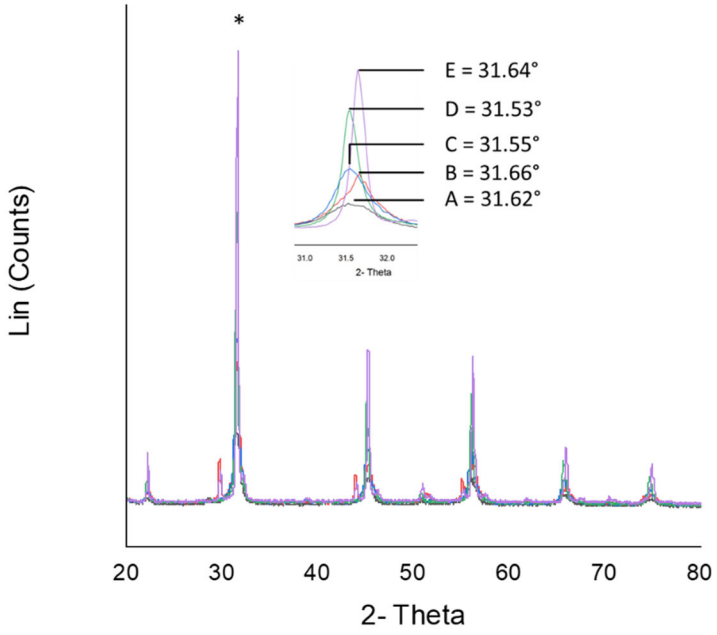

Figure 5.25. Powder X-ray diffractions demonstrating displacement of A) solely to the diffraction of $Na_{0.3}Sr_{0.7}NbO_3$ at 700 °C, B & C) to smaller angles due to slight loss of sodium content from 900 °C to 1000 °C, and B & E) when $Sr_5Nb_4O_{15}$ is present returning to bigger angles at 800 °C and1100 °C.

5.4.1.1.2 SEM EDX analysis

To obtain reliable data on the SEM during EDX analysis pellets were made. Two different temperatures were studied, specifically 900 °C and 1100 °C (Figure 5.26), when $Na_{0.3-x}Sr_{0.7+y}NbO_3$ is present, and the second temperature when it exhibits $Sr_5Nb_4O_{15}$ for a second time in the powder diffraction pattern. Differences in sodium content were not significant, 4.7 wt. % and 4.6 wt. % (appendix Figure A6), however, via elemental mapping (Figure 5.26 A) it was possible to visualize how the sample is not homogenous which, goes in agreement with what has been observed via powder diffraction pattern. On the other hand, an even elemental distribution, homogenous sample, is seen at 900 °C (Figure 5.26 B).

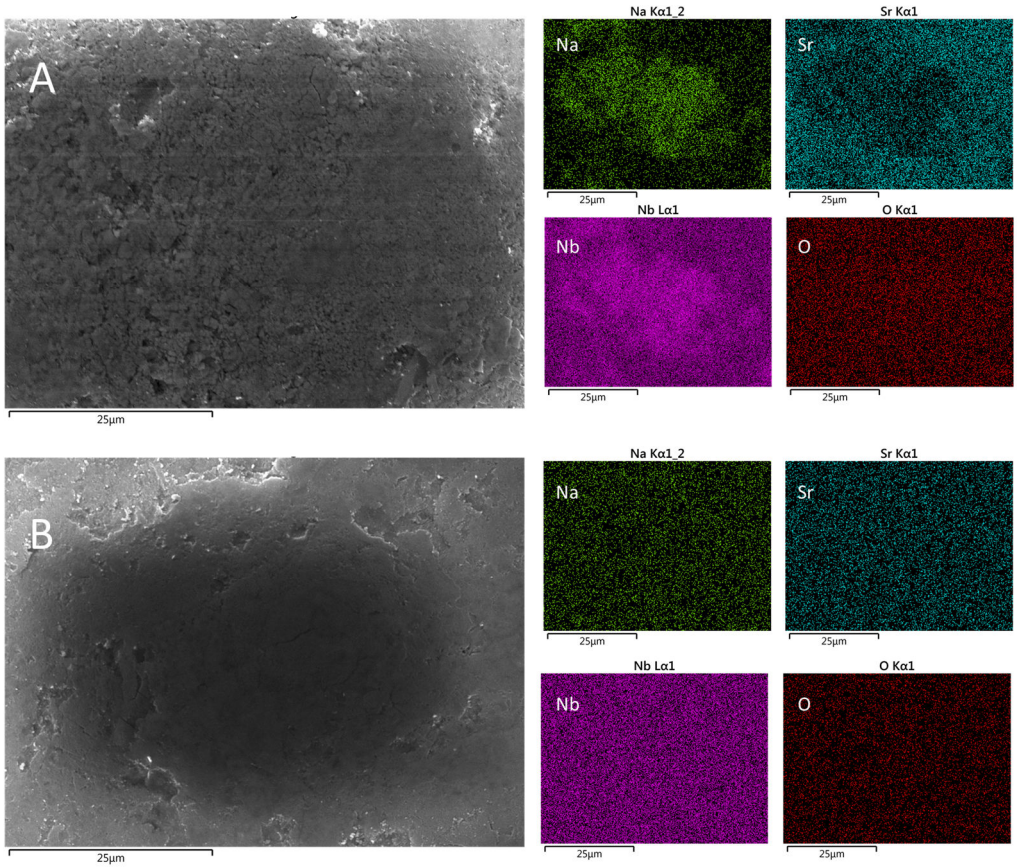

Figure 5.26. A) Scanning electron microscopy image with the elemental mapping of each respective element involved in the synthesis of a sodium strontium niobate via (emim)OAc/dextran at A)1100 °C and B) 900 °C.

5.4.1.2 Via imidazole: choline chloride DES.

5.4.1.2.1 Temperature Analysis via pXRD

The synthetic protocol is analogous to the synthesis via (emim)OAc. From powder diffraction patterns at different temperatures (Figure 5.27), clear differences are seen from the beginning. At 500 °C there are still no indexable diffractions in the pattern, meaning that amorphous mass with all the elements contained is formed, 100 °C higher than (emim)OAc where at that temperature some crystal compositions were already observed. At 600 °C broad diffractions which can be indexed by $Na_{0.3}Sr_{0.7}NbO_3$ and NaCl are seen. Moreover, 100 °C latter the strontium niobate, $Sr_5Nb_4O_{15}$, is again spotted but in higher intensities as the observed by the synthesis using (emim)OAc. As expected, the formation of a chlorinated crystal composition is formed which stands higher temperature, this is notorious by the fact that at 900 °C both crystal compositions composed with sodium are present. By this point $Sr_5Nb_4O_{15}$ has already completely reacted. From 1000 °C to 1100 °C instead of forming a, like the synthesis via (emim)OAc, strontium niobate and a crystal composition containing sodium, a new diffraction patterns is observed. This diffraction pattern does not belong to any of the possible crystal composition formed by strontium, niobium, and sodium, nor the any mix of this elements. It does seem to indicate that when stable-at-higher-temperature crystal compositions are formed, they can undergo a new re-combination process, forming in this case an entirely new crystal composition.

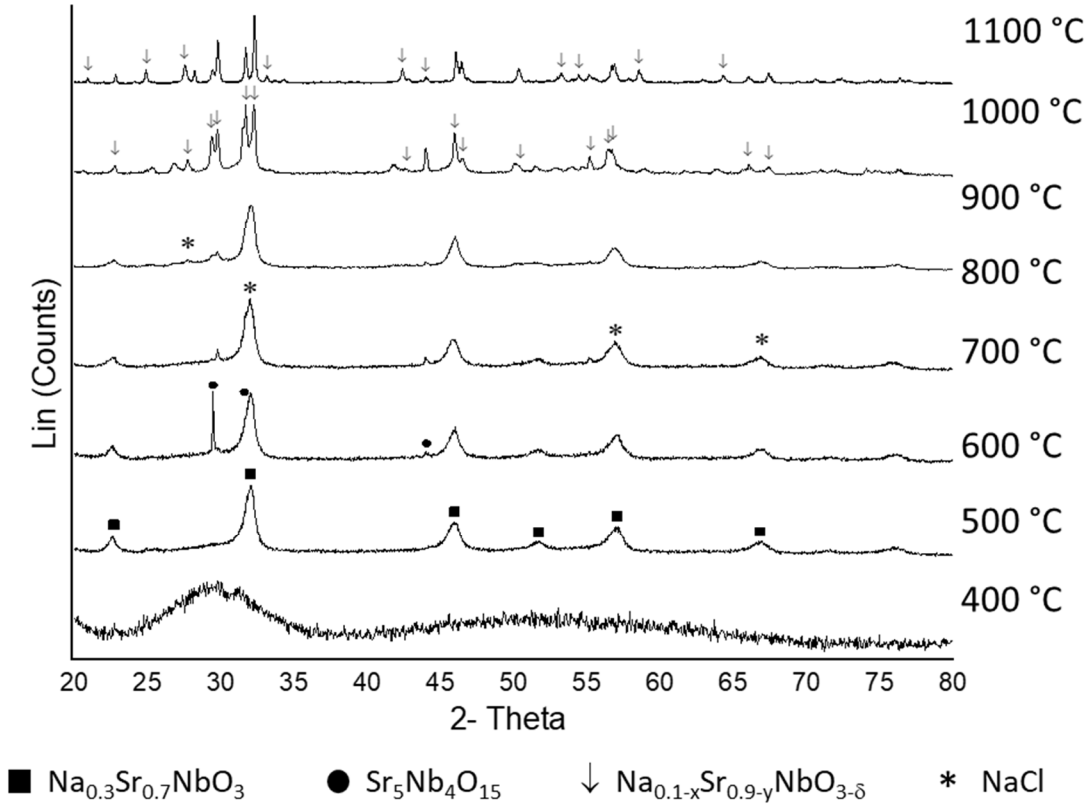

Figure 5.27. Temperature analysis of the crystal growth via powder X-ray diffraction patterns of the synthesis of a sodium strontium niobate via imidazole: choline chloride DES/dextran.

5.4.1.2.2 SEM EDX analysis

SEM EDX analysis was performed to study the evolution of sodium content along the calcination temperature. A clear decrease of sodium content is observed along the different temperatures with 3.1 % wt. % of the whole at 700 °C, 2.8 wt. % at 900 °C, and 1.7-2.0 % at 1100 °C (Figure 5.28). This is suggesting that the new crystal composition must have lower sodium content than the initial $Na_{0.3}Sr_{0.7}NbO_3$. It was impossible to digest most of the sample for ICP-OES analysis but, with what was digested (very low concentration) it was possible to stablish the Sr/Nb molar ratio, being 0.89:1. Moreover, via SEM-EDX and TEM-EDX the crystal composition was studied. SEM-EDX agrees with Sr/Nb ratio that was obtained via ICP-OES, 0.82-0.75 for strontium, and sodium ratio was stablished to be 0.16- 0.18. Furthermore, elemental mapping shown a perfect evenly distribution of the metal cations, confirming that the powder diffraction pattern could belong to a new crystal composition (Figure 5.29).

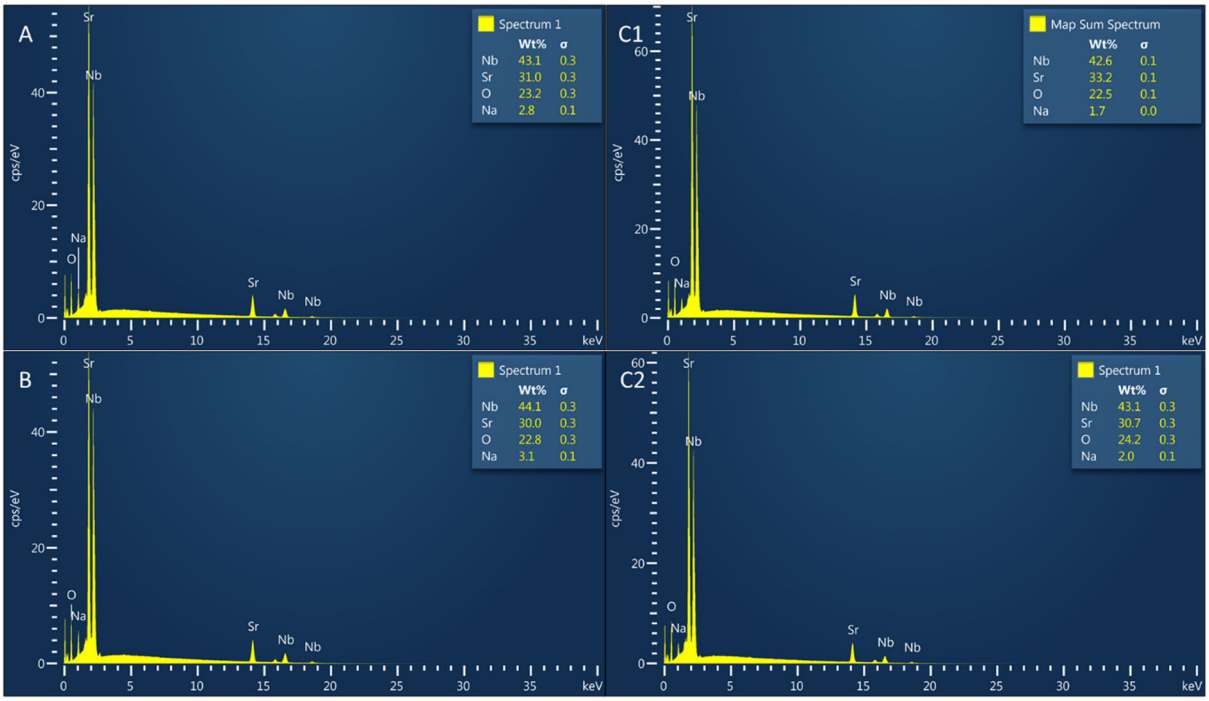

Figure 5.28. Scanning Electron microscopy energy dispersive X-ray analysis of the synthesis of a sodium strontium niobate via imidazole: choline chloride DES/dextran at: A) 700 °C, B) 900 °C, and C1&C2) 1100 °C. Insets show the quantitative analysis of elemental composition.

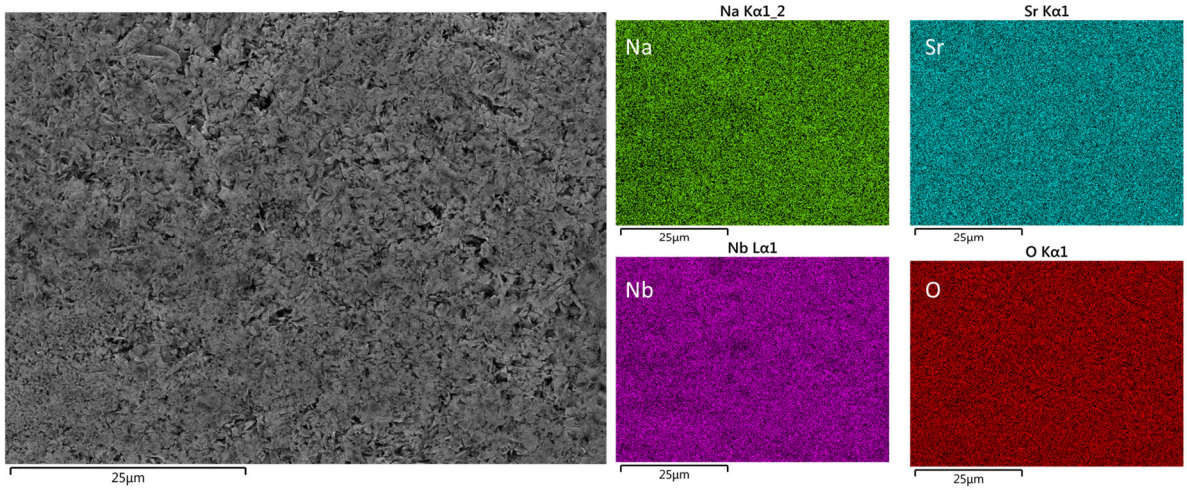

Figure 5.29. Scanning electron microscopy image with the elemental mapping of each respective element involved in the synthesis of a sodium strontium niobate via imidazole: choline chloride DES/dextran at 1100 °C.

5.4.1.2.3 HRTEM- EDX analysis

Further analysis using HRTEM was carried out. Being a polycrystalline sample, by SAED a ring pattern is observed. The distances measured agreed with diffractions observed via the powder diffraction pattern, i.e. 3.90 Å, 3.22 Å, 2.98 Å, 2.36 Å, and 2.05 Å which correspond to 22.78 °, 27.68 °, 29.86 °, 38.07 °, and 44.14 ° respectively (Figure 5.30 C). Also, via HRTEM images it was possible to measure the interplanar distance, namely 3.56 Å, 2.75 Å, and 1.61 Å, which correspond to the diffraction of the angles 24.96 °, 32.5 °, and 56.82 ° (Figure 5.30 D1-D3). The fact that via two different techniques were able to spot different diffractions indicates once again that the powder diffraction does not belong to separate crystal compositions but rather one.

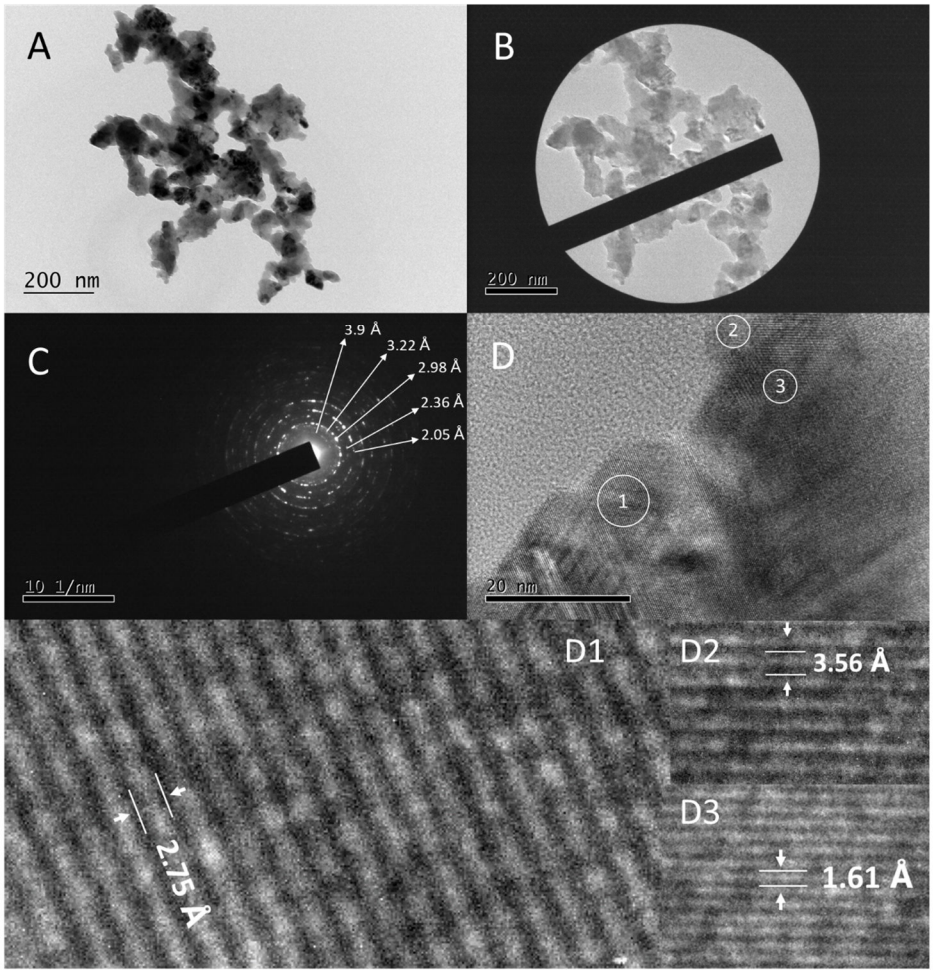

Figure 5.30. A) HRTEM image of the crystallites synthesised via imidazole: choline chloride DES, and B) showing where the SAED pattern was taken. C) SAED diffraction pattern. D) HRTEM image where different crystal fringes are visible. D1-3) Insets are zooming zones to measure the interplanar distance. White circles showing the exact area where the interplanar distance was measured.

Using TEM EDX on eight different crystallites (Table 5.1) we were able to compare compositions obtained via other medias, ICP-OES for Sr and Nb, and SEM-EDX for all the elements involved. The average values obtained are 1 for Sr, 1 for Nb, 0.1 for Na, and 5.5 for O. This time values are slightly different, specially Sr concentration being higher than the stablish via SEM-EDX and ICP-OES. On the other hand, sodium concentration represents lower values in comparison with values obtained via SEM-EDX. The oxygen content is not a reliable read via any EDX analysis however there is an increase in concentration if we compare it with SEM-EDX results.

	Na	Sr	Nb	O
	0.1	1.1	1	6.0
	0.1	1.0	1	6.0
	0.1	1.0	1	3.9
	0.1	0.9	1	4.0
	0.1	1.1	1	4.7
	0.1	1.1	1	4.8
	0.1	1.0	1	7.2
	0.1	1.0	1	7.2
Average	0.1	1.0	1	5.5

Table 5.1. Values obtained via HRTEM-EDX analysis of the elemental composition of the sodium strontium niobate synthesized via imidazole: choline chloride DES/dextran.

Also, is important to highlight is that elemental mapping via HRTEM also shown an even distribution of all the elements involved (Figure 5.31).

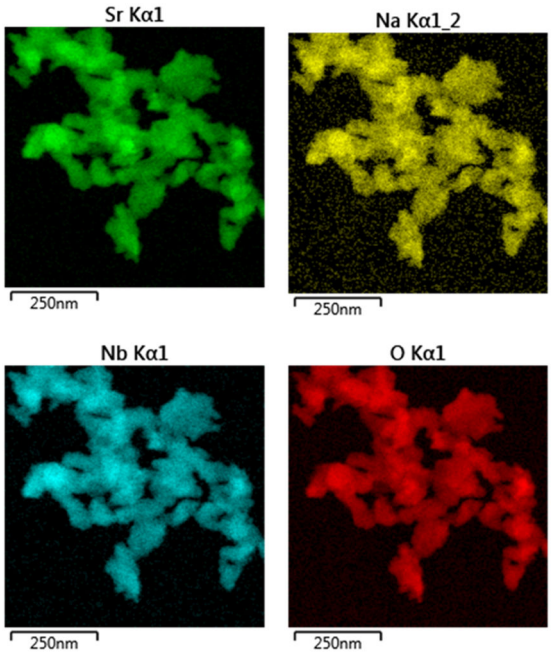

Figure 5.31. HRTEM-EDX analysis of the sodium strontium niobate synthesised via imidazole: choline chloride DES/dextran. All the elements involved are evenly distributed along the crystal.

5.4.2 Third Conclusions

Different crystal growth of sodium strontium niobates has been proven. On one side, via (emim)OAc it was expected to form carbonates which indeed are present in the form of $Sr(CO_3)$. Furthermore, with the formation of the carbonate, the crystal composition $Na_{0.3}Sr_{0.7}NbO_3$ is immediately synthesized and did not alter after synthesis until 1100 °C. On the other hand, via imidazole: choline chloride, also as expected, chlorinated crystal compositions are synthesized during the calcination process. The fact that part of the sodium is contained in two separate crystal compositions allow a further re-combination via solid state reactions forming an entirely new sodium strontium niobate crystal composition. This proves that different reactions can take place depending on the speed of crystal formation, and in some ways, is beneficial to slow the crystal growth to later form, via re-recombination, crystal compositions that might be formed in a very narrow window of temperature/time gradient. Based on the different characterization techniques for the elemental content, it is assumed that the new crystal composition is close to $Na_{0.1}Sr_{0.9}NbO_3$.

5.5 Bibliography

(1) Bednorz, J. G.; Müller, K. A. Possible HighT c Superconductivity in the Ba-La-Cu-O System. *Zeitschrift für Phys. B Condens. Matter* **1986**, *64* (2), 189–193.

(2) Danks, A. E.; Hall, S. R.; Schnepp, Z. The Evolution of 'Sol–gel' Chemistry as a Technique for Materials Synthesis. *Mater. Horizons* **2016**, *3* (2), 91–112.

(3) Antonietti, M.; Kuang, D.; Smarsly, B.; Zhou, Y. Ionic Liquids for the Convenient Synthesis of Functional Nanoparticles and Other Inorganic Nanostructures. *Angew. Chemie Int. Ed.* **2004**, *43* (38), 4988–4992.

(4) Sun, J.-K.; Kochovski, Z.; Zhang, W.-Y.; Kirmse, H.; Lu, Y.; Antonietti, M.; Yuan, J. General Synthetic Route toward Highly Dispersed Metal Clusters Enabled by Poly(Ionic Liquid)S. *J. Am. Chem. Soc.* **2017**, *139* (26), 8971–8976.

(5) Cota, I.; Fernandez Martinez, F. Recent Advances in the Synthesis and Applications of Metal Organic Frameworks Doped with Ionic Liquids for CO_2 Adsorption. *Coord. Chem. Rev.* **2017**, *351*, 189–204.

(6) Gómez Rojas, O.; Song, G.; Hall, S. R. Fast and Scalable Synthesis of Strontium Niobates with Controlled Stoichiometry. *CrystEngComm* **2017**, *19* (36), 5351–5355.

(7) Green, D. C.; Glatzel, S.; Collins, A. M.; Patil, A. J.; Hall, S. R. A New General Synthetic Strategy for Phase-Pure Complex Functional Materials. *Adv. Mater.* **2012**, *24* (42), 5767–5772.

(8) Duan, X.; Ma, J.; Lian, J.; Zheng, W. The Art of Using Ionic Liquids in the Synthesis of Inorganic Nanomaterials. *CrystEngComm* **2014**, *16* (13), 2550-2559.

(9) Ma, Z.; Yu, J.; Dai, S. Preparation of Inorganic Materials Using Ionic Liquids. *Adv. Mater.* **2010**, *22* (2), 261–285.

(10) Dai, Y.; van Spronsen, J.; Witkamp, G.-J.; Verpoorte, R.; Choi, Y. H. Natural Deep Eutectic Solvents as New Potential Media for Green Technology. *Anal. Chim. Acta* **2013**, *766*, 61–68.

(11) Armand, M.; Endres, F.; MacFarlane, D. R.; Ohno, H.; Scrosati, B. Ionic-Liquid Materials for the Electrochemical Challenges of the Future. In *Materials for Sustainable Energy*; Co-Published with

Macmillan Publishers Ltd, UK, 2010; pp 129–137.

(12) Saha, S.; Hayashi, S.; Kobayashi, A.; Hamaguchi, H. Crystal Structure of 1-Butyl-3-Methylimidazolium Chloride. A Clue to the Elucidation of the Ionic Liquid Structure. *Chem. Lett.* **2003**, *32* (8), 740–741.

(13) Elaiwi, A.; Hitchcock, P. B.; Seddon, K. R.; Srinivasan, N.; Tan, Y.-M.; Welton, T.; Zora, J. A. Hydrogen Bonding in Imidazolium Salts and Its Implications for Ambient-Temperature Halogenoaluminate(III) Ionic Liquids. *J. Chem. Soc. Dalt. Trans.* **1995**, *0* (21), 3467-3472.

(14) Mele, A.; Tran, C. D.; De Paoli Lacerda, S. H. The Structure of a Room-Temperature Ionic Liquid with and without Trace Amounts of Water: The Role of C-H···O and C-H···F Interactions in 1-n-Butyl-3-Methylimidazolium Tetrafluoroborate. *Angew. Chemie* **2003**, *115* (36), 4500–4502.

(15) Zhou, Y.; Antonietti, M. Synthesis of Very Small TiO_2 Nanocrystals in a Room-Temperature Ionic Liquid and Their Self-Assembly toward Mesoporous Spherical Aggregates. *J. Am. Chem. Soc.* **2003**, *125* (49), 14960–14961.

(16) Nakashima, T.; Kimizuka, N. Interfacial Synthesis of Hollow TiO_2 Microspheres in Ionic Liquids. *J. Am. Chem. Soc.* **2003**, *125* (21), 6386–6387.

(17) Wang, P.; Zakeeruddin, S. M.; Comte, P.; Exnar, I.; Grätzel, M. Gelation of Ionic Liquid-Based Electrolytes with Silica Nanoparticles for Quasi-Solid-State Dye-Sensitised Solar Cells. *J. Am. Chem. Soc.* **2003**, *125* (5), 1166–1167.

(18) Deetlefs, M.; Seddon, K. R. Assessing the Greenness of Some Typical Laboratory Ionic Liquid Preparations. *Green Chem.* **2010**, *12* (1), 17–30.

(19) Plechkova, N. V.; Seddon, K. R. Applications of Ionic Liquids in the Chemical Industry. *Chem. Soc. Rev.* **2008**, *37* (1), 123–150.

(20) Romero, A.; Santos, A.; Tojo, J.; Rodríguez, A. Toxicity and Biodegradability of Imidazolium Ionic Liquids. *J. Hazard. Mater.* **2008**, *151* (1), 268–273.

(21) Zhang, Q.; De Oliveira Vigier, K.; Royer, S.; Jérôme, F. Deep Eutectic Solvents: Syntheses, Properties and Applications. *Chem. Soc. Rev.* **2012**, *41* (21), 7108.

(22) Abbott, A. P.; Capper, G.; Davies, D. L.; Munro, H. L.; Rasheed, R. K.; Tambyrajah, V. Preparation of Novel, Moisture-Stable, Lewis-Acidic Ionic Liquids Containing Quaternary Ammonium Salts with Functional Side Chains. *Chem. Commun.* **2001**, *0* (19), 2010–2011.

(23) Dai, Y.; van Spronsen, J.; Witkamp, G.-J.; Verpoorte, R.; Choi, Y. H. Natural Deep Eutectic Solvents as New Potential Media for Green Technology. *Anal. Chim. Acta* **2013**, *766*, 61–68.

(24) Dai, Y.; Witkamp, G.-J.; Verpoorte, R.; Choi, Y. H. Tailoring Properties of Natural Deep Eutectic Solvents with Water to Facilitate Their Applications. *Food Chem.* **2015**, *187*, 14–19.

(25) Paiva, A.; Craveiro, R.; Aroso, I.; Martins, M.; Reis, R. L.; Duarte, A. R. C. Natural Deep Eutectic Solvents – Solvents for the 21st Century. *ACS Sustain. Chem. Eng.* **2014**, *2* (5), 1063–1071.

(26) Choi, Y. H.; van Spronsen, J.; Dai, Y.; Verberne, M.; Hollmann, F.; Arends, I. W. C. E.; Witkamp, G.-J.; Verpoorte, R. Are Natural Deep Eutectic Solvents the Missing Link in Understanding Cellular Metabolism and Physiology? *PLANT Physiol.* **2011**, *156* (4), 1701–1705.

(27) Marr, P. C.; Marr, A. C. Ionic Liquid Gel Materials: Applications in Green and Sustainable Chemistry. *Green Chem.* **2016**, *18* (1), 105–128.

(28) Zhang, Z.; Zaworotko, M. J. Template-Directed Synthesis of Metal–organic Materials. *Chem. Soc. Rev.* **2014**, *43* (16), 5444–5455.

(29) Smiglak, M.; Pringle, J. M.; Lu, X.; Han, L.; Zhang, S.; Gao, H.; MacFarlane, D. R.; Rogers, R. D. Ionic Liquids for Energy, Materials, and Medicine. *Chem. Commun.* **2014**, *50* (66), 9228–9250.

(30) Zhang, S.; Dokko, K.; Watanabe, M. Porous Ionic Liquids: Synthesis and Application. *Chem. Sci.* **2015**, *6* (7), 3684–3691.

(31) Smith, B. C. *Infrared Spectral Interpretation : A Systematic Approach*; CRC Press, New York USA, 1999.

(32) Coates, J. Interpretation of Infrared Spectra, A Practical Approach. In *Encyclopedia of Analytical Chemistry*; John Wiley & Sons, Ltd: Chichester, UK, 2006.

(33) Aissaoui, T. Novel Contribution to the Chemical Structure of Choline Chloride Based Deep Eutectic Solvents. *Pharm. Anal. Acta* **2015**, *6* (11), 448.

(34) Bîrzescu, M.; Roşu, D.; Milea, M.; Pascariu, M.; Rafailă, M. Coordination compounds obtained through oxidation of diols with metal nitrates. Part I: Synthesis-Structure relationship. *New Front. Chem.* **2016**, *25* (1), 39–52.

(35) Niculescu, M.; Pascariu, M.-C.; Muntean, C.; Sasca, V.; Lupa, L.; Milea, M.-S.; Birzescu, M. Thermal and Spectroscopic Analysis of Co(II)–Fe(III) Polyglyoxylate Obtained through the Reaction of Ethylene Glycol with Metal Nitrates. *J. Therm. Anal. Calorim.* **2018**, *131* (1), 127–136.

(36) Bauman, J. E.; Wang, J. C. Imidazole Complexes of Nickel(II), Copper(II), Zinc(II), and Silver(I). *Inorg. Chem.* **1964**, *3* (3), 368–373.

(37) Wu, W.; Xie, J.; Xie, D. Two Copper Complexes with Imidazole Ligands: Syntheses, Crystal Structures and Fluorescence. *Russ. J. Inorg. Chem.* **2010**, *55* (3), 384–389.

(38) Godlewska, S.; Jezierska, J.; Baranowska, K.; Augustin, E.; Dołęga, A. Copper(II) Complexes with Substituted Imidazole and Chlorido Ligands: X-Ray, UV–Vis, Magnetic and EPR Studies and Chemotherapeutic Potential. *Polyhedron* **2013**, *65*, 288–297.

(39) Eastaugh, N. *The Pigment Compendium : A Dictionary of Historical Pigments*; Elsevier Butterworth-Heinemann, Oxford, UK, 2004.

(40) Krushna, C.; Mohapatra, C.; Dash, K. C. 4-, 5- and 6-Coordinate Complexes of Copper(II) with Substituted Imidazoles. *J. Inorg. Nucl. Chem.* **1977**, *39* (7), 1253–1258.

(41) Wu, M. K.; Ashburn, J. R.; Torng, C. J.; Hor, P. H.; Meng, R. L.; Gao, L.; Huang, Z. J.; Wang, Y. Q.; Chu ', C. W. Superconductivity at 93 K in a New Mixed-Phase Y-Ba-Cu-0 Compound System at Ambient Pressure. *Phys. Rev. Lett.* **1987**, *58* (2).

(42) Boston, R.; Foeller, P. Y.; Sinclair, D. C.; Reaney, I. M. Synthesis of Barium Titanate Using Deep Eutectic Solvents. *Inorg. Chem.* **2017**, *56* (1), 542–547.

(43) Green, D. C.; Boston, R.; Glatzel, S.; Lees, M. R.; Wimbush, S. C.; Potticary, J.; Ogasawara, W.; Hall, S. R. On the Mechanism of Cuprate Crystal Growth: The Role of Mixed Metal Carbonates. *Adv. Funct. Mater.* **2015**, *25* (29), 4700–4707.

(44) Chow, M.-Y.; Chen, X.-M.; Mak, T. C. W. Simultaneous Binding of Betaine and Pseudohalide to Cadmium: Structures of Four Polymeric Mixed-Ligand Cadmium(II) Complexes. *J. Chem. Soc. Dalt. Trans.* **1993**, *0* (22), 3413.

(45) Quagliano, J. V.; Kida, S.; Fujita, J. Preparation and Infrared Studies of Metal Complexes Containing the Zwitterion Ligand Betaine , (CH)NCHCOO. *J. Am. Chem. Soc.* **1962**, *84* (5), 724–729.

(46) Wang, B.; Qin, L.; Mu, T.; Xue, Z.; Gao, G. Are Ionic Liquids Chemically Stable? *Chem. Rev.* **2017**, *117* (10), 7113–7131.

(47) Abbott, A. P.; Harris, R. C.; Ryder, K. S.; D'Agostino, C.; Gladden, L. F.; Mantle, M. D. Glycerol Eutectics as Sustainable Solvent Systems. *Green Chem.* **2011**, *13* (1), 82–90.

(48) Abbott, A. P.; Capper, G.; Gray, S. Design of Improved Deep Eutectic Solvents Using Hole Theory. *ChemPhysChem* **2006**, *7* (4), 803–806.

(49) Ma, Z.; Yu, J.; Dai, S. Preparation of Inorganic Materials Using Ionic Liquids. *Adv. Mater.* **2010**, *22* (2), 261–285.

(50) Sunshine, S. A.; Siegrist, T.; Schneemeyer, L. F.; Murphy, D. W.; Cava, R. J.; Batlogg, B.; Van Dover, R. B.; Fleming, R. M.; Glarum, S. H.; Nakahara, S.; et al. Structure and Physical Properties of Single Crystals of the 84-K Superconductor $Bi_{2.2}Sr_2Ca_{0.8}Cu_2O_{8+y}$. *Phys. Rev. B* **1988**, *38* (1), 893–896.

(51) Subramanian, M. A.; Torardi, C. C.; Calabrese, J. C.; Gopalakrishnan, J.; Morrissey, K. J.; Askew, T. R.; Flippen, R. B.; Chowdhry, U.; Sleight, A. W. A New High-Temperature Superconductor: Bi_2Sr_{3-x} Ca_x Cu_2O8_{+y}. *Science* **1988**, *239* (4843), 1015–1017.

Chapter 6
Other results, general conclusions and future work

6.1 Other results

6.1.1 Different atmospheres

One of the most interesting tools for the crystal growth is the use of different atmospheres such as argon, carbon dioxide, and hydrogen gas to modify the oxygen content of the result crystal composition. A few attempts were carried out in this area, where firstly 1 ml of strontium nitrate (0.1M) was mixed with 1 ml of ionic liquid and dehydrated at 70 °C for over 2 hours. Niobium ethoxide was added after that and left another hour to ensure complete dehydration. Finally, a paste-like was formed adding 100 mg of dextran and calcined immediately at 600 °C for 2 h. For the sake of comparison and reproducibility, all the attempted syntheses were done targeting the phase $Sr_5Nb_4O_{15}$. The product was then sintered in different atmospheres at different temperatures. The ramp rate remained constant during all the calcination procedures, being 5 °C min^{-1}. The idea was that, as seen in chapter 3, at 600 °C powder diffraction patterns showed diffractions that could belong to the crystal phase $SrNbO_3$, therefore, probably under a neutral or even reducing atmosphere it could be possible to form a reduced Nb (IV) crystal composition, however, none of the attempts were successful.

6.1.1.1 Carbon dioxide

Carbon dioxide is not a reducing gas but is in fact the opposite. As expected, all the reactions attempted under this atmosphere gave fully oxidized crystal compositions. The temperature selected for the experiments were 1000 °C and calcined for 2 h. Random results were obtained; sometimes high yields of a single-phase material resulted (Figure 6.1 A) however, some other attempts gave a mix of two phases. The reason behind this could be the fact that the oxygen is limited and less available forcing domains to crystalize into different crystal compositions (Figure 6.1 B).

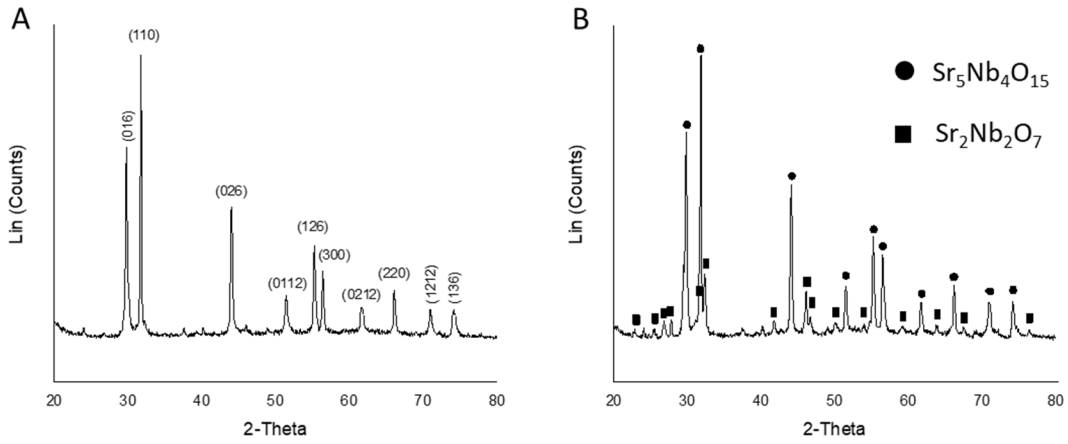

Figure 6.1. Left: powder diffraction pattern of A) almost phase pure material. Indexed planes correspond to the $Sr_5Nb_4O_{15}$ crystal composition, and B) exhibiting a mix of two different crystal compositions, $Sr_5Nb_4O_{15}$ and $Sr_2Nb_2O_7$.

6.1.1.2 Argon

Argon is quite interesting because it is possible to eliminate all oxygen sources of the furnace. After running the experiment, it was noticed that despite the absence of oxygen, fully oxidised samples were obtained. This indicates that the mass formed at 600 °C must already contain enough oxygen to form the crystalline material containing Nb (V) (Figure 6.2). Two different temperatures where studied and at 800 °C it was already possible to observe the diffractions corresponding to the fully oxidised $Sr_5Nb_4O_{15}$ crystal composition. At 1000 °C clear diffractions of the crystal composition are shown.

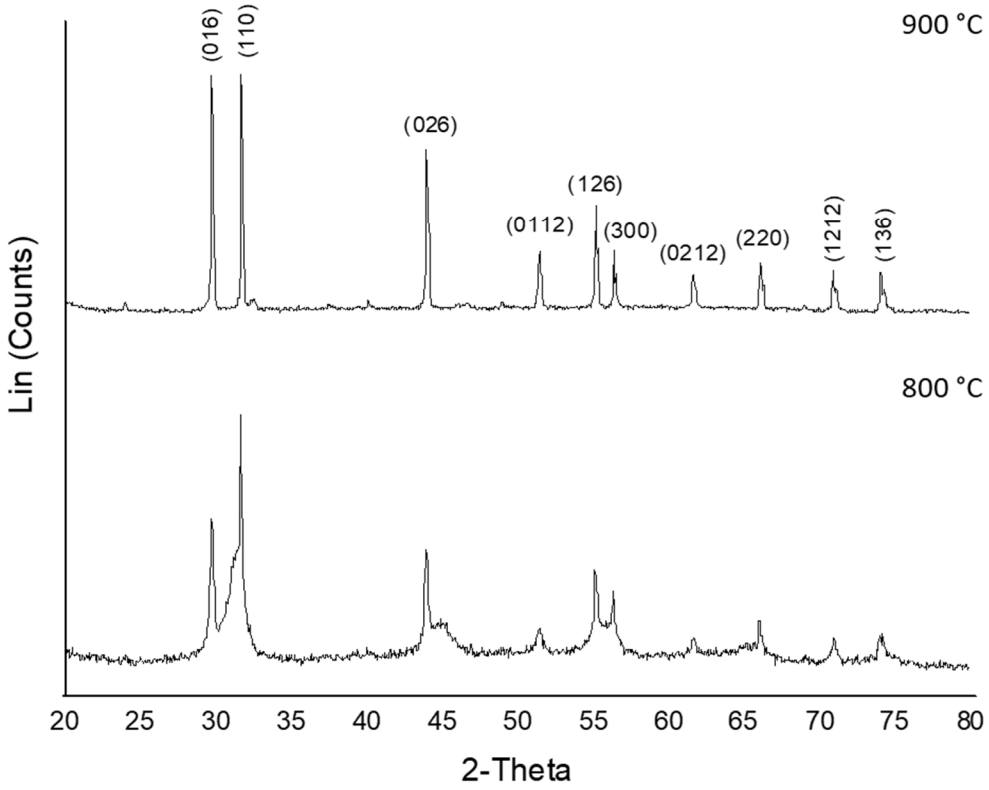

Figure 6.2. Powder diffraction pattern of the synthesis of $Sr_5Nb_4O_{15}$ under argon atmosphere at two different temperatures, showing clear diffractions of a single phase at 900 °C.

Attempts to do the reaction without pre-calcination process derived in carbonaceous material (Figure 6.3). The dwelling temperature was 1000 °C and dwelling time 2 h. The idea was to see if carbonaceous material could drag some oxygen of the crystal composition forming CO_2, forcing the reduction of niobium. After analysing via powder diffraction pattern, it was possible to index diffractions belonging to strontium carbonate however, noise ratio signal is very low as expected due to most of the material not being able to crystallize.

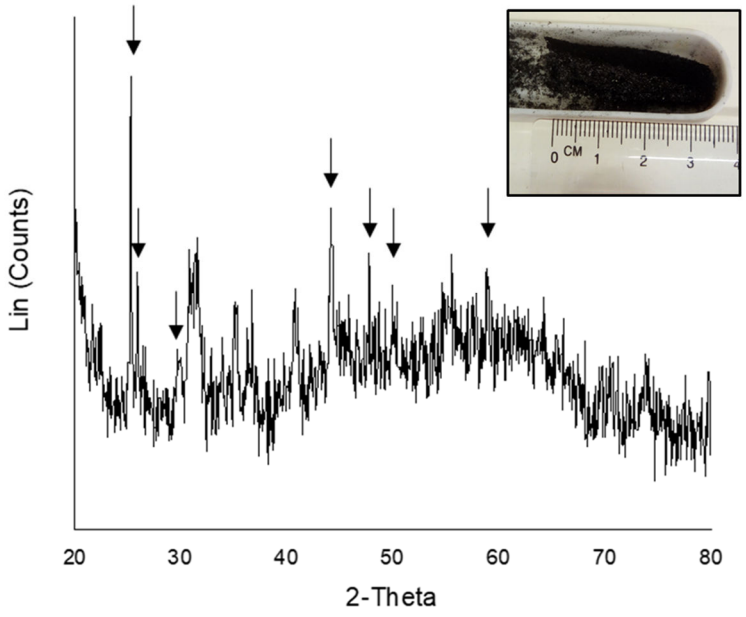

Figure 6.3. Powder diffraction of the reaction under argon atmosphere without pre-calcination process. Arrows indicate strontium carbonate diffractions. Inset is a photo of the carbonaceous material obtained.

6.1.1.3 Hydrogen

Lastly, in the last attempt to reduce the material, hydrogen atmosphere was used. The experiment was run at different temperatures, namely 1000 °C, 1100 °C, 1400 °C, and ~1450 °C. The first two temperatures shown a single-phase $Sr_5Nb_4O_{15}$ crystal composition. No reduction indications are visually seen, such as a change in colour. At 1400 °C the powder diffraction pattern shown a majority of a $Sr_5Nb_4O_{15}$ crystal composition however, what it looks like the diffraction of $Sr_2Nb_2O_7$ are also visualized. The last temperature, 1450 °C, was very hard to attain due to lack of equipment capacity to generate enough power to rise the temperature to such temperature. The powder diffraction pattern showed only $Sr_2Nb_2O_7$ but this time some sort of reduction process is expected to happen due to a change in coloration of the power, from white to blue-greyish coloration. Despite such high temperatures and a reducing atmosphere, the fact that the patterns seem to belong to still fully oxidised material is not so much of a surprise, as to reduce strontium niobates molybdenum foil must be used, for the synthesis of $SrNbO_3$,[1] or plasma hydrogen at 2000 °C for the synthesis of $Sr_5Nb_5O_{16}$.[2]

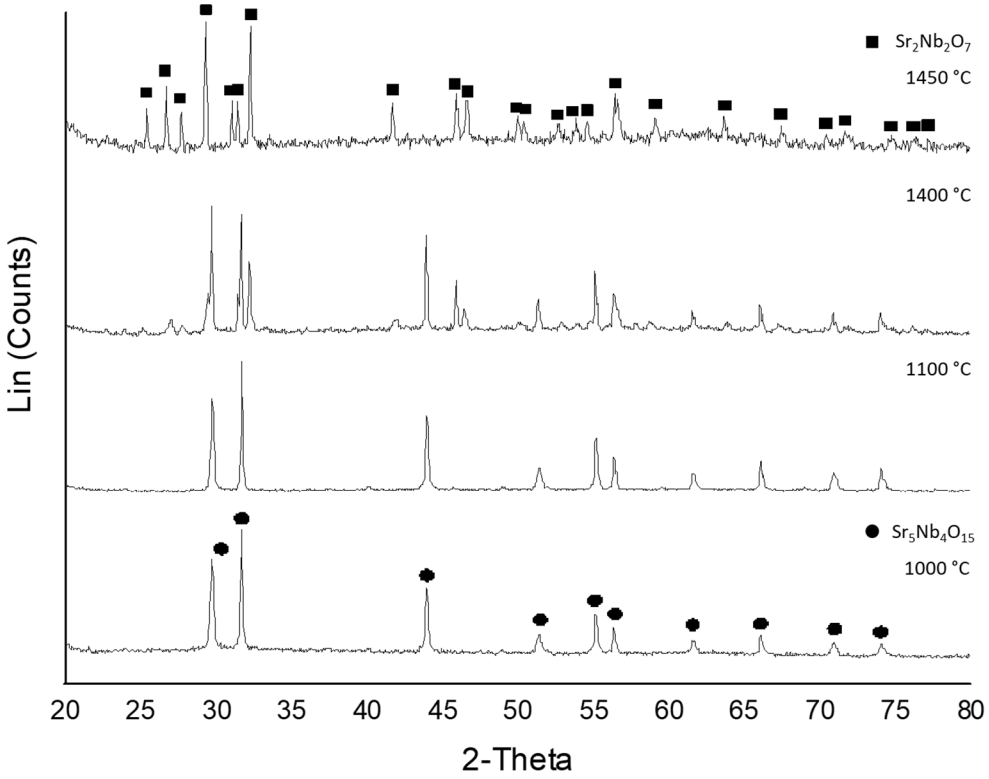

Figure 6.4. Powder diffraction patterns of the sintering of strontium niobate powder at different temperatures under hydrogen atmosphere.

Despite the fact that it was not possible to accomplish the reduction of the strontium niobate it is still very interesting to explore, joint with the vast versatility of ionic liquids/deep eutectic solvents, the synthesis of crystalline material under different atmospheres.

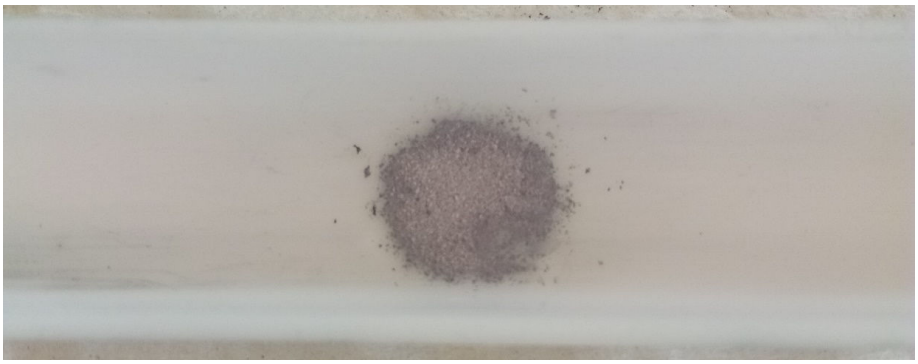

Figure 6.5. Photography of the powder obtained at 1450 °C under hydrogen atmosphere exhibiting different colours due to possible reduction.

6.2 General conclusions

Chapter 3 proves that the ionic liquid synthetic method is a reliable technique to produce metal oxides. It has proven to be fast and simple, in terms of equipment and ease of use, to produce high yields (> 98 %) of a metal oxide. It was also proven that it is possible to obtain different crystal compositions by varying the molar ratios between metal cations. The crystal compositions of the strontium niobates obtained are $Sr_4Nb_2O_9$, $Sr_5Nb_4O_{15}$, $Sr_2Nb_2O_7$, $SrNb_2O_6$, $SrNb_6O_{16}$. Moreover, it was possible to synthesize, straightforward, five different crystal compositions with proximity to the $Sr_4Nb_2O_9$. Based on different characterization techniques, such as ICP-OES and Rietveld refinement, it was possible to establish the Sr/Nb molar ratios of the five different crystal composition, being 3.37, 2.88, 2.70, 2.53, and 2.08 respectively. Finally, the chelating properties of every component of the technique were tested, proving that the ionic liquid was the main chelator agent, capable of producing, without the use of a polysaccharide, high yields of a metal oxide.

Chapter 4 provides more in-depth information about the interaction of the polysaccharide and the ionic liquid. It was proven that without considering the type of polysaccharide in use, i.e. cellulose, chitosan, starch, and dextran, all provided, when studied via powder x-ray diffraction patterns, high yields of the metal oxides explored, namely $Sr_5Nb_4O_{15}$ and $YBa_2Cu_3O_{7-\delta}$. However, further characterization on the superconductive phase, via SQUID magnetometry, indicated by changes on the Tc, that the oxygen varied depending on the polysaccharide used. The highest critical temperature exhibited belongs to dextran with $T_{c\ onset}$ = 94 K and cellulose with the second highest $T_{c\ onset}$ = 91 K, chitosan exhibited $T_{c\ onset}$ = 66 K and starch $T_{c\ onset}$ = 60 K. Furthermore, for the synthesis of the strontium niobate, where low and high concentrations of the organic source (1 g and 0.1g) were employed, only dextran provided single phase powder x-ray diffraction patterns.

Morphological evidence indicates that when the concentration of the organic source is low (0.1 g), the morphology exhibited is dictated by the ionic liquid, with exception of chitosan who also shown

structural changes at low concentrations. However, increasing the concentration of the polysaccharide delivered differences in the morphology of the resultant crystallites. Cellulose has shown drastic changes from agglomerates of poly-crystallites to elongated particles.

In chapter 5 via a mechanistic study of the crystal growth of $YBa_2Cu_3O_{7-\delta}$ in different synthetic medias, namely one ionic liquid ((emim)OAc), two deep eutectic solvents (ethylene glycol: choline chloride, and imidazole: choline chloride), and two mono-molecular chelating agents (ethylene glycol, and imidazole), the role of the IL/DES in the synthesis of metal oxides was elucidated. First, it was proven that the IL/DES in interaction with the metal cations, produce metal nanoparticles, stabilized by the surrounding anion layer, and the cation acting as a surfactant. Therefore, the system is not a homogenous multicationic solution but rather a heterogenous nanoparticulate system. Second, extra components, such as chlorine will take part in the reaction and create metal chloride associate phases. These phases when stable along the whole temperature setup, will not re-react obstructing the formation of the desire crystal phase. Third, by identifying precursory phases needed to form the target crystal phase and allowing the formation of such at earlier stages, will speed up the crystal formation, meaning a reduction of the maximum temperature required. Lastly, it was proven that the anion layer is key factor to obtain the desire crystal phase. In the case of the YBCO superconductor only the carboxylic group provided by (emim)OAc produced above 95 % of the superconductive crystal. Attempts to synthesize this crystal without a carboxylic group were not successful (no superconductive phase present), when DES with chlorine were used, namely ethylene glycol: choline chloride and imidazole: choline chloride, and only lower yields of the superconductor were obtained, below 40 %, when monomolecular chelators such as ethylene glycol and imidazole were utilized. This is due to the production of barium carbonate at early stages of the calcination process by the direct link of the acetate of (emim)OAc with the metal nanoparticle. On the other hand, barium chloride will be formed when DES with chlorine where employed, and barium nitrate is seen when the synthetic process was carried out with both monomolecular chelators.

As a prove of concept and to lower the overall expenses of the synthetic process, a DES made by mixing betaine and D-(+)-glucose in 5:2 molar ratio, was used for the synthesis of $Bi_2Sr_2CaCu_2O_{8+x}$ superconductor. Via the use of this DES it was possible to obtain > 93 % of the superconductive phase when the DES was freshly prepared. However, when the DES was aged notorious changes happened in the chelating properties of the solvent, represented by a significant growth, observed via powder diffraction patterns, of a precursory crystal phase. This is also visually observed by the changes of colour in the DES, from transparent to light yellow in 2 months, and dark brown in 6 months. The mixture of the polysaccharide and betaine seems to continuously interact uninterruptedly oxidizing the polysaccharide therefore, changing the chelating properties of the solvent.

Finally, it was demonstrated that the formation of carbonate phases will indeed speed up the reaction process however, this is not always beneficial. The synthesis of a new sodium strontium niobate was synthesize via imidazole: choline chloride DES. The crystal growth was also carried out using (emim)OAc and both compared. The IL produced a carbonate phase in the form of strontium carbonate, along with $Na_{0.3}Sr_{0.7}NbO_3$ crystal phase. The latter will remain unchanged along the whole synthetic process. On the other hand, when the DES was used, two different crystal phases containing sodium where produced during the calcination process, namely $Na_{0.3}Sr_{0.7}NbO_3$ and NaCl. The fact that the overall sodium content was contained in two different crystals allowed, via solid state reactions, a further recombination resulting in an entirely new sodium strontium niobate crystal composition. Based on the different characterization techniques for the elemental content, it is assumed that the new crystal composition is close to $Na_{0.1}Sr_{0.9}NbO_3$.

6.3 Future work

6.3.1 Solvate ionic liquids/metal based DES

This idea comes from work done in 1965 by Austen Angell, where a new class of molten salt mixture using hydrated multivalent cations as independent cation species was proposed.[3] In 2011 he then classified such systems as solvate ionic liquids.[4] The basic idea is to incorporate solvated cations as a constituent of ILs.[5–7]

Similarly, Metal based DES are formed between metal salts and simple organic alcohols or amides. An example is the production of eutectic mixtures with metal nitrates and urea[8-9], or the used of a metal salt, such as $ZnCl_2$, with hydrogen bond donors like urea, acetamide, ethylene glycol, and hexanediol[10]. Both candidates must be considered for future work on this area.

6.3.2 Acid based DES

Perhaps these candidates represent the best option for the synthesis of metal oxides via the IL/DES method. Acid based DES contain components that are widely known as good chelators, such as oxalic acid and citric acid[11]. Both organic molecules belong to the family of carboxylic acids which have shown during this work, to be relevant in the production of high yields of metal oxides, as well as speeding the overall crystallization process of the desire crystal phase.

6.3.3 Control over the morphology/dynamic light scattering analysis (DLS)/ Thermogravimetric analysis (TGA)

It is well known that the control over the morphology is crucial for the enhancement performance of several applications[12-17] therefore, it is absolutely needed to work over this specific area to obtain basic knowledge, which will provide this synthetic protocol to extend control over that too. Until now it was believed that the IL/DES will form a multicationic homogenous solution however, during this work it was

proven that the IL/DES in interaction with metal salts will form nanoparticles therefore, an inhomogeneous solution. During this work it was also proven that the morphology of the resultant crystal phases, despite using the same ionic liquid for the synthesis, will change while varying the metal cations. This could possibly be explained by relating the size of the nanoparticles formed, measured via DLS, with the resultant morphology. Also, it would be interesting to unveil how the nanoparticle size distribution is affecting the overall crystallization process.

It is also relevant to highlight the importance of TG analysis to provide a better understanding of the reaction process of the system. Comparing this technique with the size distribution of nanoparticles in the system, can provide high valuable information of the size-dependence reactivity of the system This could be used to improve the overall reaction protocol.

6.4 Bibliography

(1) Xu, X.; Randorn, C.; Efstathiou, P.; Irvine, J. T. S. A Red Metallic Oxide Photocatalyst. *Nat. Mater.* **2012**, *11* (7), 595–598.

(2) Schückel, K.; Müller-Buschbaum, H. Ein Weiteres Gemischtvalentes Oxoniobat: $Sr_5Nb_3^{4+}Nb_2^{5+}O_{16}$. *Zeitschrift für Anorg. und Allg. Chemie* **1985**, *528* (9), 91–97.

(3) Angell, C. A. A New Class of Molten Salt Mixtures The Hydrated Dipositive Ion as an Independent Cation Species. *J. Electrochem. Soc.* **1965**, *112* (12), 1224.

(4) Austen Angell, C.; Ansari, Y.; Zhao, Z. Ionic Liquids: Past, Present and Future. *Faraday Discussions*, **2012**, 154, 9–27.

(5) Zhang, P.; Gong, Y.; Lv, Y.; Guo, Y.; Wang, Y.; Wang, C.; Li, H. Ionic Liquids with Metal Chelate Anions. *Chem. Commun.* **2012**, *48* (17), 2334.

(6) Mandai, T.; Yoshida, K.; Ueno, K.; Dokko, K.; Watanabe, M. Criteria for Solvate Ionic Liquids. *Phys. Chem. Chem. Phys.* **2014**, *16* (19), 8761.

(7) Kar, M.; Winther-Jensen, B.; Forsyth, M.; MacFarlane, D. R. Chelating Ionic Liquids for Reversible Zinc Electrochemistry. *Phys. Chem. Chem. Phys.* **2013**, *15* (19), 7191.

(8) Gambino M.,Gaune M., Nabavian M., Gaune-Escard M., Bros J.P. Enthalpie de fusion de l'uree et de quelques melanges eutectiques a base d'uree. Thermochimica Acta. **1987**, 111, 37-47.

(9) Gambino M., Bros J.P. Capacite calorifique de l'uree et de quelques melanges eutectiques a base d'uree entre 30 et 140° C. Thermochimica Acta. 1988, **127**, 223-236.

(10) P. Abbott P.A., Barron J.C., Ryder K.S., Wilson D. Eutectic-Based Ionic Liquids with Metal-Containing Anions and Cations. Chemistry a european journal. **2007**, 13 (22), 6495-6501.

(11) Acton A. Q. Citrates—Advances in Research and Application. In Scholarly editions, Scholarly editionstm. eBook 2012.

(12) Korotcenkov, G. The Role of Morphology and Crystallographic Structure of Metal Oxides in Response of Conductometric-Type Gas Sensors. *Mater. Sci. Eng. R Reports* **2008**, *61* (1–6), 1–39.

(13) Hua, M.; Zhang, S.; Pan, B.; Zhang, W.; Lv, L.; Zhang, Q. Heavy Metal Removal from

Water/Wastewater by Nanosized Metal Oxides: A Review. *J. Hazard. Mater.* **2012**, *211–212*, 317–331.

(14) Oh, S. W.; Bang, H. J.; Bae, Y. C.; Sun, Y.-K. Effect of Calcination Temperature on Morphology, Crystallinity and Electrochemical Properties of Nano-Crystalline Metal Oxides (Co_3O_4, CuO, and NiO) Prepared via Ultrasonic Spray Pyrolysis. *J. Power Sources* **2007**, *173* (1), 502–509.

(15) Hu, J.-S.; Zhong, L.-S.; Song, W.-G.; Wan, L.-J. Synthesis of Hierarchically Structured Metal Oxides and Their Application in Heavy Metal Ion Removal. *Adv. Mater.* **2008**, *20* (15), 2977–2982.

(16) Ren, Y.; Ma, Z.; Bruce, P. G. Ordered Mesoporous Metal Oxides: Synthesis and Applications. *Chem. Soc. Rev.* **2012**, *41* (14), 4909.

(17) Yuan, C.; Wu, H. Bin; Xie, Y.; Lou, X. W. D. Mixed Transition-Metal Oxides: Design, Synthesis, and Energy-Related Applications. *Angew. Chemie Int. Ed.* **2014**, *53* (6), 1488–1504.

Appendix

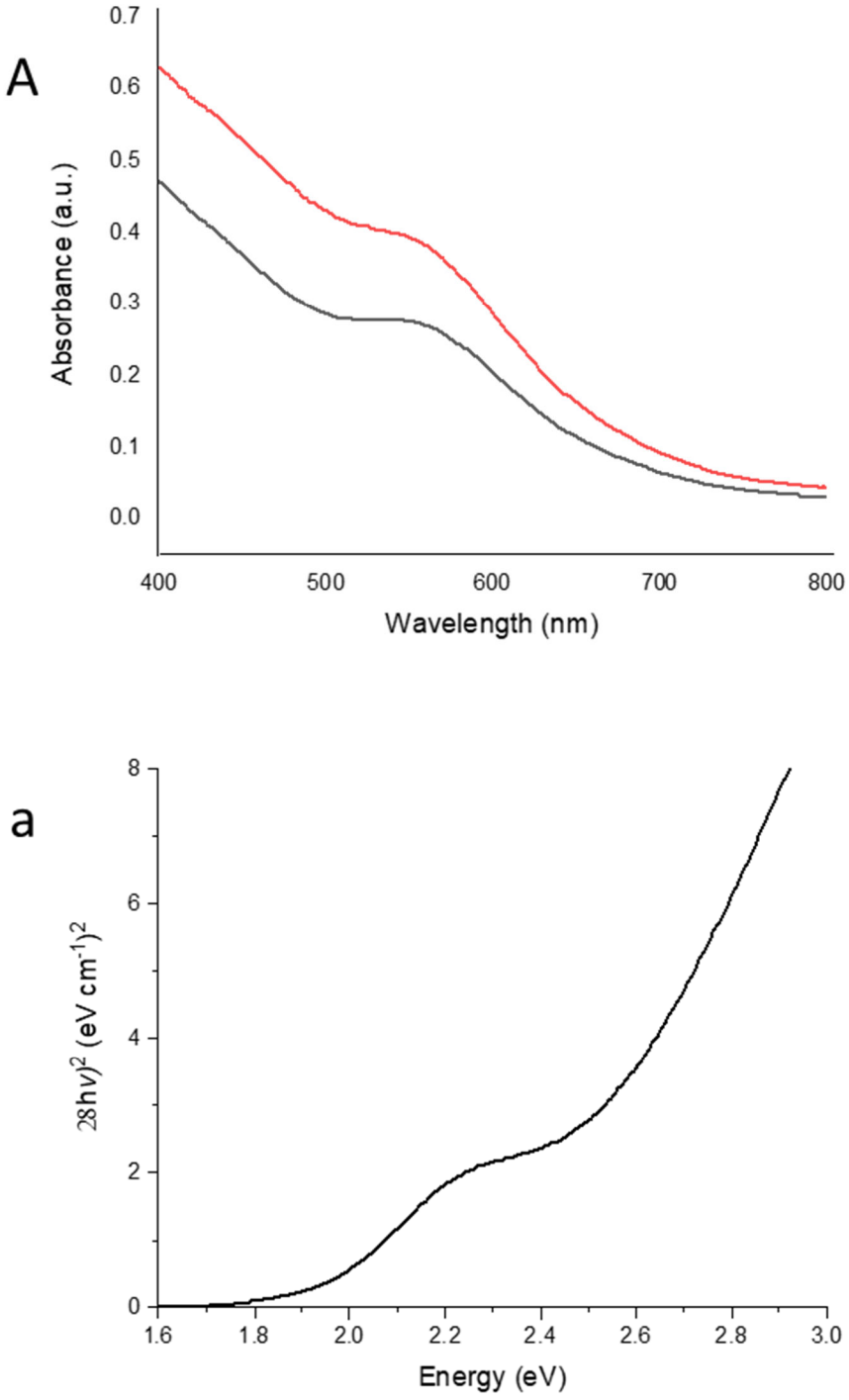

Figure A1. A) Uv-vis spectra of the crystal compositions based on the molar ratio of Sr/Nb (*X/Y*): 2.18 - 2.09. a) Tauc plot of the same crystal composition. Sample was prepared using (emim)OAc/dextran as chelating agents.

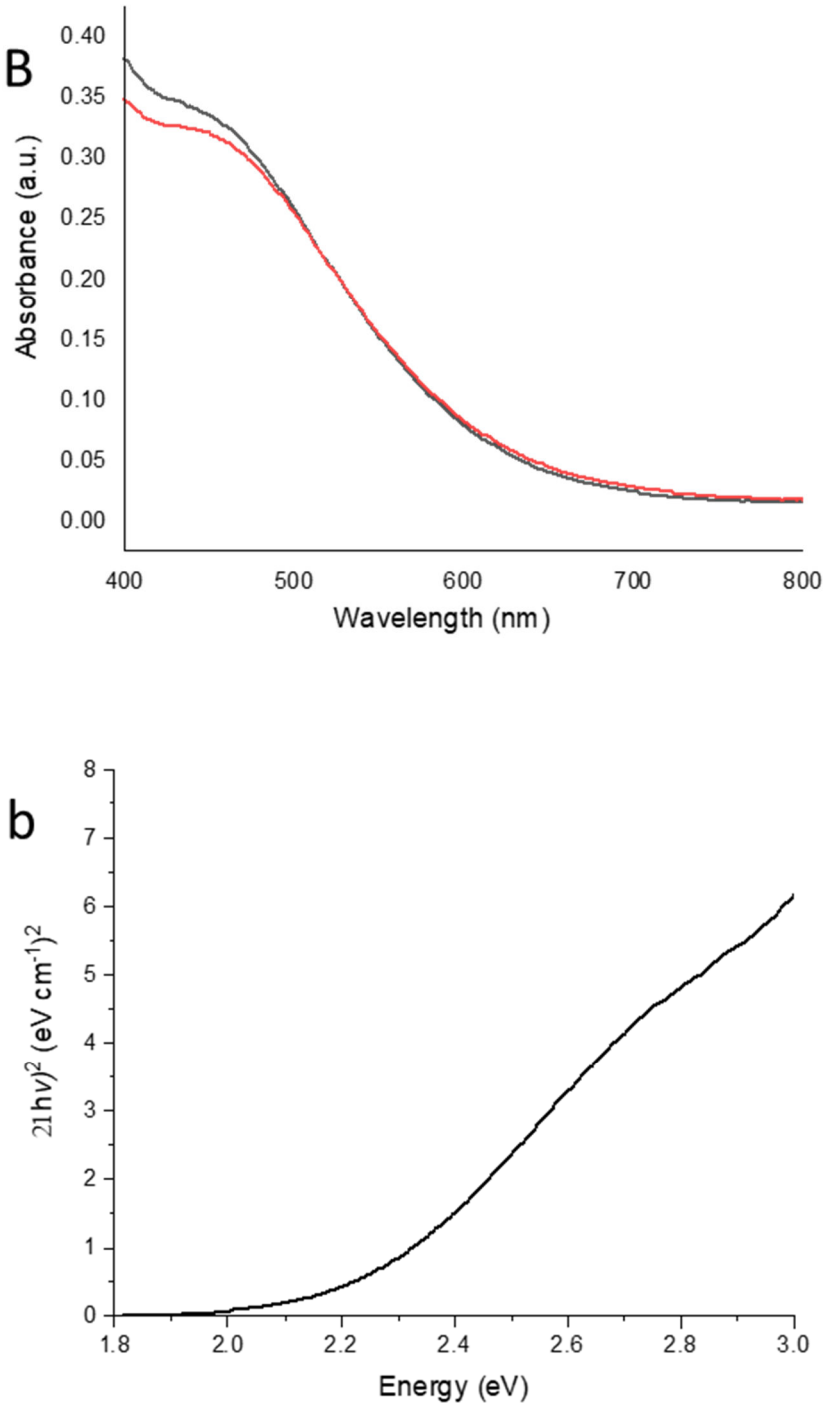

Figure A2. B) Uv-vis spectra of the crystal compositions based on the molar ratio of Sr/Nb (*X/Y*): 2.00 - 1.93. b) Tauc plot of the same crystal composition. Sample was prepared using (emim)OAc/dextran as chelating agents.

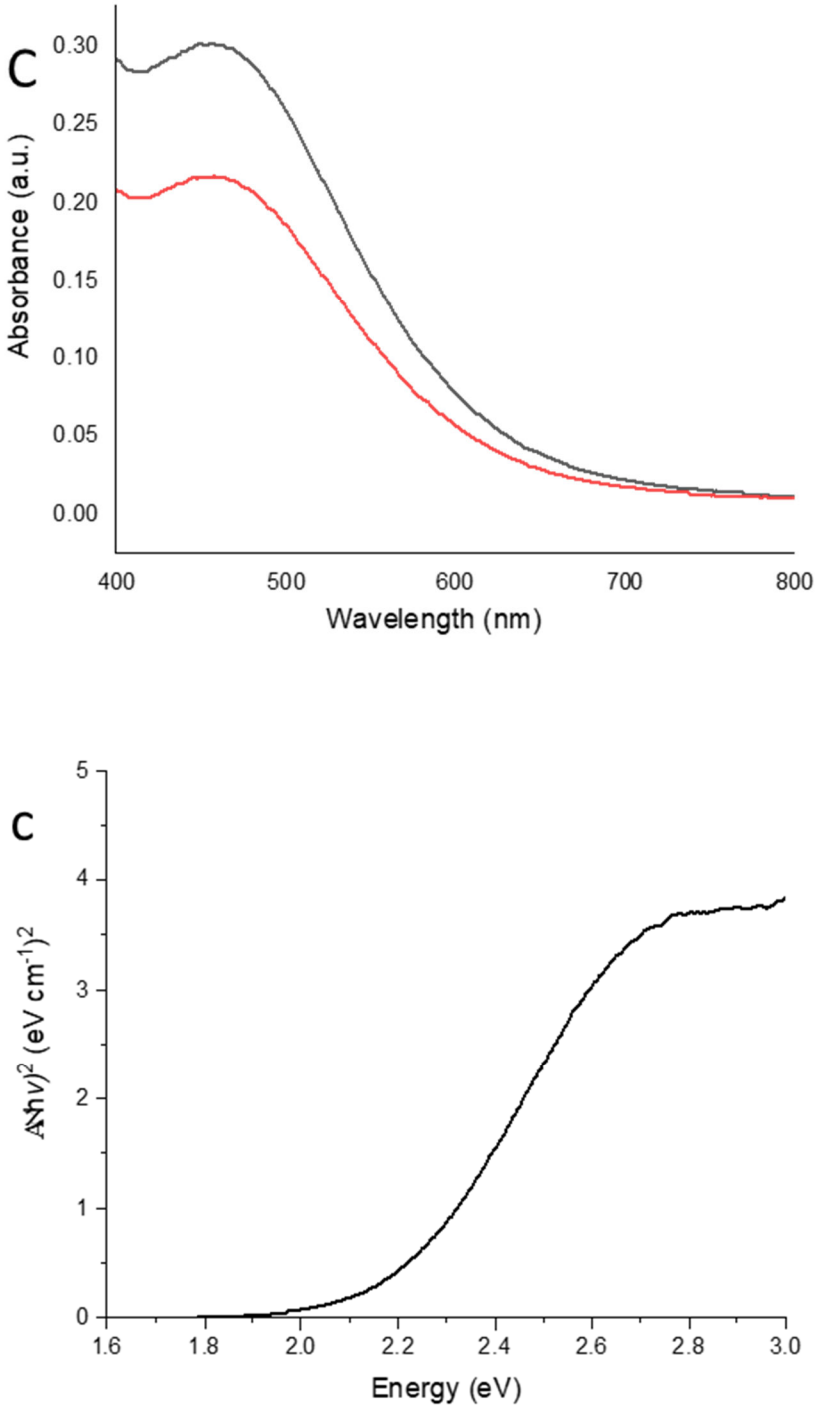

Figure A3. C) Uv-vis spectra of the crystal compositions based on the molar ratio of Sr/Nb (*X/Y*): 1.85 - 1.79. c) Tauc plot of the same crystal composition. Sample was prepared using (emim)OAc/dextran as chelating agents.

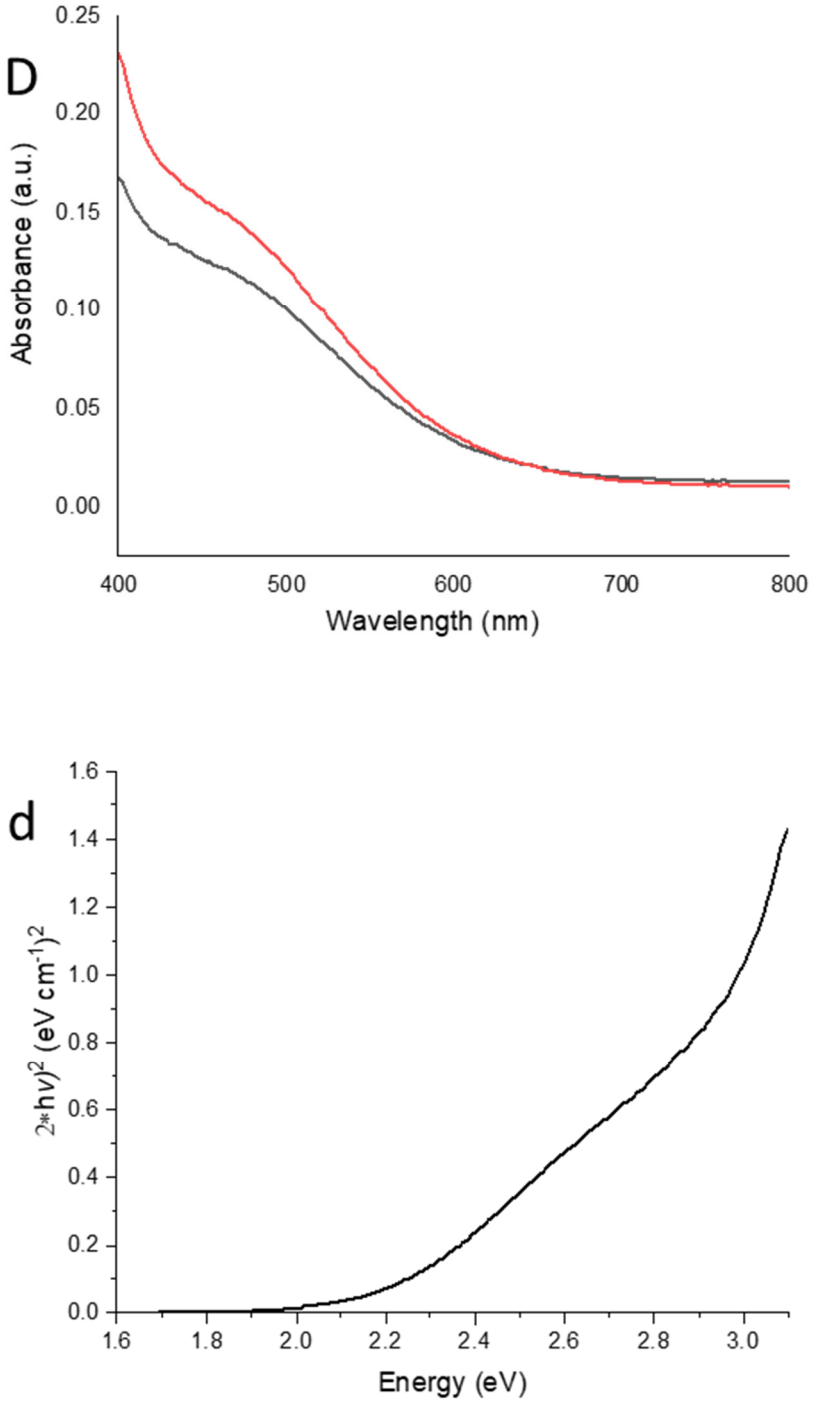

Figure A4. D) Uv-vis spectra of the crystal compositions based on the molar ratio of Sr/Nb (*X/Y*): 1.73 - 1.67. d) Tauc plot of the same crystal composition. Sample was prepared using (emim)OAc/dextran as chelating agents.

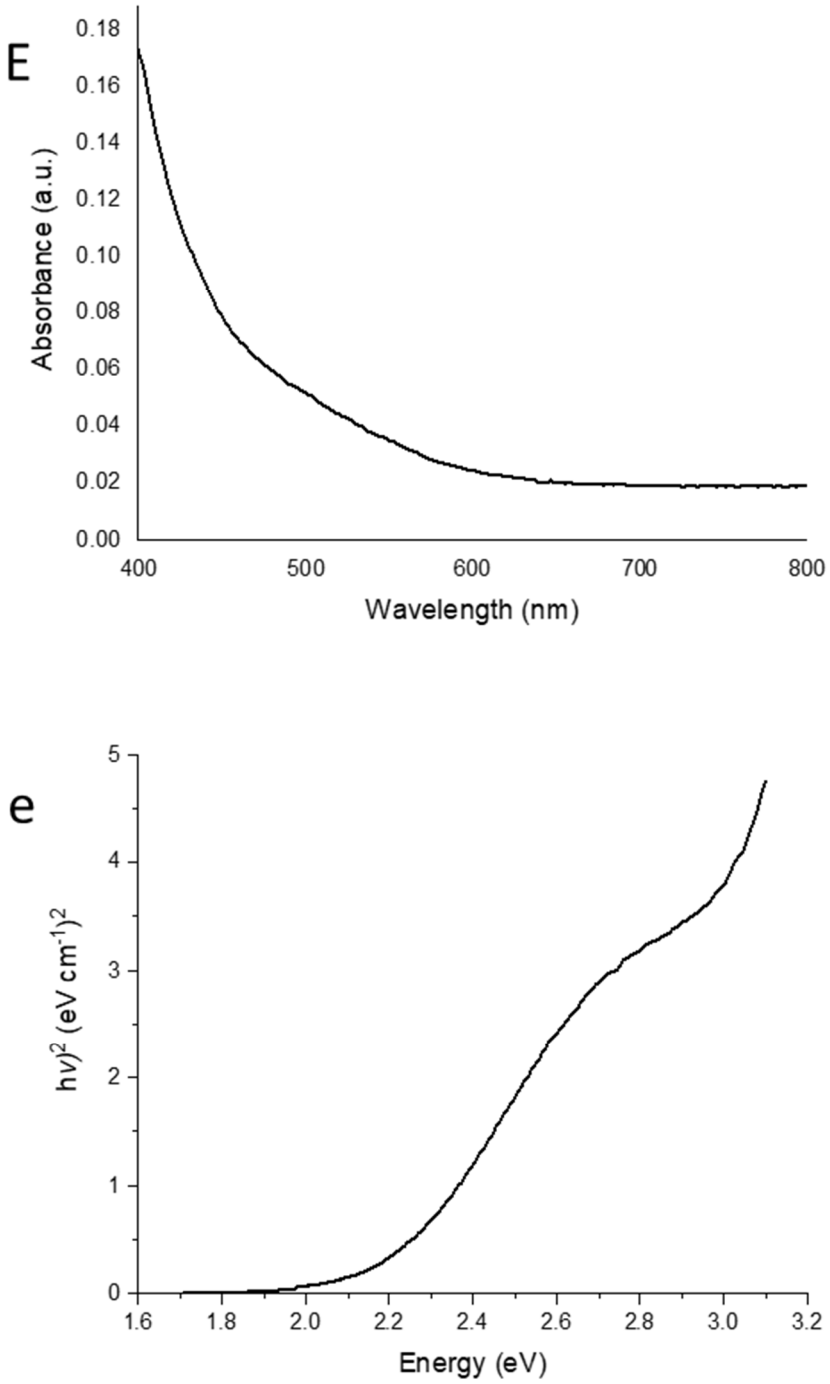

Figure A5. E) Uv-vis spectra of the crystal compositions based on the molar ratio of Sr/Nb (*X/Y*): 1.61 – 1.56. e) Tauc plot of the same crystal composition. Sample was prepared using (emim)OAc/dextran as chelating agents.

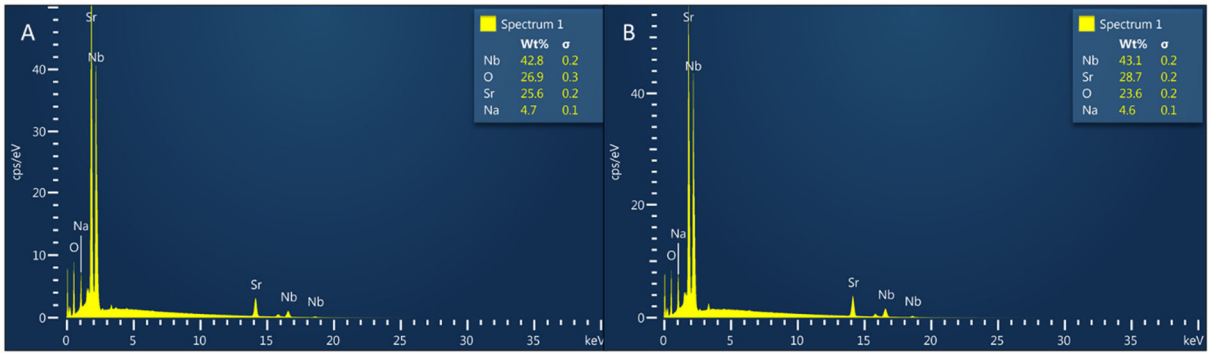

Figure A6. Scanning Electron microscopy energy dispersive X-ray analysis of the synthesis a sodium strontium niobate via (emim)OAc at: A) 900 °C and B) 1100 °C. Insets show the quantitative analysis of elemental composition.

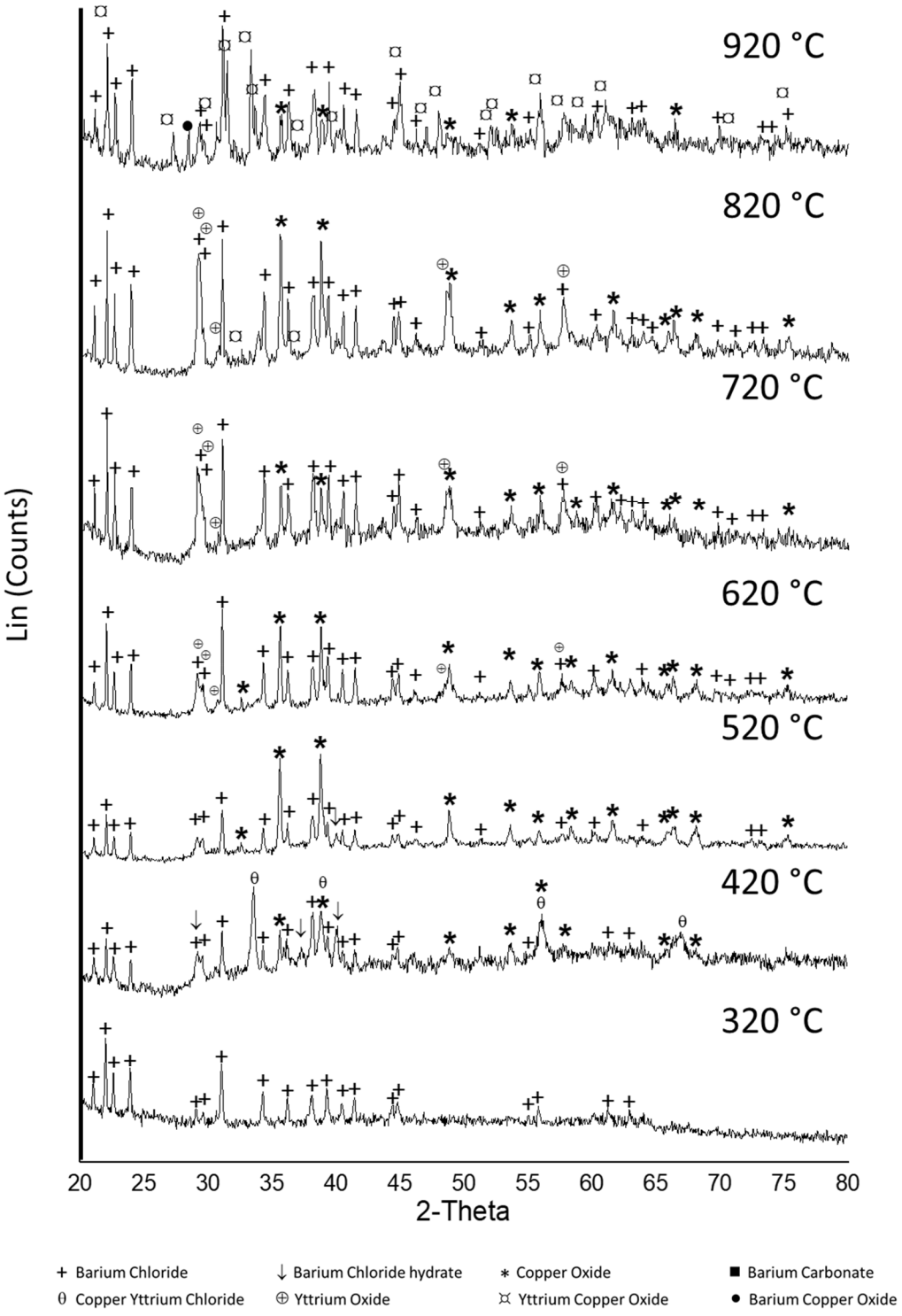

Figure A6. Temperature analysis via powder X-ray diffraction patterns of the crystal growth of the synthesis of YBCO (123) superconductor via ethylene glycol: choline chloride DES/dextran.

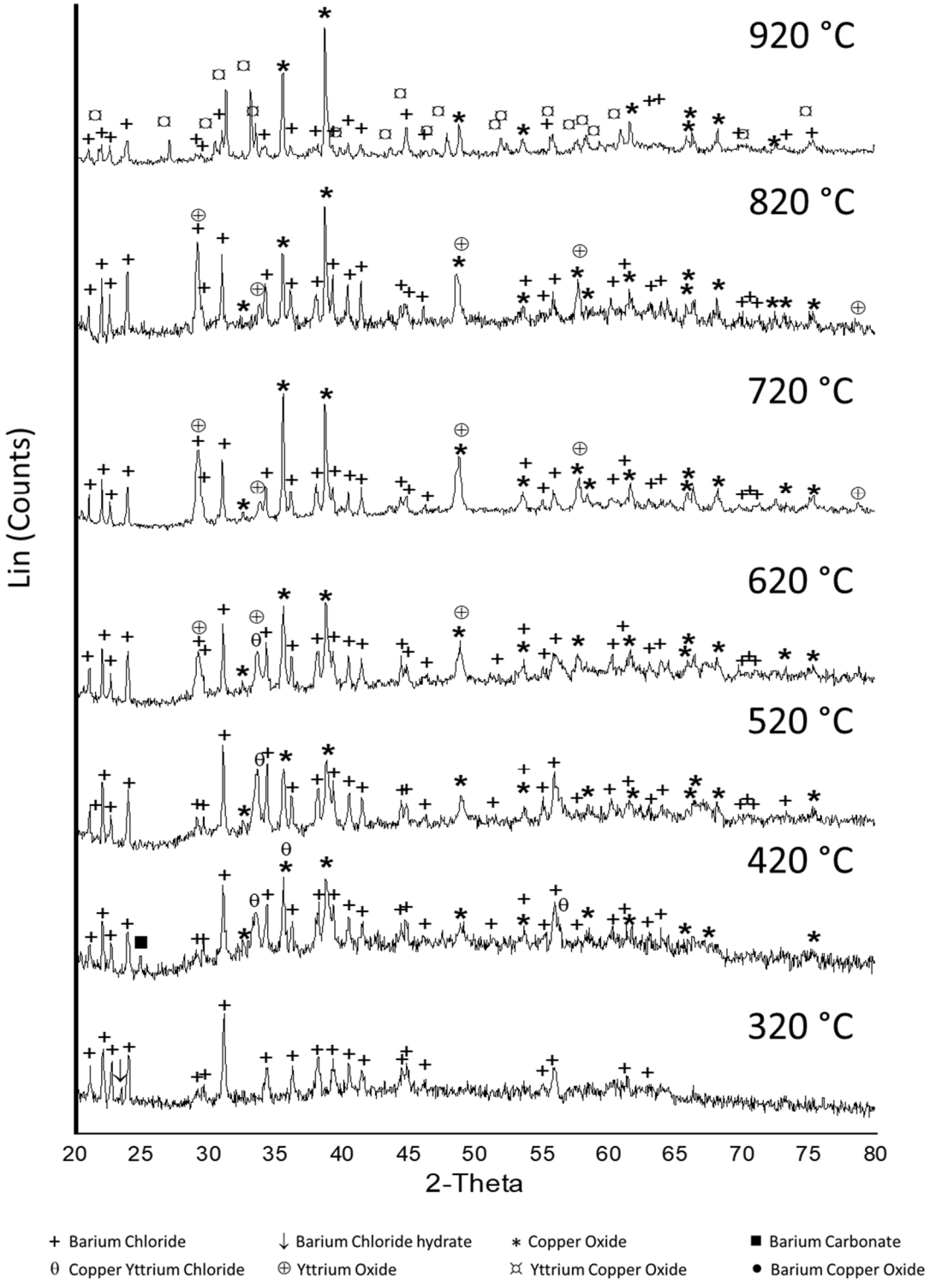

Figure A7. Temperature analysis via powder X-ray diffraction patterns of the crystal growth of the synthesis of YBCO (123) superconductor via imidazole: choline chloride DES/dextran.

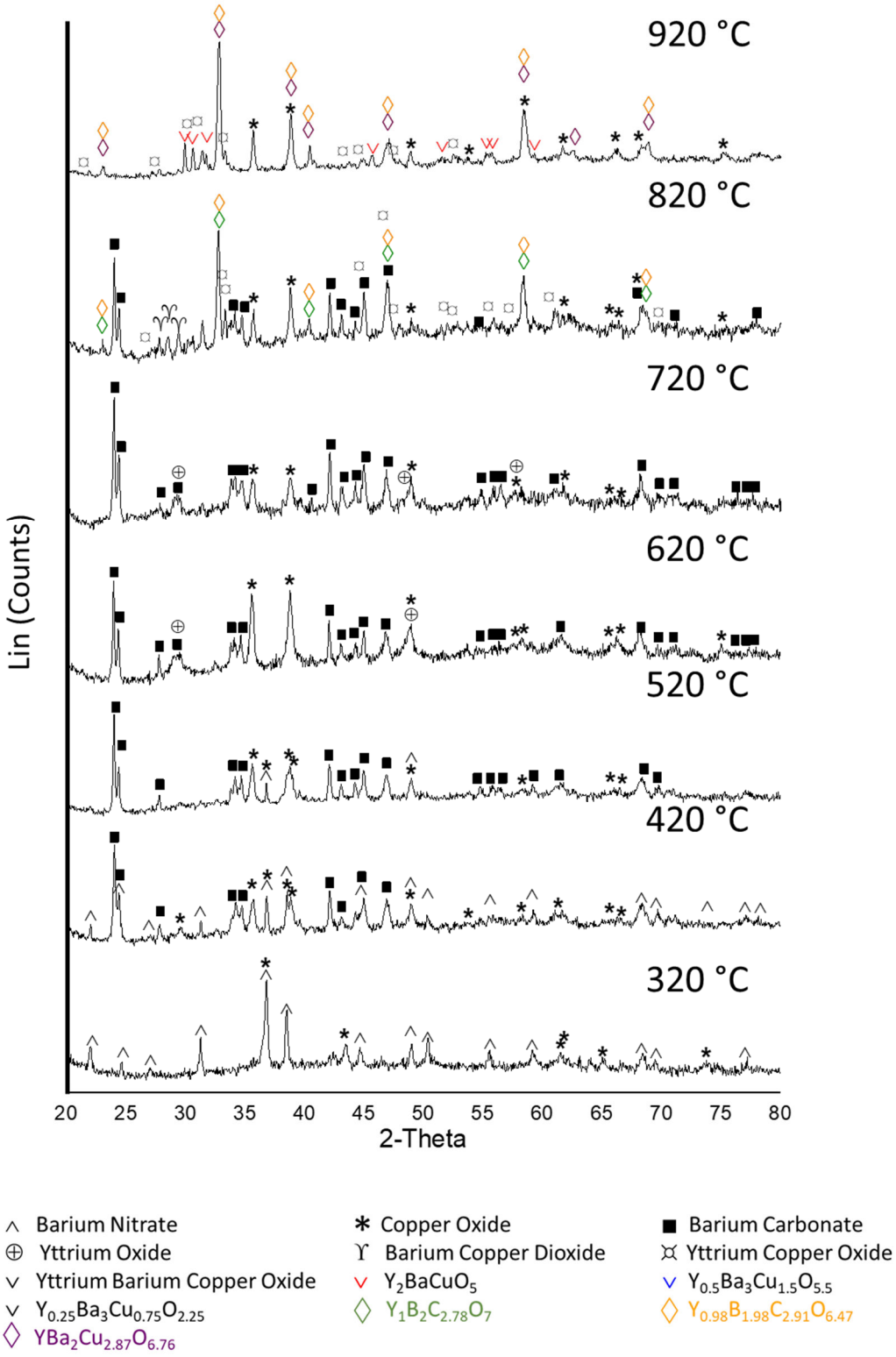

Figure A8. Temperature analysis via powder X-ray diffraction patterns of the crystal growth of the synthesis of YBCO (123) superconductor via ethylene glycol/dextran.

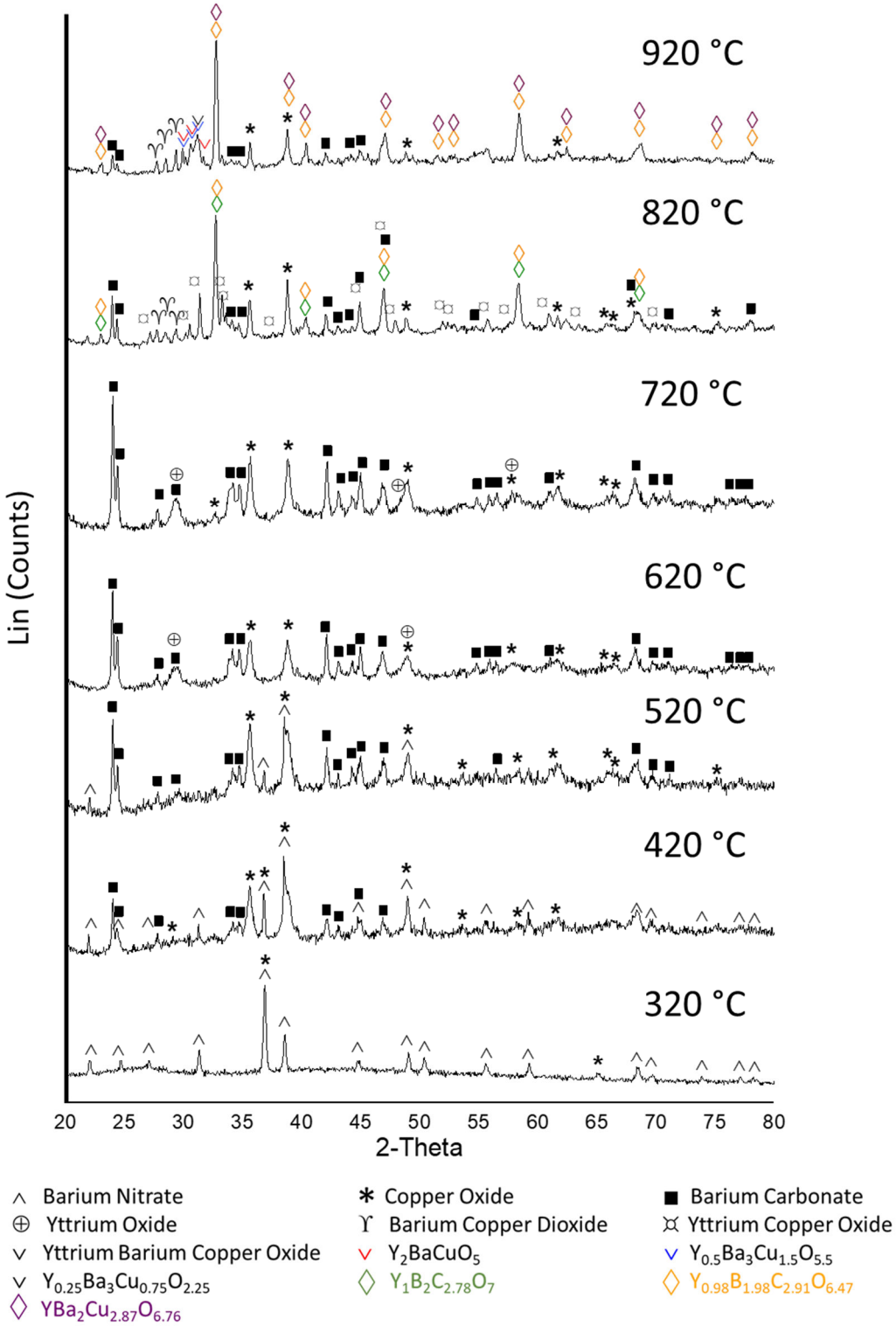

Figure A9. Temperature analysis via powder X-ray diffraction patterns of the crystal growth of the synthesis of YBCO (123) superconductor via imidazole/dextran.

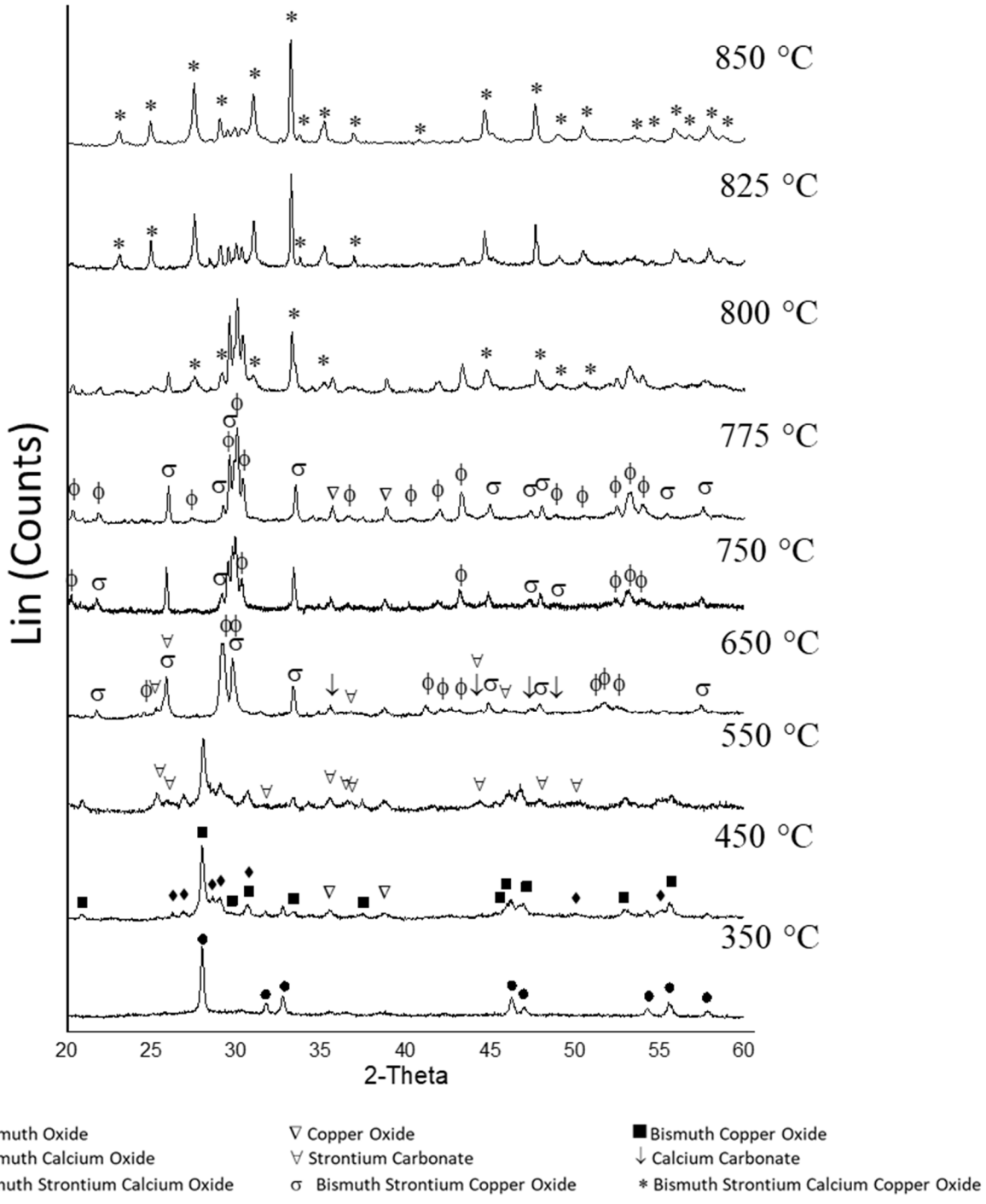

Figure A10. Temperature analysis via powder X-ray diffraction patterns of the crystal growth of the synthesis of Bi-2212 superconductor via betaine: glucose DES aged 21 days.